이학박사 학위논문

Optimizing Electronic Properties of Single-Layer Graphene for Device Applications by Noncovalent Chemical Doping

비공유 화학적 도핑을 이용한 단일층 그래핀 소자의 전자특성 최적화

2022 년 8 월

서울대학교 대학원

화학부 물리화학 전공

김 화 랑

Optimizing Electronic Properties of Single-Layer Graphene for Device Applications by Noncovalent Chemical Doping

Advisor: Byung Hee Hong

Submitting a Ph.D. Dissertation of Chemistry
August 2022

Seoul National University
Graduate School
Department of Chemistry

Hwa Rang Kim

Confirming the Ph.D. Dissertation written by
Hwa Rang Kim
June 2022

Chair	Jung Ho Lee	(Seal)
Vice Chair	Byung Hee Hong	(Seal)
Examiner	Sung-Pyo Cho	(Seal)
Examiner	Dongha Shin	(Seal)
Examiner	Youngsoo Kim	(Seal)

Abstract

Optimizing Electronic Properties of Single-Layer Graphene for Device Applications by Noncovalent Chemical Doping

Hwa Rang Kim
Department of Chemistry
Graduate School
Seoul National University

Since its first discovery as a flake-form from mechanical exfoliation of highly-oriented pyrolytic graphite (HOPG) using tape in 2004, numerous studies have shown that graphene has outstanding and extraordinary thermal, mechanical, electrical, electronic and optical properties. In 2009, large-area synthesis of polycrystalline graphene using a chemical vapor deposition (CVD) method became experimentally possible, thereby establishing a foothold for the graphene to be applied to various fields. In particular, the field of application using electrical and electronic characteristics of graphene is in the spotlight. Graphene is a remarkable material with high electron mobility, electrical conductivity and thermal conductivity. Furthermore, the pristine single-layer graphene (SLG) has zero gap, a theoretical value calculated by a tight-binding (TB) approximation model.

Engineering the electronic properties of materials is an essential process for application to electronic devices, and doping is one of the methods mainly used to control electronic properties. By doping graphene, electrical and electronic characteristics such as band gap, electrical conductivity, and work function (WF) can be modified and controlled. Doping methods for graphene include atomic substitution, applying electric field, physisorption (physical adsorption) of molecules and metal nanoparticles, etc. Among those methods, the physisorption is widely used as a graphene doping method because it can obtain a simple and superior doping effect without crystallographic defects. This paper describes researches on optimization methods of the electronic properties of graphene synthesized by CVD

method and its applications of electronic devices. Noncovalent chemical doping by the physisorption was selected as the optimization method of the electronic properties of graphene, and the possibility of application of the doped graphene to an electronic device was verified.

Chapter 1 delineates the physical properties of graphene, focusing on the electrical and electronic properties. In addition, the doping method used in the study and the charge transfer phenomenon of doped graphene were introduced.

Chapter 2 gives a detailed description of the procedure such as the synthesis, transfer, and doping methods of graphene. Graphene used in these researches was synthesized by CVD method, and the synthesized graphene was manufactured as electronic device specimens through copper etching and transfer processes. Graphene is chemically doped by the physisorption method using various nanomaterials such as molecules forming self-assembled monolayers (SAM). Through Raman spectroscopy, the quality of graphene specimens immediately after synthesis and doping process was evaluated. Moreover, the electronic properties of graphene were analyzed by a 3-electrode system using field-effect transistor (FET) devices

Chapter 3 depicts a study on electronic devices showing changes in chemical doping effects by sequentially providing various nanomaterials to graphene synthesized by CVD method. Gold nanoparticles were used as dopants on the surface of graphene by physisorption for a noncovalent functionalization, and the doped graphene was manufactured as FET devices. SAM is formed by adsorbing 4-mercaptobenzoic acid (4-MBA) molecules onto gold nanoparticles on the manufactured graphene device. And then, if mercury ions are injected, a carboxyl group of 4-MBA molecules constructing SAM acts as a ligand to capture mercury ions, thereby assembling a chelate complex. Through the analyses of the electronic properties of the graphene FET devices in each step, it can be seen that the doping effect of the graphene surface is finely adjusted by each nanomaterial element. Through this study, the possibility of chemical functionalization of graphene FET devices was exactly clarified.

Chapter 4 describes the improvement in the performance of graphene thermoelectric devices using n-type doping by introducing *n*-alkylamine (H_2NC_n) molecules onto SLG film synthesized by CVD method. The *n*-alkylamine molecules form SAM on the surface of graphene and provide electrons to graphene through noncovalent functionalization. Graphene doped by *n*-alkylamine molecules with different lengths of carbon chain was manufactured as FET devices and analyzed by a 3-electrode system. Graphene FET devices were proved clearly that the concentration of charge carriers of graphene specimens could be regulated by chemical doping method using each molecule. Graphene thermoelectric devices was manufactured by sequentially stacking a gallium oxide (Ga_2O_3) thin film layer and a eutectic gallium-indium alloy (EGaIn) bulk layer onto the *n*-alkylamine SAM formed on each graphene specimen. An induced-gap state was introduced into the graphene layer in graphene thermoelectric devices (SLG//H_2NC_n//Ga_2O_3/EGaIn) by noncovalent junctions of *n*-alkylamine molecules. Through comparison with thermoelectric devices with a conventional structure (Au/SC_n/Ga_2O_3/EGaIn) composed of the junction of gold thin film layer and *n*-alkanethiolates (SC_n) molecules, it was shown that the graphene thermoelectric devices produced by the above method have improved and outstanding thermoelectric properties.

Keyword: graphene, chemical doping, self-assembled monolayer, noncovalent functionalization, field-effect transistor, thermoelectric device

Student Number: 2016-20339

Table of Contents

List of Tables

Chapter 1.

Chapter 2.

Chapter 3.

Chapter 4.

List of Figures

Chapter 1.

Chapter 2.

Chapter 3.

Chapter 4.

Chapter 1.

Introduction to Graphene

1. 1. Discovery and Advancement of Graphene

Graphene is a unique and eccentric material. Single-layer graphene (SLG) was studied theoretically by P. R. Wallace in 1947 for understanding the electronic characteristics of 3-dimensional (3D) graphite.[**1**] Prior to its discovery, there was a hypothesis that the existence of graphene was impossible accordance with Mermin-Wagner theorem of condensed matter physics in 1968.[**2**] This theorem means that symmetries in 0-, 1-, or 2-dimensional (0D, 1D, or 2D) systems cannot be broken spontaneously at finite temperatures. In other words, even if a system is composed of well-ordered atoms, the order of the whole system is broken by small fluctuations that occur accidentally. Therefore, graphene was believed to be structurally unstable for a lone time.

Graphene, however, is a 2D material first introduced to the world by K. S. Novoselov and A. K. Geim in 2004.[**3**] **(Figure 1-1)** SLG, however, was isolated by repeated mechanical exfoliation from highly-oriented pyrolytic graphite (HOPG). They pulled and rubbed Scotch tape with graphene few layers onto silicon oxide (SiO_2) thin film on a silicon wafer. This very simple method called Scotch tape technique is mainly used to obtain single-crystalline graphene flakes for solid state physics research.

Since discovery of graphene, numerous studies have been conducted to synthesize graphene in a large-area. Finally, Korean scientist B. H. Hong succeeded in synthesizing large-area few layer graphene using the chemical vapor deposition (CVD) method.[**4**] **(Figure 1-2)** The first synthesis method was to synthesize graphene on a nickel metal catalyst using methane gas as a precursor, and then it was changed to a method mainly using copper as a metal catalyst for single-layer synthesis.[**5**] **(Figure 1-3)** Recent research trends related to large-area synthesis have been continuing to synthesize and commercialize single-crystalline graphene by changing carbon precursor, metal catalysts, synthesis temperature, and experimental systems, etc.[**6**,**7**]

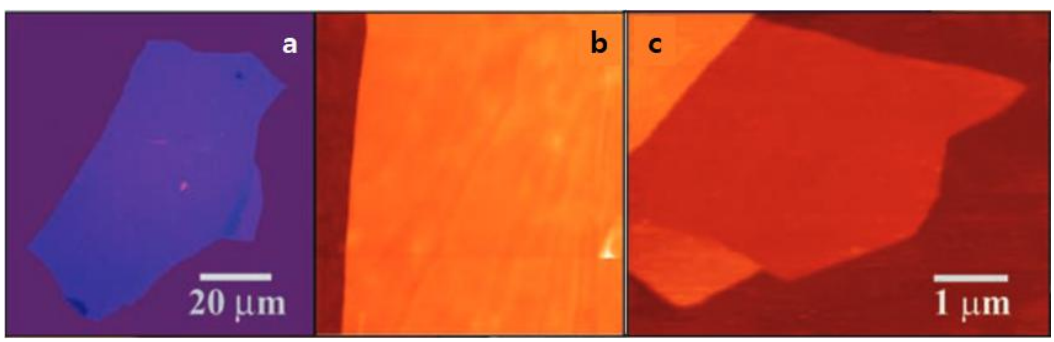

Figure 1-1. Graphene films by exfoliation. (a) Optical microscope (OM) image of a relatively large multi-layer graphene (MLG) flake with thickness ~3 nm on SiO_2 layer. (b) Atomic force microscope (AFM) image of 2 μm by 2 μm area of the edge of graphene flake with height 3 nm above SiO_2 layer. (c) AFM image of SLG film near the bottom, which exhibits a differential height of ~0.4 nm. (Reprinted from ref. [**3**], Copyright 2004 American Association for the Advancement of Science)

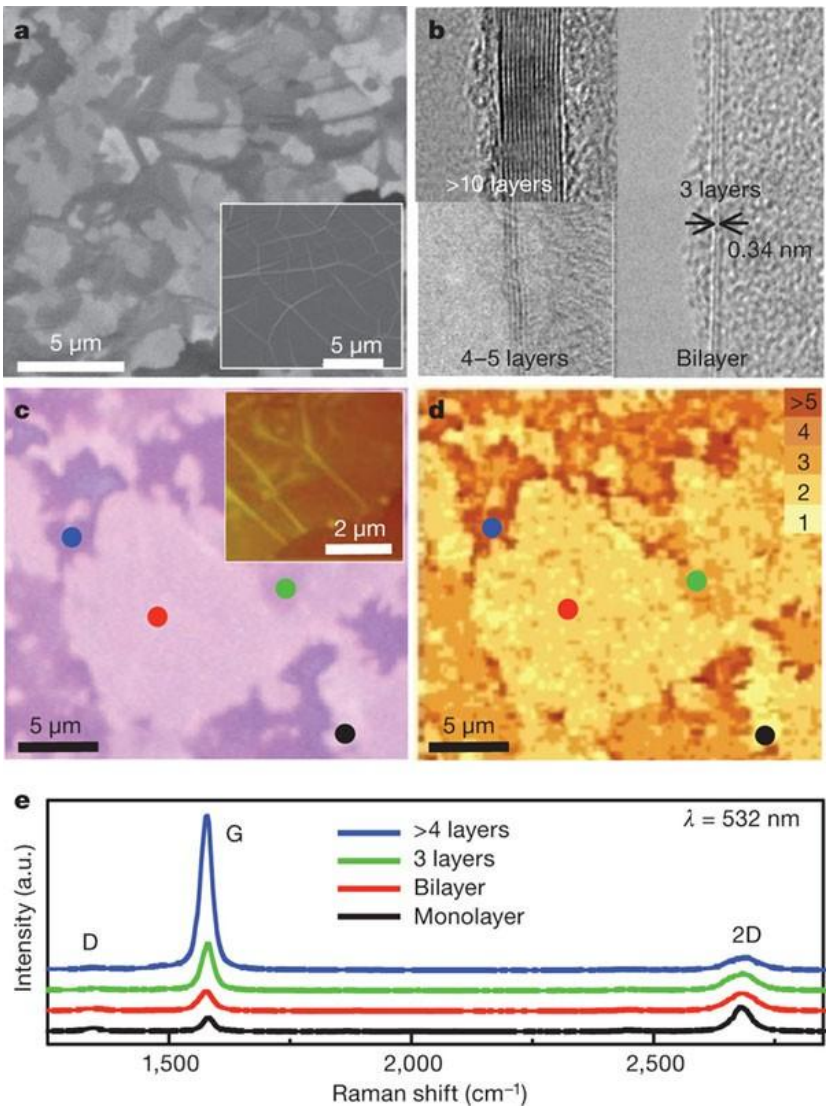

Figure 1-2. Graphene films on Ni by CVD method. (a) Scanning electron microscope (SEM) images of as-grown graphene films on 300 nm nickel thin films and 1mm Ni thick foils (inset). (b) Transmission electron microscope (TEM) images of graphene films of different thicknesses. (c) OM image of the graphene film transferred to a 300 nm SiO_2 layer. The inset AFM image shows typical rippled structures. (d) A confocal scanning Raman image corresponding to (c). The number of layers is estimated from the intensities, shapes and positions of the G and 2D band peaks. (e) Raman spectra (532 nm laser wavelength) obtained from the corresponding colored spots in (c) and (d). a.u., arbitrary units. (Reprinted from ref. [**4**], Copyright 2009 Nature Publishing Group)

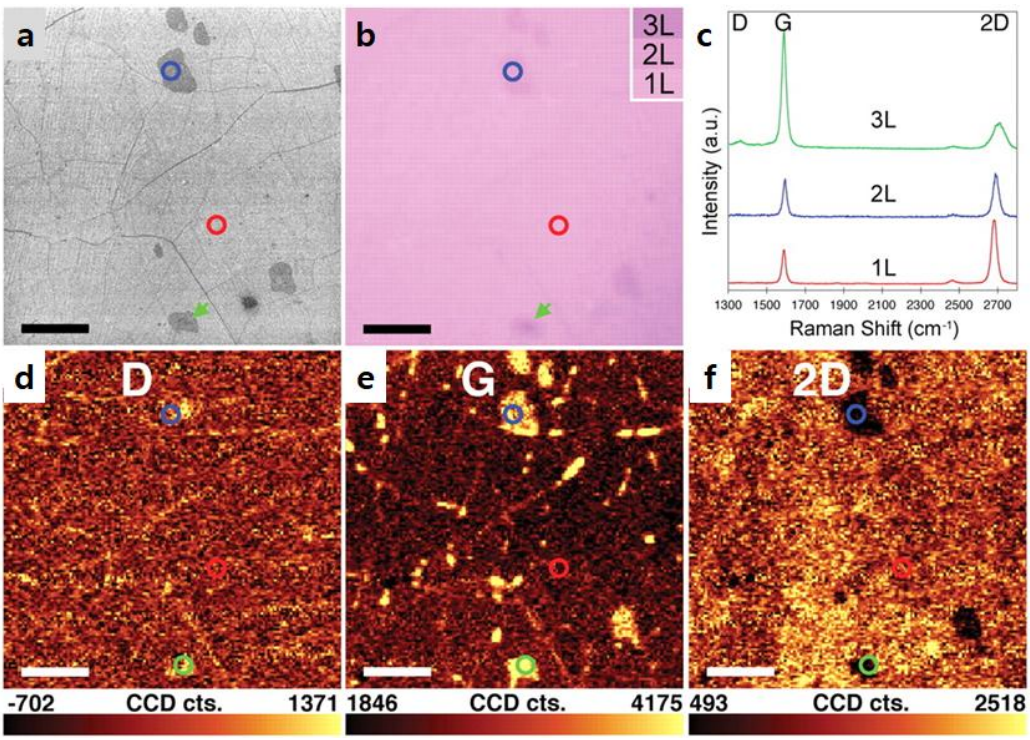

Figure 1-3. Graphene films on Cu by CVD method. (a) SEM image of graphene transferred on 285 nm SiO_2 layer, showing wrinkles, as well as double- and triple-layer regions. (b) OM image of the same regions as in (a). (c) Raman spectra (532 nm laser wavelength) from the marked spots with corresponding colored circles or arrows showing the presence of single-, double-, and triple-layers of graphene. a.u., arbitrary units. (d to f) Raman mapping images of (d) the D (1300 to 1400 cm^{-1}); (e) G (1560 to 1620 cm^{-1}); and (f) 2D (2660 to 2700 cm^{-1}) bands, respectively. CCD cts., charge-coupled device counts. Scale bars, 5 μm. (Reprinted from ref. [**5**], Copyright 2009 American Association for the Advancement of Science)

1. 2. Structure of Graphene

1. 2. 1. Hexagonal Lattice: Electronic Configurations of Carbon Atoms

The structure of graphene, strictly speaking, refers to a single-layer plane of a hexagonal honeycomb lattice in which carbon atoms are covalently bonded.[**8**–**10**] **(Figure 1-4g and 1-4h)** One carbon atom has six electrons, **(Figure 1-4a)** which have an electronic configuration of $1s^2 2s^2 2p_x^1 2p_y^1 2p_z^0$ in the ground state.[**10**–**12**] **(Figure 1-4b, 1-5a and 1-6b)**

According to valence bond theory (VBT), it is explained that covalent bonds are formed in such a way that valence orbitals with unpaired electrons approach and overlap each other to form electron pairs. In VBT, bonds are largely classified into σ bond and π bond. However, new concepts such as promotion and hybridization should be introduced and explained in the case of molecules that cannot be explained by VBT alone. Promotion of electrons is a concept introduced to explain that the number of bonds is more than that of unpaired electrons, and refers to the excitation process of replacing already paired electrons at lower energy levels as unpaired electrons at higher energy levels by absorbing energy. **(Figure 1-5b)** In addition, hybridization is a concept introduced to explain a phenomenon in which the bond length of certain molecules (e.g., methane) bonded through electron promotions is the same. **(Figure 1-5c)**

As the electrons of one carbon atom are excited by the electronic configuration **(Figure 1-5b)**,[**10**–**12**] one carbon atom covalently bonds the adjacent two, three or four carbon atoms through sp, sp^2 or sp^3 hybridized orbital, respectively.[**11**,**12**] **(Figure 1-5c)** Among them, sp^2 hybridized orbitals participate in the bonding between carbon atoms constituting graphene. The covalent bond between sp^2 (also sp or sp^3) hybridized orbitals is called σ bond.[**10**,**13**] **(Figure 1-4e)** Meanwhile, the $2p_z$ orbital in which one remaining outer-shell electron is located exists perpendicular to the plane where the σ bond by sp^2 hybridized orbitals is located. Attraction also acts among the $2p_z$ orbitals of surrounding atoms, and this additional out-of-plane bond is called a π bond.[**10**,**13**] **(Figure 1-4e)**

Molecular orbital theory (MOT) is another theory that explains chemical bonds along with VBT. VBT assumes that electrons are localized and only valence electrons participate in bonds, while MOT assumes that electrons are delocalized and all electrons in atoms participate in bonds. When carbon atoms get closer to each other, atomic orbitals also overlap to form molecular orbitals. **(Figure 1-6a)** Linear combination of atomic orbitals (LCAO) is introduced as a mathematical technique to explain the bond between

two carbon atoms. In this situation, if the electrons of the two carbon atoms are filled from the low energy level of the molecular orbital formed by MOT, all electrons are paired, and no unpaired electrons remain. **(Figure 1-6b)** This is a property shared by all carbon allotropes and can explain their zero paramagnetic contributions.[**12**] Of course, graphene belongs to the carbon allotropes.[**12**,**14**] **(Figure 1-7)**

Ultimately, graphene is naturally placed in a stable energy state. The resulting bond order is $4/3$. The bond length of graphene (or lattice constant) is 0.142 nm, which is the distance between two closest carbon atoms,[**8**,**10**] and the distance between of an atom and the second neighboring atom is 0.246 nm. **(Figure 1-4f)** In addition, the height of SLG is 0.335 nm, which is an interplanar spacing in graphite.[**15**]

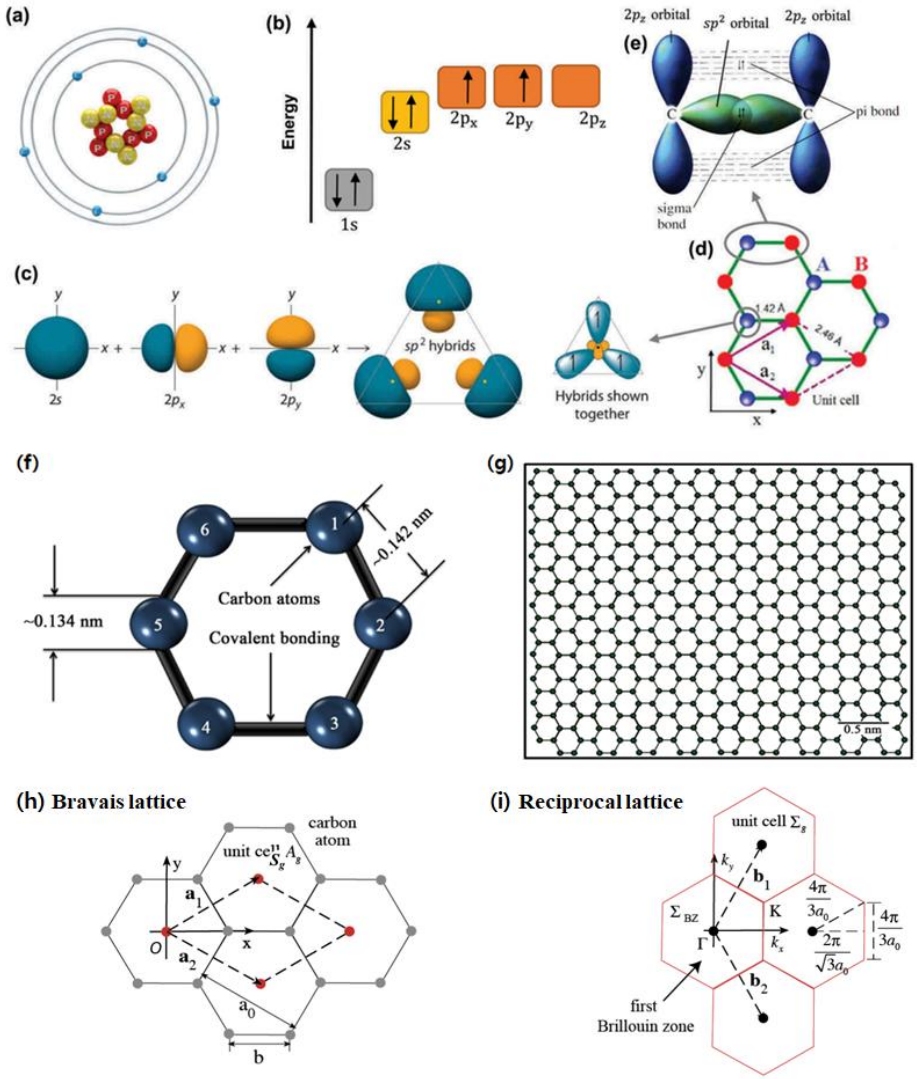

Figure 1-4. The description of graphene hexagonal lattice. (a) Atomic structure of a carbon atom. (b) Energy levels of outer electrons in carbon atoms. (c) The formation of sp^2 hybridized orbitals. (d) The crystal lattice of graphene, where A and B are carbon atoms belonging to different sub-lattices, $\boldsymbol{a}_1$ and $\boldsymbol{a}_2$ are unit-cell vectors. (e) σ bond formed by sp^2 hybridized orbitals and π bond formed by $2p_z$ orbitals. (Reprinted from ref. [**10**], Copyright 2018 Taylor and Francis Ltd.) (f) Schematic diagram of hexagonal cell of graphene structure. (g) Graphene sheet comprising of 2D hexagonal network of carbon atoms combined by strong covalent bonding by sp^2 hybridized orbitals and $2p_z$ orbitals. (Reprinted from ref. [**8**], Copyright 2016 Scientific Research Publishing Inc.) (h, i) The lattice of graphene; (h) Bravais lattice; (i) reciprocal lattice. (Reprinted from ref. [**9**] Copyright 2014 MDPI)

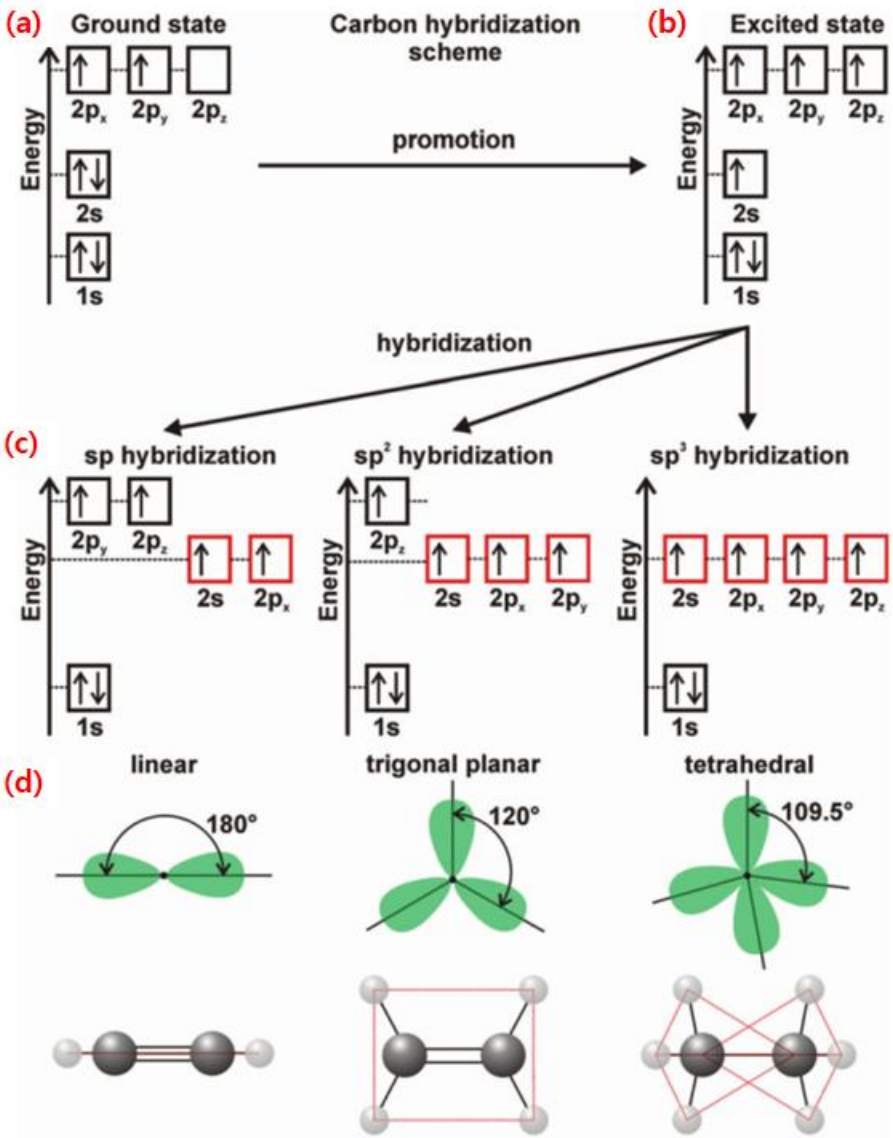

Figure 1-5. Schematic description of sp, sp^2, and sp^3 hybridization in carbon with an illustration of the bonding structure. (a) Ground state. (b) Excited state. (c) Hybridized state. (d) The types of covalent bond corresponding to hybridized states. (Reprinted from ref. [**12**], Copyright 2018 The Royal Society of Chemistry)

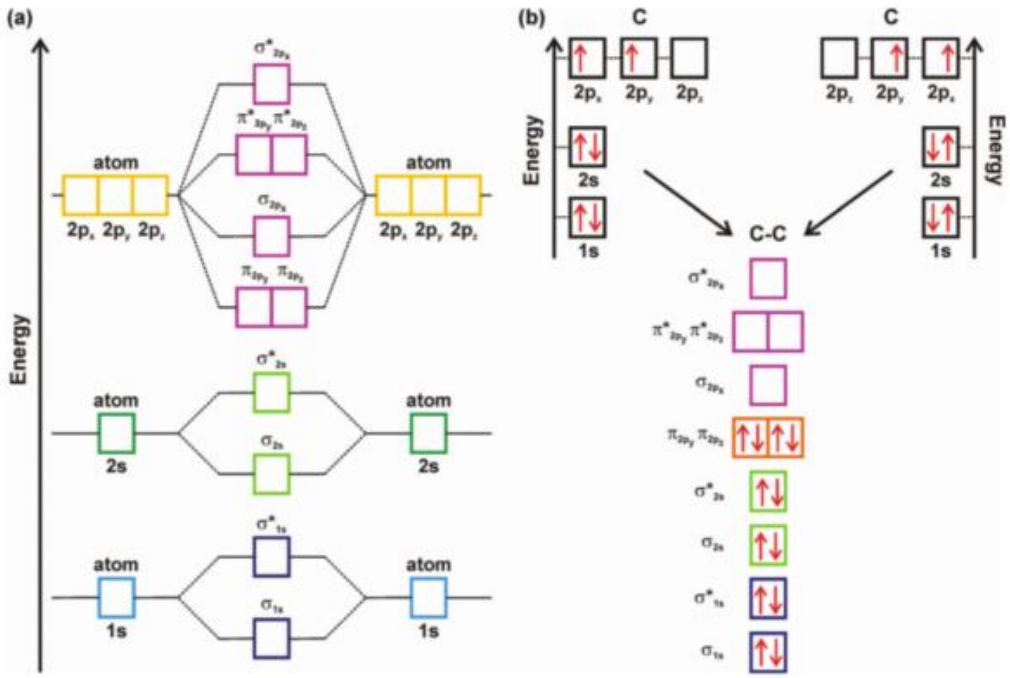

Figure 1-6. The molecular orbitals of C-C bonding. (a) General molecular orbital energy-level diagram for the first two energy levels showing the formation of molecular bonding $(s,\ p)$ and antibonding $(s^*,\ p^*)$ orbitals. (b) Bonding scheme for two carbon atoms providing evidence for pairing of all the spins, confirming thus the diamagnetic nature of the C–C pair. (Reprinted from ref. [**12**], Copyright 2018 The Royal Society of Chemistry)

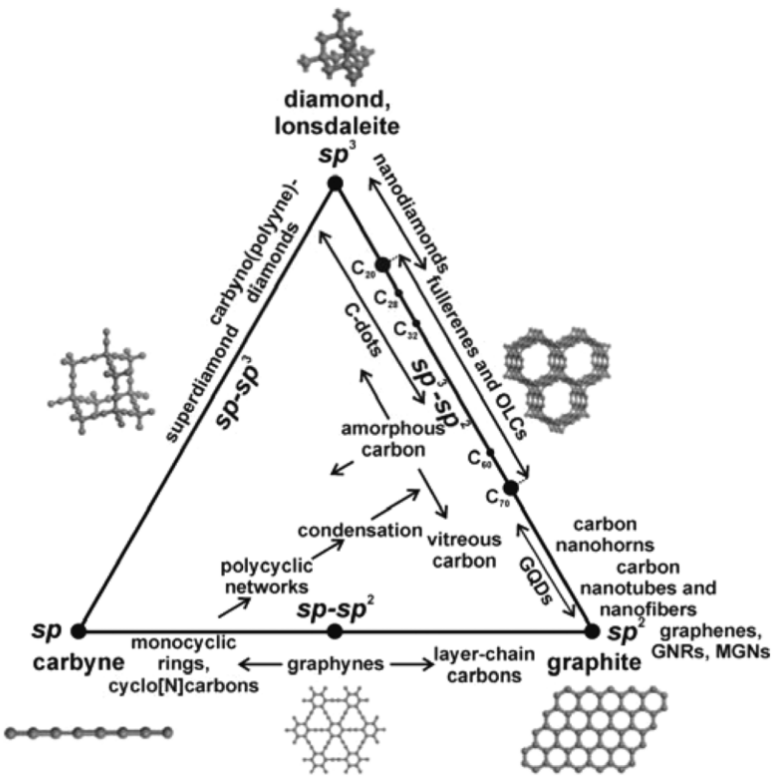

Figure 1-7. A ternary phase diagram of carbon materials. The diagram showing materials consisting of carbon in a single hybridization state at the vertices, materials containing mixtures of two hybridization states along the edges, and materials with all three hybridization states within the triangle. (Reprinted from ref. [**14**], Copyright 2015 ACS Publications)

1. 2. 2. Structural Defects of Graphene

SLG synthesized by conventional CVD method is generally polycrystalline 2D material because the metal catalyst on which graphene grows is polycrystalline.[**4**,**5**,**13**,**16**–**21**] Polycrystalline graphene sheet inevitably includes crystallographic defects such as point defect and line defect in **Figure 1-8**.[**16**–**24**]

Point defect of graphene is a generic term for Stone-Wales (SW) defects, single vacancies (SV), double vacancies (DV), carbon adatoms including inverse Stone-Wales (ISW) defects, foreign adatoms, and substitutional impurities, etc.[**17**] **(Figure 1-9)**

Line defects of graphene are dislocation-like defects.[**17**] **(Figure 1-10)** Dislocation is mainly classified into edge and screw. In the former or latter, the Burgers vector is perpendicular or parallel to the direction of dislocation line, respectively. Real dislocation appearing in 3D crystals is typically mixed dislocation. Because the conventional concept of dislocation including a Burgers vector and a dislocation line can only be represented in 3D crystals and screw dislocation in particular requires a 3D strain field, line defects of graphene are different from that of 3D crystals.

The size of grains and the arrangement of grain boundaries (GB) affect the properties of polycrystalline materials, especially 2D materials including graphene synthesis by CVD method. Crystallographic defects in graphene crystal act as a factor that degrades thermal, mechanical, electrical, electronic, and optical properties.[**16**,**17**,**25**,**26**] **(Figure 1-8)**

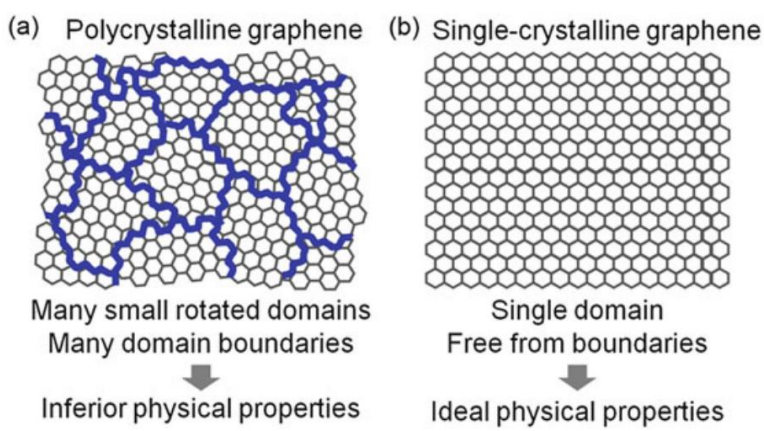

Figure 1-8. Domain structures of graphene. (a) Polycrystalline graphene generally observed for CVD grown samples. Thick lines correspond to boundaries. (b) Ideal single-crystalline graphene. Single-crystalline graphene is expected to show higher mobility and better mechanical properties than polycrystalline graphene. (Reprinted from ref. [**16**], Copyright 2015 Springer Japan)

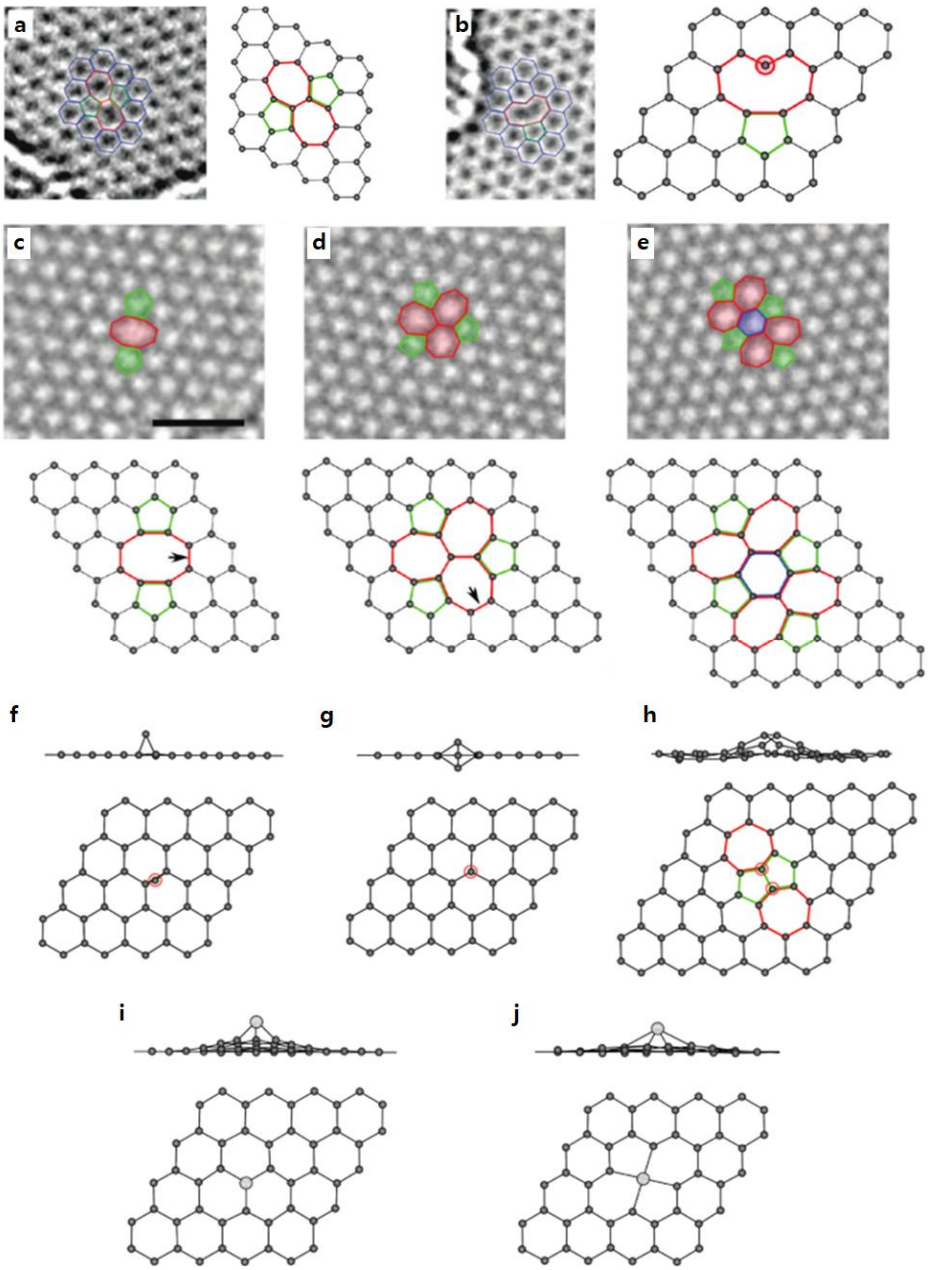

Figure 1-9. Point defects of graphene. (a) SW defect, SW(55-77). (b) SV defect, V_1(5-9). (c-e) DV defects; (c) V_2(5-8-5); (d) V_2(555-777) by rotating a bond marked in (c) from V_2(5-8-5); (e) V_2(5555-6-7777) by rotating another bond marked in (d) from V_2(555-777). (f-h) Carbon adatoms; (f) Single adatom in the bridge; (g) Single adatom in the dumbbell; (h) Double adatoms, ISW defect, I_2(7557). (i-j) Foreign adatoms (transition metal atoms) adsorbed on (i) SV; and (j) DV, respectively. (Reprinted from ref. [**17**], Copyright 2011 ACS Publications)

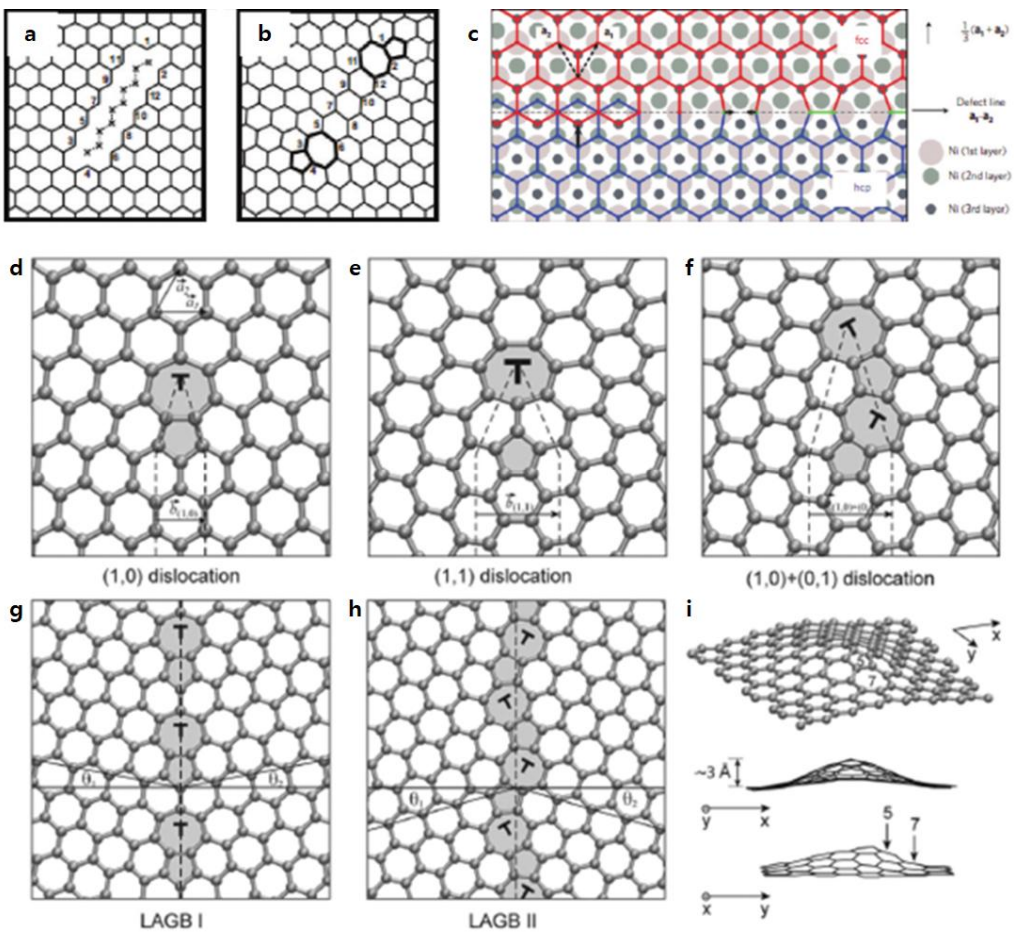

Figure 1-10. Line defects of graphene. (a, b) Line defect formation from aligned vacancy structures. (c) GB defect structure consisting of pentagon-pairs and octagons in graphene grown on a Ni substrate. (d-i) Dislocations in graphene; (d-f) Atomic structures of (d) $(1, 0)$ and (e) $(1, 1)$ dislocations; and (f) a $(1, 0) + (0, 1)$ dislocation pair, respectively; Atomic structures of (g) the $\theta = 21.8°$ large-angle GB (LAGB); and (h) the $\theta = 32.2°$ symmetric large-angle GB; (i) Buckling of the graphene layer due the presence of a $(1, 0)$ dislocation. (Reprinted from ref. [**17**], Copyright 2011 ACS Publications)

1. 3. Band structure of Graphene

1. 3. 1. Band Theory of Graphene

The electronic band theory of graphite was explored by P. R. Wallace in 1947.[**1**] He proposed a tight-binding (TB) approximation model for the first time to illuminate the band structure of SLG. TB approximation represents that the nearest-neighbor interactions are very large and decrease quickly along the increase of the distance.[**27**] In description of P. R. Wallace, nearest- and next-nearest-neighbor interactions for the $2p_z$ orbitals of graphene were considered, but the overlap among basis functions centered at different atoms was neglected.[**1**] **Figure 1-11** shows the shape of the TB wave function.[**27**]

These days, the TB approximation model developed by R. Saito *et al*. in 1998 is chiefly used, instead of the method of P. R. Wallace. The description of R. Saito *et al*. also considered nearest- and next-nearest-neighbor interactions for the $2p_z$ orbitals of graphene, and took account of the non-finite overlap among basis functions including only nearest-neighbor interactions within the graphene.[**28**]

After that, the study of TB approximation model considering third-neighbor interactions was also published by S. Reich *et al*. in 2002.[**29**] The more interactions among more distant neighbors is considered, the closer it is to the result calculated by *ab-initio* calculation.

Graphene lattice is a structure in which a hexagonal lattice system of carbon atoms is spread out on an infinite plane. In order to analyze the band structure of a material, the concept of the reciprocal space must be introduced. First, a unit cell containing two carbon atoms is determined from the Bravais lattice of graphene in the real space, **(Figure 1-4h and 1-12a)** and then a reciprocal lattice corresponding thereto is drawn in the reciprocal space.[**1**,**9**–**11**,**28**–**32**] **(Figure 1-4i and 1-12b)**

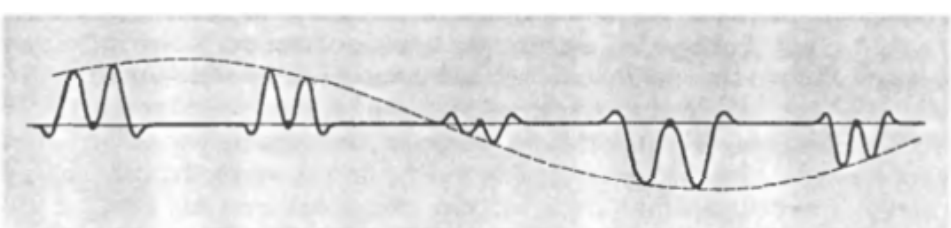

Figure 1-11. Characteristic spatial variation of the real (or imaginary) part of the TB wave function. (Reprinted from ref. [**27**], Copyright 1976 Harcourt, Inc.)

1. 3. 2. Lattice Vector and Reciprocal Lattice Vector

In this thesis, the band theory of graphene using TB approximation model by R. Saito *et al*. is introduced. The lattice vector ($\boldsymbol{a}_1$ or $\boldsymbol{a}_2$) is directed from a carbon atom (red) in unit cell shown in **Figure 1-12a** to each next-nearest-neighbor atom, respectively. Prior to the development of the equation, the vectors in this paper is indicated by the Cartesian coordinates. The position of each carbon atom in the real space is indicated by a vector $\boldsymbol{R}$ which is defined as

$$\boldsymbol{R} = n_1\boldsymbol{a}_1 + n_2\boldsymbol{a}_2 \tag{1-1}$$

where n_1 and n_2 are two integers, and the values of the lattice vectors $\boldsymbol{a}_1$ and $\boldsymbol{a}_2$ are given by

$$\boldsymbol{a}_1 = a\left(\frac{3}{2}, \frac{\sqrt{3}}{2}\right),\ \boldsymbol{a}_2 = a\left(\frac{3}{2}, -\frac{\sqrt{3}}{2}\right), \tag{1-2}$$

Where a is the lattice constant, 0.142 nm. In addition, the positions of the nearest-neighbor atoms can be written as

$$\boldsymbol{\delta}_1 = a\left(\frac{1}{2}, \frac{\sqrt{3}}{2}\right),\ \boldsymbol{\delta}_2 = a\left(\frac{1}{2}, -\frac{\sqrt{3}}{2}\right),\ \boldsymbol{\delta}_3 = a(-1,\ 0), \tag{1-3}$$

and the positions of the next-nearest-neighbor atoms are given by

$$\boldsymbol{\delta'}_{\pm1} = \pm\boldsymbol{a}_1,\ \boldsymbol{\delta'}_{\pm2} = \pm\boldsymbol{a}_2,\ \boldsymbol{\delta'}_{\pm3} = \pm(\boldsymbol{a}_2 - \boldsymbol{a}_1), \tag{1-4}$$

which is expressed as unit vectors in **Equation (1-2)**. The reciprocal vectors must satisfy the following conditions: $\boldsymbol{a}_i \cdot \boldsymbol{b}_j = 2\pi\delta_{ij}$, where a_i is the vector represented in **Equation (1-2)**, δ_{ij} is Kronecker delta defined as $\delta_{ij} = \begin{cases} 0 & (i \neq j) \\ 1 & (i = j) \end{cases}$, and then the reciprocal vectors shown in **Figure 1-12b** are placed at

$$\boldsymbol{b}_1 = \frac{2\pi}{a}\left(\frac{1}{3}, \frac{\sqrt{3}}{3}\right),\ \boldsymbol{b}_2 = \frac{2\pi}{a}\left(\frac{1}{3}, -\frac{\sqrt{3}}{3}\right) \tag{1-5}$$

corresponding to a lattice constant of $4\pi/3a$ in reciprocal space. The remarkable points in **Figure 1-12b** are high-symmetry points $\boldsymbol{\Gamma}$, $\boldsymbol{K}$, $\boldsymbol{K'}$, and $\boldsymbol{M}$ in the first Brillouin zone

(BZ), which are located at its center, its corners and the center of its sides, respectively. Each point can be written as

$$\boldsymbol{\Gamma} = (0,\ 0),\ \boldsymbol{M} = \frac{2\pi}{3a}(1,\ 0),\ \boldsymbol{K} = \frac{2\pi}{3a}\left(1,\ \frac{\sqrt{3}}{3}\right),\ \boldsymbol{K'} = \frac{2\pi}{3a}\left(1,\ -\frac{\sqrt{3}}{3}\right). \qquad \textbf{(1-6)}$$

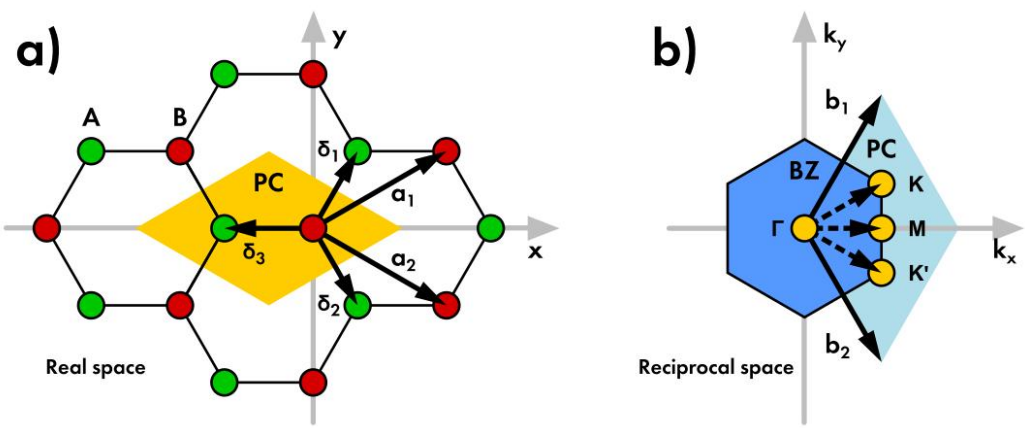

Figure 1-12. Graphene Lattice in the real and the reciprocal spaces. (a) Graphene structure in the real space. The atoms are distinguished in accordance to the two sub-lattices *A* (green) and *B* (red) to which they belong. Unit vectors ($\boldsymbol{a_1}$ and $\boldsymbol{a_2}$) and nearest-neighbor vectors ($\boldsymbol{\delta_1}$, $\boldsymbol{\delta_2}$ and $\boldsymbol{\delta_3}$) are marked. The unit cell (primitive cell; PC) is highlighted (yellow area). (b) Corresponding reciprocal lattice of graphene. Reciprocal unit vectors ($\boldsymbol{b_1}$ and $\boldsymbol{b_2}$), and the high-symmetry points $\boldsymbol{\Gamma}$, $\boldsymbol{K}$, $\boldsymbol{K'}$, and $\boldsymbol{M}$ (yellow) are marked. The unit cell and the first BZ are highlighted (blue area). (Reprinted from ref. [**11**], Copyright 2019 MDPI)

1. 3. 3. Bloch Theorem

The TB approximation is developed under the assumption that each atom has a weak interaction with other atoms. According to Bloch theorem, the wave function of particles in a space with a periodic potential appears in the form in which the function of a plane wave is modulated by a periodic function. In other words, the electrons present inside a crystal with a periodic potential are independent of translations along the lattice vectors. Bloch theorem is satisfied with the following equation:

$$T_{\boldsymbol{a}_i}\psi = \mathrm{e}^{\mathrm{i}\boldsymbol{k}\cdot\boldsymbol{a}_i}\psi, \tag{1-7}$$

where, $T_{\boldsymbol{r}}$ is a translation operator along the direction of a vector $\boldsymbol{r}$ which is position in a real space, and a wave function ψ is an eigenstate of all of translation operators, and wave vector $\boldsymbol{k}$ is crystal momentum vector, which is can be written as a linear combination of the reciprocal lattice vectors:

$$\boldsymbol{k} = k_1\boldsymbol{b}_1 + k_2\boldsymbol{b}_2. \tag{1-8}$$

Meanwhile, the mathematical technique for reconstructing the total wave function of an unknown system is to use the LCAO for each element constituting the system. To do this, the wave function of each element must be known in advance. LCAO technique is also used to find the total wave function of the polyatomic system, and then each element is each single atom.[**28**,**31**,**33**,**34**] In general, the form of a wave function is LCAO for plane waves, which is easy for the integration of wave functions and has numerical accuracy by only dependence on the number of wave functions.[**28**] On the other hand, the difficulty of representing atomic orbitals in a crystal as the wave functions of plane waves and a large scale of computation are the disadvantages for LCAO.[**28**] Despite its limitations that there are no simple method to improve numerical accuracy and no information on the interatomic region, TB approximation model using LCAO has the advantage of having fewer the number of basis functions than that of plane waves and ease of modification of many physical properties.[**28**]

A periodic function, which satisfies Bloch theorem, has the same periodicity (as the crystal) and can be expressed as $u(\boldsymbol{r})$. As an equation, it can be denoted as $u(\boldsymbol{r}) = u(\boldsymbol{r} + \boldsymbol{a}_i)$, which, that is, means

$$u(\boldsymbol{r}) = u(\boldsymbol{r} + \boldsymbol{R}). \tag{1-9}$$

The Bloch function ψ is the following equation:

$$\psi(\boldsymbol{k}, \boldsymbol{r}) = \mathrm{e}^{\mathrm{i}\boldsymbol{k}\cdot\boldsymbol{r}} u(\boldsymbol{r}). \tag{1-10}$$

Bloch Theorem is stated in this form:

$$\psi(\boldsymbol{k}, \boldsymbol{r} + \boldsymbol{R}) = \mathrm{e}^{\mathrm{i}\boldsymbol{k}\cdot\boldsymbol{R}} \psi(\boldsymbol{k}, \boldsymbol{r}) \tag{1-11}$$

for every position of atom $\boldsymbol{R}$ in the Bravais lattice, by the combination of **Equation (1-9) and (1-10)**.

If n atoms in a unit cell in a crystal, n atomic wave functions φ_j exist in a unit cell. A TB Bloch function ϕ_j of j-th atom in the solid can be written as

$$\phi_j(\boldsymbol{k}, \boldsymbol{r}) = \frac{1}{\sqrt{N}} \sum_{\boldsymbol{R}}^{N} \mathrm{e}^{\mathrm{i}\boldsymbol{k}\cdot\boldsymbol{R}} \varphi_j(\boldsymbol{r} - \boldsymbol{R}), \qquad (j = 1, \cdots, n), \tag{1-12}$$

where N is the number of unit cells in solid crystal. The proof that $\phi_j(\boldsymbol{k}, \boldsymbol{r})$ is a Bloch function is the following relations:

$$\begin{aligned}
\phi_j(\boldsymbol{k}, \boldsymbol{r} + \boldsymbol{R}') &= \frac{1}{\sqrt{N}} \sum_{\boldsymbol{R}}^{N} \mathrm{e}^{\mathrm{i}\boldsymbol{k}\cdot\boldsymbol{R}} \varphi_j\big((\boldsymbol{r} + \boldsymbol{R}') - \boldsymbol{R}\big) \\
&= \frac{1}{\sqrt{N}} \sum_{\boldsymbol{R}}^{N} \mathrm{e}^{\mathrm{i}\boldsymbol{k}\cdot\left((\boldsymbol{R}-\boldsymbol{R}')+\boldsymbol{R}'\right)} \varphi_j\big(\boldsymbol{r} - (\boldsymbol{R} - \boldsymbol{R}')\big) \\
&= \frac{1}{\sqrt{N}} \sum_{\boldsymbol{R}}^{N} \mathrm{e}^{\mathrm{i}\boldsymbol{k}\cdot\boldsymbol{R}'} \mathrm{e}^{\mathrm{i}\boldsymbol{k}\cdot(\boldsymbol{R}-\boldsymbol{R}')} \varphi_j\big(\boldsymbol{r} - (\boldsymbol{R} - \boldsymbol{R}')\big) \\
&= \mathrm{e}^{\mathrm{i}\boldsymbol{k}\cdot\boldsymbol{R}'} \frac{1}{\sqrt{N}} \sum_{\boldsymbol{R}-\boldsymbol{R}'}^{N} \mathrm{e}^{\mathrm{i}\boldsymbol{k}\cdot(\boldsymbol{R}-\boldsymbol{R}')} \varphi_j\big(\boldsymbol{r} - (\boldsymbol{R} - \boldsymbol{R}')\big) \\
&= \mathrm{e}^{\mathrm{i}\boldsymbol{k}\cdot\boldsymbol{R}'} \phi_j(\boldsymbol{k}, \boldsymbol{r}).
\end{aligned} \tag{1-13}$$

As this time, if $\boldsymbol{R} = \boldsymbol{a}_i$,

$$\phi(\boldsymbol{k}, \boldsymbol{r} + \boldsymbol{a}_i) = \phi_j(\boldsymbol{k}, \boldsymbol{r}), \qquad (i = 1, 2) \qquad \left(\because\ \mathrm{e}^{\mathrm{i}\boldsymbol{k}\cdot\boldsymbol{a}_i} = 1\right). \tag{1-14}$$

The eigenfunction in the whole crystal $\psi_j(\boldsymbol{k}, \boldsymbol{r})$ is represented by a linear combination of $\phi_{j'}(\boldsymbol{k}, \boldsymbol{r})$ as follows

$$\psi_j(\boldsymbol{k}, \boldsymbol{r}) = \sum_{j'=1}^{n} C_{jj'}(\boldsymbol{k})\phi_j(\boldsymbol{k}, \boldsymbol{r}), \qquad (j, j' = 1, \cdots, n), \tag{1-15}$$

where the coefficients $C_{jj'}(\boldsymbol{k})$ are the constants determined by given conditions, and thus $\psi_j(\boldsymbol{k}, \boldsymbol{r})$ is also a Bloch function with same value of $\boldsymbol{k}$.

1. 3. 4. The Eigenvalue of Hamiltonian and The Secular Equation

The j-th eigenvalue $E_j(\boldsymbol{k})$, $(j = 1, \cdots, n)$ is can be written as

$$E_j(\boldsymbol{k}) = \frac{\langle \psi_j | \mathcal{H} | \psi_j \rangle}{\langle \psi_j | \psi_j \rangle} \tag{1-16}$$

where $\mathcal{H}$ is the Hamiltonian operator of the crystal. By substitution **Equation (1-15)** into **Equation (1-16)** and change of variables, the following equation,

$$\begin{aligned} E_i(\boldsymbol{k}) &= \frac{\sum_{j,\, j'=1}^{n} C_{ij}^{*} C_{ij'} \langle \phi_j | \mathcal{H} | \phi_{j'} \rangle}{\sum_{j,\, j'=1}^{n} C_{ij}^{*} C_{ij'} \langle \phi_j | \phi_{j'} \rangle} \\ &= \frac{\sum_{j,\, j'=1}^{n} \mathcal{H}_{jj'}(\boldsymbol{k}) C_{ij}^{*} C_{ij'}}{\sum_{j,\, j'=1}^{n} S_{jj'}(\boldsymbol{k}) C_{ij}^{*} C_{ij'}}, \qquad (i,\, j,\, j' = 1, \cdots, n) \end{aligned} \tag{1-17}$$

is obtained, where $(n \times n)$ matrices

$$\mathcal{H}_{jj'}(\boldsymbol{k}) \equiv \langle \phi_j | \mathcal{H} | \phi_{j'} \rangle \tag{1-18}$$

and

$$S_{jj'}(\boldsymbol{k}) \equiv \langle \phi_j | \phi_{j'} \rangle \tag{1-19}$$

are called transfer integral and overlap integral, respectively. In order to minimize $E_i(\boldsymbol{k})$, the coefficient C_{ij}^{*} is optimized. This is done under the local minimum condition, in which the partial derivative of E_i for the C_{ij}^{*} is zero, as follows

$$\begin{aligned} \frac{\partial E_i}{\partial C_{ij}^{*}} &= \frac{\sum_{j'=1}^{n} \mathcal{H}_{jj'} C_{ij'}}{\sum_{j,\, j'=1}^{n} S_{jj'} C_{ij}^{*} C_{ij'}} - \frac{\left(\sum_{j,\, j'=1}^{n} \mathcal{H}_{jj'} C_{ij}^{*} C_{ij'}\right)\left(\sum_{j'=1}^{n} S_{jj'} C_{ij'}\right)}{\left(\sum_{j,\, j'=1}^{n} S_{jj'} C_{ij}^{*} C_{ij'}\right)^2} \\ &= 0. \end{aligned} \tag{1-20}$$

The following equation obtained by organizing **Equation (1-20)** is given by

$$\sum_{j'=1}^{n} \mathcal{H}_{jj'} C_{ij'} = E_i \sum_{j'=1}^{n} S_{jj'} C_{ij'} \qquad \text{or} \qquad \sum_{j'=1}^{n} \left(\mathcal{H}_{jj'} - E_i S_{jj'}\right) C_{ij'} = 0. \tag{1-21}$$

Equation (1-21) that omits subscript j is represented by

$$(\mathcal{H} - E_i S)\boldsymbol{C}_i = 0, \tag{1-22}$$

where $\boldsymbol{C}_i$ is defined as column vector,

$$\boldsymbol{C}_i = \begin{pmatrix} C_{i1} \\ \vdots \\ C_{in} \end{pmatrix}. \tag{1-23}$$

For the value of the left-hand matrix of **Equation (21)** to be zero, the determinant of the matrix $(\mathcal{H} - E_i S)$ should be zero or the coefficient vector $\boldsymbol{C}_i$ should be the null vector. Since the latter means no wave function in the crystal solid, the following condition is stated by

$$\det(\mathcal{H} - ES) = 0, \tag{1-24}$$

where **Equation (1-24)** is called the secular equation.[**11**,**28**,**31**,**33**,**34**]

1. 3. 5. Transfer Integral and Overlap Integral

For graphene structure, a sp^2 hybridized orbital makes three in-plane σ bonds, while, and a $2p_z$ orbital creates one out-of-plane π bond. Because π energy bands are of paramount importance for determining the electronic properties of SLG. Each Bloch function is constructed by each atomic orbital from two inequivalent sub-lattices A (green) and B (red) in the graphene structure shown in **Figure 1-12a**. Two basis functions for graphene are obtained by substituting the sub-lattice A or B into the variable j of **Equation (1-12)** as follows

$$\begin{aligned} \phi_A(\boldsymbol{r}) &= \frac{1}{\sqrt{N}}\sum_{\boldsymbol{R}_A}^{N} \mathrm{e}^{\mathrm{i}\boldsymbol{k}\cdot\boldsymbol{R}_A}\varphi_j(\boldsymbol{r}-\boldsymbol{R}_A), \\ \text{and} \quad \phi_B(\boldsymbol{r}) &= \frac{1}{\sqrt{N}}\sum_{\boldsymbol{R}_B}^{N} \mathrm{e}^{\mathrm{i}\boldsymbol{k}\cdot\boldsymbol{R}_B}\varphi_j(\boldsymbol{r}-\boldsymbol{R}_B), \end{aligned} \tag{1-25}$$

where $\boldsymbol{R}_A$ or $\boldsymbol{R}_B$ is corresponding to the atom sites A or B, respectively. For example, $\boldsymbol{R}_A - \boldsymbol{R}'_A = \boldsymbol{\delta}'_{\pm i}, \cdots$ and $\boldsymbol{R}_A - \boldsymbol{R}'_B = \boldsymbol{\delta}_i, \cdots$ by **Equation (1-4) and (1-3)**, respectively. The transfer integrals, $\mathcal{H}_{jj'}$, $(j, j' = A, B)$ obtained by substituting **Equation (1-25)** into **Equation (1-18)** can be written as

$$\begin{aligned} \mathcal{H}_{AA} &= \frac{1}{N}\sum_{\boldsymbol{R}_A,\,\boldsymbol{R}'_A}^{N} \mathrm{e}^{\mathrm{i}\boldsymbol{k}\cdot(\boldsymbol{R}_A-\boldsymbol{R}'_A)}\langle\varphi_A(\boldsymbol{r}-\boldsymbol{R}_A)|\mathcal{H}|\varphi_A(\boldsymbol{r}-\boldsymbol{R}'_A)\rangle \\ &= \frac{1}{N}\left(\sum_{\boldsymbol{R}_A=\boldsymbol{R}'_A}\epsilon_{2p} + \sum_{\boldsymbol{R}_A=\boldsymbol{R}'_A\pm\boldsymbol{\delta}'_{\pm i}} \mathrm{e}^{\mathrm{i}\boldsymbol{k}\cdot\boldsymbol{\delta}'_{\pm i}}\langle\varphi_A|\mathcal{H}|\varphi_A\rangle + \cdots\right) \\ &= \epsilon_{2p_z} + \frac{1}{N}\left(\sum_{\boldsymbol{\delta}'_{\pm i}} \mathrm{e}^{\mathrm{i}\boldsymbol{k}\cdot\boldsymbol{\delta}'_{\pm i}}\langle\varphi_A|\mathcal{H}|\varphi_A\rangle + \cdots\right) \\ &\approx \epsilon_{2p_z}, \end{aligned} \tag{1-26}$$

$$\begin{aligned} \mathcal{H}_{BB} &= \frac{1}{N}\sum_{\boldsymbol{R}_B,\,\boldsymbol{R}'_B}^{N} \mathrm{e}^{\mathrm{i}\boldsymbol{k}\cdot(\boldsymbol{R}_B-\boldsymbol{R}'_B)}\langle\varphi_B(\boldsymbol{r}-\boldsymbol{R}_B)|\mathcal{H}|\varphi_B(\boldsymbol{r}-\boldsymbol{R}'_B)\rangle \\ &= \cdots \\ &\approx \epsilon_{2p_z}, \end{aligned} \tag{1-27}$$

$$\begin{aligned}\mathcal{H}_{AB} &= \frac{1}{N}\sum_{\boldsymbol{R}_A,\,\boldsymbol{R}'_B}^{N} \mathrm{e}^{\mathrm{i}\boldsymbol{k}\cdot(\boldsymbol{R}_A-\boldsymbol{R}'_B)}\langle\varphi_A(\boldsymbol{r}-\boldsymbol{R}_A)|\mathcal{H}|\varphi_B(\boldsymbol{r}-\boldsymbol{R}'_B)\rangle \\ &= \frac{1}{N}\left(\sum_{\boldsymbol{R}_A=\boldsymbol{R}'_B+\boldsymbol{\delta}_i} \mathrm{e}^{\mathrm{i}\boldsymbol{k}\cdot\boldsymbol{\delta}_i}\langle\varphi_A|\mathcal{H}|\varphi_B\rangle + \cdots\right) \\ &= \langle\varphi_A|\mathcal{H}|\varphi_B\rangle\left(\mathrm{e}^{\mathrm{i}\boldsymbol{k}\cdot\boldsymbol{\delta_1}} + \mathrm{e}^{\mathrm{i}\boldsymbol{k}\cdot\boldsymbol{\delta_2}} + \mathrm{e}^{\mathrm{i}\boldsymbol{k}\cdot\boldsymbol{\delta_3}}\right) + \cdots \\ &\approx tf(\boldsymbol{k})\end{aligned} \tag{1-28}$$

and

$$\mathcal{H}_{BA} = \langle\phi_B|\mathcal{H}|\phi_A\rangle = \langle\phi_A|\mathcal{H}|\phi_B\rangle^* = \mathcal{H}^*_{AB}, \tag{1-29}$$

where ϵ_{2p_z} is the $2p_z$ orbital energy,[**28**,**35**] $t \equiv \langle\varphi_A|\mathcal{H}|\varphi_B\rangle$, and

$$\begin{aligned}f(\boldsymbol{k}) &\equiv \mathrm{e}^{\mathrm{i}\boldsymbol{k}\cdot\boldsymbol{\delta_1}} + \mathrm{e}^{\mathrm{i}\boldsymbol{k}\cdot\boldsymbol{\delta_2}} + \mathrm{e}^{\mathrm{i}\boldsymbol{k}\cdot\boldsymbol{\delta_3}} \\ &= \mathrm{e}^{\mathrm{i}\boldsymbol{k}\cdot a\left(\frac{1}{2},\frac{\sqrt{3}}{2}\right)} + \mathrm{e}^{\mathrm{i}\boldsymbol{k}\cdot a\left(\frac{1}{2},-\frac{\sqrt{3}}{2}\right)} + \mathrm{e}^{\mathrm{i}\boldsymbol{k}\cdot a(-1,\,0)} \\ &= \mathrm{e}^{\mathrm{i}\frac{1}{2}k_1 a}\left(\mathrm{e}^{\mathrm{i}\frac{\sqrt{3}}{2}k_2 a} + \mathrm{e}^{-\mathrm{i}\frac{\sqrt{3}}{2}k_2 a}\right) + \mathrm{e}^{-\mathrm{i}k_1 a} \\ &= 2\mathrm{e}^{\mathrm{i}\frac{1}{2}k_1 a}\cos\left(\frac{\sqrt{3}}{2}k_2 a\right) + \mathrm{e}^{-\mathrm{i}k_1 a}.\end{aligned} \tag{1-30}$$

Using **Equation (1-19)**, the overlap integrals, $S_{jj'}$, $(j, j' = A, B)$ are given by

$$S_{AA} = \langle\phi_A|\phi_A\rangle = 1, \tag{1-31}$$

$$S_{BB} = \langle\phi_B|\phi_B\rangle = 1, \tag{1-32}$$

$$\begin{aligned}S_{AB} &= \langle\phi_A|\phi_B\rangle \\ &= \langle\varphi_A|\varphi_B\rangle\left(\mathrm{e}^{\mathrm{i}\boldsymbol{k}\cdot\boldsymbol{\delta_1}} + \mathrm{e}^{\mathrm{i}\boldsymbol{k}\cdot\boldsymbol{\delta_2}} + \mathrm{e}^{\mathrm{i}\boldsymbol{k}\cdot\boldsymbol{\delta_3}}\right) + \cdots \\ &\approx sf(\boldsymbol{k})\end{aligned} \tag{1-33}$$

and

$$S_{BA} = \langle\phi_B|\phi_A\rangle = \langle\phi_A|\phi_B\rangle^* = S^*_{AB}, \tag{1-34}$$

where $s \equiv \langle\varphi_A|\varphi_B\rangle$.

1. 3. 6. π Energy Bands of Graphene

Thus, the explicit forms for $\mathcal{H}$ and S can be written as

$$\mathcal{H} = \begin{pmatrix} \epsilon_{2p_z} & tf(\boldsymbol{k}) \\ tf(\boldsymbol{k})^* & \epsilon_{2p_z} \end{pmatrix} \quad and \quad S = \begin{pmatrix} 1 & sf(\boldsymbol{k}) \\ sf(\boldsymbol{k})^* & 1 \end{pmatrix}. \tag{1-35}$$

where $\mathcal{H}$ and S are Hermitian matrices, by substituting equations from **Equation (1-26) to (1-29)** and from **Equation (1-31) to (1-34)**, respectively, the parameters t and s are called the nearest-neighbor hopping energy and the next-nearest-neighbor hopping energy, which are the transition energy between adjacent and sub-adjacent atoms, respectively. [**28**,**35**] Before finding the eigenvalues E, the value of $\sqrt{f(\boldsymbol{k})^* f(\boldsymbol{k})}$ is first calculated as follows

$$\begin{aligned} w(\boldsymbol{k}) &\equiv \sqrt{f(\boldsymbol{k})^* f(\boldsymbol{k})} \\ &= \left| 2\mathrm{e}^{\mathrm{i}\frac{1}{2}k_1 a} \cos\left(\frac{\sqrt{3}}{2}k_2 a\right) + \mathrm{e}^{-\mathrm{i}k_1 a} \right| \\ &= \left(\left(2\cos\left(\tfrac{1}{2}k_1 a\right)\cos\left(\tfrac{\sqrt{3}}{2}k_2 a\right) + \cos(k_1 a)\right)^2 \right. \\ &\quad \left. + \left(2\sin\left(\tfrac{1}{2}k_1 a\right)\cos\left(\tfrac{\sqrt{3}}{2}k_2 a\right) - \sin(k_1 a)\right)^2 \right)^{1/2} \\ &= \left(1 + 4\cos^2\left(\tfrac{\sqrt{3}}{2}k_2 a\right) + 4\cos\left(\tfrac{\sqrt{3}}{2}k_2 a\right) \right. \\ &\quad \left. \times \left(\cos\left(\tfrac{1}{2}k_1 a\right)\cos(k_1 a) - \sin\left(\tfrac{1}{2}k_1 a\right)\sin(k_1 a)\right)\right)^{1/2} \\ &= \sqrt{1 + 4\cos\left(\tfrac{3}{2}k_1 a\right)\cos\left(\tfrac{\sqrt{3}}{2}k_2 a\right) + 4\cos^2\left(\tfrac{\sqrt{3}}{2}k_2 a\right)} \\ &= \sqrt{3 + 4\cos\left(\tfrac{3}{2}k_1 a\right)\cos\left(\tfrac{\sqrt{3}}{2}k_2 a\right) + 2\cos\left(\sqrt{3}k_2 a\right)}. \end{aligned} \tag{1-36}$$

The secular equation which is **Equation (1-24)** for π energy bands of graphene is given by

$$\begin{aligned} 0 &= \det(\mathcal{H} - ES) \\ &= \det\begin{pmatrix} \epsilon_{2p_z} - E & (t - sE)f(\boldsymbol{k}) \\ (t - sE)f(\boldsymbol{k})^* & \epsilon_{2p_z} - E \end{pmatrix} \\ &= \left(\epsilon_{2p_z} - E\right)^2 - (t - sE)^2 f(\boldsymbol{k})^* f(\boldsymbol{k}) \\ &= \left(\epsilon_{2p_z} - E\right)^2 - (t - sE)^2 \left(w(\boldsymbol{k})\right)^2, \end{aligned} \tag{1-37}$$

yielding the eigenvalues of the energy dispersion relations of **Equation (1-37)** written as

$$E_{\pi}^{\pm}(\boldsymbol{k}) = \frac{\epsilon_{2p_z} \pm tw(\boldsymbol{k})}{1 \pm sw(\boldsymbol{k})} \approx \epsilon_{2p_z} \pm tw(\boldsymbol{k}) - sw(\boldsymbol{k}) + \cdots, \quad \textbf{(1-38)}$$

where the positive $(+)$ or negative $(-)$ sign means the energy band of π or π^* molecular orbital, that is the valence or the conduction band, respectively. The hopping energy parameters t and s are non-identified, but the range of t is typically $[-3.033\ \text{eV}, 2.8\ \text{eV}]$ and the range of s is $[0.07\ \text{eV}, 0.129\ \text{eV}]$ or $[0.02t, 0.2t]$ from theoretical or experimental values.[**11**,**13**,**28**,**29**,**32**]. In **Figure 1-13a**, the hopping means the transition of an electron from $2p_z$ orbital in an atom to $2p_z$ orbital in another atom.

In **Figure 1-14**, the 3D full electronic dispersion of graphene is described by **Equation (1-38)** substituting the parameters $\epsilon_{2p_z} = 0$, $t = 2.7\ \text{eV}$, $s = 0.2t$, and $a = 0.142\ \text{nm}$ in order to recreate the TB approximation calculation of the bands of graphene.[**32**] The electronic dispersion in the honeycomb lattice may be symmetric near zero energy if $s = 0$. However, the spectrum of electronic dispersion (blue plots in **Figure 1-13e**) is asymmetric because it is actually $s \neq 0$.[**36**] This fact means that the electron-hole symmetry is broken.[**32**] **(Figure 1-13c and 1-13e)** A zoom in **Figure 1-13e or 1-14** shows the bands, where the vertices of the two conicals meet around zero energy, called Dirac cones. The point is commonly said Dirac point (DP) at the $\boldsymbol{K}$ or $\boldsymbol{K'}$ point in the BZ, which is represented by **Equation (1-6)**. **(Figure 1-12b and 1-13b)** It was proved that the value of band gap is zero, and graphene is the semi-metallic. **Equation (1-38)** with $\epsilon_{2p_z} = 0$ and $\boldsymbol{k} = \boldsymbol{K} + \boldsymbol{q}$, $(|\boldsymbol{q}| \ll |\boldsymbol{K}|)$ using the notation from P. R. Wallace is as follows

$$E_{\pi}^{\pm}(\boldsymbol{q}) = \pm\frac{3ta}{2}|\boldsymbol{q}| + O\left(\left(\frac{|\boldsymbol{q}|}{|\boldsymbol{K}|}\right)^2\right), \quad \textbf{(1-39)}$$

where $\boldsymbol{q}$ is a relative momentum vector to the DP.[**1**,**13**,**28**,**32**,**35**] **Equation (1-39)** can be changed to an equation:

$$E_{\pi}^{\pm}(\boldsymbol{q}) \approx \pm\hbar v_{\mathrm{F}}|\boldsymbol{q}|, \quad \textbf{(1-40)}$$

where v_{F} is the Fermi velocity, defined as $v_{\mathrm{F}} = 3ta/2\hbar$, with a value of $v_{\mathrm{F}} \approx c/300 \approx 1 \times 10^6 \mathrm{m/s}$.[**1**,**13**,**32**,**36**] Ultimately, graphene was proved to be a zero gap material.

In this paper, the band structure of graphene was solved using TB approximation model, and in addition to this method, it can be proved using pseudo-potential calculation[**37**] and density functional theory (DFT)[**38**], etc.

Since R. Saito's TB model is the approximation, the result is naturally some difference from that of *ab-initio* calculation. **(Figure 1-13c and 1-13d)** In order to be similar to the *ab-initio* result, the parameters t and s should be set well. As discussed, in molecules with π bonds, the number of π bonds participating in the conjugation increases the delocalized electrons throughout the molecules. As a result, the energy gap between highest occupied molecular orbital (HOMO) and the lowest unoccupied molecular orbital (LUMO) of the molecules, called HOMO-LUMO gap, decreases due to the conjugation of the π bonds formed by the overlap of the p orbitals. The zero band gap of graphene can be regarded as an extension of the discussion. Furthermore, the σ energy bands of graphene can be considered in order to draw the remaining bands (red) from the full band structure in **Figure 1-13e**.[**36**] $2s$, $2p_x$, and $2p_y$ orbitals, which contribute to sp^2 hybridized orbital, participate in the calculation of the σ bands.[**28**]

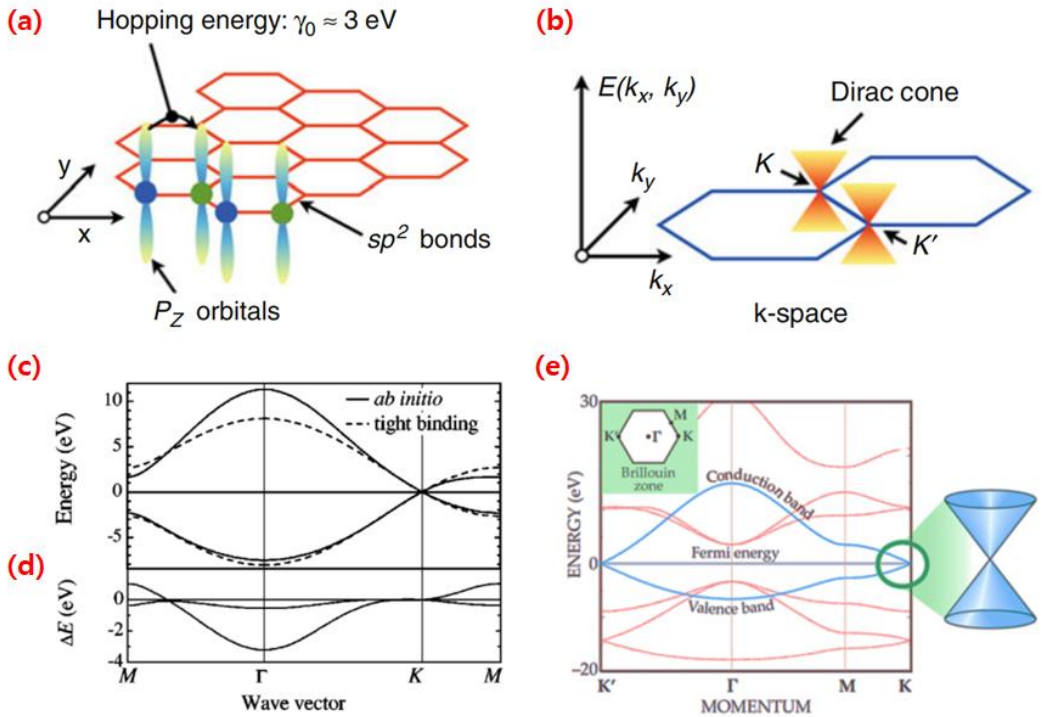

Figure 1-13. Dirac cone on graphene lattice and phonon dispersion of graphene. (a) Chemical bonds of graphene, showing the sp^2 hexagonal structure, and the $2p_z$ orbitals that impart graphene its conductivity. (b) The hexagonal symmetry of electrons in the momentum space, and the Dirac cones originating from the mobile π electrons. (Reprinted from ref. [**39**], Copyright 2007 American Institute of Physics) (c, d) *Ab-initio* and the nearest-neighbor TB dispersions of graphene. (c) The converged *ab-initio* calculation of the graphene π and π^* electronic bands is shown by the full lines. The dashed lines represent the TB dispersion of **Equation (1-38)** with $t = 2.7$ eV and $s = 0$. (d) Difference ΔE between the *ab-initio* and TB band structures. (Reprinted from ref. [**29**], Copyright 2002 American Physical Society) (e) Graphene's band structure. Orbital energies depend on the momentum of charge carriers in the crystal BZ (inset, right) (Reprinted from ref. [**36**], Copyright 2007 American Institute of Physics)

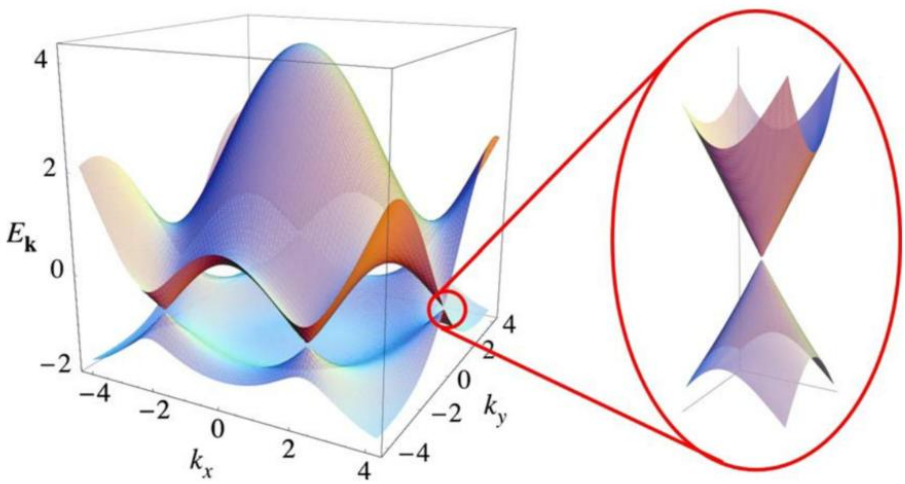

Figure 1-14. Electronic dispersion of honeycomb lattice. Inset: zoom-in of energy bands close to one of DP. (Reprinted from ref. [**32**], Copyright 2009 American Physical Society)

1. 4. Group Theory to Analyze Graphene

1. 4. 1. Group Theory for Graphene

Raman spectroscopy, which will be discussed in **Paragraph 2. 5. 1.**, is a very important tool for analyzing graphene. To interpret the Raman spectrum of SLG, it is first necessary to understand the real lattice (**Figure 1-12a**) and reciprocal lattice (**Figure 1-12b**) of SLG. In **Figure 2-12b**, the high-symmetry point is $\boldsymbol{\Gamma}$, $\boldsymbol{K}$, $\boldsymbol{K'}$, and $\boldsymbol{M}$, etc., as mentioned in **Paragraph 1. 3. 2.** Next, it is necessary to know the vibration mode of the phonons in order to analyze graphene. The group theory covered in inorganic chemistry or physical chemistry is applied for graphene study. The phonon symmetries are explained as the irreducible representation of the crystal point group.

A space group of perfect crystalline SLG (on an isotropic medium) is $P6/mmm$ (D_{6h}^{1}) in Hermann-Mauguin (Schoenflies) notation.[**40**,**41**] The group of wavevector (GWV) of the crystal has D_{6h} as a crystallographic point group at $\boldsymbol{\Gamma}$ point in Schoenflies notation.[**40**,**41**,**50**,**42**–**49**] SLG is 2D material, but space group must be considered to deal with out-of-plane phonons. For graphene, it is necessary to know the irreducible representation at the center and edge of the BZ.[**49**] The representation of the total lattice vibration Γ^{lv} can be decomposed into each irreducible representation using the following equation by (internal) direct product:

$$\Gamma^{\mathrm{lv}} = \Gamma^{\mathrm{eq}} \otimes \Gamma^{\mathrm{vec}} \qquad \textbf{(1-41)}$$

where Γ^{eq} and Γ^{vec} are the equivalence representation (for the atomic sites) and representation of real space vectors in Mulliken notation, respectively.[**41**,**49**] The equivalence representation means the invariance under the symmetry operations and is reducible in general.[**49**]

Figure 1-15 shows all symmetry operations and unit cell of SLG. 2 carbon atoms exist in primitive unit cell. Thus, lattice vibration of perfect crystalline SLG has 6 normal modes, which is characteristic vibrational modes independent of each other[**40**,**46**].

1. 4. 2. Phonons at $\boldsymbol{\Gamma}$ point

The GWV at $\boldsymbol{\Gamma}$ point ($\boldsymbol{q} = \boldsymbol{\Gamma} = \mathbf{0}$) of the graphene crystal is D_{6h} shown in **Figure 1-15**.[**40**,**41**,**50**,**42**–**49**] The atom equivalence representation $\Gamma_{\boldsymbol{\Gamma}}^{\mathrm{eq}}$ is reduced to the irreducible representations as follows

$$\Gamma_{\boldsymbol{\Gamma}}^{\mathrm{eq}} = A_{1g} \oplus B_{1u} \tag{1-42}$$

And x, y and z vector representation $\Gamma_{D_{6h}}^{\mathrm{vec}}$ is reduced to the irreducible representations as follows

$$\Gamma_{D_{6h}}^{\mathrm{vec}} = A_{2u} \oplus E_{1u} \tag{1-43}$$

The normal modes of $\boldsymbol{\Gamma}$ points in the reciprocal lattice of perfect crystalline SLG is the following relation from **Equation (1-41)**:

$$\begin{aligned} \Gamma_{\boldsymbol{\Gamma}}^{\mathrm{lv}} &= \Gamma_{\boldsymbol{\Gamma}}^{\mathrm{eq}} \otimes \Gamma_{D_{6h}}^{\mathrm{vec}} \\ &= A_{2u} \oplus B_{2g} \oplus E_{1u} \oplus E_{2g}. \end{aligned} \tag{1-44}$$

Each vibration mode of $\Gamma_{\boldsymbol{\Gamma}}^{\mathrm{lv}}$ is illustrated in **Figure 1-16**. Detailed calculations for the above equations can be found from **Table 1-1**.

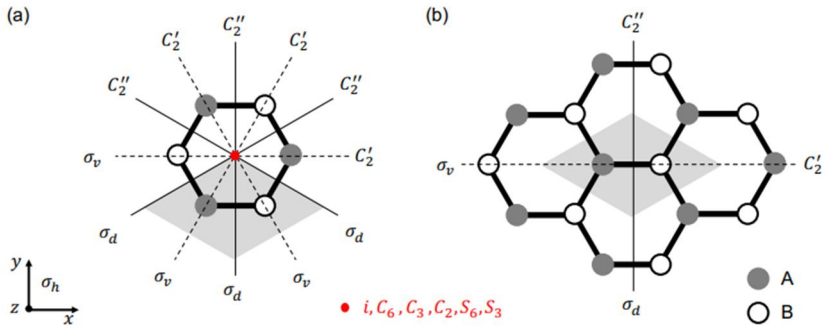

Figure 1-15. All symmetry operations of SLG. The primitive unit cell (gray diamond) contains 2 inequivalent atoms A (gray filled circle) and B (open black circle). (a) Top view of a SLG with 6 atoms (one hexagon) represented. The inversion center i and the axis (along z axis) of the C_6, C_3, C_2, S_6 and S_3 operations is illustrated as a red dot. The horizontal σ_h reflection is in the xy plane. The axis of the $C_2^{'}$ and $C_2^{''}$ are illustrated in black dashed and solid lines, respectively. The vertical planes for the σ_v and σ_d reflections are demonstrated as black dashed and solid lines, respectively. (b) Top view of a SLG with more hexagons. Each operation of $C_3^{'}$, $C_3^{''}$, σ_v and σ_d is drawn. This sketch is useful to determine the characters of the equivalence representation. (Reprinted from ref. [**48**], Copyright 2017 Guillaume Froehlicher)

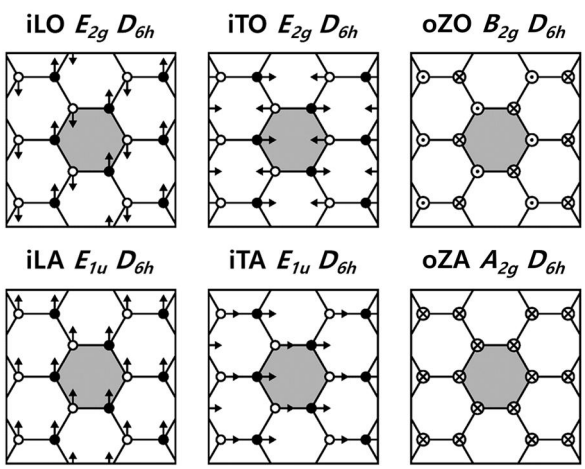

Figure 1-16. The eigenvectors for the in-plane phonons relevant to the high symmetry $\boldsymbol{\Gamma}$ point of the BZ of SLG. Each of these 6 modes is labeled and their atom displacements are indicated as the method from ref. [**45**]. i/o stands for in-plane/out-of-plane; L/T/Z stands for longitudinal/transverse(i)/transverse(o); O/A stands for optical/acoustic. (Reprinted from ref. [**40**], Copyright 2011 WILEY-VCH Verlag GmbH & Co. KGaA, Weinheim)

D_{6h}	E	$2C_6(z)$	$2C_3$	C_2	$3C_2'$	$3C_2''$	i	$2S_3$	$2S_6$	$\sigma_h(xy)$	$3\sigma_d$	$3\sigma_v$	Linear, Rotation	Quadratic	Cubic
A_{1g}	+1	+1	+1	+1	+1	+1	+1	+1	+1	+1	+1	+1		$x^2+y^2,\ z^2$	
A_{2g}	+1	+1	+1	+1	−1	−1	+1	+1	+1	+1	−1	−1	R_z		
B_{1g}	+1	−1	+1	−1	+1	−1	+1	−1	+1	−1	+1	−1			
B_{2g}	+1	−1	+1	−1	−1	+1	+1	−1	+1	−1	−1	+1			
E_{1g}	+2	+1	−1	−2	0	0	+2	+1	−1	−2	0	0	(R_x, R_y)	(xz, yz)	
E_{2g}	+2	−1	−1	+2	0	0	+2	−1	−1	+2	0	0		(x^2-y^2, xy)	
A_{1u}	+1	+1	+1	+1	+1	+1	−1	−1	−1	−1	−1	−1			
A_{2u}	+1	+1	+1	+1	−1	−1	−1	−1	−1	−1	+1	+1	z		$z^3, z(x^2+y^2)$
B_{1u}	+1	−1	+1	−1	+1	−1	−1	+1	−1	+1	−1	+1			$x(x^2-3y^2)$
B_{2u}	+1	−1	+1	−1	−1	+1	−1	+1	−1	+1	+1	−1			$y(3x^2-y^2)$
E_{1u}	+2	+1	−1	−2	0	0	−2	−1	+1	+2	0	0	(x, y)		$(xz^2, yz^2), [x(x^2+y^2), y(x^2+y^2)]$
E_{2u}	+2	−1	−1	+2	0	0	−2	+1	+1	−2	0	0			$[xyz, z(x^2-y^2)]$
													Representation	Direct Sum	
χ^{eq}	+2	0	+2	0	0	+2	0	+2	0	+2	+2	0	Γ^{eq}	$A_{1g} \oplus B_{1u}$	
χ^{vec}	+3	+2	0	−1	−1	−1	−3	−2	0	+1	+1	+1	Γ^{vec}	$A_{2u} \oplus E_{1u}$	
χ^{lv}	+6	0	0	0	0	−2	0	−4	0	+2	+2	0	Γ^{lv}	$A_{2u} \oplus B_{2g} \oplus E_{1u} \oplus E_{2g}$	

Table 1-1. (upper) Character table for D_{6h} point group. (lower) Representations for GWV at Γ point in the reciprocal lattice of SLG.

1. 4. 3. Phonons at $\boldsymbol{K}^{(\prime)}$ point

The GWV at $\boldsymbol{K}$ point ($\boldsymbol{q} = \boldsymbol{K}$) of the graphene crystal is D_{3h} shown in **Figure 1-17**.[**40**,**45**,**47**–**49**] The atom equivalence representation $\Gamma_{\boldsymbol{K}}^{\mathrm{eq}}$ is originally the irreducible representations as follows

$$\Gamma_{\boldsymbol{K}}^{\mathrm{eq}} = E' \tag{1-45}$$

And x, y and z vector representation $\Gamma_{D_{3h}}^{\mathrm{vec}}$ is reduced to the irreducible representations as follows

$$\Gamma_{D_{3h}}^{\mathrm{vec}} = E' \oplus A_2'' \tag{1-46}$$

The normal modes of $\boldsymbol{K}$ points in the reciprocal lattice of perfect crystalline SLG is the following relation from **Equation (1-41)**:

$$\begin{aligned} \Gamma_{\boldsymbol{K}}^{\mathrm{lv}} &= \Gamma_{\boldsymbol{K}}^{\mathrm{eq}} \otimes \Gamma_{D_{3h}}^{\mathrm{vec}} \\ &= A_1' \oplus A_2' \oplus E' \oplus E''. \end{aligned} \tag{1-47}$$

It can be induced in the same way for $\boldsymbol{K}'$ point.

$$\begin{aligned} \Gamma_{\boldsymbol{K}'}^{\mathrm{lv}} &= \Gamma_{\boldsymbol{K}'}^{\mathrm{eq}} \otimes \Gamma_{D_{3h}}^{\mathrm{vec}} \\ &= A_1' \oplus A_2' \oplus E' \oplus E''. \end{aligned} \tag{1-48}$$

Each vibration mode of $\Gamma_{\boldsymbol{K}}^{\mathrm{lv}}$ or $\Gamma_{\boldsymbol{K}'}^{\mathrm{lv}}$ is illustrated in **Figure 1-18**. Detailed calculations for the above equations can be found from **Table 1-2**.

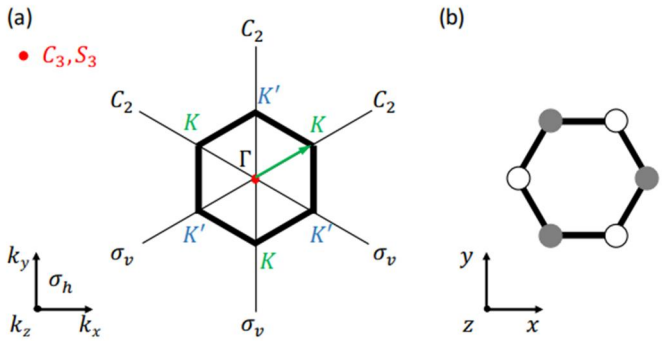

Figure 1-17. Symmetry operations of $\boldsymbol{K}^{(\prime)}$ point on SLG lattice. (a) Symmetry operation of the $\boldsymbol{K}$ vector in the BZ of SLG. The center of the BZ, $\boldsymbol{\Gamma}$ point and the 3 equivalent $\boldsymbol{K}$ and $\boldsymbol{K'}$ points, respectively, are indicated. The axis (along k_z axis) of the C_3 and S_3 operations is illustrated as a red dot. The horizontal σ_h reflection is in the $k_x k_y$ plane. The axis of the C_2 and the planes of the σ_v reflections are illustrated in black solid lines. (b) Top view of the corresponding SLG with 2 inequivalent atoms A (gray filled circle) and B (open black circle). (Reprinted from ref. [**48**], Copyright 2017 Guillaume Froehlicher)

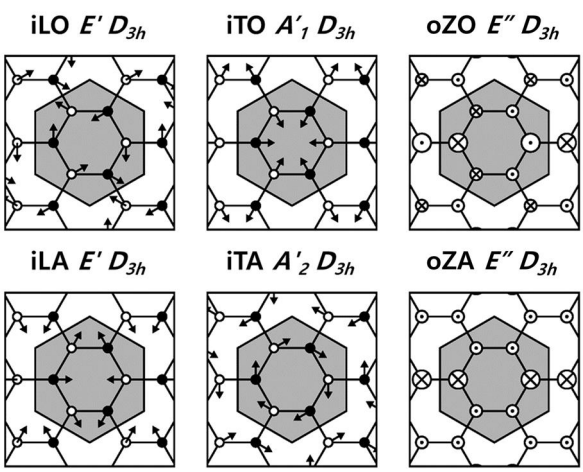

Figure 1-18. The eigenvectors for the in-plane phonons relevant to the high symmetry $\boldsymbol{K}^{(\prime)}$ point of the BZ of SLG. Each of these 6 modes is labeled and their atom displacements are indicated as the method from ref. [**45**]. i/o stands for in-plane/out-of-plane; L/T/Z stands for longitudinal/transverse(i)/transverse(o); O/A stands for optical/acoustic. (Reprinted from ref. [**40**], Copyright 2011 WILEY-VCH Verlag GmbH & Co. KGaA, Weinheim)

D_{3h}	E	$2C_3(z)$	$3C_2^{'}$	$\sigma_h(xy)$	$2S_3$	$3\sigma_v$	Linear, Rotation	Quadratic	Cubic
A_1'	+1	+1	+1	+1	+1	+1		$x^2+y^2,\ z^2$	$x(x^2-3y^2)$
A_2'	+1	+1	−1	+1	+1	−1	R_z		$y(3x^2-y^2)$
E'	+2	−1	0	+2	−1	0	(x,y)	(x^2-y^2,xy)	$(xz^2,yz^2),[x(x^2+y^2),y(x^2+y^2)]$
A_1''	+1	+1	+1	−1	−1	−1			
A_2''	+1	+1	−1	−1	−1	+1	z		$z^3,z(x^2+y^2)$
E''	+2	−1	0	−2	+1	0	(R_x,R_y)	(xz,yz)	$[xyz,z(x^2-y^2)]$
							Representation	Direct Sum	
χ^{eq}	+2	−1	0	+2	−1	0	Γ^{eq}	E'	
χ^{vec}	+3	0	−1	+1	−2	+1	Γ^{vec}	$E'\oplus A_2''$	
χ^{lv}	+6	0	0	+2	+2	0	Γ^{lv}	$A_1'\oplus A_2'\oplus E'\oplus E''$	

Table 1-2. (upper) Character table for D_{3h} point group. (lower) Representations for GWV at $\boldsymbol{K}^{(\prime)}$ point in the reciprocal lattice of SLG.

1. 5. Chemical Doping of Graphene

1. 5. 1. Several Methods for Band Gap Opening in Graphene

Transistors, one of the great inventions of the 20th century using the knowledge of quantum mechanics, are electronic devices using the electronic properties of semiconductor. Despite its excellent electrical and electronic properties, the zero gap characteristic of SLG **(Figure 1-14)** acts as major obstacle to being used as a transistor, one of the electronic devices. Scientists have used several methods for opening a band gap of graphene.

1. Graphene nanoribbon (GNR)[**51**–**58**] and graphene quantum dot (GQD)[**59**–**67**]:
   Splitting a structure in which carbon atoms are bonded in an infinite 2D plane into a narrow 1D strip or a small 0D particle creates a bandgap by the quantum confinement effect[**52**,**53**,**55**–**57**,**62**].
2. Functionalized graphene:
   When various functional groups are combined with the dangling bond at the edge of the graphene nanoflake,[**68**] the physical properties including bandgap are changed (e.g., graphene oxide (GO)[**69**–**71**], reduced GO (RGO) and hydrogenated graphene[**72**,**73**]).
3. Multi-layer graphene (MLG)[**74**,**75**,**84**–**93**,**76**–**83**]:
   A structure with a double-layer or higher creates a band gap due to the overlap of band structure of SLG. Particularly, since the van der Waals (vdW) material,[**94**–**99**] including graphene does not have strong interlayer bonds by vdW force, there is a possibility of a change in the interlayer angle. Since the change in the twisted angle means a change in the layer-stacked structure, it affects the band gap.[**75**–**77**,**83**,**86**,**90**]
4. Field-tuned graphene:
   When an electric field,[**3**,**100**,**101**] a magnetic field,[**102**–**106**] or a strain field[**107**–**109**] is applied to graphene, a change in positions of carbon atoms constituting graphene, that is, a change in the structure of graphene, and thus a band gap is generated.

Numerous studies on the above methods have continued, but major drawbacks of these methods are the complexity of the fabrication process and poor reproducibility. Moreover, the biggest disadvantage is that these methods is not suitable for the purpose because they break the hexagonal lattice of graphene and degrades its excellent electronic properties. Due to scattered problems, graphene is more likely to be applied to transparent electrodes[**110**–**115**] or thin film heaters[**116**,**117**] than transistors. Although the large-area synthesis of graphene has taken a step closer to commercialization, there is an electrical resistivity that is difficult to ignore because polycrystalline graphene is synthesized at the current technology level.

1. 5. 2. Doping Methods of Graphene

That is, there is a need for a method of opening a band gap or lowering resistivity without breaking graphene lattice. A solution to this is doping, a method mainly used in the field of semiconductor engineering. The graphene doping methods are largely classified into 'carrier injection' and 'Fermi level control'.

The former is a method of increasing the concentration of charge carriers by injecting them directly in graphene. It is similar to hitting the dopant ions accelerated to the surface of wafer for doping in a semiconductor engineering. There are two methods of 'atomic substitution' and 'chemisorption' in the carrier injection method, where 'chemisorption' is a compound word of 'chemical adsorption'. Atomic substitution is a method of converting carbon atoms located at vertices of graphene hexagonal lattice into other species (hetero atoms such as boron[**118**,**119**] and nitrogen[**120**–**128**]) similar in size to carbon atoms. Macroscopically, this method can be seen as the functionalization of graphene. In addition, chemisorption is a method of inducing covalent bond with a functional group by changing the bond characteristic of sp^2 carbon of graphene to sp^3. The carrier injection method naturally causes destruction of the hexagonal lattice system and creation of the defects into its lattice, eventually resulting in unwanted degradation of graphene quality.

On the other hand, the latter is a method of causing a change in carrier concentration by controlling the Fermi level, E_F of graphene. (The definition of Fermi level will be described later in **Paragraph 1. 6.**) This method includes 'applying gate voltage' and 'physisorption', where 'physisorption' is a compound of 'physical adsorption'. Applying gate voltage refers to a method of temporarily changing the carrier concentration of graphene and controlling the current (I_{DS}) flowing through the channel by applying a gate voltage (V_{GS}) to a graphene channel in the graphene transistor to modify E_F of graphene. In fact, this method changes E_F while minimizing the lattice distortion of graphene by tuning the weak field. Whereas, physisorption is a method of inducing a change in the E_F of graphene by physically adsorbing dopants such molecules and nanoparticles on the graphene surface. Unlike carrier injection, the method controlling E_F has the merit of doping while maintaining the outstanding intrinsic properties of graphene by not causing a large change in the graphene lattice. It can also use both methods that belong to it at the same time.

The conventional physisorption methods can obtain low resistivity and high conductivity, but doping stability is insufficient. In **Figure 1-19 and 1-20**, the stability of physisorption method tends to be less than that of chemisorption because the dopants are less bound to graphene surface and the distance from graphene surface is longer.[**129**,**130**] This thesis introduces researches on the change of E_F of graphene without changing its lattice by doping graphene with physisorption.

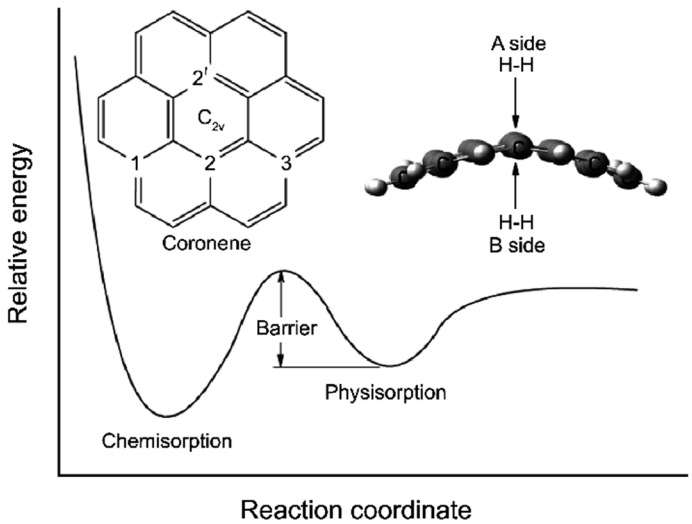

Figure 1-19. Potential energy surface for hollow-site (2-2') dissociative adsorption of H_2 on graphene. (Reprinted from ref. [**129**], Copyright 2011 KISTI)

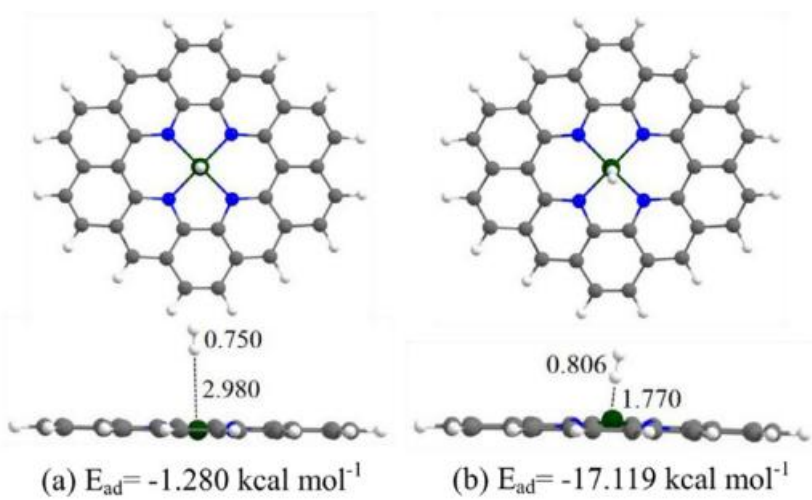

Figure 1-20. The adsorption energy of H_2 molecule on $Co/N_4/G$ dramatically enhanced by injecting positive charges on the adsorbent. Top (upper) and side (lower) views of the most stable configurations of a single H_2 molecule absorbed on the (a) neutral and (b) 5e positively charged $Co/N_4/G$ clusters. The white, gray, blue, and green balls represent H, C, N and Co atoms, respectively, and the adsorption energies of the H_2 molecule on the considered $Co/N_4/G$ clusters are reported. G, graphene. (Reprinted from ref. [**130**], Copyright 2017 Elsevier B.V.)

1. 6. Properties of Doped Graphene

1. 6. 1. Fermi Level

The properties of the doped graphene are entirely determined by the presence or absence of a change in the hexagonal lattice. Since the experiments were conducted to minimize the deformation of the graphene hexagonal lattice using the physisorption method, it is assumed that there is no change in the shape of the band structure of SLG.

The schematic band structure of pristine SLG has a linear energy-momentum dispersion relation around the DP in **Figure 1-13 and 1-14**. Its cone-shaped band structures of n-type-doped, pristine and p-type doped graphene are illustrated in the order mentioned in **Figure 1-21**.[**131**] The doping type is closely related to Fermi level, E_{F} determined by Fermi-Dirac (F-D) distribution. In the band theory of crystalline solids, electrons occupy the continuous energy states which are called bands comprised of each single-particle energy eigenstate, ϵ. Electron follows F-D distribution because it belongs to fermion. The F-D distribution presents the probability of an energy state occupied by an electron at thermodynamic equilibrium as follows[**27**,**132**]

$$f(\epsilon) = \frac{1}{\mathrm{e}^{(\epsilon-\mu)/k_{\mathrm{B}}T} + 1}. \qquad \textbf{(1-49)}$$

E_{F} is defined as the energy level at which the probability of existence of electrons given by F-D distribution is $1/2$ because electron is fermion as follow

$$f(\epsilon = E_{\mathrm{F}}) = \frac{1}{\mathrm{e}^{(E_{\mathrm{F}}-\mu)/k_{\mathrm{B}}T} + 1} = \frac{1}{2}. \qquad \textbf{(1-50)}$$

Because the band structure is different for each material, E_{F} may belong to the band or exist in the forbidden region. According to the first principle calculation, E_{F} of graphene accurately exists in DP. p- or n-type doping means a phenomenon in which the type of major charge carrier is determined as positive or negative charge carriers are donated with a material, respectively. In addition, major carriers of p- or n-type materials are generally holes and electrons, respectively. In the case of p-type doped materials, electrons are donating to the outside to form empty space (holes) in the band, and thus the position of E_{F} related to the probability of electron presence is lowered. (the right in **Figure 1-21**) On the contrary, in the case of n-type doped materials, electrons are donating from the outside, and thus E_{F} rises in the band structure. (the left in **Figure 1-21**)

1. 6. 2. Doping by Physisorption

For the physisorption of molecules, where the LUMO of dopants is lower than E_F of pristine graphene, electrons are donated from graphene to dopants, and thus a hole is formed in graphene and p-type doping of graphene is performed. On the other hand, n-type doping is performed by donating electrons from the dopants to the graphene when the HOMO of the dopants is higher than E_F of pristine graphene.[**133**] (shown in **Figure 1-21**) Even the physisorption involves fine lattice deformation, so a small gap should actually exist in the middle (DP) of the cone-shaped band structure.

Copious studies have been conducted on p-type doping of graphene and its application due to the reason that p-type doping is relatively easier than n-type. In fact, graphene is p-type doped by itself through its synthesis and transfer process and the etching process of metal catalyst, or by supporting substrate (generally Si/SiO_2 wafer) and atmospheric environment, etc.[**134**,**135**,**144**–**147**,**136**–**143**]

Conventionally known p-type dopants of graphene include water vapor, No_2 gas, Br_2 and I_2 molecules, organic molecules with electron withdrawing groups such as tetracyanoethylene (TCNE), 2,3,5,6-tetrafluoro-7,7,8,8-tetracyanoquinodimethane (F4-TCNQ) and 1,3,6,8-Pyrenetetrasulfonic acid tetrasodium salt, self-assembled monolayer (SAM) of fluoroalkyltrichlorosilane (FTS) and metal atoms with high electron affinity like bismuth (Bi), antimony (Sb) and gold (Au), etc.[**133**] On the other hand, the n-type dopants of graphene are less known than the p-type dopants. These include ammonia (NH_3), poly(ethyleneimine) (PEI) which is an electron-donating polymer, and aromatic molecules with donating groups and potassium (K), etc.[**133**]

In the DP of pristine graphene, positive and negative carriers exist as equal numbers, and only a few intrinsic carriers by thermal excitation can rise to the conduction band at the finite temperature. Therefore, in transfer characteristic curve of pristine graphene, the voltage corresponding to the DP is zero, and the current corresponding to the same point is close to zero. (**Figure 1-22**) The gate voltage at DP is called a charge neutrality point (V_{CNP}; Dirac point voltage). In the transfer characteristic curve, the left and right regions of V_{CNP} are hole- and electron-dominant regions, respectively. When p-type doping is performed, the plot moves to the right, **(Figure 1-23a)** and when n-type doping is performed, it moves to the left **(Figure 1-23b)**. A detailed description of electrical transfer characteristics will be given in **Paragraph 2. 6..**

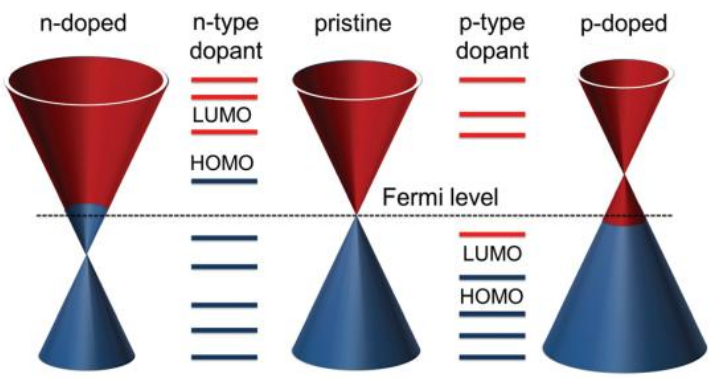

Figure 1-21. Schematic band structures of graphene at the ground state and the HOMO-LUMO levels of dopants. (center) Band structure of pristine graphene with zero gap. E_F is at the cross-over point. Band structures of (right) p-type and (left) n-type graphene with the band gap. E_F lies in valence and conduction band, respectively. (Reprinted from ref. [**131**], Copyright 2015 The Royal Society of Chemistry)

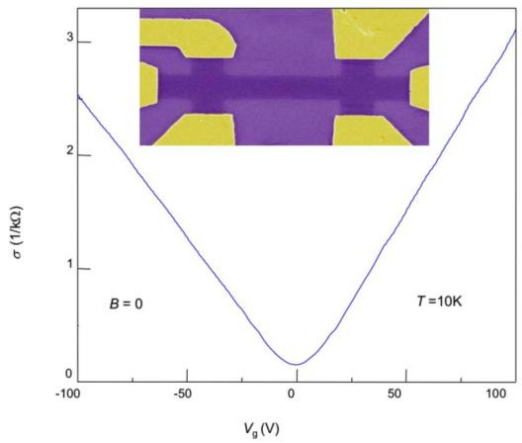

Figure 1-22. Changes in conductivity σ of graphene with varying gate voltage $V_g(=V_{GS})$ and carrier concentration n. Here σ is proportional to n. Note that samples with higher mobility (> 1 $m^2 \cdot V^{-1} \cdot s^{-1}$) normally show a sublinear dependence, presumably indicating the presence of different types of scatterers. Inset: SEM image of one of experimental devices in false colors matching those seen in visible optics. The scale of the micrograph is given by the width of the Hall bar, which is 1 μm. (Reprinted from ref. [**32**], Copyright 2009 American Physical Society)

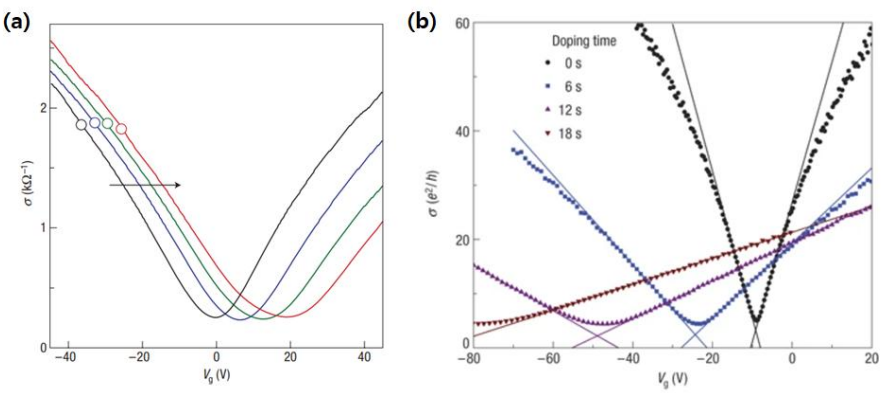

Figure 1-23. Examples of charge transfer characteristics of graphene FET: (a) p-type doped and (b) n-type doped. (a) Doping increased from the leftmost (black), the pristine sample to the rightmost (red) due to increasing exposure to NO_2. (Reprinted from ref. [**148**], Copyright 2007 Springer Nature) (b) Doping increased from the rightmost (black) to the leftmost (dark red) due to increasing exposure to potassium at 20 K in UHV. (Reprinted from ref. [**149**], Copyright 2008 Nature Publishing Group)

Chapter 2.

Experimental

2. 1. Graphene Synthesis by Chemical Vapor Deposition

2. 1. 1. The Early History of Graphene Synthesis

After its first discovery,[**3**] which is the top-down method, numerous researchers continued their attempts to make graphene through the bottom-up method. In other words, graphene is synthesized from a small molecule to a large crystal. Since graphene consists of only carbon atoms, the precursor must be a material containing carbon atoms. Since the mid-2000s, graphene was synthesized through epitaxial growth using silicon carbide (SiC) substrate.[**150**–**156**] However, this approach had disadvantages in that it required high vacuum conditions and high-cost crystalline substrates, and that it was difficult to grow only SLG.

Finally, K. S. Kim *et al.*, succeeded in growing graphene on a catalyst substrate by injecting precursor molecules,[**4**] focusing on the CVD process, which is essential for semiconductor engineering processes. Particularly, the CVD method has the advantage of not only being able to easily synthesize large-area graphene, but also obtaining reproducibility by ensuring the lower limit of the quality. In addition, it is also a great merit that mass production of graphene is possible at a relatively low-cost compared to the epitaxial growth method. A year later, the same laboratory surprised the world once again by enabling high-speed synthesis of graphene at a 30-inch scale through a roll-to-roll (R2R) process.[**157**]

2. 1. 2. Metal Catalyst Requirement for Graphene Growth

Numerous studies have been reported using various transition metals as catalysts for synthesis of carbon allotropes including graphite[**158**–**164**], diamond[**163**,**165**–**168**] and carbon nanotube (CNT)[**161**,**169**–**173**]. In order to grow graphene through the CVD method, a metal catalyst is further required. The reason is that the metal catalyst absorbs/adsorbs carbon atoms from carbon precursor molecules under high temperature conditions, and serves as a substrate of graphene formed through bonding among carbon atoms during the cooling process.

For elements in the red box of periodic table represented in **Figure 2-1**, it has been reported that their carbon solubility is appropriate. It is well known that the injected hydrocarbon molecules are decomposed at high temperature[**158**,**164**,**174**,**175**] to form an amorphous carbon phase on the surface of the transition metal catalysts[**158**,**174**,**176**,**177**] (particularly VIII group transition metals including Fe, Co and Ni), and crystals through sp^2 carbon are formed during the cooling process.

In **Figure 2-2a**, iron (Fe) mainly derives various phases of Fe and cementite (Fe_3C) phases which is the stable carbide during cooling, and precipitation of graphitic carbon is shown only through specific cooling process.[**177**] Since iron has high carbon affinity, carbon atoms in iron should compete between carbide formation and graphitic carbon precipitation. In **Figure 2-2b and 2-2c**, a metastable carbide (Co_3C or Ni_3C) formed from cobalt (Co) or nickel (Ni) at high temperature separates into pure metal and graphitic carbon during cooling of metal-carbon solid solution. The nucleation process begins with carbon atoms precipitation from defects such as grain boundaries of polycrystalline metals. Since these metals have high carbon solubility, a large amount of carbon atoms is precipitated during cooling to form multi-layered graphite. While copper (Cu) has very low carbon solubility and low carbon affinity enough not to form any carbide phase, and thus graphite is not formed even after cooling process. **(Figure 2-2d)**

In general, the higher the temperature, the higher the carbon solubility of the metal. Different carbon solubility of the various transition metals (from Fe to Cu) result from electronic configurations as follow

^{26}Fe	$[Ar]3d^6 4s^2$	~2.09 wt% at ~1154 ℃,
^{27}Co	$[Ar]3d^7 4s^2$	~0.9 wt% at ~1320 ℃,
^{28}Ni	$[Ar]3d^8 4s^2$	~0.6 wt% at ~1326 ℃,
^{29}Cu	$[Ar]3d^{10} 4s^1$	~0.0076 wt% at ~1084 ℃.

Fe to Co have asymmetric electron distributions in $3d$-shell. In particular, Fe has a higher carbon affinity[**178**,**179**] owing to relatively large mutual repulsion among electrons, thereby forming a cementite phase.[**179**] Cu, on the other hand, is less reactive because its

$3d$-shell is fully-filled and has the most stable electronic configuration with spherical symmetry.[**178**,**180**–**183**] That is, a sp^2 carbon atom shares an electron in Cu $4s^1$ orbital remaining one electronic state to form a weak bond, which adsorbs carbon atoms on the Cu surface.[**178**,**180**] In the case of Co[**174**,**184**] and Ni[**184**–**186**], it has the characteristics between Fe and Cu. In **Figure 2-3**, the thicker the metals, the larger the number of synthesized graphene layers. For that reason, the first metal catalyst used for graphene synthesis through the CVD method was nickel,[**4**,**187**] but now most of the graphene is synthesized using copper.[**5**,**157**,**187**–**189**] Graphene synthesized on the Cu (111) film is a single-domain, whereas graphene synthesized on the film such as Cu (100) has a multi-domain of two main orientation with a 30° difference.[**190**] (shown in **Figure 2-4**)

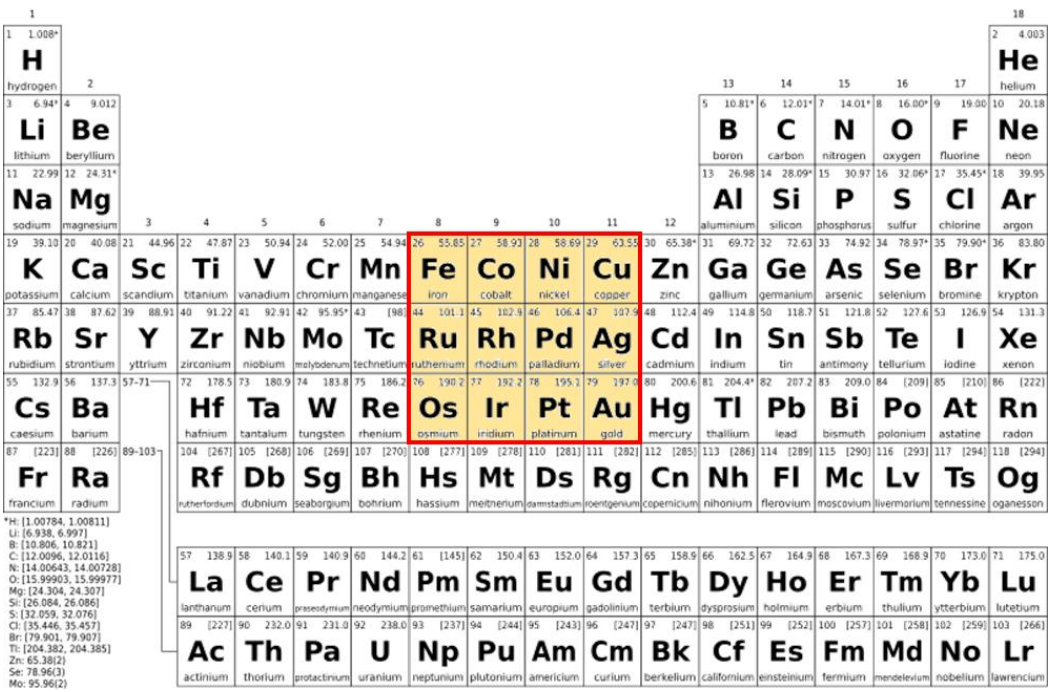

Figure 2-1. Periodic Table. (Red box) Carbon affinity to different transition metals is reported. The affinity decreases moving from Fe to Cu. (No Copyright)

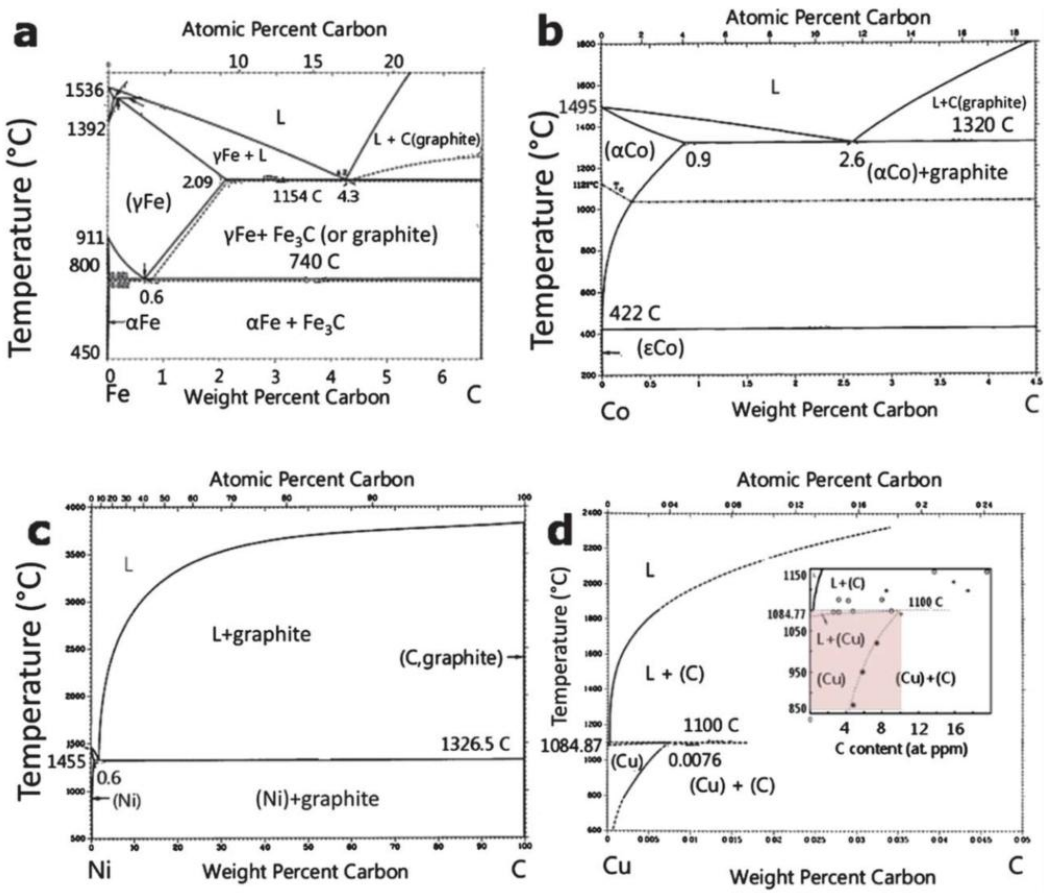

Figure 2-2. Binary phase diagrams of transition metals and carbon: (a) Fe-C; (b) Co-C; (c) Ni-C; (d) Cu-C. (Reprinted from ref. [**184**], Copyright 2002 ASM International) Inset of panel (d): The carbon solubility in Cu, of ~0.008 weight % at ~1084 °C. (Reprinted from ref. [**183**], Copyright 2004 Elsevier B. V.)

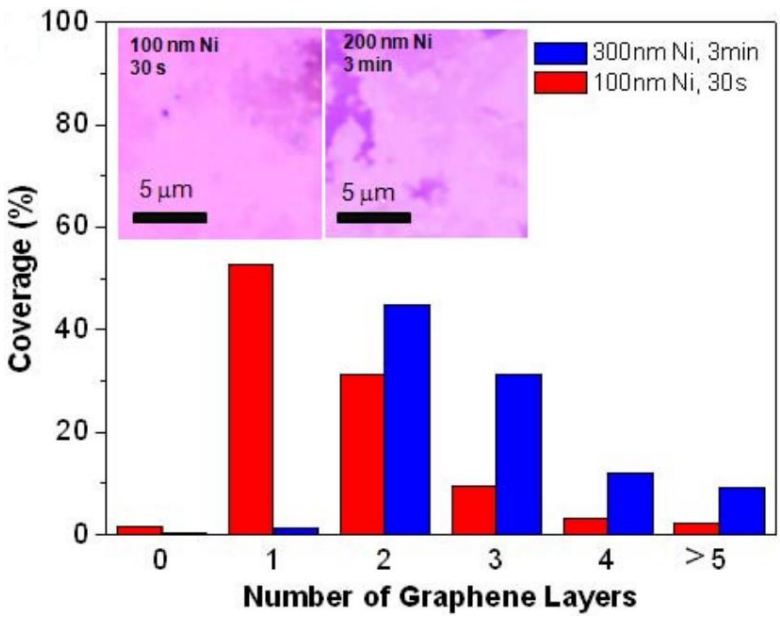

Figure 2-3. A histogram of the number of graphene layers two representative growth with different Ni thickness and growth time. (Reprinted from ref. [**4**], Copyright 2009 Nature Publishing Group)

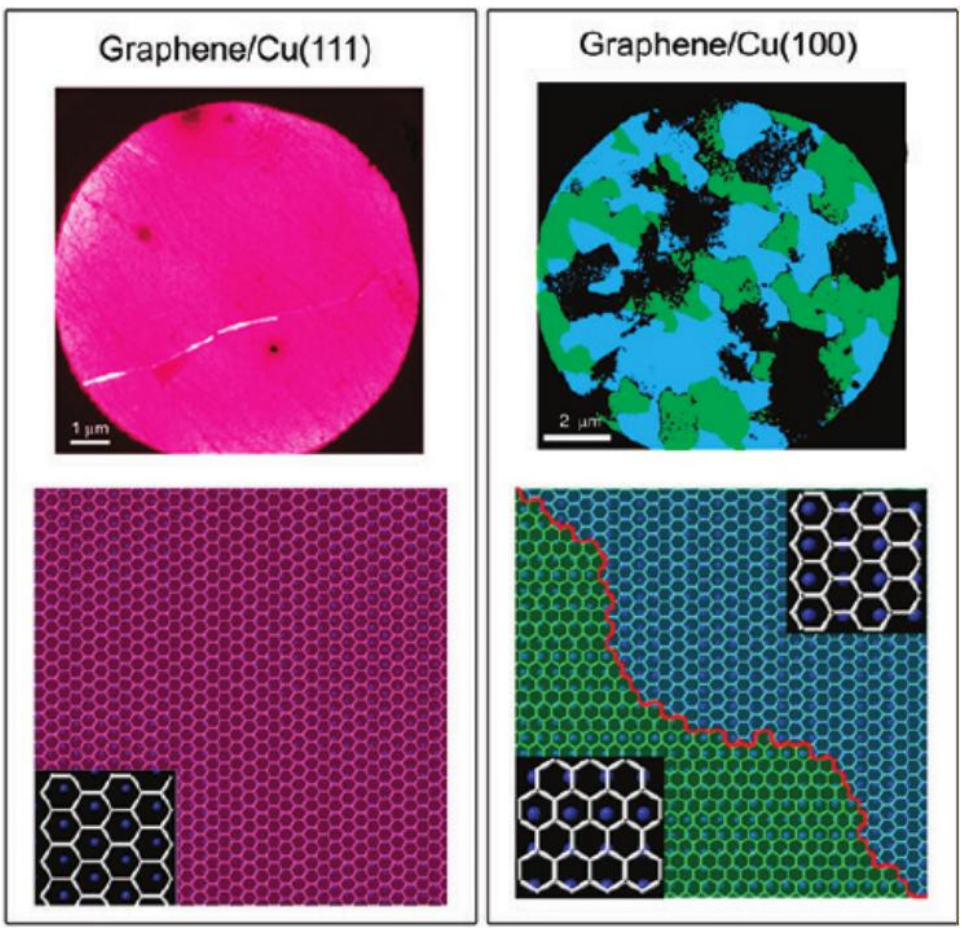

Figure 2-4. Spatial distribution and atomic models of graphene domains on Cu(111) (left) and Cu(100) (right). Graphene domains are determined from the dark field (DF) low energy electron microscope (LEEM) images. (Reprinted from ref. [**190**], Copyright 2012 ACS Publications)

2. 1. 3. Graphene Synthesis Process and Mechanism

The CVD method was used to synthesize SLG, a material for research on graphene devices. **Figure 2-5 and 2-6** show the graphene synthesis process through the CVD method.[**179**,**191**] As discussed above, copper foil is used as a metal catalyst and methane (CH_4) gas is used as a carbon precursor.[**4**,**5**,**179**,**187**] First, in the chamber, put the inner quartz tube with copper foil and hold a low vacuum of ~10^{-4} Torr. After that, the temperature is raised to 1000 ℃ while introducing hydrogen (H_2) gas. This process of 1 hour corresponds to annealing. Since copper naturally forms a native oxide layer on the surface, it is necessary to remove oxide and increase the crystallinity of the foil under hydrogen gas serving as an etchant and high temperature conditions. Next, methane gas is introduced for 1 hour while maintaining the previous conditions to grow graphene islands from the carbon seeds nucleated on the surface. Each graphene island generally grows with its orientation following the characteristics of the copper surface. They become grains of a full-grown graphene film, and when they meet adjacent islands, they form grain boundaries and stop growing. After the growth process is completed, a cooling process is performed to lower the temperature to room temperature, in which the carbon atoms constituting graphene are slightly rearranged. The time, temperature, gas flow rate, etc. of each step may vary depending on equipment, environmental conditions, experimental purposes, etc.

The size of the first graphene by the CVD process was only about one hand, but a R2R high-speed synthesis method was developed one year later, and graphene with a width of 30 cm and a desired length could be obtained for one synthesis.[**157**] (shown in **Figure 2-7a**) Since then, the R2R synthesis method has been further improved by numerous researchers, such as successful synthesis of graphene of 100 m length.[**192**] In addition, a R2R method of improving the quality of the synthesized graphene by spatially separating the annealing zone and the growth zone and supplying the methane only to the growth zone has been developed.[**193**] (shown in **Figure 2-7b**) The R2R method has become an essential method for building a mass production system of graphene. In addition to graphene synthesis, R2R methods in metal catalyst etching, graphene doping, patterning, and transfer processes over substrates have been proposed and are being studied for commercialization.[**191**,**194**] (shown in **Figure 2-7c**) In these studies, graphene synthesized using R2R CVD equipment was used.[**188**,**189**]

During the annealing process, hydrogen gas removes oxides and impurities from the copper surface[**195**] and coarsens the grains by unifying the orientation of adjacent grains of the copper[**179**,**196**]. In addition, an appropriate amount of hydrogen must be supplied to the growth stage because the higher the partial pressure of hydrogen, the smaller the grain size, but the more perfect hexagon-shaped grain is formed.[**197**] If the partial pressure of hydrogen is too high, an environment is created to form an additional layer by helping the carbon atom penetrate under the as-grown SLG.[**198**] The graphene is

synthesized under the conditions corresponding to the window of the partial pressure of hydrogen in which hexagon-shaped graphene flakes are formed.[**199**,**200**] (shown in **Figure 2-8**) When the plasma-enhanced CVD (PECVD) method is used, hydrogen gas generated during the decomposition of methane acts on the growth of graphene even without additional hydrogen gas.[**201**]

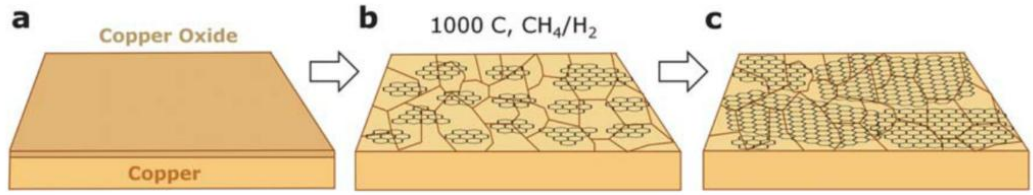

Figure 2-5. Schematic illustrating the three main stages of SLG growth on copper by CVD: (a) Cu foil with native oxide; (b) the exposure of the Cu foil to CH_4/H_2 atmosphere at 1000 °C leading to the nucleation of graphene islands; (c) enlargement of the graphene flakes with different lattice orientations. (Reprinted from ref. [**179**], Copyright 2011 The Royal Society of Chemistry)

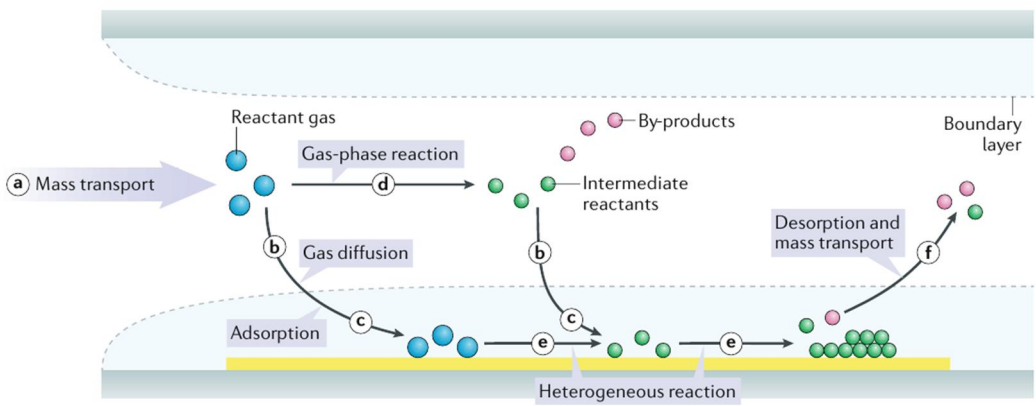

Figure 2-6. Schematic of general elementary steps of a typical CVD process. (a) First, reactant gases (blue) are transported into the reactor. Then, there are two possible routes for the reactant gases: (b) directly diffusing through the boundary layer and (c) adsorbing onto the substrate; or (d) forming intermediate reactants (green) and by-products (red) via the gas-phase reaction and being deposited onto the substrate by (b) diffusion and (c) adsorption. (e) Surface diffusion and heterogeneous reactions take place on the surface of substrate before the formation of thin films or coatings. (f) Finally, by-products and unreacted species are desorbed from the surface and forced out of the reactor as exhausts. (Reprinted from ref. [**191**], Copyright 2021 Nature Publishing Group)

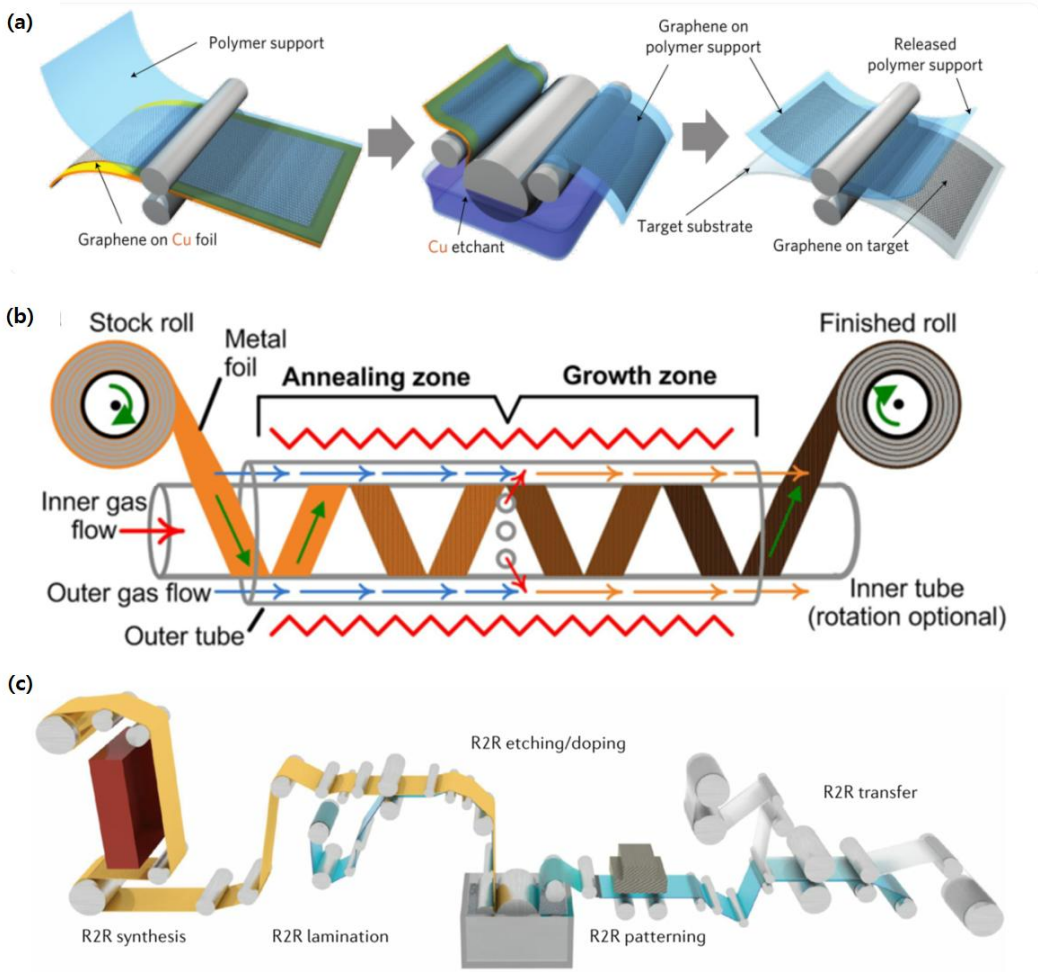

Figure 2-7. Graphene synthesis by R2R process. (a) Schematic of the roll-based production of graphene films grown on a copper foil. The process includes adhesion of polymer supports, copper etching (rinsing) and dry transfer-printing on a target substrate. A wet-chemical doping can be carried out using a set-up similar to that used for etching. (Reprinted from ref. [**157**], Copyright 2010 Nature Publishing Group) (b) Concentric tube CVD system configured for R2R graphene growth on Cu foil. System schematic showing the helical feed path (left to right), sequential treatment zones, and internal gas injection holes. (Reprinted from ref. [**193**], Copyright 2015 Nature Publishing Group) (c) Full R2R production of graphene films. CVD synthesis of graphene on copper (yellow), lamination, etching/doping and patterning/transfer to target substrates (blue) for graphene film production. (Reprinted from ref. [**191**], Copyright 2021 Nature Publishing Group)

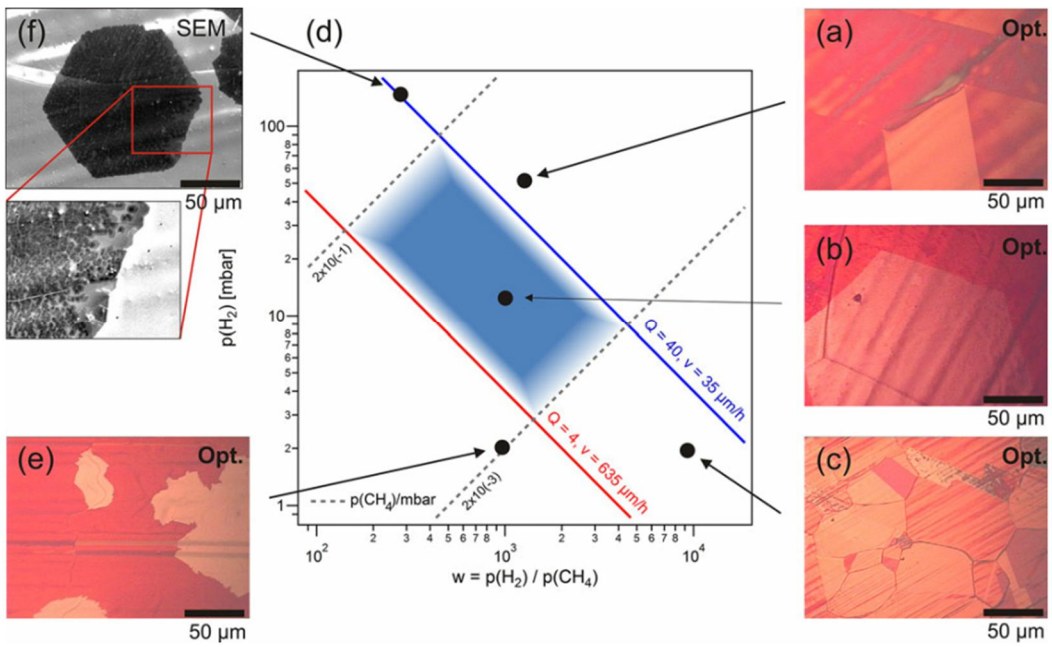

Figure 2-8. Log-log plot of a $p(\mathrm{H_2}) - w$ parameter space (the window of the partial pressure of hydrogen). The plot of the parameter space is used to systematically explore the effect of the applied partial pressures on the formation of SLG. Identification of the CVD parameter space which can be used for the growth of high-quality SLG on Cu at $T = 1333$ K. (a), (b), (c) and (e) OM and (f) SEM data display the Cu foil after 1 hour treatment at the indicated CVD parameters which are compiled in (d) a $p(\mathrm{H_2}) - w$ diagram. The optimum parameter range is indicated by a blue square. Microscopy data with image sizes of $170 \times 220\ \mu\mathrm{m}^2$: (a) No graphene growth at $p(\mathrm{H_2}) = 50$ mbar, $w = 1333$, $Q = 67$, (b) growth of 210 µm sized SLG flake at $p(\mathrm{H_2}) = 20$ mbar, $w = 1000$, $Q = 25$, (c) no graphene growth within growth time at $p(\mathrm{H_2}) = 0.3$ mbar, $w = 1000$, $Q = 0.3$, (e) nucleation during growth of dendritic flakes at $p(\mathrm{H_2}) = 2$ mbar, $w = 1000$, $Q = 2$, (f) MLG growth at $p(\mathrm{H_2}) = 150$ mbar, $w = 625$, $Q = 45$, which is clearly observed by the characteristic dark contrast of MLG in the SEM zoom shown in the inset. All experiments were performed on carbon depleted Cu foils. (Reprinted from ref. [**200**], Copyright 2017 Wiley-VCH)

2. 2. Pre-treatment Process for Graphene Transfer

Graphene by CVD method is synthesized on both sides of copper foil. To use a cleaner surface of graphene, the opposite surface of graphene is removed by plasma etching. This is an anisotropic dry etching method called reactive etching (RIE). Oxygen (O_2) plasma is generally used to remove graphene.

To transfer graphene onto a substrate, copper must be etched. Since SLG is one atomic layer, a film supporting graphene is required. If copper is etched without a supporting film, the graphene on the etching solution does not maintain the shape of the film and crumples. A supporting film on the graphene is formed by spin coating a solution obtained by dissolving poly(methyl methacrylate) (PMMA) in chlorobenzene.[**5**] For large-area graphene larger than wafer size, the supporting film is formed by laminating thermal release tape (TRT) instead of spin coating PMMA.[**157**]

The copper surface without graphene is floated down on the etching solution. At this time, it should be noted that the specimen is floated so that bubbles do not form between the specimen and the solution. An ammonium persulfate (APS; $(NH_4)_2S_2O_8$) aqueous solution[**157**,**202**] or an iron(III) chloride ($FeCl_3$) aqueous solution[**4**,**5**] is used as the etching solution. In this research, the APS was used. Using the APS solution, etching is completed within a few hours.

After etching is completed, a rinsing step is performed to clean the residual etchant on the surface of graphene.[**157**] Graphene floating on the solution is transferred onto deionized (DI) water using a piece of polyethylene terephthalate (PET). One rinse is performed on DI water for about 30 minutes, and this step is finished by repeating it two or three times.

2. 3. Graphene Transfer Process

The graphene transfer method is classified into a wet method and a dry method according to the process environment. As mentioned in **Paragraph 2. 2.**, as long as the method has been invented so far, etching of the metal catalyst is possible only in a solution process. The criterion for dividing the wet and dry methods is whether a solution is used in the transfer process after etching.

Wet transfer is a traditional method of transferring graphene synthesized through the CVD method. The substrate (e.g., SiO_2) is placed under the graphene flake on the water and then used to scoop up the graphene. Thereafter, the graphene film is dried for several hours or overnight so that it is firmly attached to the substrate. In some cases, a hot plate may be used for good adhesion between graphene and the substrate.

In general, a dry transfer method is used for the transfer of large-area graphene. Unlike the wet method, the dry method does not have a solution process. After graphene is brought into contact with the substrate, TRT is removed by laminating at a temperature of 110 to 120 ℃.

Although not used in these studies, the technique used in the transfer process is also used for stacking graphene as can be seen in **Figure 2-9 and 2-10a**.[**203**] There is also a method of stacking SLG on a substrate one after another (**Figure 2-10b**),[**203**] but this method is not used now because there is a disadvantage that supporting film must be coated several times.

Annealing after transfer has an effect of increasing adhesion between graphene and the substrate. According to empirical research, when the transferred graphene is heated for about 1 to 2 hours in a temperature range between 100 and 300 ℃ in a hydrogen gas or a vacuum atmosphere, an annealing effect may be seen without a negative effect on the specimen. Through change in charge transfer characteristics before and after annealing, the results are obtained that residues and impurities on the graphene surface are removed and electrochemically reduced.[**204**] (**Figure 2-11**)

Figure 2-9. Schematics of stacking graphene. The schematics shows the processes (a) from graphene synthesis to wet transfer and (b) from graphene synthesis to dry transfer.

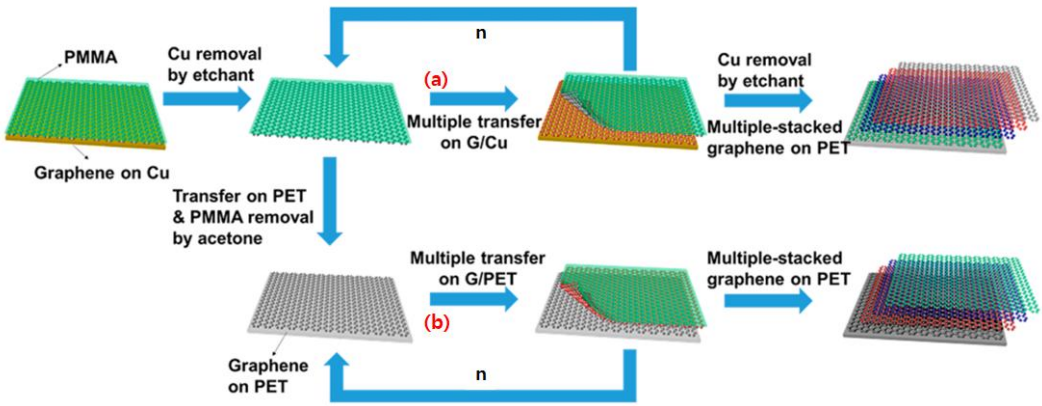

Figure 2-10. A schematic representation showing the graphene stacking processes with PMMA removal steps. The processes with (a) a single PMMA removal step (upper) and (b) multiple PMMA removal steps (lower). (Reprinted from ref. [**203**], Copyright 2015 ACS Publications)

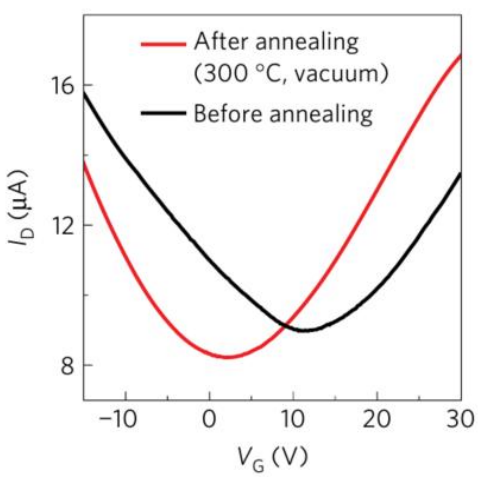

Figure 2-11. Comparison of electrical transfer characteristics of a monolithic graphene–graphite back-gate FET ($V_{DS} = 0.1$ V) before (black) and after (red) annealing. (Reprinted from ref. [**204**], Copyright 2012 Nature Publishing Group)

2. 4. Graphene Doping by Physisorption

The definition and principle of physisorption are discussed in **Paragraph 1. 6. 2.** In the physisorption process, the material shall be quantitatively coated on the substrate and shall not be deformed. Typical methods of physisorption include dip coating, spin coating, spray coating, organic vapor phase deposition and evaporation deposition, etc.[**205**] It is important to choose the appropriate method depending on the material.

The research in **Chapter 3** showed continuous chemical doping of SLG by introducing gold nanoparticles, SAM of 4-mercaptobenzoic acid, and mercury ion to the surface of SLG sequentially. The research in **Chapter 4** depicted that Cu//SLG doped by SAM of *n*-alkylamine was used as an electrode of a thermoelectric device to significantly improve thermoelectric performance. In both studies, dopants were physisorbed through a simple dip coating method shown in **Figure 2-12**, and graphene surface was successfully modified.

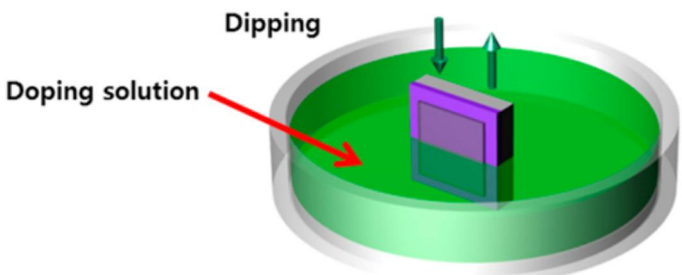

Figure 2-12. Schematic process of dip coating. (Reprinted from ref. [**205**], Copyright 2014 ACS Publications)

2. 5. Raman Spectroscopic Analyses for Graphene

2. 5. 1. Raman Spectroscopy

Light interacts with matter and then goes through several processes: reflection, transmission, absorption and scattering, etc. (**Figure 2-13a**) When the incident light is irradiated to the matter, the scattered light may be observed as a result of the interaction of light and matter. If the wavelength of the scattered light is the same as that of the incident light, the phenomenon is called Rayleigh scattering. On the other hand, if the two wavelengths are different, it is called Raman scattering. Thus, Rayleigh and Raman scattering are elastic or inelastic scattering, respectively. Emission or absorption of phonons occurs by lattice vibration. In this process, Raman scattering occurs due to the loss or gain of the energy of the optical phonon, the former and the latter being referred to as Stokes and anti-Stokes Raman scattering, respectively. (**Figure 2-13b**)

A typical Raman spectroscopy uses Stokes Raman scattering, which detects scattered light with a lower energy than the energy of incident light. In addition to Stokes Raman scattering, energy level diagrams for several emission signals can be found in **Figure 2-13c**. Raman spectroscopy is used as a tool to study the vibration modes of the molecule or the crystal or to specify the material by observing the Raman scattering of the material irradiated with monochromatic light (e.g. laser) and analyzing the spectrum of scattered light. The optical properties and phonon properties of the material can be identified through this analysis method.

Moreover, Raman spectroscopy is a non-destructive analysis method that does not damage the material during the analysis process. In particular, Raman spectroscopy is considered a very important analysis method in the study of 2D materials including graphene. With this spectroscopy, physical characteristics of graphene, such as defect,[**206**–**208**] strain,[**209**–**212**] doping level,[**208**,**209**,**213**–**215**] the number of layers,[**50**,**216**,**217**] electrical conductivity[**188**,**218**] and thermal conductivity,[**210**] can be measured.

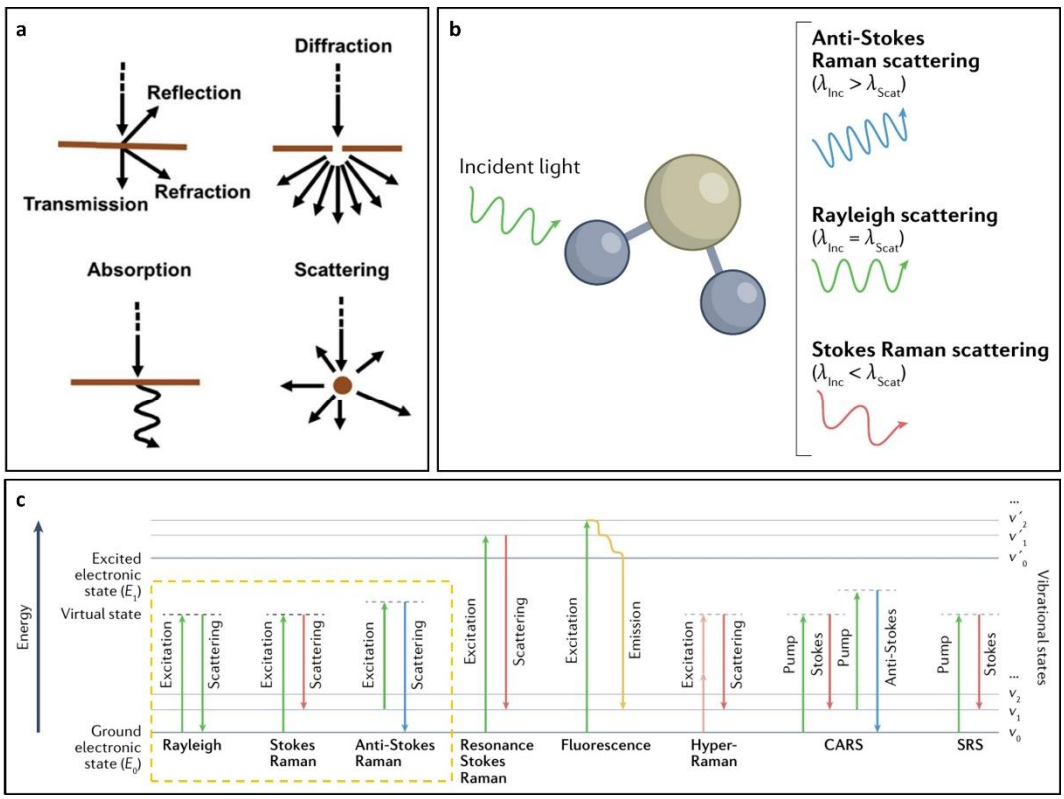

Figure 2-13. Principle of Raman spectroscopy. (a) Schematic processes of light-matter interactions: reflection, refraction, transmission, diffraction, absorption and scattering (Reprinted from ref. [**219**], Copyright 2019 The Royal Society of Chemistry) (b) Raman spectroscopy working principles. Three types of scattering signal that are generated as a result of interactions between light and a molecule. (c) Jablonski diagrams showing transition of energy level for the generation of emission signals. Colors of the arrows represent the wavelength. (Yellow dotted box) For Rayleigh and Raman (Stokes and anti-Stokes) scattering, the molecule is excited to a virtual energy state and then returns to a lower energy level, accompanied by light scattering. In contrast, for resonance Raman scattering and fluorescence emission, the molecule undergoes a transition to a higher electronic state, generating a much stronger emission signal. Hyper-Raman scattering relies on a nonlinear two- photon process. Coherent Raman scattering (CRS), including coherent anti- Stokes scattering (CARS) and stimulated Raman scattering (SRS), is another type of nonlinear optical process based on the interaction between pump and Stokes lasers. (Reprinted from ref. [**220**], Copyright 2021 Nature Publishing Group)

2. 5. 2. Graphene's Bands in Raman Spectra

Under the condition of laser wavelength $\lambda_{\text{laser}} = 514.5$ nm (or laser excitation energy $E_{\text{laser}} = 2.414$ eV), the Raman spectrum of SLG exhibits the specific peaks of G, D and $2D$ (or G') bands at around 1580, 1350 and 2700 cm^{-1}, respectively. The Raman processes of vibration modes are shown in **Figure 2-14 and 2-15**. In particular, **Figure 2-15** shows each Raman process corresponding to the order and the number of phonons of the resonance. Note the contents of **Paragraph. 1. 4.**

'G' of the G band means 'graphite'.[**71**] The peak of the G band is the main spectral feature of sp^2 carbon-based materials including graphite, graphene, fullerene and CNT. (**Figure 2-16a**) Since E_{2g} symmetry (stretching) at $\boldsymbol{\Gamma}$ point corresponds to Raman active, the G band can be observed through the single resonance process (**Figure 2-14**) which consists 2 degenerate iLO/iTO phonon modes.[**221**] (**Table 2-1**) The energy difference between the incident light and the scattered light corresponds to energy of phonon, and the momentum of light is negligible compared to the size of the BZ. To satisfy the conservation law of energy/momentum conservation, the momentum of phonon corresponds to $\boldsymbol{\Gamma}$ point, the center of the BZ. In this case, there is always an electron-hole pair, and the G band is independent of λ_{laser} (or E_{laser}).

'D' of the D band means 'disorder-induced'[**221**,**222**] or 'defect-induced'[**223**] due to lattice vibrations of the corner of the BZ. Since A_1' symmetry (breathing) at $\boldsymbol{K}$ point corresponds to Raman active, the D band can be observed through the double resonance process which consists nondegenerate iTO phonon mode[**224**,**225**] at a defect[**226**–**228**]. (**Figure 2-16b**) '2D' of the $2D$ band means twice the Raman shift of D band. Another name, G' band is an original name of $2D$ band and 'G' of G' band means another unique Raman-allowed spectral feature observed in the perfect crystal, not the G band. The $2D$ band is an overtone band[**40**,**222**] and shows that graphene has perfect symmetry of hexagonal lattice.[**42**,**225**,**229**] the D and $2D$ band are the dispersive behaviors by double or triple resonance process (**Figure 2-14**) and are dependent of λ_{laser} (or E_{laser}).[**230**] G and $2D$ bands represent the phonon interactions at the $\boldsymbol{\Gamma}$ and $\boldsymbol{K}$ points in the BZ, respectively, and the positions and intensities of the points verify strain, doping level and the number of graphene layers.

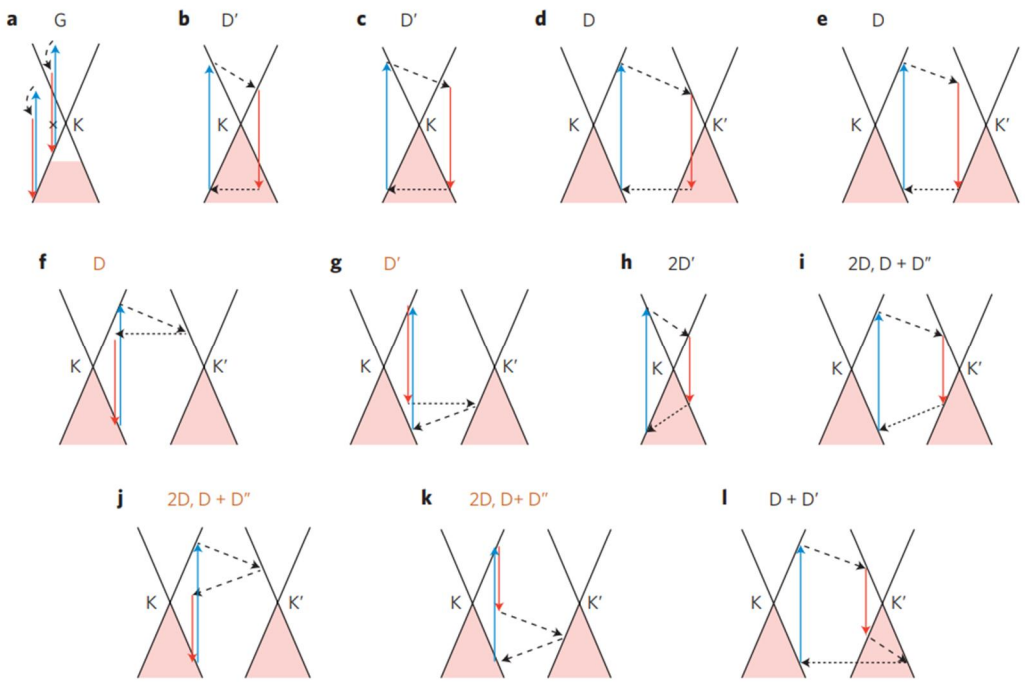

Figure 2-14. Raman processes on SLG. Electron dispersion (solid black lines), occupied states (shaded areas), interband transitions neglecting the photon momentum, accompanied by photon absorption (blue arrows) and emission (red arrows), intraband transitions accompanied by phonon emission (dashed arrows), electron scattering on a defect (horizontal dotted arrows). (a) One-phonon processes responsible for the G band, which interfere destructively. Some processes can be eliminated by doping, such as the one that is crossed out. (b–g) In the presence of defects, the phonon wavevector need not be zero, producing the D' band for intravalley scattering (b, c), and D band for intervalley scattering (d–g). Besides the e-h or h-e processes, where the electron and the hole participate in one act of scattering each (b–e), there are contributions (e-e and h-h) where only the electron (f) or the hole (g) are scattered. (h–k) For two-phonon scattering, momentum can be conserved by emitting two phonons with opposite wavevectors, producing the $2D'$ band for intravalley scattering (h) and the $2D$, $D + D''$ bands for intervalley scattering (i–k). The e-e and h-h processes are shown in (j, k). (l) With defects, one intravalley and one intervalley phonon can be emitted, producing the $D + D'$ band. The processes (f, g, j, k) give a small contribution, as indicated by the orange band labels. 'e' and 'h' in e-e, e-h, h-e and h-h are electron and hole, respectively. (Reprinted from ref. [**225**], Copyright 2013 Nature Publishing Group)

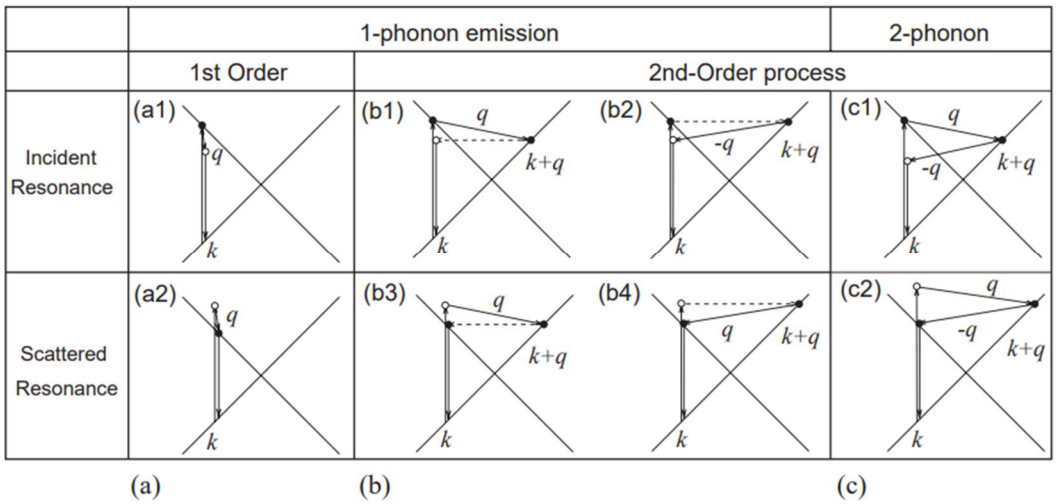

Figure 2-15. Raman processes on SLG expressing resonances. (a) First-order (single), (b) one-phonon second-order (double) and (c) two-phonon second-order (double) resonance Raman spectral processes. (top) incident photon resonance and (bottom) scattered photon resonance conditions. For one-phonon, second-order transitions, one of the two scattering events is an elastic scattering event (dashed lines). Resonance points are shown as solid circles. (Reprinted from ref. [**231**], Copyright 2005 Elsevier B.V.)

	Phonon Type	Raman Activity	IR Activity
A_{2u}	oZA	Inactive	**Active**
B_{2g}	oZO	Inactive	Inactive
E_{2g}	iLO/iTO	**Active**	Inactive
E_{1u}	iLA/iTA	Inactive	**Active**

Table 2-1. Phonon types and Raman/infrared (IR) activities according to irreducible representations at Γ point.

2. 5. 3. Analyses for Raman Spectra of Graphene

The Raman spectrum of SLG is shown in **Figure 2-16b**. Each intensity of the peaks of the G and $2D$ bands, I_G and I_{2D} of SLG with high crystallinity has a ratio of 2 or more.[**40**] In other words, if SLG is close to the perfect crystal, then $I_{2D}/I_G > 2$. As the sp^2 hybridized orbitals of carbon atoms are broken and the crystalline defects increase, the value of I_D/I_G increases.[**227**]

In **Figure 2-17c**, As the number of layers of graphene increases, the relative intensity of the peak of $2D$ band decreases and the shape of that becomes broadened.[**227**] In addition, the position of the peak of the $2D$ band is gradually blue-shifted.[**232**] (**Figure 2-17c**) On the other hand, the position of peak of the G band is almost constant.[**232**] (**Figure 2-17a**) Using the above aspect, SLG can be determined. This is the similar tendency as λ_{laser} decreases (or E_{laser} increases). [**42**] (**Figure 2-18**) The phenomenon means that the $2D$ band (also the D band) has a dispersive behavior.[**230**]

Raman spectroscopy can be used to optically differentiate between the strain effect and the charge doping effect in graphene samples. [**209**] **Figure 2-19** shows the G *versus* $2D$ peak position of graphene samples, indicating that the point of $O(\omega_G^0, \omega_{2D}^0)$ semi-empirically corresponds to the strain-free and charge-neutral state, where the values of ω_G^0 and ω_{2D}^0 are given by

$$\omega_G^0 = 1581.6 \pm 0.2 \quad \text{and} \quad \omega_{2D}^0 = 2676.9 \pm 0.7. \qquad \textbf{(2-1)}$$

If tensile strain or a p-type doping effect is applied to this graphene, the point (ω_G, ω_{2D}) moves in the direction $\boldsymbol{OT}$ or $\boldsymbol{OH}$, respectively (inset of **Figure 2-19**, where the slopes are 2.2 ± 0.2 and 0.70 ± 0.05 for $\boldsymbol{OT}$ and $\boldsymbol{OH}$, respectively).[**209**] Using this analysis tool, each contribution can be calculated by separating the strain effect and doping effect of graphene.

In general, the peak of G band in Raman spectra SLG can be used to measure the charge concentration,[**233**] indicating that 1×10^{12} cm^{-2} of the hole concentration corresponds to the range from 1 to 3 cm^{-1} of the measurement for the peak position of G band (1 cm^{-1}). Therefore, we can demonstrate that the carrier concentrations, n, derived by Raman measurements. The peak position of G band is blue-shifted by both p-type and n-type doping effects. On the other hand, the peak position of $2D$ band is red-shifted by n-type doping effect. (**Figure 2-20**) **Figure 2-21** depicts the change of the peak positions of G and $2D$ bands, full-width at half-maximum (FWHM) of G band and the intensity ration of these bands, I_{2D}/I_G by p-type and n-type doping effect through gate voltage application.

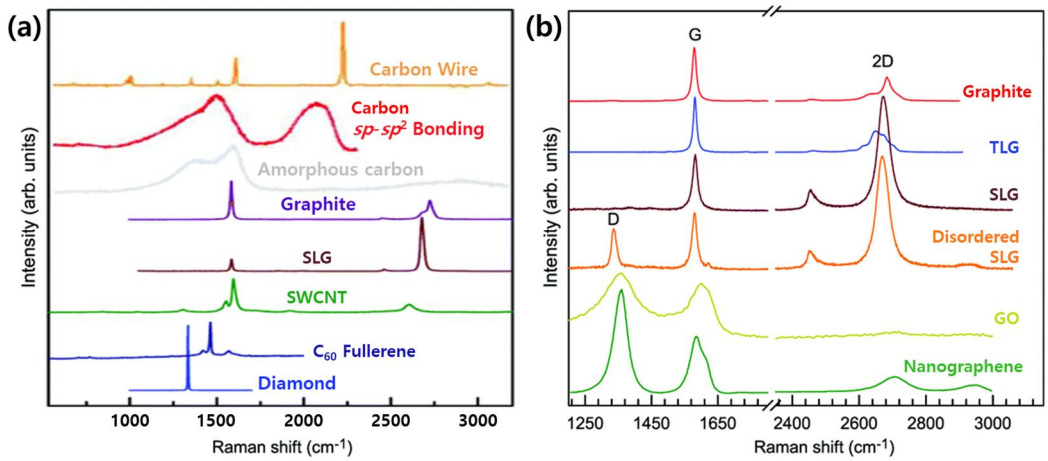

Figure 2-16. Raman spectra of carbon materials and graphene-related materials (a) Raman spectra of carbon solids and nanostructures, including 1D carbon wire, carbon $sp-sp^2$ bonding, amorphous carbon (a-C), graphite, SLG, single-walled CNT (SWCNT), C_{60} fullerene and diamond. (Reprinted from ref. [**234**], Copyright 2005 Elsevier B.V.) (b) Raman spectra of graphene-based materials, including graphite, TLG, SLG, disordered graphene, GO and nanographene. (Reprinted from ref. [**42**], Copyright 2005 Elsevier B.V.)

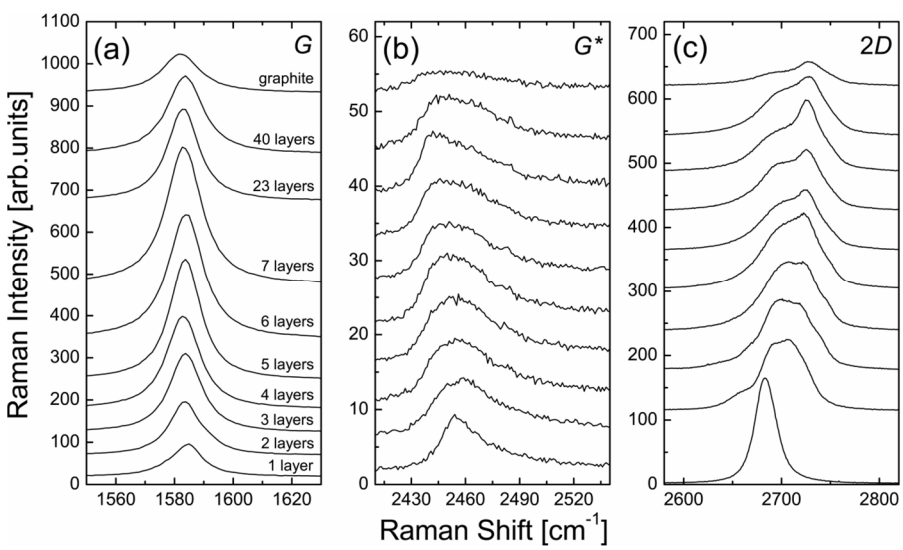

Figure 2-17. Raman spectra with the variation of graphene layers. (a) Evolutions of the (a) G band, (b) G* band, and (c) 2D band in the Raman spectrum as functions of the number of graphene layers. (Reprinted from ref. [**232**], Copyright 2009 The Korean Physical Society)

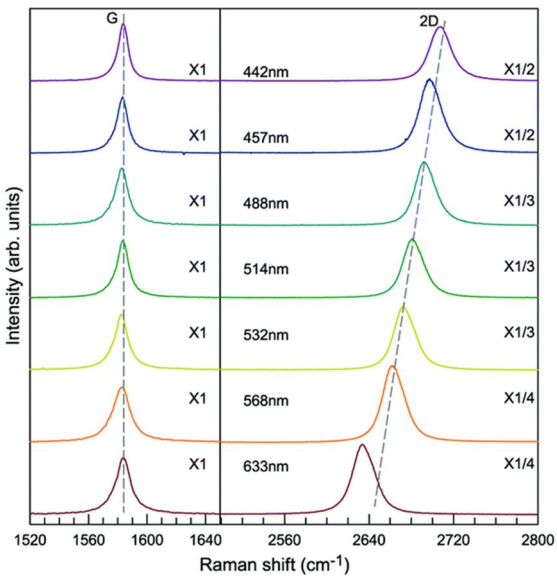

Figure 2-18. Raman spectra with the variation of excitation energy. Raman spectra of SLG measured at various excitations (λ_{laser} from 442 nm to 633 nm) in the G and $2D$ mode regions. (Reprinted from ref. [**42**], Copyright 2018 The Royal Society of Chemistry)

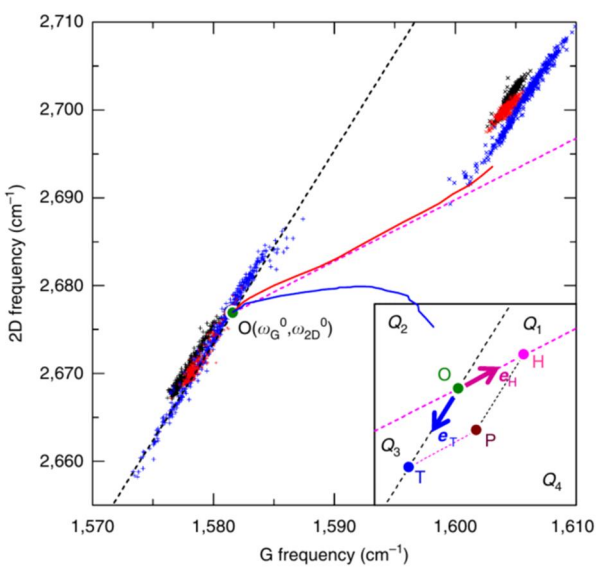

Figure 2-19. Correlation between the frequencies of the G and 2D Raman modes of graphene (ω_G, ω_{2D}). (Reprinted from ref. [**209**], Copyright 2012 Nature Publishing Group)

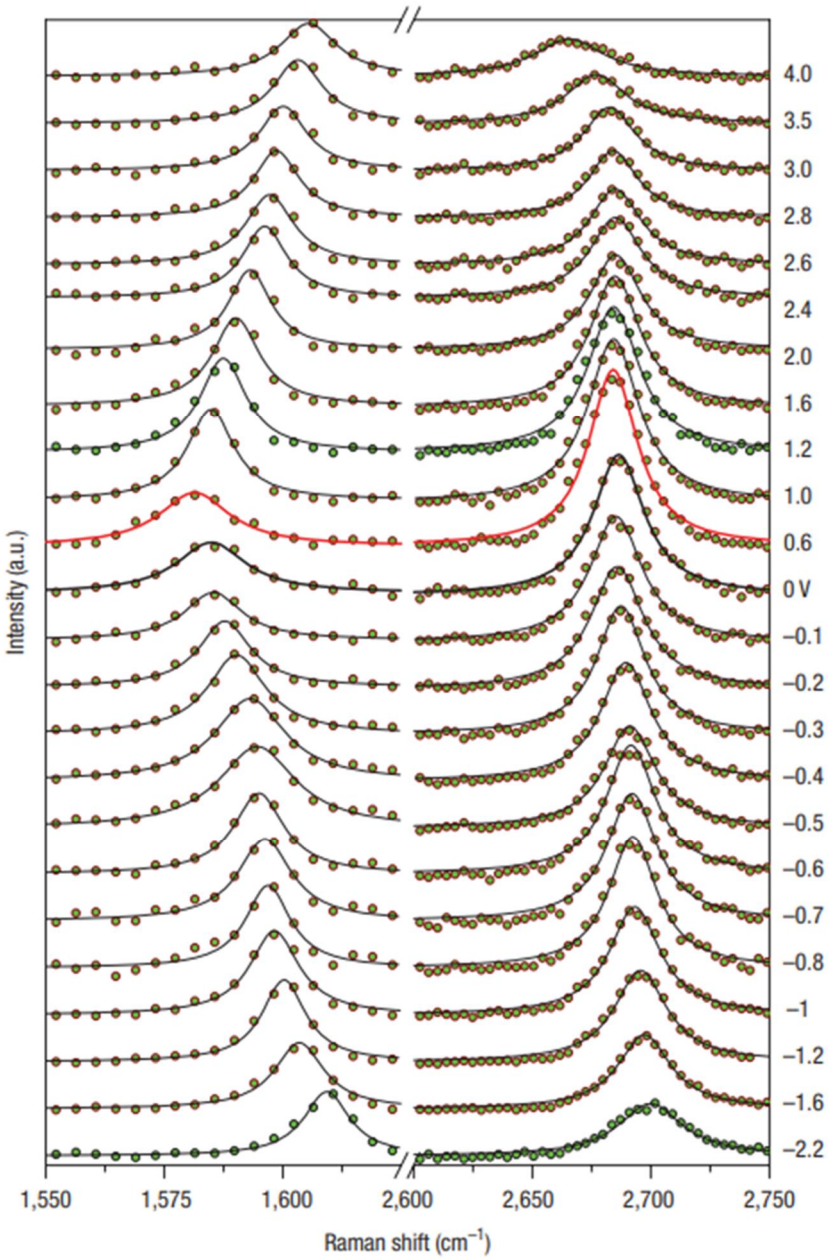

Figure 2-20. Raman spectra of graphene as a function of gate voltage, V_{GS}. Raman spectra at values of V_{GS} (top-gate) between -2.2 V and $+4.0$ V. The dots are the experimental data, the black lines are fitted Lorentzian functions, and the red line corresponds to the DP. The peak of G band is on the left and the peak of $2D$ band is on the right. (Reprinted from ref. [**42**], Copyright 2008 Nature Publishing Group)

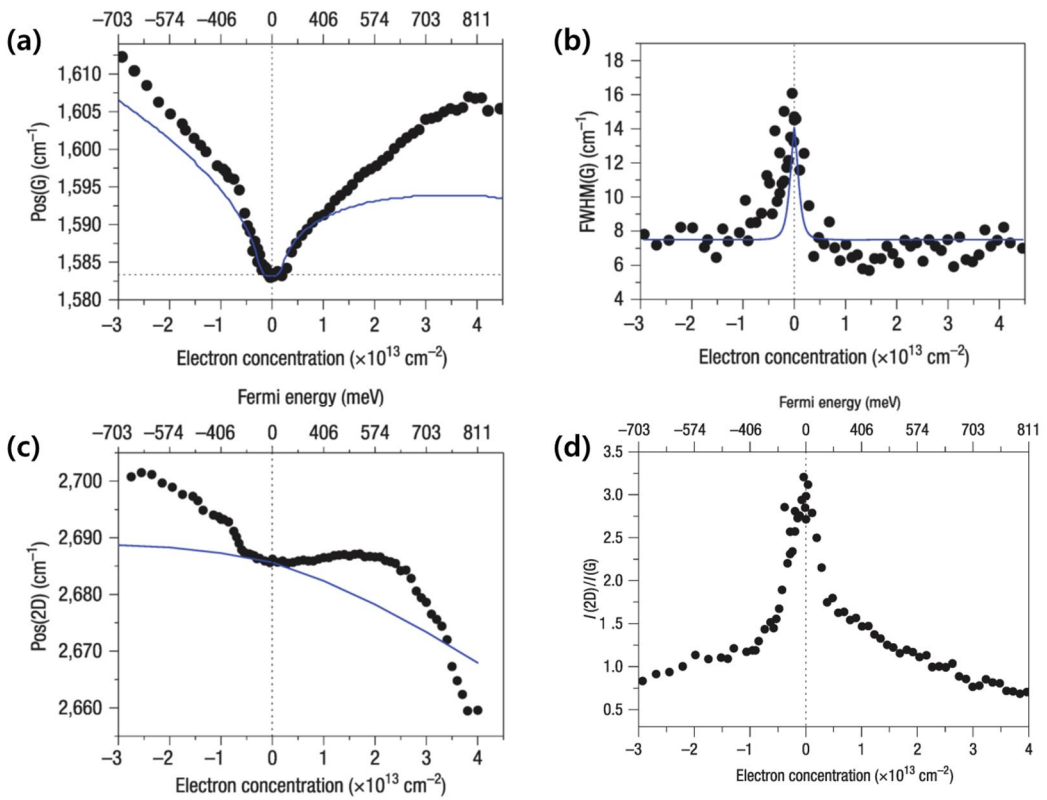

Figure 2-21. The change of G and $2D$ bands by gate voltage applications. (a) Peak position of the G band (Pos(G)) and (b) its FWHM (FWHM(G); bottom panel) as a function of p-type and n-type doping. The solid blue lines are the predicted non-adiabatic trends from ref. [**235**]. (c) Peak position of the $2D$ band (Pos($2D$)) as a function of doping. The solid blue line is the adiabatic DFT calculation from the authors of ref. [**42**]. (d) I_{2D}/I_G exhibits a clear dependence on the electron concentration of SLG doped by gate voltage application. (Reprinted from ref. [**42**], Copyright 2008 Nature Publishing Group)

2. 6. Electronic Analyses for Graphene Field-effect Transistor

2. 6. 1. Field-effect Transistor

A transistor is an electronic device that was born by the development of quantum mechanics. Transistor is an abbreviation for 'transfer resistor', which means a 3-terminal device that controls resistance.[**236**] Transistors are largely classified into the bipolar junction transistor (BJT) and the field-effect transistor (FET). The biggest difference between the two transistors is their polarity. BJT is bipolar and FET is unipolar. Compared to BJT, FET has the advantages of easy circuit analysis, advantageous for low voltage driving, and easy manufacturing process. So, historically, BJT was developed before FET, but now FET is used for more digital equipment. **Figure 2-22** shows the structure BJT, FET and potential-effect transistor (PET).

The FET controls the current by using a change in the electric field in the device. Changes in the electric field result from changes in voltage. In other words, the FET is a device that controls the intensity of current, that is, the flow of electrons, through voltage control. **Figure 2-22c** depicts the structure of FET device. Electrons flow from the source terminal to the drain terminal, and the voltage applied to the gate terminal controls the flow of the electrons. FET is also subdivided according to structure and materials, which is introduced in **Figure 2-23**. Among them, metal-oxide-semiconductor FET (MOSFET), which has many advantages, is the most commonly used transistor in the world. **Figure 2-24** shows the structure of MOSFET. There are two types of MOSFET; in general, n-p-n MOSFET is called NMOS, and p-n-p MOSFET is called PMOS.

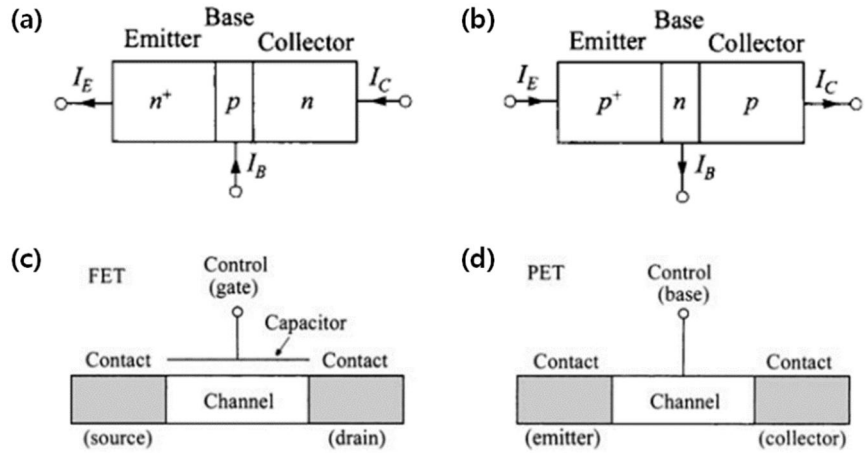

Figure 2-22. The structure of various transistor. (a) n-p-n BJT, (b) p-n-p BJT, (c) FET and (d) PET. (Reprinted from ref. [**236**], Copyright 2007 John Wiley & Sons, Inc.)

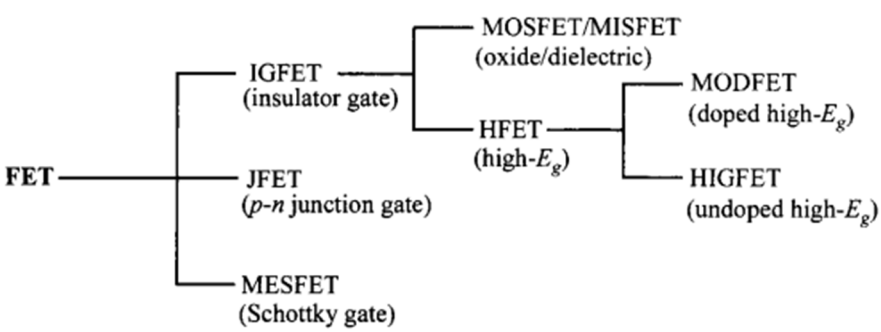

Figure 2-23. Family tree of FETs. IGFET, insulator gate FET. JFET, junction FET. MESFET, metal-semiconductor FET. MOSFET/MISFET, metal-oxide/insulator-semiconductor FET. HFET, heterojunction FET. MODFET, modulation-doped FET. HIGFET, heterojunction insulated-gate FET. (Reprinted from ref. [**236**], Copyright 2007 John Wiley & Sons, Inc.)

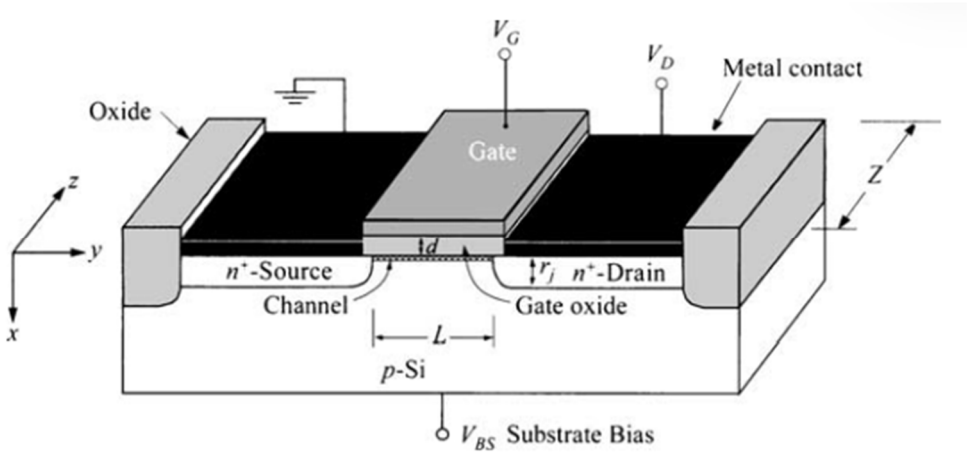

Figure 2-24. Schematic diagram of a n-type MOSFET (NMOS). (Reprinted from ref. [**236**], Copyright 2007 John Wiley & Sons, Inc.)

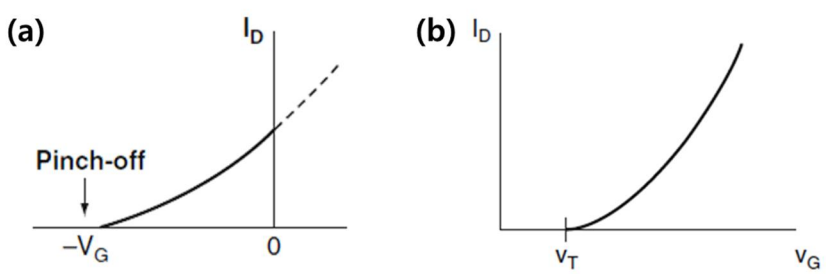

Figure 2-25. Electrical transfer characteristics of MOSFET. (a) a n-n-n MOSFET (with n-type doped channel), depletion MOSFET. (b) a n-p-n MOSFET (with p-type doped channel), enhancement MOSFET. $-V_G$, pinch-off voltage. V_T, threshold voltage. (Reprinted from ref. [**237**], Copyright 2007 Springer New York)

2. 6. 2. Current Equation in MOSFET

Electrical transfer characteristics (electrical transfer curve) is a plot showing the relationship between source-drain current, I_{DS} and gate voltage, V_{GS} at the constant source-drain voltage, V_{DS} in FET device. In order to interpret the electrical transfer characteristics of MOSFET, it is necessary to derive the (drain) current equation.[**236**]

Prior to the induction of the equation, it is assumed that MOSFET is an enhancement NMOS. The capacitance of the gate oxide is as follows

$$C_{\mathrm{ox}} = \epsilon_{\mathrm{ox}} \frac{WL}{t_{\mathrm{ox}}} = \epsilon_0 \kappa_{\mathrm{ox}} \frac{WL}{t_{\mathrm{ox}}}, \tag{2-2}$$

where C_{ox} is the capacitance of gate oxide; ϵ_{ox} is the permittivity of gate oxide; ϵ_0 is the vacuum permittivity (= 8.854×10^{-12} F·m^{-1}); κ_{ox} is the relative permittivity of gate oxide; W is the width of gate oxide; L is the length of gate oxide; t_{ox} is the thickness of gate oxide. Using **Equation (2-2)**, The current is as follows

$$I_{\mathrm{DS}} = \frac{Q_{\mathrm{ox}}}{\tau} = \frac{C_{\mathrm{ox}} V}{\tau} = \epsilon_0 \kappa_{\mathrm{ox}} \frac{WL}{t_{\mathrm{ox}}} \frac{V}{\tau}, \tag{2-3}$$

where Q_{ox} is the charge in gate oxide; V is the voltage at gate; τ is the time when the current flows. If V_{GS} is bigger than V_{T}, the channel is formed, and if V_{GS} is smaller than V_{T}, the channel is not formed. Let $V(x)$ be the voltage function for distance x in a channel,

$$V = V_{\mathrm{GS}} - V_{\mathrm{T}} - V(x). \tag{2-4}$$

Meanwhile, the relationship between the velocity of charge v and the electric field at channel E is as follows

$$v = \mu E = \mu \frac{dV}{dx}, \tag{2-5}$$

where the coefficient is defined as μ which is the carrier mobility. The time τ is calculated as follows

$$\tau = \frac{L}{v} = \frac{L}{\mu \frac{dV}{dx}}. \tag{2-6}$$

Using **Equation (2-6)**, the time during which electrons travel in NMOS is calculated as follows

$$I_{\mathrm{DS}} = \epsilon_0 \kappa_{\mathrm{ox}} \frac{WL}{t_{\mathrm{ox}}} \frac{V_{\mathrm{GS}} - V_{\mathrm{T}} - V(x)}{\frac{L}{\mu \frac{dV}{dx}}} = \epsilon_0 \kappa_{\mathrm{ox}} \mu \frac{W}{t_{\mathrm{ox}}} [V_{\mathrm{GS}} - V_{\mathrm{T}} - V(x)] \frac{dV}{dx} \quad \textbf{(2-7)}$$

Equation (2-7) is rearranged as follows

$$I_{\mathrm{DS}} dx = \epsilon_0 \kappa_{\mathrm{ox}} \mu \frac{W}{t_{\mathrm{ox}}} [V_{\mathrm{GS}} - V_{\mathrm{T}} - V] dV. \quad \textbf{(2-8)}$$

Equation (2-8) which is variable-separated is integrated as follows

$$\int_0^L I_{\mathrm{DS}} dx = \int_0^{V_{\mathrm{DS}}} \epsilon_0 \kappa_{\mathrm{ox}} \mu \frac{W}{t_{\mathrm{ox}}} [V_{\mathrm{GS}} - V_{\mathrm{T}} - V] dV. \quad \textbf{(2-9)}$$

Equation (2-9) is summarized as follows

$$I_{\mathrm{DS}} L = \epsilon_0 \kappa_{\mathrm{ox}} \mu \frac{W}{t_{\mathrm{ox}}} \left[(V_{\mathrm{GS}} - V_{\mathrm{T}}) V_{\mathrm{DS}} - \frac{1}{2} {V_{\mathrm{DS}}}^2 \right]. \quad \textbf{(2-10)}$$

Divide both sides of **Equation (2-10)** by L,

$$I_{\mathrm{DS}} = \frac{1}{2} \mu \frac{\epsilon_0 \kappa_{\mathrm{ox}}}{t_{\mathrm{ox}}} \frac{W}{L} \left[2(V_{\mathrm{GS}} - V_{\mathrm{T}}) V_{\mathrm{DS}} - {V_{\mathrm{DS}}}^2 \right]. \quad \textbf{(2-11)}$$

Equation (2-11) is the general current equation in MOSFET. If some variables of materials are combined,

$$I_{\mathrm{DS}} = \frac{1}{2} \kappa' \frac{W}{L} \left[2(V_{\mathrm{GS}} - V_{\mathrm{T}}) V_{\mathrm{DS}} - {V_{\mathrm{DS}}}^2 \right]. \quad \textbf{(2-12)}$$

where $\kappa' = \mu \epsilon_0 \kappa_{\mathrm{ox}} / t_{\mathrm{ox}}$ is a process transconductance parameter which derived according to the manufacturing process. If some variables of materials are combined repeatedly,

$$I_{DS} = \frac{1}{2}\kappa\left[2(V_{GS} - V_T)V_{DS} - {V_{DS}}^2\right]. \quad \textbf{(2-13)}$$

where $\kappa = \kappa'(W/L) = (\mu\epsilon_0\kappa_{ox}/t_{ox})(W/L)$ is a MOSFET transconductance parameter or a gain factor which determined by device designer.

Figure 2-26a shows that the electrical transfer characteristics is divided into three regions: linear, nonlinear or saturation region. Linear and saturation region can be approximated. In linear region, $V_{GS} \geq V_T$ and $V_{DS} < V_{GS} - V_T$, **Equation (2-11)** becomes the following equation,

$$I_{DS} = \mu\frac{\epsilon_0\kappa_{ox}}{t_{ox}}\frac{W}{L}(V_{GS} - V_T)V_{DS}. \quad \textbf{(2-14)}$$

On the other hand, in saturation region, $V_{GS} \geq V_T$ and $V_{DS} \geq V_{GS} - V_T$, **Equation (2-11)** becomes the following equation,

$$I_{DS} = \frac{1}{2}\mu\frac{\epsilon_0\kappa_{ox}}{t_{ox}}\frac{W}{L}(V_{GS} - V_T)^2. \quad \textbf{(2-15)}$$

To summary is as follows **Equation (2-16) and (2-17)**. In the case of PMOS, the direction of the inequality of the condition is reversed.

For NMOS,

$$I_{DS} = \begin{cases} \mu\frac{\epsilon_0\kappa_{ox}}{t_{ox}}\frac{W}{L}(V_{GS} - V_T)V_{DS} & \text{for } V_{GS} \geq V_T \text{ and } V_{DS} < V_{GS} - V_T \\ \frac{1}{2}\mu\frac{\epsilon_0\kappa_{ox}}{t_{ox}}\frac{W}{L}(V_{GS} - V_T)^2 & \text{for } V_{GS} \geq V_T \text{ and } V_{DS} \geq V_{GS} - V_T \end{cases}. \quad \textbf{(2-16)}$$

For PMOS,

$$I_{DS} = \begin{cases} \mu\frac{\epsilon_0\kappa_{ox}}{t_{ox}}\frac{W}{L}(V_{GS} - V_T)V_{DS} & \text{for } V_{GS} \leq V_T \text{ and } V_{DS} > V_{GS} - V_T \\ \frac{1}{2}\mu\frac{\epsilon_0\kappa_{ox}}{t_{ox}}\frac{W}{L}(V_{GS} - V_T)^2 & \text{for } V_{GS} \leq V_T \text{ and } V_{DS} \leq V_{GS} - V_T \end{cases}. \quad \textbf{(2-17)}$$

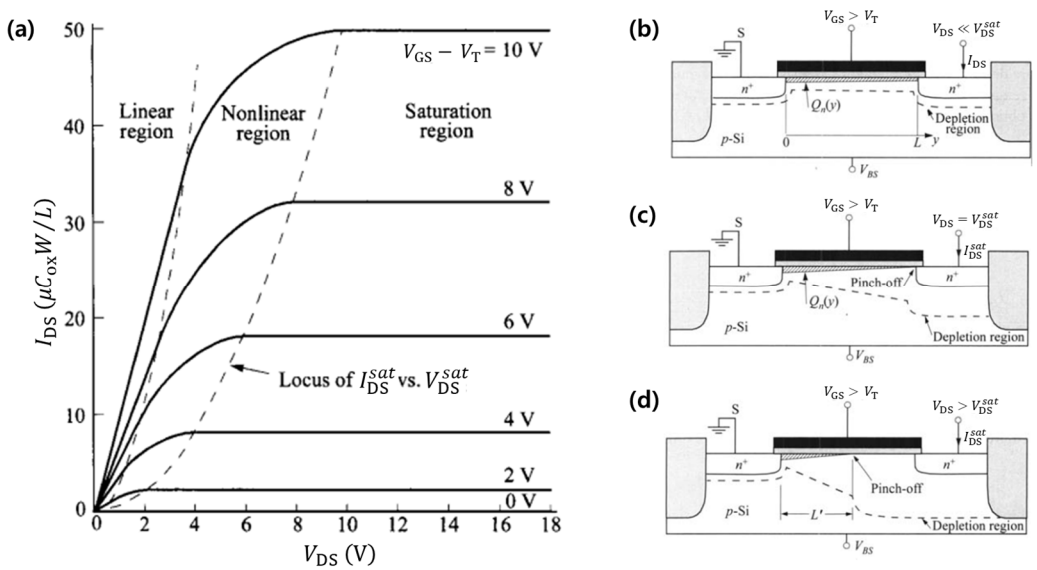

Figure 2-26. Full electrical transfer characteristics and the structures of MOSFET. (a) Idealized drain characteristics (I_{DS} *vs.* V_{DS}) of a MOSFET. The dashed lines separate the linear, nonlinear, and saturation regions. MOSFET operated (b) in the linear region (low V_{DS}), (c) at onset of saturation, and (d) beyond saturation (effective channel length is reduced). (Reprinted from ref. [**236**], Copyright 2007 John Wiley & Sons, Inc.)

2. 6. 3. Graphene Field-effect Transistor

Graphene was once praised for having a potential performance in practical applications. One of the expected applications was a semiconductor device that replaced the current MOSFET. However, as shown in **Paragraph 1. 3. 6.**, graphene cannot be used as a semiconductor because it is a zero gap material. Currently, device research using other semiconductor 2D materials is underway. This paragraph describes the structure, the measurement method of physical properties, and limitations of graphene FET.

A graphene FET is an FET in which graphene is a channel of a device. The general shape shown in **Figure 2-27** of the graphene FET is not much different from that of the MOSFET. In the actual experiment, the back-gated FET in **Figure 2-27a** did not make a back-gate contact but used a p-type doped Si wafer as an electrode. In general, the physical properties measured in the top-gated FET are better than those measured in the back-gated FET. In addition, dual-gated FET in **Figure 2-27b** is an FET using both top-gate and back-gate contacts, and has better performance than each FET. **Figure 2-27c** shows the FET manufactured after directly growth of epitaxial graphene on a silicon carbide (SiC) substrate. OM image in **Figure 2-28** shows that my real graphene FET by electron-beam lithography (EBL). The graphene FET devices are produced by photolithography (PL), EBL and masked deposition, etc.

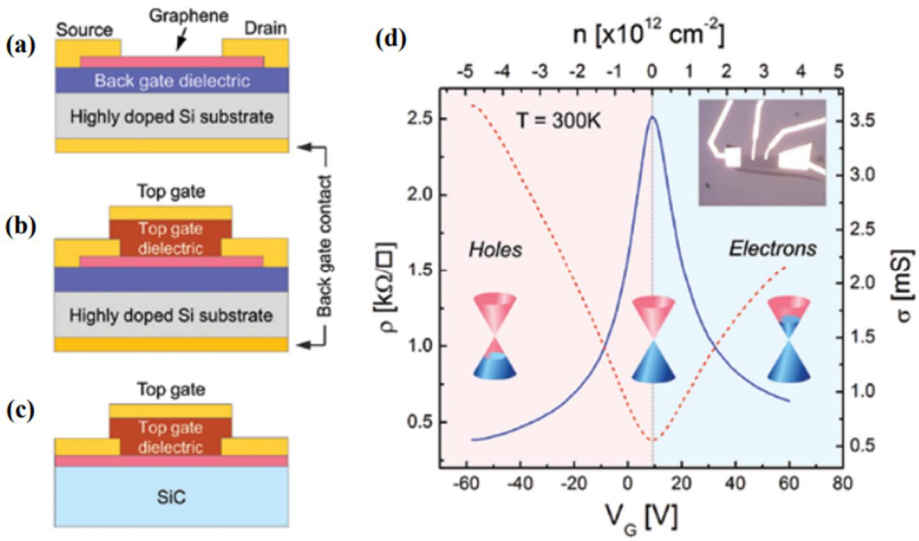

Figure 2-27. The structures and electrical transfer characteristics of graphene FET. (a) Back-gated graphene transistor; (b) dual-gated graphene transistor; (c) epitaxial graphene from SiC and transistor structure; (d) typical transfer curve for a single-layer graphene transistor: channel resistivity (blue line) and channel conductivity (red dashed line) vs. gate voltage. The inset in (d) shows an OM image of the graphene transistor. The distance between the two outer electrodes is 10 μm. (Reprinted from ref. [**238**], Copyright 2013 IOP Publishing)

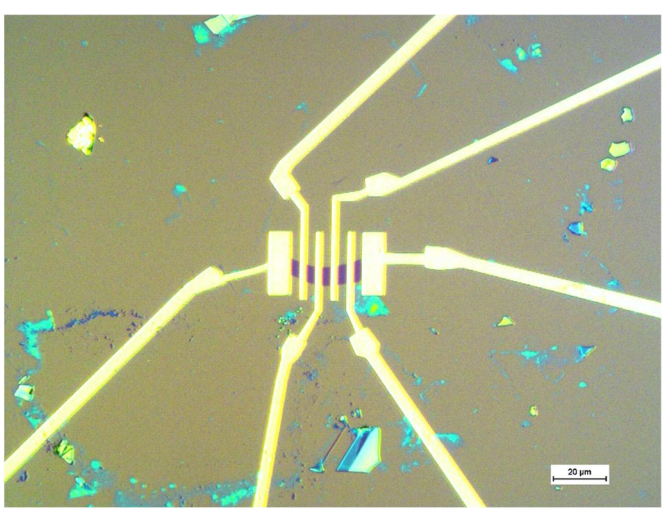

Figure 2-28. Graphene transistor. The device is fabricated on exfoliated graphene flake by EBL. OM image. Scale bar, 20 μm.

2. 6. 4. Electrical Transfer Characteristics of Graphene

Figure 1-22, 1-23, 2-11, 2-27b and 2-29a describe I_{DS} as a function of V_{GS} at constant source-drain voltage V_{DS} in graphene FET. These curves are different from the plot of MOSFET (shown in **Figure 2-25**). MOSFET has a characteristic of rectifying action, so an electric current flows in one direction with respect to a specific voltage ($-V_{\mathrm{G}}$ or V_T in **Figure 2-25**), whereas graphene FET has a current that flows to the left and right of V_{CNP}.

In **Figure 2-27b**, it can be seen that the major carrier changes to the left and right of the V_{CNP}. This is a phenomenon that occurs when the charge carrier concentration varies depending on the value of V_{GS}, and is interpreted through the band structure corresponding to each region. The left and right sides of V_{CNP} are hole-dominant and electron-dominant regions, respectively. The gate voltage change has a similar effect to doping.

We calculated the carrier mobility of the doped graphene using the standard model of the MOSFET (**Equation (2-16) and (2-17)**). In the linear region of the transfer curve (also known as the ohmic region or triode region), I_{DS} is linearly proportional to V_{GS}. **Equation (2-16) or (2-17)** is summarized in terms of carrier mobility as follows

$$\mu = \frac{1}{C_{\mathrm{ox}}} \frac{L}{W} \frac{1}{V_{\mathrm{DS}}} \frac{\partial I_{\mathrm{DS}}}{\partial V_{\mathrm{GS}}}. \qquad \textbf{(2-18)}$$

When doping is performed, electrons or holes are provided in the bands, and thus the effect of permanently applying the gate voltage may be obtained. That is, p-type doping moves the plot to the left, and n-type doping moves the plot to the right.

The values of V_{CNP} can be determined through electrical transfer curves, from which carrier concentration, n can be calculated from **Equation (2-19)**.

$$n = \frac{C_{\mathrm{ox}}}{e} \Delta V_{\mathrm{CNP}} = \frac{\epsilon_0 \kappa_{\mathrm{ox}}}{e t_{\mathrm{ox}}} \Delta V_{\mathrm{CNP}}, \qquad \textbf{(2-19)}$$

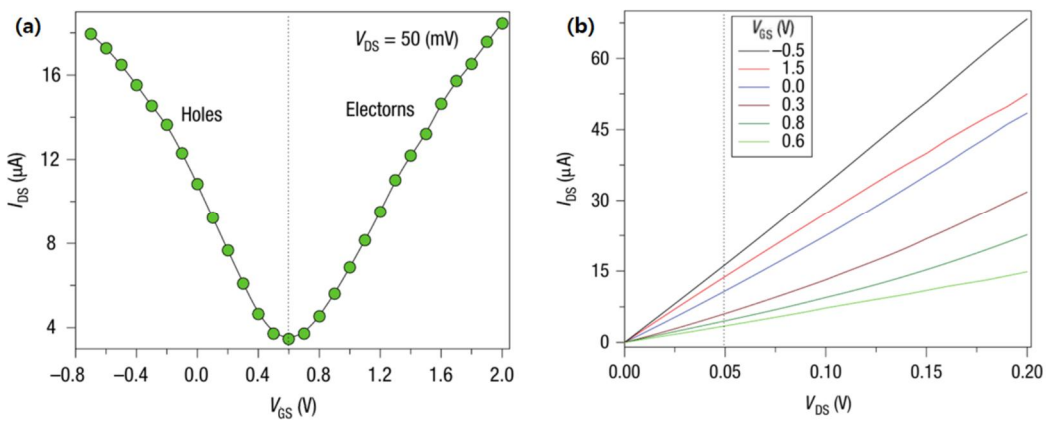

Figure 2-29. Electrochemically top-gated graphene transistor. (a) I_{DS} as a function of V_{GS}. The dotted line corresponds to the CNP (DP). (b) I_{DS} *versus* V_{DS} at different V_{GS}. The black dotted line corresponds to the value of V_{DS} at which the data in (a) was measured. (Reprinted from ref. [**42**], Copyright 2008 Nature Publishing Group)

2. 6. 5. Fermi Level Calculation of Graphene

The definition of Fermi level, E_F is introduced in **Paragraph 1. 6. 1.** The following induction process is performed to calculate E_F from the experimental values. The induction method was referred to as the method described in ref. [**237**]

Let N_{2D} be the number of states (population density) of 2D electron gas (2DEG) in 2D space. It is not possible to count the exact number of N_{2D}. If the smallest reciprocal area is A_1^*, it means a fundamental unit in reciprocal space (k space).

$$A_1^* = k_x k_y = \frac{2\pi}{\lambda_x}\frac{2\pi}{\lambda_y} = \frac{(2\pi)^2}{A_1}, \tag{2-21}$$

where k_x (or k_y) is an unit momentum of x^* (or y^*) direction in reciprocal space; $\lambda_x = 2\pi/k_x$ and $\lambda_y = 2\pi/k_y$ in real space; $A_1 = \lambda_x\lambda_y$ is the real area. If a reciprocal area occupied by N_{2D} is A_N^*, the reciprocal area A_N^* is approximated to the circle area with radius k because each state is very close.

$$A_N^* = \pi k^2. \tag{2-22}$$

Nondegenerate N_{2D} is calculated as follows

$$N_{2D} = \frac{A_N^*}{A_1^*} = \frac{\pi k^2}{(2\pi)^2/A_1} = \frac{k^2}{(2\pi)^2}A_1. \tag{2-23}$$

However, 2DEG on the surface of SLG is double degenerate. If **Equation (2-23)** is modified in consideration of degeneracy, the equation is as follows

$$N_{2D} = g_v g_s \frac{A_N^*}{A_1^*} = 2 \cdot 2 \cdot \frac{k^2}{4\pi}A_1 = \frac{k^2}{\pi}A_1, \tag{2-24}$$

where $g_v = 2$ is valley degeneracy; $g_s = 2$ is spin degeneracy. The density of states (DOS), n_{2D} is obtained by dividing N_{2D} by A_1.

$$n_{2D} = \frac{N_{2D}}{A_1} = \frac{k^2}{\pi}. \tag{2-25}$$

Since it deals with 2DEG of SLG, if the subscript '2D' is omitted and k is defined as Fermi wavevector, k_F, the equation is as follows

$$k_{\mathrm{F}} = \sqrt{n\pi}. \tag{2-26}$$

When the energy of electron in graphene is located at the Fermi level, **Equation (1-40)** is as follows

$$E_F = \hbar v_{\mathrm{F}} k_{\mathrm{F}} \tag{2-27}$$

If **Equation (2-26) and (2-19)** is substituted for **Equation (2-27)**, Fermi level, E_F is as follows

$$E_F = \hbar v_{\mathrm{F}} \sqrt{\pi n} = \hbar v_{\mathrm{F}} \sqrt{\frac{\pi \epsilon_0 \kappa_{\mathrm{ox}} \Delta V_{\mathrm{CNP}}}{e t_{\mathrm{ox}}}}. \tag{2-28}$$

Since DOS is a measure of how much carrier such as electron exists in matter, it can be considered as carrier concentration. The DOS obtained by this method is the value near E_F. That is E_F can be obtained by substituting the carrier concentration obtained from electrical transfer characteristics into **Equation (2-28)**. Equations for electron gas in 1D or 3D space can also be induced in a similar manner.

Figure 2-30 shows the result of matching the phonon dispersion and DOS of SLG. And the plot of dos shows the band gap of materials. More information on **Figure 2-30** can be found in the **Paragraph. 1. 3. And 1. 4.**

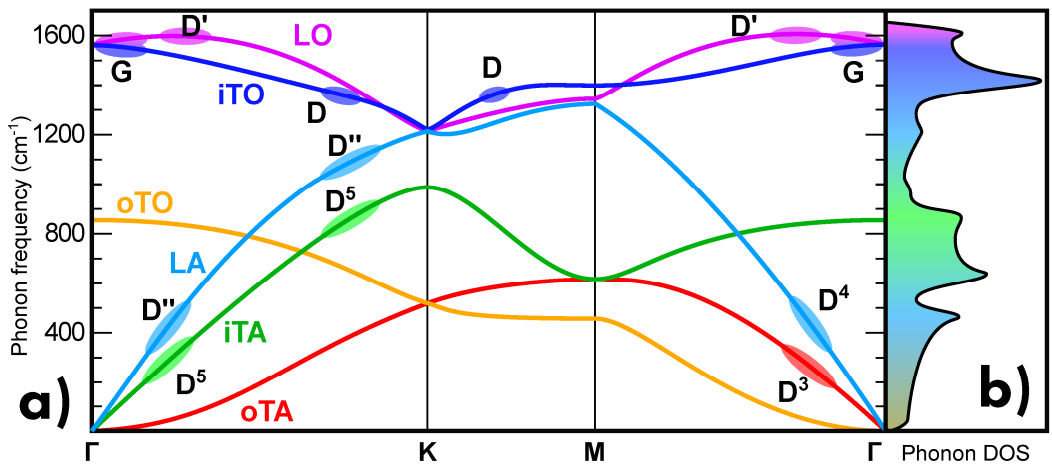

Figure 2-30. The relation between phonon dispersion and DOS of SLG. (a) Phonon dispersion relation for SLG along the direction connecting the high-symmetry points ***Γ***, ***K*** and ***M***. The phonon branches are labeled in accordance with their type of atomic displacement. Various Raman contribution is indicated, as well as the corresponding range of phonon wavevector. (b) Phonon DOS of SLG. The contribution of Raman mode at different phonon frequency is indicated by color. (Reprinted from ref. [**11**], Copyright (2019) MDPI)

Chapter 3.

Gold nanoparticle-mediated noncovalent functionalization of graphene for field-effect transistors

[* The contents of this chapter are reproduced and modified from:
Dongha Shin[†], Hwa Rang Kim[†], and Byung Hee Hong[*], Nanoscale Advances 3, 1404 (2021). Copyright 2021 The Royal Society of Chemistry][**188**]

3. 1. Abstract

Since its discovery, graphene has attracted much attention due to its unique electrical transport properties that can be applied to high-performance FET devices. However, mounting chemical functionalities onto graphene inevitably involves the breaking of covalent bonds by sp^2 hybridized orbitals or $2p_z$ orbitals of carbon atoms that construct graphene, resulting in the degradation of the mechanical and electrical properties compared to pristine graphene. Here, we report a new strategy to chemically functionalize graphene for use in FET devices without affecting the electrical performance. The key idea is to control the E_{F} of the graphene using the consecutive treatment of gold nanoparticles and 4-MBA molecules forming SAM, inducing p-type and n-type doping effects, respectively, by flipping the electric dipoles between gold nanoparticles and SAM by 4-MBA molecules. Based on this method, we demonstrate a V_{CNP} switcher on a graphene FET device using heavy metal ions on functionalized graphene, where the carboxyl functional groups of the mediating SAM efficiently form complexes with the metal ions and, as a result, the V_{CNP} can be positively shifted by different charge doping on graphene films. We believe that the nanoparticle-mediated SAM functionalization of graphene can pave the way to developing high-performance chemical, environmental, and biological sensors that fully utilize the pristine properties of graphene.

[†] D. S. and H. R. K. contributed equally to this work.
[*] To whom correspondence may be addressed.

3. 2. Introduction

Graphene was the first of the recently realized ideal 2D materials.[**3**] Its extraordinary mechanical,[**239**] electrical[**240**–**242**] and optical properties[**243**–**245**] have led to a variety of novel new devices, such as flexible transistors,[**246**] ultrafast lasers,[**247**] photodetectors[**248**,**249**] and optical modulators.[**250**,**251**] Among these, the ultrahigh carrier mobility (both electron and hole) of graphene makes it a promising material for nanoelectronic devices.[**240**,**252**,**253**] The upper limit of the outstanding electrical properties of a graphene-based FET device is already well-known.[**254**,**255**] Much effort has been done to develop new graphene FET devices for suitable purposes. Chemical functionalization can allow graphene FET devices to be realized as various chemical[**148**,**256**,**265**–**267**,**257**–**264**] and biological sensing platforms.[**268**–**277**] The most frequent way to implement such functions has been accomplished by the direct covalent bonding of molecules to graphene,[**120**,**122**,**125**,**265**,**266**,**278**,**279**] such as through an azide group.[**68**,**280**]

This method, however, converts the sp^2 hybridized orbital, which is the intrinsic characteristic of graphene, to a broken sp^3 hybridized orbital, and thus inevitably degrades the pristine electrical property of graphene.[**278**] In addition, if not that severe, adopting the heterogeneous species including functional molecules, in general, cannot avoid a significant doping effect, which substantially shifts the V_{CNP} from the pristine value and limits the detection range in real applications. Thus, our interest is to determine how to introduce functional groups on graphene FET devices without impairing the pristine sp^2 hybridized orbitals.

In this work, we have proposed a novel method to modulate the electrical properties of graphene FET devices by adopting gold nanoparticles and 4-MBA molecules. Consecutive treatment of the nanoparticles and SAM by molecules induces the p-type and n-type doping effects, respectively. By analyzing the doped characteristics both electrically and optically, we realized a functionalized graphene FET device that preserves the close pristine electronic state of graphene.

3. 3. Experimental

3. 3. 1. Synthesis of Graphene

Graphene films were synthesized on a copper foil which has thickness of 25 μm by low pressure CVD method. The carbon precursor is methane gas (50 sccm) and etchant is hydrogen gas (5 sccm). The vacuum level is kept at $\sim 10^{-4}$ Torr before injecting gases. Using this method, graphene is formed on both sides of the copper foil. To remove a relatively poor-quality graphene on one side, the RIE was applied on that side: power of 100 W, etching time of 20 s, plasma etchant as oxygen gas (20 sccm) and working pressure of 100 mTorr.

3. 3. 2. Transfer of Graphene

The graphene was transferred on substrate through the process of PMMA coating, copper etching, transfer on wafer and PMMA removal. First, PMMA layer was spin-coated on the face of copper foil where graphene exists. Then, the substrate was floated on the APS solution (20 mM with DI water) in order to etch out copper metal. As a substrate, highly p-type doped Si wafers covered with SiO_2 (300 nm) or PET films were prepared. The PMMA-supported graphene was rinsed with DI water repeatedly and transferred onto the substrates prepared. Then, the substrate was dipped into acetone to remove PMMA for 30 min.

3. 3. 3. Fabrication of graphene FET devices

Onto graphene on substrate, the electrodes of FET devices were fabricated by thermal deposition of chrome (3 nm) and gold (50 nm) layers, with using the pre-patterned stencil masks. The PMMA-supported graphene was rinsed with DI water repeatedly and transferred onto the patterned gold electrodes with care. Then, the substrate was dipped into acetone to remove PMMA for 30 min. Each graphene device was separated by EBL, with gate width of 100 μm and gate length of 40 μm. Finally, in order to remove impurities and charge puddles, graphene devices were thermally annealed at 300 ℃ for 3 hours under the atmosphere of hydrogen and argon as etchant (50 sccm) and carrier gas (200 sccm), respectively.

3. 3. 4. Doping of Graphene

Hydrogen tetrachloroaurate (III) hydrate (≥ 99.9%), 4-mercaptobenzoic acid (99%), 4-mercaptophenol (99%), 4-mercaptofluorobenzene (99%), 4-mercaptotoluene (99%), mercury (II) chloride (99.5+%), lead (II) chloride (99.999%), platinum (II) chloride (≥ 99.9%) and palladium chloride (II) (99%) were purchased from Sigma Aldrich (no further purification). Gold nanoparticle was deposited on graphene surface by dipping the substrate into the aqueous $HAuCl_4$ solution (0.1 mM or 1 mM, see **Figure 3-2**) for 30 min. Then, the substrates were dipped into ethanolic solution of thiol molecules (0.1 mM) for 10 min to make SAM on gold nanoparticle surface. The metal ions were captured by the substrate as dipping into the aqueous solutions (0.1 mM) for 10 min at each experiment.

3. 3. 5. Characterization of graphene films

First of all, we proceeded with XPS (AXIS-His, Kratos Analytical, UK) to verify that the graphene made by CVD method was well synthesized, and that the doping was well done by each nanocomponent. The CASA XPS program (CasaXPS 2.3.16 PR 1.6, Casa Software Ltd, UK) was used for the evaluation and analysis of the XPS data using Shirley's method.

Electrical property of graphene FET was measured by the 3-terminal (source, drain, and gate) probe station (MS Tech 5500, MS Tech, Korea) at ambient condition. We changed the gate voltage in the range between −40 and +140 V, while keeping the source to drain voltage as 1 mV. (Agilent B2912A, Agilent Technologies, USA). We have tested FET measurements with more than 15 kinds of devices.

The Raman analysis were conducted by inVia Raman Microscope (Renishaw, UK) using Ar laser with less than 1 mW of power. The wavelength of laser and grating are 514.5 nm, 2400 gr/mm and 632.8 nm, 1800 gr/mm, respectively. We integrated the signal for 10 s in all measurements for each point. The Raman mapping (with a side of 14.5 μm) was completed for about 12 hours.

The deposited gold nanoparticles were characterized by a noncontact mode of AFM (XE-100, Park System, Korea).

The sheet resistance (mapping) of the SLG transferred on the PET, in a square with a side of 5 cm, using non-contact method of a sheet resistance measuring device (EddyCus TF map 2525SR, Suragus GmbH, German), and the sheet resistance values inside a center square with a side of 3 cm were extracted (as shown in Fig. 3-13b). In addition, a 4-point probe portable sheet resistance measuring device (FPP-40k, DASOL ENG, Korea) was used to measure the sheet resistance at a point.

3. 4. Results and Discussion

3. 4. 1. Fabrication Process of Graphene-based FET devices

Figure 3-1 schematically shows the process of sequential treatment on a graphene surface. Firstly, we prepared patterned gold electrodes onto silicon oxide with 300 nm thickness on silicon (Si/SiO_2) wafers which is doped as p-type, and then the as-prepared graphene synthesized by CVD method[**4**] was transferred onto gold electrodes (step 1). Next, we incorporated the gold nanoparticles onto the graphene surface, and this is the key step (step 2) in our experiments. As shown by the step 3 process in **Figure 3-1**, the gold nanoparticles were deposited onto the graphene surface by the spontaneous reduction of a solution-based metal precursor ($AuCl_4^-$), induced by the redox potential difference (the galvanic exchange) between them.[**281**,**282**] This electroless method is cost-effective and straightforward since it does not require any extra linking molecules or reducing agents. Only the dipping time, along with precursor concentration (in stock solution), needed to be controlled. (**Figure 3-2**) For the same dipping time, it was found that the higher the concentration of $HAuCl_4$, the higher the shift of V_{CNP}, and the devices were destroyed by the high voltage near a concentration of 1 mM, making it impossible to measure V_{CNP}. Thus, several attempts were made to determine the appropriate concentration of the precursor of the gold nanoparticles. More detailed studies on such spontaneous reductions of gold nanoparticles, such as substrate dependency, have been reported in previous papers.[**281**,**282**] AFM analysis confirmed that our deposited gold nanoparticles are uniformly distributed, at ~4 nm in height. **(Figure 3-3)**

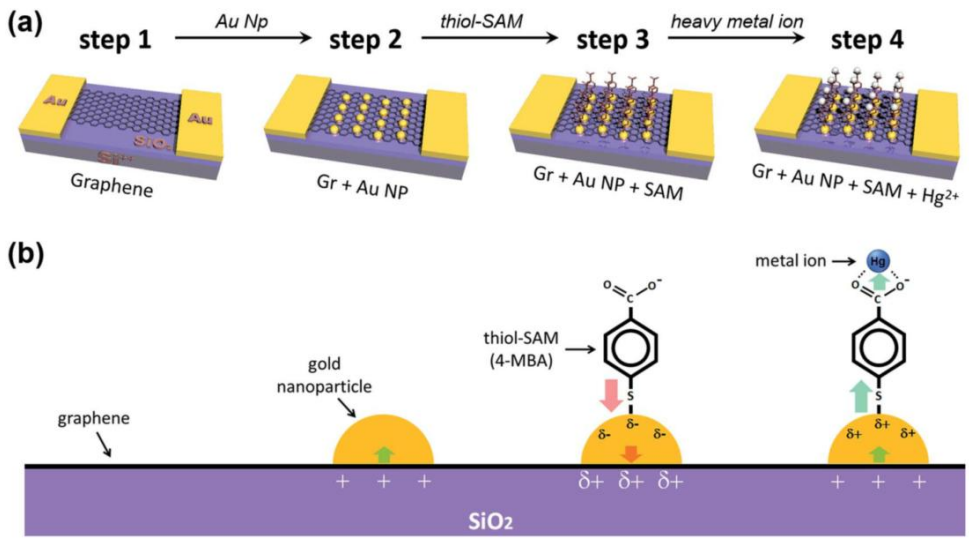

Figure 3-1. Schematics of experiments. (a) Schematic diagram to show the fabrication process of a graphene FET device and (b) enlarged views, denoting the configurations and charge transfer direction in each step. Deposited gold nanoparticles induce the partial p-type doping on graphene (step 2), while the thiol molecules (4-MBA) induce n-type doping (step 3). Step 4 shows that the captured heavy metal ion induces p-type doping on graphene (step 4). Au NP, gold nanoparticles, and thiol-SAM, SAM by thiol molecules (including 4-MBA).

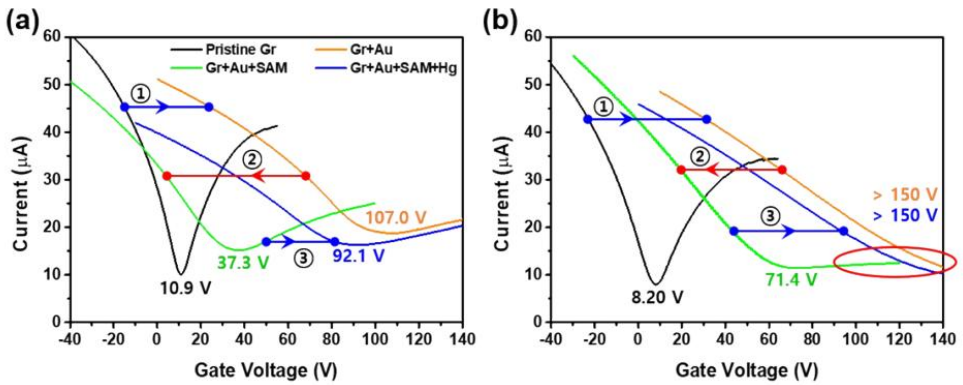

Figure 3-2. The more concentrated chloroauric acid ($HAuCl_4$) (*aq*) induces more p-type doping effect on graphene FET device. (a) 0.1 mM (original conditions) and (b) 1 mM. (compare the shift ① in blue arrow)

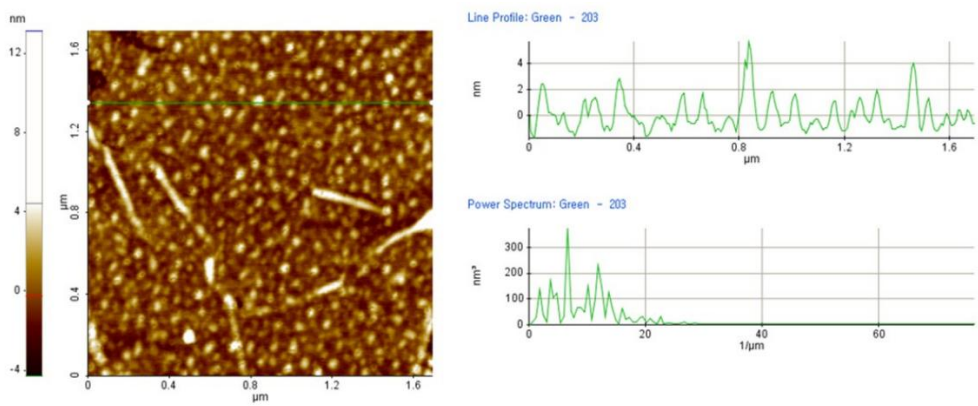

Figure 3-3. AFM analysis shows that deposited gold nanoparticles are uniformly distributed with having ~4 nm height.

3. 4. 2. XPS Analysis of Doped Graphene

XPS was used to verify that the desired treatment of each step was achieved through the dipping method. The spectra on the far left of each row in **Figure 3-4** represent the wide scan range of XPS at each step. **(Figure 3-4a, 3-4c, 3-4f and 3-4j)** Covalent bond between graphitic carbon atoms in SLG represents an asymmetric curve in the XPS spectra due to intrinsic interactions between the inner core hole and the electrons in the valence band.[**283**–**286**] **Figure 3-4b** reflects this and indicates that the pristine graphene by the CVD method is well-formed without breaking its hexagonal symmetry. In addition, **Figure 3-4d, 4g and 4k** show that the symmetry is not broken by the nanocomponent treated at each stage and remains intact.

The process of forming gold nanoparticles above graphene is extremely interesting, and the XPS spectra results of the Au $4f$ levels show that three chemical species of gold exist. From the results in **Figure 3-4e**, we can see that the Au ions that disassembled from $HAuCl_4$ exist in the Au^{3+} state, and when they are reduced to gold nanoparticles, they exist in the Au^0 state, or some in the Au^+ state. Each binding energy corresponding to $4f_{7/2}$ of Au^0, Au^+, and Au^{3+} is about 84 to 84.5, 85 to 86, and 86 to 87 eV.[**287**–**291**] In **Figure 3-4e** (as well as in **Figure 3-4h and 3-4l**), the energy difference, Δ, is separated in the Au $4f$ region due to orbital energy splitting as a result of spin-orbit coupling in the $4f$ orbital of the heavy metal elements. The value of Δ between Au $4f_{7/2}$ and $4f_{5/2}$ is 3.67 eV,[**290**,**291**] and this can be found from XPS spectra for the gold nanoparticles. In this process, gold nanoparticles are reduced by the graphene and the surface of graphene is doped as p-type. (step 2 in **Figure 3-1**)

In addition, sulfur peaks of 4-MBA molecules forming SAM which were not found in the wide scan range of the XPS spectra in the previous process, were found as weak signals in **Fig. 3-4f and 3-4i**. Those values correspond exactly to the S $2p$ level between a binding energy of 161 and 164 eV.[**292**] In **Figure 3-4h**, it can be observed that the intensity of the Au^{3+} peak has decreased, while the intensities of the Au^0 and Au^+ peaks have increased, due to the negative charge of the carboxyl group in SAM (step 3 in **Figure 3-1**).

In order to investigate the electrical properties at each step, we conducted FET measurements using a three-point probe station at ambient conditions. **Figure 3-5a** shows that the representative electrical transfer curve in pristine graphene (black curve, Gr) has shifted to the right, representing p-type doping (blue arrow, ①) of the gold nanoparticles-adsorbed graphene (orange curve, Gr + Au).

For the next step, we carried out molecular functionalization onto this substrate. (step 3 in **Figure 3-1**) Rather than using conventional azide group-containing molecules, we chose more convenient thiol molecules that can form a spontaneously SAM on the gold surface through gold-sulfur bonds. Due to its self-assembling character, the molecule

should have a vertical (slightly tilted) standing configuration, and without the gold surface this molecule should be deposited onto the graphene surface directly via $\pi - \pi$ interactions, favoring a horizontal laying-down configuration.

Next, we demonstrated the performance of our graphene FET devices: pendent carboxyl group of 4-MBA molecules as a mercury ion captor. Step 4 in **Figure 3-1** shows the capture of a mercury ion by the carboxyl group in our FET platform. It is well-known that carboxyl groups make complexes (chelating bidentate forms) with various transition metal cations due to the high stability constant of the reactions.[**293**–**295**] Hg^{2+} ions act as bidentate ligands in this step. In addition, the XPS results show that the Hg $4f$ region is separated by 4.05 eV energy splitting, the same as the Au $4f$ region.[**296**] In addition, since the substrates used in the study were Si/SiO_2 substrates, we must be careful about overlapping Si $2p$ peak positions in the XPS analysis of Hg $4f$.[**297**,**298**]

Thus, after dipping the substrate (step 3 in **Figure 3-1**) into the mercury ion solution, the measured FET character showed a shift (blue arrow, ③) of the transfer curve to the p-type doped state of Hg^{2+}-captured 4-MBA SAM-combined gold nanoparticle-adsorbed graphene (blue curve, Gr + Au + 4-MBA + Hg^{2+}) in **Figure 3-5a**. This can be seen by the further decrease in the intensity of the Au^0 peak in **Figure 3-4l**, and that the intensity of the Au^+ peak increased significantly.

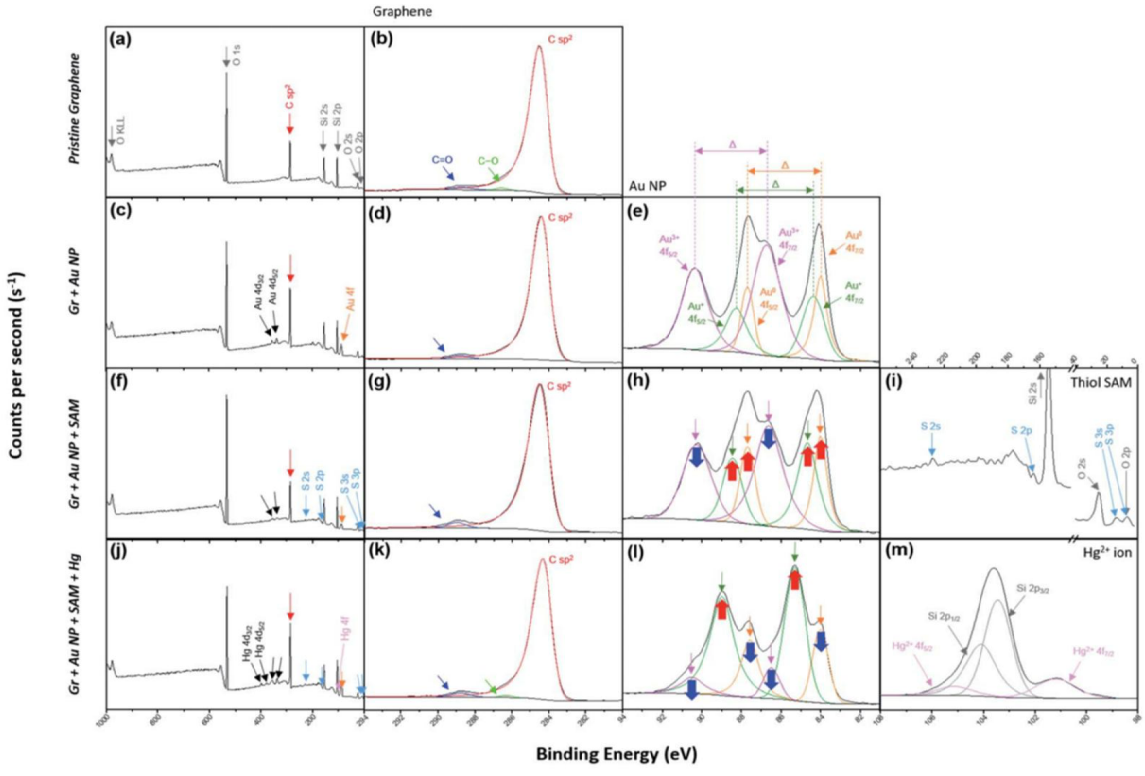

Figure 3-4. XPS data for bare and doped graphene samples. (a) The wide scan and (b) C $1s$ range for the XPS of the pristine graphene film (step 1 in **Figure 3-1**). (c) The wide scan, (d) C $1s$ and (e) Au $4f$ ranges for the XPS of Gr + Au (step 2 in **Figure 3-1**). (f) The wide scan, (g) C $1s$, (h) Au $4f$ and (i) S $2p$ ranges for the XPS of Gr + Au + SAM (step 3 in **Figure 3-1**). (j) The wide scan, (k) C $1s$, (l) Au $4f$ and (m) Hg $4f$ ranges for the XPS of Gr +Au+ SAM + Hg (step 4 in **Figure 3-1**).

3. 4. 3. Electronic Analysis of Doped Graphene

Figure 3-5b shows the change in charge neutrality point (ΔV_{CNP}) value at each step. Although some variation was observed (device to device variation) at each step, sequential treatments generally induced the change in doping state in graphene, from pristine to p-type doped to n-type doped to p-type doped (V_{CNP}: 8.14 → 95.86 → 24.03 → 90.86 V). We calculated the hole mobility of the doped graphene using the standard model of the MOSFET. The corresponding band structures at the $\boldsymbol{K}$ point in the BZ of the pristine SLG are shown in **Figure 3-5d**.

For **Equation (2-18)**, substitute the following values: μ is the carrier mobility; C_{ox} is the capacitance of gate material, 300 nm SiO_2 (= 1.08×10^{-8} F·cm^{-2}); W is the gate width (= 100 μm); L is the gate length (= 40 μm); V_{GS} is the applied gate voltage from −40 to 140 V; and V_{DS} is the drain-source voltage difference (= 1 mV). Hole carrier mobility, μ_{h} of graphene can be measured indirectly from electrical transfer curves using **Equation (2-18)**. **Figure 3-5c** shows the mobility of each step with corresponding V_{CNP} values: 10236 → 6563.1 → 6087.3 → 5401.2 cm^2·V^{-1}·S^{-1}. Compared with some previous reports,[**240**,**299**,**300**] our system shows relatively high mobility that is advantageous in sensing capability. This is attributed to the low charge puddles or surface defect concentration (see the **Figure 3-9d** for low I_D/I_G ratio) induced by unbroken the bond characteristics of graphene.

As a control experiment of step 3 in **Figure 3-1**, we tested the effect of treatment of 4-MBA molecules on graphene without a gold nanoparticle deposition step, and this revealed that 4-MBA molecules induce an opposite p-type doping effect on graphene. (see **Figure 3-7a**) Interestingly, we can observe from **Figure 3-5a** that treatment of 4-MBA molecules has moved the transfer curve of the gold nanoparticle-adsorbed state (orange curve, Gr + Au) to the left, and this means the induction of the n-type doping effect (red arrow, ②) of 4-MBA SAM-combined gold nanoparticle-adsorbed graphene (green curve, Gr + Au + 4-MBA). According to previous reports,[**301**–**304**] noble metal nanoparticles are highly susceptible to interactions with external molecules, resulting in a surface potential (electronic state) change depending on the character of the adsorbed molecule. It has been known that thiol functionalization is likely to induce a n-type doping effect, which is electron donating, on the interface of gold nanoparticle.[**305**] Such SAM-induced electron donation on the gold nanoparticles then concurrently induces n-type doping on the graphene. Therefore, such succeeding p-type (gold nanoparticles) and n-type (SAM by 4-MBA molecules) doping effects finally result in the restoration of the electronic state of graphene that is close to its pristine state, and this can be used as a metal ion captor in the next step through the functionalized pendent chemical group.

In order to confirm its generality, we also compared the FET responses using other kinds of thiol molecules, showing that all of the thiol molecules induce a similar n-type

doping effect on graphene, while exhibiting different doping levels depending on the molecular type. Such differences might be associated with molecular dipole moments.[**305**] **(Figure 3-6)**

In addition, as a control experiment of step 4 in **Figure 3-1**, we confirmed that without treatment of 4-MBA molecules, a mercury ion solely induces an opposite n-type doping effect on gold nanoparticle-deposited graphene FET devices. (see **Figure 3-7b**) In addition, we also observed that (4-mercaptotoluene (4-MT))-based FET devices show a negligible response to mercury ion treatment, verifying the strong interaction between the carboxyl group of 4-MBA molecules and the mercury ion. **(Figure 3-8)**

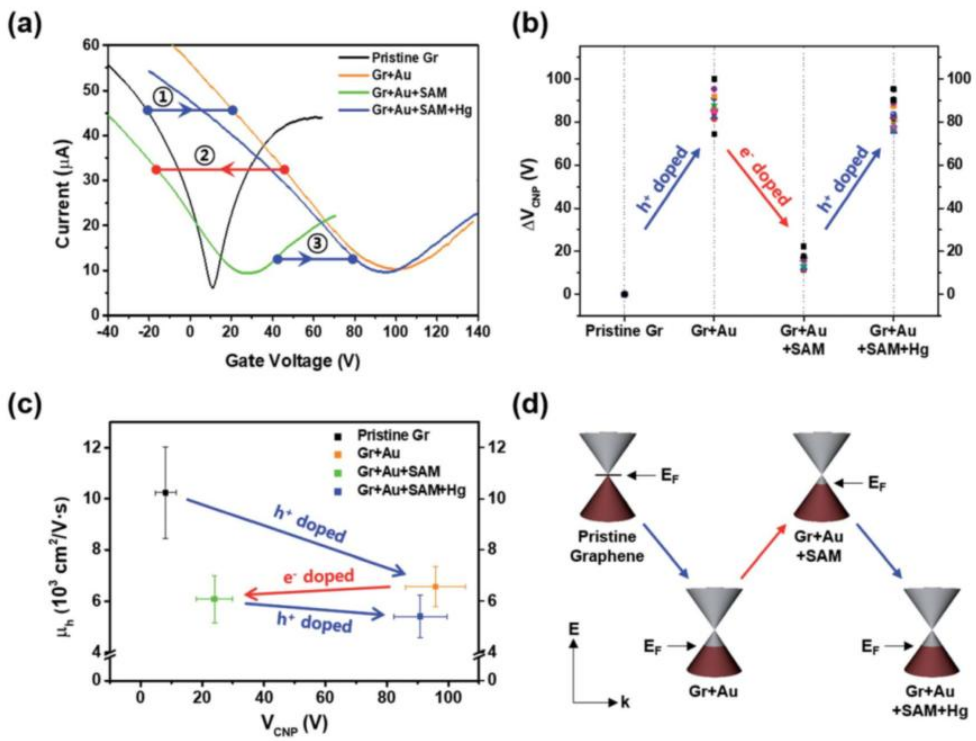

Figure 3-5. Electronic analyses of graphene FETs. (a) Representative electrical transfer curves of graphene FET devices measured at each doping step. (b) V_{CNP} variation at each step. (c) Hole carrier mobility (μ_{h}) plot with respect to V_{CNP}. (d) Schematic illustration of the band structures and the variation in the E_{F} of graphene.

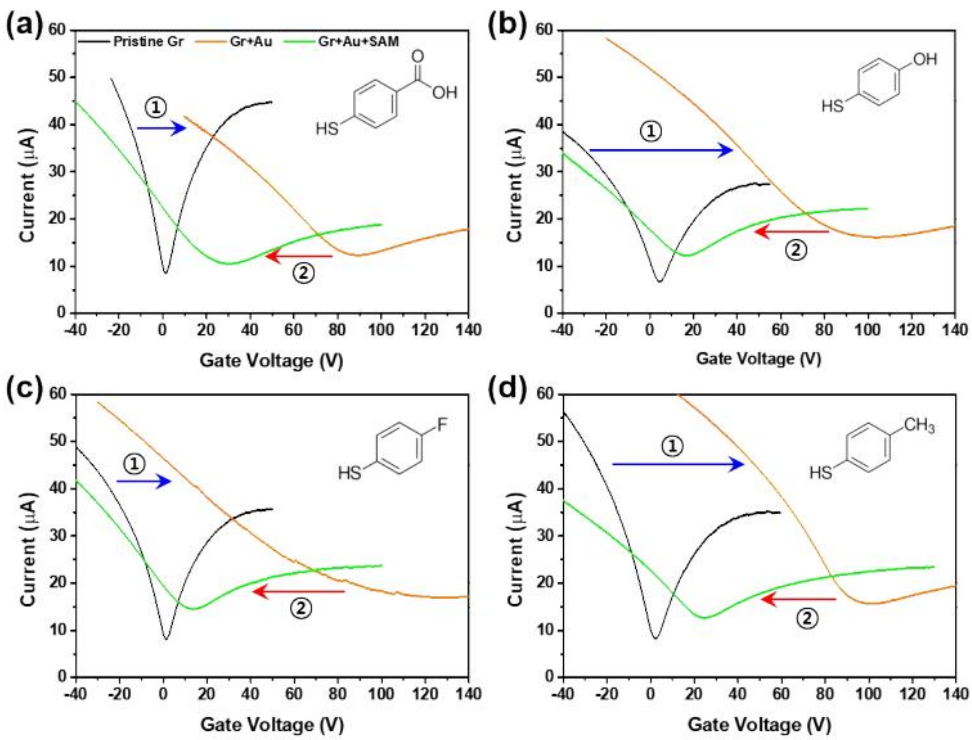

Figure 3-6. The electrical transfer characteristics of graphene samples which doped by various thiol-SAM. The curves show that the various thiol-SAM molecules induce universal n-type doping effect on graphene through the pre-deposited gold nanoparticle. (a) 4-MBA, (b) 4-mercaptophenol (4-MP), (c) 4-mercaptofluoro-benzene (4-MFB) and (d) 4-mercaptotoluene (4-MT). All other experimental conditions are the same.

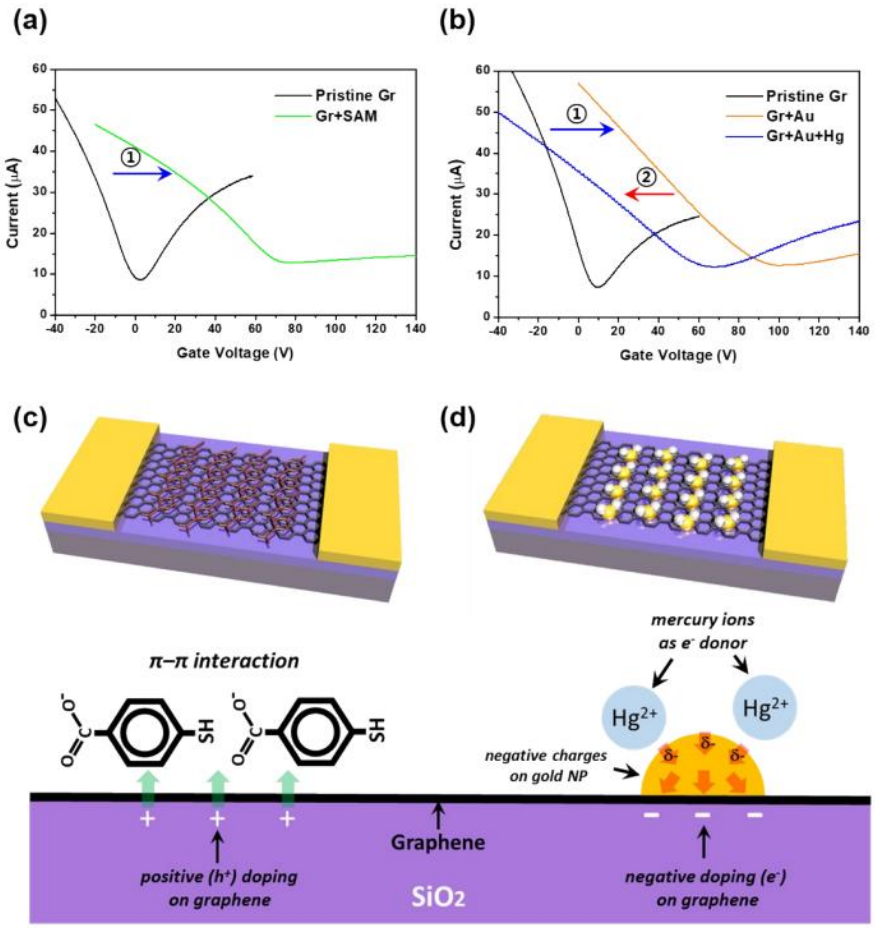

Figure 3-7. The electrical transfer characteristics of graphene FET devices, (a) treated by only 4-MBA molecule directly on graphene and (b) treated by mercury ion on gold nanoparticle without 4-MBA SAM. (c) and (d) schematically show the corresponding situation of (a) and (b), respectively. These are conducted for the control experiments.

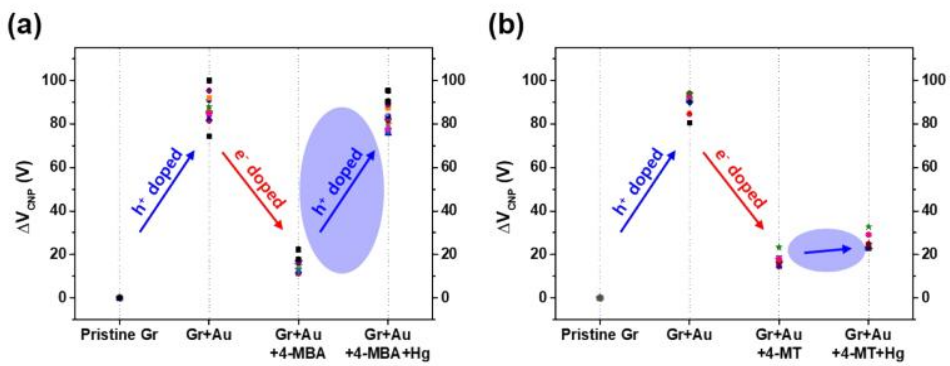

Figure 3-8. V_{CNP} measured at each step. The plots show that (a) (4-MBA)-based FET responds dramatically to the mercury ion treatment (blue shaded circle), while (b) (4-MT)-based one responds negligibly. This verifies the strong interaction between carboxyl group and mercury ion.

3. 4. 4. Raman Spectroscopic Analysis of Doped Graphene

Raman spectroscopy is one of the valuable optical technique when analyzing the electrical property of graphene.[**50**] **Figure 3-9** shows the Raman analyses of graphene FET devices at each step, measured at ambient conditions. For all measurements, we used 514.5 nm laser light (< 1 mW) with a spot size of 2 mm to reduce the damage on the samples. First of all, it should be noted that the original (not in ours) pristine graphene that is strain-free and charge-neutral shows the G and $2D$ bands at 1581.6 ± 0.2 and 2676.9 ± 0.7 cm^{-1}, respectively, and such G and $2D$ peaks signify the frequencies of the phonon interactions at the $\boldsymbol{\Gamma}$ and $\boldsymbol{K}$ points in the BZ, respectively. In our case shown in **Figure 3-9a and 3-9b**, the pristine graphene shows G and $2D$ peak positions at 1584.21 ± 1.98 and 2682.75 ± 3.47 cm^{-1}, respectively. After the gold nanoparticles were deposited, the peaks shifted to the higher positions at 1594.36 ± 2.98 and 2692.59 ± 4.59 cm^{-1} and, after 4-MBA treatment, returned to 1585.95 ± 1.22 and 2684.96 ± 2.98 cm^{-1}, respectively. Finally, mercury ion treatment induces a shift of the G and $2D$ peak positions to 1590.64 ± 1.50 and 2687.72 ± 0.34 cm^{-1}, respectively.

According to Lee *et al*.,[**209**] Raman spectroscopic analysis can interpret the strain effect and the charge doping effect in graphene samples separately shown in **Figure 2-19**. A detailed description is given in the **Paragraph 2. 5. 3. Figure 3-9c** shows the G *versus* $2D$ peak position of our samples, indicating that the point of $O(\omega_G^0, \omega_{2D}^0)$ semi-empirically corresponds to the strain-free and charge-neutral state, where the values of ω_G^0 and ω_{2D}^0 are given by **Equation (2-1)**. Even though our pristine graphene state (black square) is slightly far away from the point of origin, $O(\omega_G^0, \omega_{2D}^0)$, it is still positioned along the blue dashed line, which means that only compressive strain has been applied to our pristine sample. Since graphene has an intrinsically negative thermal expansion coefficient in the range of 200 to 400 °C,[**306**–**309**] annealing at 300 °C and cooling to room temperature unavoidably results in compressive strain on graphene, and this is the situation in our case. Next, our experiments showed that, in the consecutive treatment of the gold nanoparticles, 4-MBA molecules and mercury ions, the graphene states in the plot **(Fig. 3-9c)** change from black to orange, green, and finally to blue squares. It should be noted that all these states are still along the red dashed line, indicating that all the treatments only result in a charge-induced doping effect on graphene, and not a mechanical strain effect. These results correlate well with the shifts of V_{CNP} in graphene FET devices.

On the other hand, the intensity ratio between the $2D$ and G peaks (I_{2D}/I_G) is also a good parameter to evaluate the doping strength in a graphene sample. **Figure 3-9d** shows that it decreased from 3.004 ± 0.193 for the pristine state (step 1) to 1.769 ± 0.132 for the mercury ion-treated state (step 4). Furthermore, it is well-known that the D band in Raman spectra is related to the defect density of graphene films. In all of our

treatments, the intensity ratio of the D to G peak has remained relatively small in the range of 0.152 ± 0.004 to 0.311 ± 0.029, indicating that only small defects are generated on graphene.

In the Raman analyses of **Figure 3-9**, we only used a laser with a wavelength of 514 nm. However, in order to observe the surface-enhanced Raman scattering (SERS) signal by gold nanoparticles,[**310**] we should use a 633 nm laser instead of a 514 nm laser. In **Figure 3-10**, the Raman spectra with a full range (100 to 3200 cm^{-1}) of pristine graphene is compared with those with the 514 nm and 633 nm lasers. In the upper figure (514 nm), we can clearly observe the G and $2D$ peak characteristics of graphene, but in the lower figure (633 nm), the intensities of the two peaks are relatively low. Therefore, we used the 514 nm laser in this research. To observe the SERS effect by the gold nanoparticles, the Raman spectrum for each step (in **Figure 3-1**) with a 633 nm laser is shown in **Figure 3-11**.[**281**,**282**,**304**,**311**,**312**] At a Raman shift between 1000 and 1700 cm^{-1}, we can observe the Raman peak of the gold nanoparticles, which was invisible in the case of pristine graphene. When a 4-MBA molecule acts as ligand[**301**,**302**,**313**,**314**] to a Hg^{2+} ion,[**315**–**319**] a much stronger peak intensity was observed by the surface-enhanced effect of the gold nanoparticles. Furthermore, the SERS effects by physisorption of 4-MBA SAM on gold nanoparticles were observed at Raman shift between 175 and 525 cm^{-1}, as shown in **Figure 3-11c and 3-11d**.[**302**] In **Figure 3-10a** (514 nm), the positions of the red arrows are the intrinsic peaks of the silicon nanostructure (substrate).[**320**] It is necessary to pay attention to **Figure 3-11c and 3-11d**. When adding Hg^{2+} ions, they are chelated by carboxyl groups of 4-MBA molecules forming SAM bound to the gold nanoparticles. The symmetric stretching mode of COO^- is blue shifted, which results in the formation of a chelating (bidentate) structure rather than a unidentate or bridging structure.[**313**] Moreover, in the same process, the peak near 1630 cm^{-1} was removed because the stretching mode of C=O in the carboxyl acid form disappeared as it formed the bidentate form.[**313**,**317**]

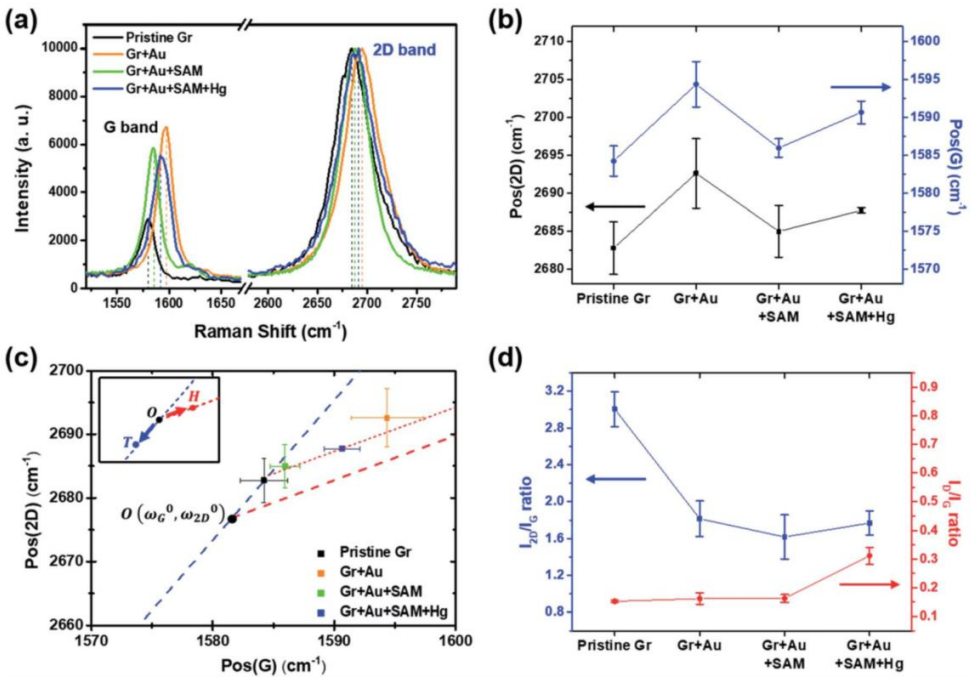

Figure 3-9. Raman spectroscopic analyses of graphene films. (a) Measured Raman signals for graphene FET devices at each doping step. Only the G and $2D$ peaks are shown for comparison. (b) Peak positional changes of the G and $2D$ peaks at each step. (c) The $2D$ and G peak position plot, revealing that our treatment induces charge doping rather than a strain effect (from ref. [**276**]). (d) The variation in the I_{2D}/I_G and I_D/I_G ratios at each step.

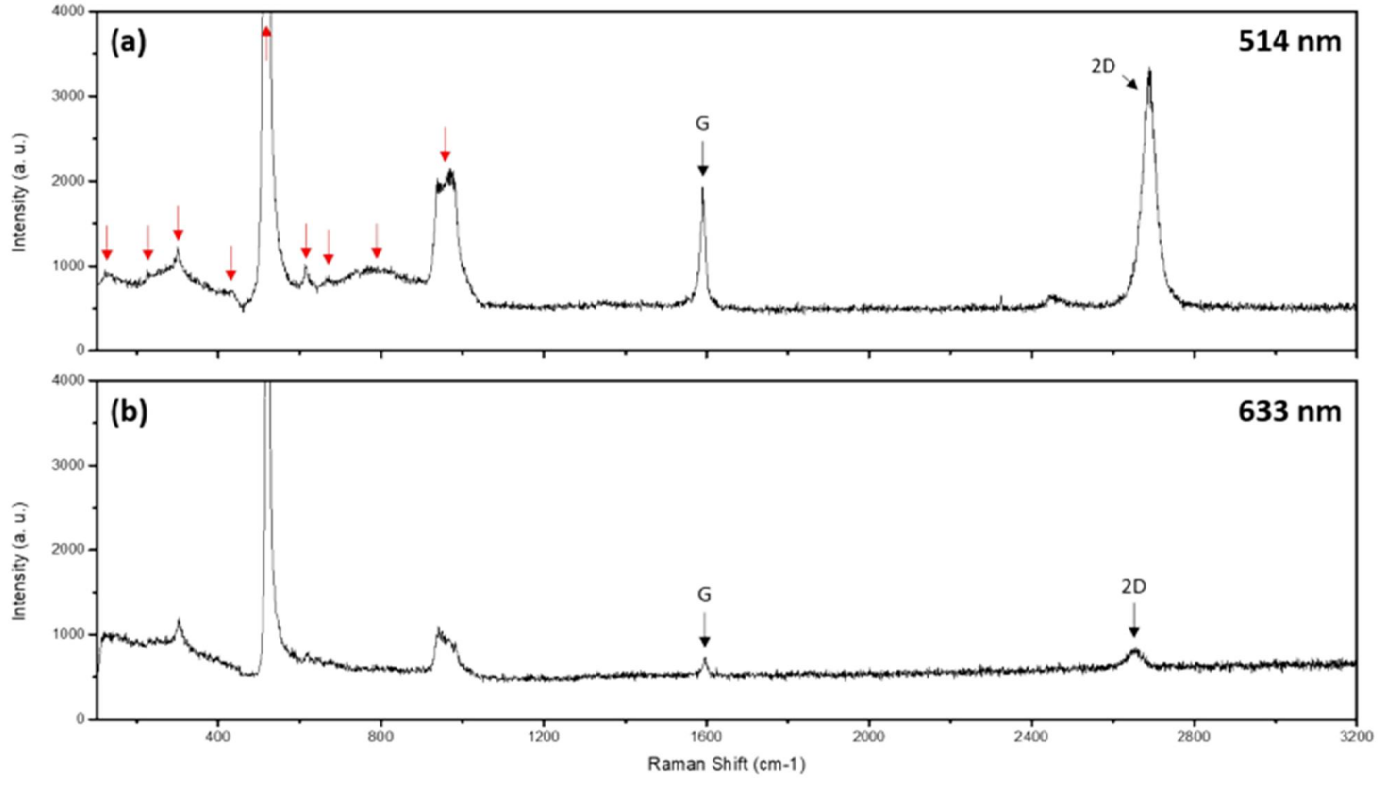

Figure 3-10. Raman Spectra of the pristine graphene (step 1 of **Figure 3-1**) by variation of wavelength. (a) 514 nm and (b) 633 nm laser. The range of Raman shift in these spectra is full range (from 100 to 3200 cm^{-1}). The positions of the red arrow are the intrinsic peaks of the silicon nanostructure (substrate).

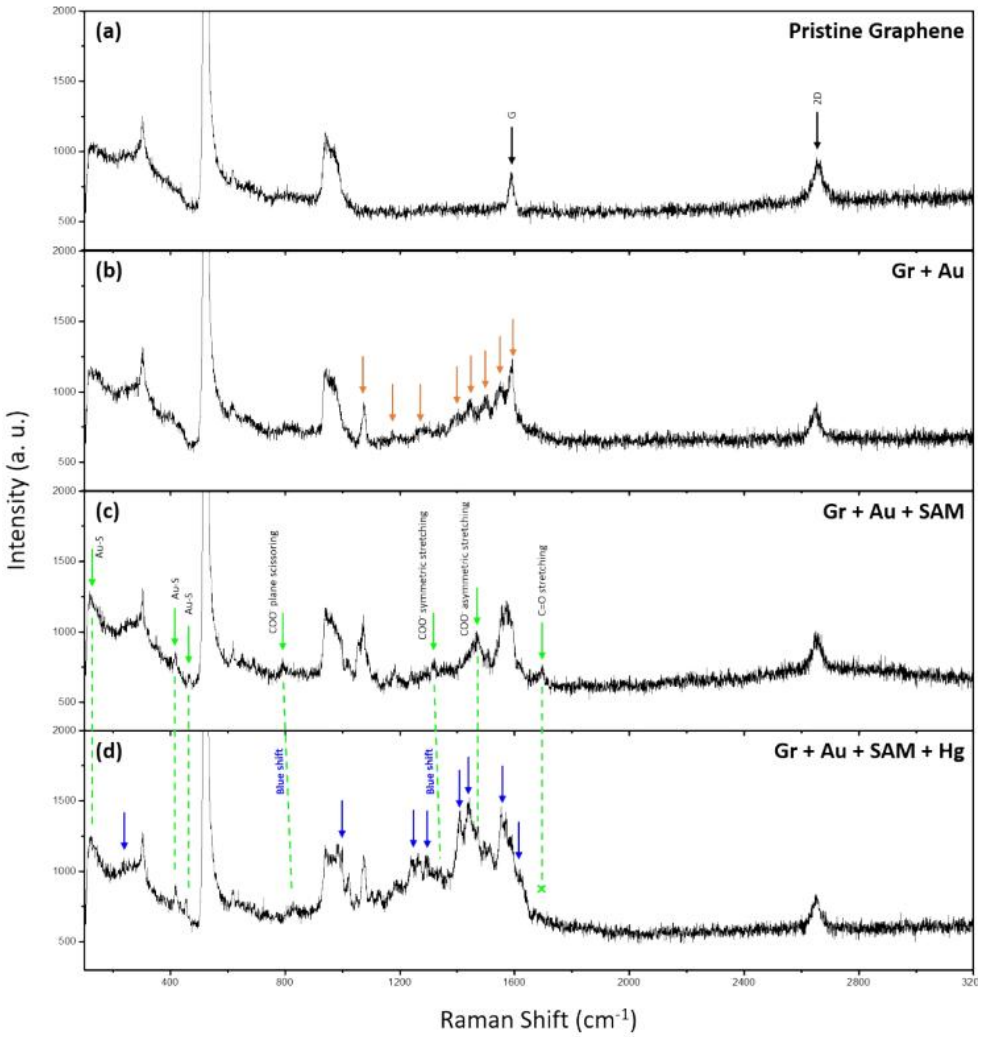

Figure 3-11. Raman Spectra of each step by 633 nm laser. Step (a) 1, (b) 2, (c) 3 and (d) 4 of **Figure 3-1**. The range of Raman shift in these spectra is full range (from 100 to 3200 cm^{-1}). The positions of the (b) orange, (c) green, and (d) blue arrow are the peaks by the SERS effect of gold nanoparticles, the gold-sulfur bond or the vibration of carboxyl group of 4-MBA molecules, and SERS effect of Hg^{2+} ions or chelation of Hg^{2+} ions by carboxyl group of 4-MBA molecules, respectively.

3. 4. 5. Comparison between Raman Spectroscopic and Electronic Analyses

Table 3-1 compares the charge carrier concentration of the graphene sample, which is estimated from the shifts of the V_{CNP} and G peak positions.[**233**,**321**,**322**] In the standard carrier density model,[**322**,**323**] the hole concentration of the graphene film is quantitatively calculated by **Equation (2-19)**, where ϵ_0 is the vacuum permittivity (= 8.854×10^{-12} F·m^{-1}); e is the elementary charge (1.602×10^{-19} C); C_{ox}, κ_{ox} or t_{ox} is the electric capacity, the relative permittivity (= 3.9) or the thickness(= 300 nm) of the gate material, SiO_2, respectively. As is well known, κ_{ox} depends on t_{ox}. Generally, in Raman spectra of graphene, the G peak can be used to measure the charge concentration,[**233**] indicating that 1×10^{12} cm^{-2} of the hole concentration corresponds to the range from 1 to 3 cm^{-1} of the G peak positional measurements (1 cm^{-1}). Therefore, we can demonstrate that the carrier concentrations, n, derived by Raman measurements, are comparable to the value for FET measurements, showing the reliability of our FET measurements in each step.

		Pristine Graphene	Gr+Au	Gr+Au+SAM	Gr+Au+SAM+Hg
FET	V_{CNP} (V)	8.14 ± 3.33	95.86 ± 9.82	24.03 ± 5.92	90.86 ± 8.65
	ΔV_{CNP} (V)		87.72 ± 6.71	15.89 ± 2.75	82.72 ± 5.52
	n (10^{12} cm^{-2})		6.30 ± 0.48	1.14 ± 0.20	5.94 ± 0.40
Raman	ω_G (cm^{-1})	1584.21 ± 1.98	1594.36 ± 2.98	1585.95 ± 1.22	1590.64 ± 1.50
	$\Delta\omega_G$ (cm^{-1})		10.14 ± 2.74	1.74 ± 1.98	6.43 ± 2.10
	n (10^{12} cm^{-2})		10.14 ± 2.74	1.74 ± 1.98	6.43 ± 2.10

Table 3-1. Estimated hole concentrations, n at each step, derived from the shift values of V_{CNP} and the G peak positions.

3. 4. 6. Electrical Analysis of Doped Graphene: Sheet Resistance, Compared with Raman Spectroscopic Analysis

We performed Raman mapping, using a 514 nm laser, on graphene films throughout each step in **Figure 3-1**. Raman mapping images in **Figure 3-12a** show a summary of the whole results of **Figure 3-9**. From this, we have optically confirmed that the graphene films have clearly been doped by each nanocomponent.

Figure 3-12b represents the sheet resistance, R_S of graphene films, as another form of mapping image. A square graphene film with one side of 5 cm was transferred onto the PET substrate, and after doping by each step process (as shown in **Figure 3-1**), the sheet resistance of the center area (see the yellow square in **Figure 3-13**) with one side of 3 cm was measured using a non-destructive method that applies magnetic fields to generate eddy current. In the case of pristine graphene, R_S is 849.50 ± 13.25 $\Omega \cdot \square^{-1}$ The other cases, however, are 372.85 ± 5.09, 445.53 ± 6.31, and 400.68 ± 16.93 $\Omega \cdot \square^{-1}$, in sequence. These results, from 30 different positions of the graphene films in **Figure 3-13** of measurements using the 4-point probe method, depict the same patterns as the mapping. **Figure 3-12c** and d show the R_S values of each step: $849.50 \pm 13.43 \rightarrow 372.01 \pm 4.19 \rightarrow 445.44 \pm 5.97 \rightarrow 399.11 \pm 10.79$ $\Omega \cdot \square^{-1}$. These can be said to have the same values within a margin of error.

From **Figure 3-12d**, in particular, it can be observed that change patterns of the sheet resistance values are similar to the change patterns of the hole carrier mobility in **Figure 3-5c**, and the I_{2D}/I_G values of the Raman spectra in **Figure 3-9d**. This suggests that each property of the graphene surface that is affected by doping for each nanocomponent is correlated with each other.

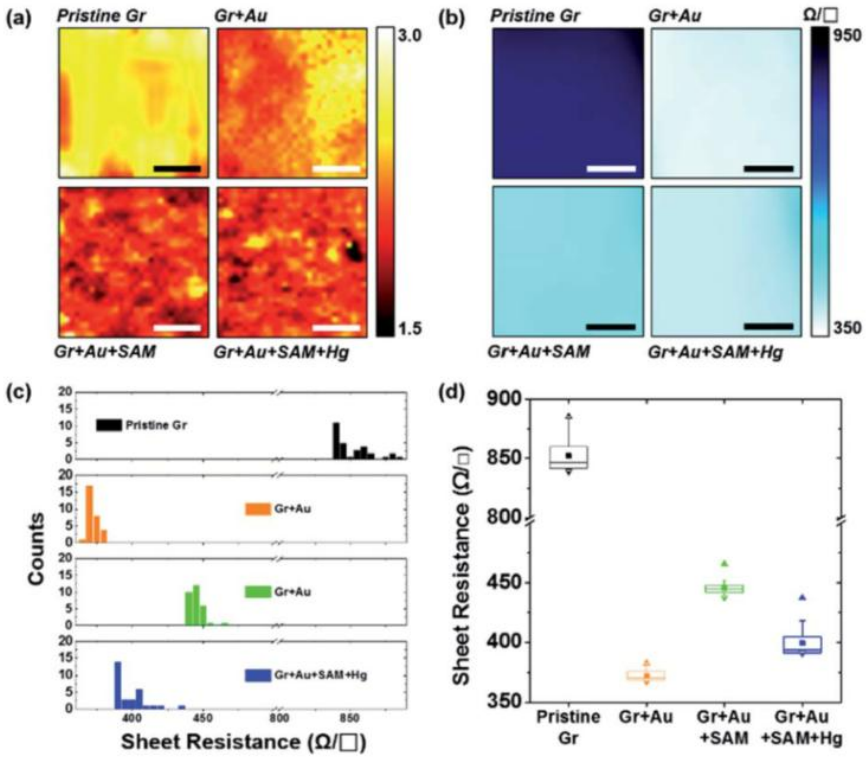

Figure 3-12. The relation between Raman spectroscopic analyses and sheet resistance measurement of graphene samples. (a) Raman mapping images (scale bar is 5 mm) of the I_{2D}/I_G values of graphene film on Si/SiO_2 substrates for each step in **Figure 3-1**. (b) Sheet resistance mapping images (scale bar is 1 cm), (c) a histogram of the sheet resistance, and (d) the plots for the averages and distributions of the sheet resistance of graphene film on PET substrates for each step in **Figure 3-1**.

3. 4. 7. Analyses of Effects of Heavy Metal Ions

As already mentioned above (see **Figure 3-8**), in our FET device, exchanging the metal specific-carboxyl group with a nonspecific methyl group substantially decreases the response of V_{CNP} to the mercury ion, verifying the strong interaction between the carboxyl group with the mercury ion. Then, as a next step, we conducted experiments to compare the effects of different types of heavy metal ions on the carboxyl functional group. **Figure 3-14** shows the different doping degrees depending on the metal type, whilst all still showing the substantial p-type doping effect and highly correlated behavior between V_{CNP} and the Raman peak position.

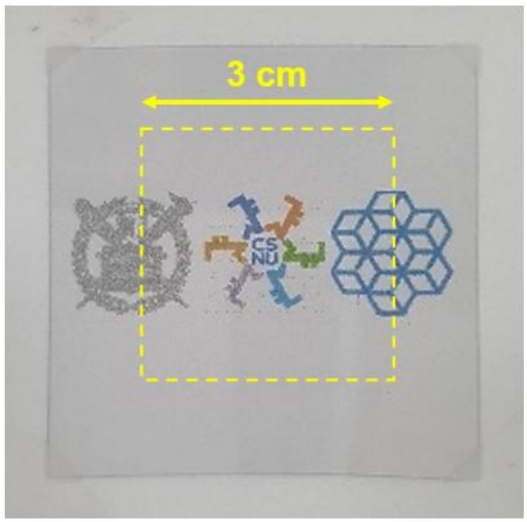

Figure 3-13. The pristine graphene transferred on the PET substrate for the measuring sheet resistance. Subsequently, the conditions required by each step of **Figure 3-1** were dealt with. The sheet resistance of the dashed yellow square area was measured.

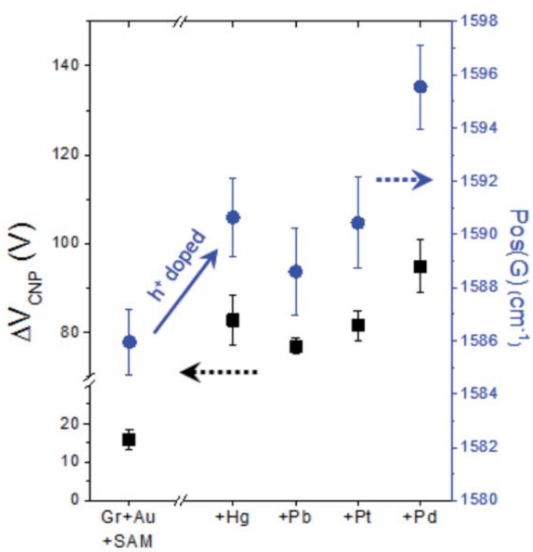

Figure 3-14. The four kinds of heavy metal ions (mercury, lead, platinum, and palladium), showing a substantial p-type doping effect on graphene (through the 4-MBA molecules and gold nanoparticles) and exhibiting the highly correlated behavior of ΔV_{CNP} and Raman G peak positions with respect to the metal types.

3. 5. Conclusion

In summary, we have developed a novel strategy to implement chemical functionality on graphene FET devices with the fine tuning of doping effects on graphene. Compared to the conventional destructive direct covalent bond formation (through azide groups) on the basal plane of graphene, gold nanoparticle-mediated functionalization by 4-MBA SAM maintains the mechanical and electrical properties of pristine graphene without affecting the characteristics of hexagonal carbon lattices in SLG, allowing for its application as a high-performance V_{CNP} switcher for FET devices. The analyses of Raman spectra confirm that the gold nanoparticle-SAM functionalization induces a clear charge doping effect on graphene without the formation of defects, and the estimated charge carrier concentration matches well with the one from electrical transport measurements in the FET devices. These results were also consistent with changes in the values of the sheet resistance. Considering the variety of chemical functional groups in thiol SAM that can be combined to gold nanoparticles, our strategy is expected to provide a new route to develop highly potent graphene FET devices in the near future.

Chapter 4.

Enhanced Thermopower of Saturated Molecules by Noncovalent Anchor-Induced Electron Doping of Single-Layer Graphene Electrode

[* The contents of this chapter are reproduced and modified from:
Sohyun Park[†], Hwa Rang Kim[†], Juhee Kim, Byung Hee Hong[*], and Hyo Jae Yoon[*] *Advanced Materials* **33**, 2103177 (2021). Copyright 2021 Wiley-VCH][**189**]

4. 1. Abstract

Enhancing thermopower is a key goal in organic and molecular thermoelectrics. This paper shows that introducing the noncovalent contact with SLG electrode improves thermopower of saturated molecules as compared to the traditional gold-thiolate covalent contact. Thermoelectric junction measurements with a liquid metal technique reveal that the value of Seebeck coefficient, S in large-area junctions based on *n*-alkylamine (H_2NC_n) SAM on SLG is increased up to five-fold compared to the analogous junction based on *n*-alkanethiolate (SC_n) SAM on gold. Experiments with Raman spectroscopy and FET analysis indicate that such enhancements benefit from the creation of new in-gap states and electron doping through noncovalent interaction between amine anchor and SLG electrode, which leads to reduced energy offset between E_F and transport channel. Our work demonstrates that control of interfacial bonding nature in molecular junctions improves Seebeck effect in saturated molecules.

[†] S. P. and H. R. K. contributed equally to this work.
[*] To whom correspondence may be addressed.

4. 2. Introduction

Achieving the Seebeck effect which is a conversion of heat energy into electricity through organic matter can solve problems that existing inorganic thermoelectric generators encounter. While the majority of organic thermoelectrics research has extensively focused on bulk materials of π-extended molecules and polymers, the Seebeck effect of saturated hydrocarbon systems at the molecular level remains incompletely understood. Thermoelectric molecular junctions containing single molecules or monolayers offer the opportunity to interrogate the fundamental mechanism of charge movements and draw inferences about atomic detailed structure-thermopower relationships.[**324**–**332**] Among others, significant efforts have gone into understanding how changes in molecular and non-molecular junction components including the length of the active molecule,[**325**,**333**–**336**] the chemical structure of molecular backbone,[**336**,**337**] structural flexibility[**325**,**338**] anchoring moiety,[**329**,**333**,**335**,**339**] radical,[**340**] and electrode's material[**341**] affect the Seebeck effect across molecular junctions. Thermoelectric molecular junctions have also shown the potential for developing tiny thermoelectric devices. For example, the Peltier device has been recently demonstrated with SAM of organic molecules;[**342**] the power factor of single molecule and SAM has been recently demonstrated.[**343**,**344**]

We herein report that the introduction of noncovalent contact SLG for a bottom electrode enhances S of SAM-based large-area junctions (**Figure 4-1a**). Particularly, we observed that SLG-based junctions formed with *n*-alkylamine (H_2NC_n, where $n = 4, 6, 8, \ldots, 18$ as shown in **Figure 4-1b**) molecules led to increases in S values up to by five times compared to the analogous junctions based on *n*-alkanethiolate (SC_n, where $n = 2, 4, 6, \ldots, 18$ used in this study) molecules on gold. Further experiments with Raman spectroscopy, UPS, and FET characteristics indicate that the enhanced S values stemmed from the new gap states around -0.1 eV and n-type doping arising from the junction of SLG//H_2NC_n that is noncovalent contact, which resulted in smaller energy offset between E_F and accessible energy state than the covalent sulfur/gold (S/Au) contact.

Our modeling of Seebeck coefficient was conducted based on the previously reported methods.[**333**,**341**] The simple toy model based on a traditional transmission function accounts for the correlation between the energy topography across a molecular junction and S [μV/K]:[**330**]

$$\tau(E) = \frac{\Gamma_L \cdot \Gamma_R}{\left(\frac{\Gamma_L + \Gamma_R}{2}\right)^2 + (E - E_{MO})^2} \quad \textbf{(4-1)}$$

$$S \equiv -\frac{\pi^2 {k_B}^2 T}{3e} \frac{\partial \ln(\tau(E))}{\partial E}\bigg|_{E=E_F} \quad \textbf{(4-2)}$$

Here, $\tau(E)$ is the transmission coefficient; E_{MO} is the energy level of accessible molecular orbital; and Γ_L and Γ_R are the broadenings due to left (bottom) and right (top) contacts, respectively; e is the charge of an electron; k_B is the Boltzmann constant; E_F is the Fermi level of electrode; and T is the average absolute temperature of the junction. According to this model,[**341**,**345**] the slope of lorentzian-shaped E_{MO} which is the energy level of HOMO or LUMO at E_F corresponds to S. As the slope is steeper, the value of S becomes larger **(Figure 4-1c and 4-1d)**.

The following structural modifications of active molecules or change in the work function (WF) of electrode have been demonstrated to make a significant influence on thermopower of junction: (i) unsaturated hydrocarbons yield higher S values than saturated ones in the backbone of molecules,[**324**,**343**,**346**] (ii) the S value increases with increasing π-conjugation length of the backbone, (iii) the electronic structural tuning in aryl molecules via substitution affects S,[**341**] (iv) the S value can be enhanced by a rational design of binding moiety over a metal lead,[**341**] and (v) different electrodes (Pt, Au, and Ag) allow access to control of thermopower.[**347**] All these approaches boil down to the conclusion that reducing the energy offset (ΔE) between E_{MO} and E_F induces an increase in thermopower of junction **(Figure 4-1c and 4-1d)**, which concurs with the model of **Equation (4-2)**.

The model fits properly with unsaturated or conjugated molecules, such as oligophenylenes and oligothiophenes where the shape and location of frontier orbital energies are well defined and straightforwardly predictable. The remaining question is the mechanism of thermopower generation in saturated molecules. Unlike for unsaturated molecules wherein frontier orbitals are dominated by the molecular backbone, the frontier orbitals in saturated molecules are localized on the anchor group (e.g., sulfur atom in a traditional thiol anchor). Hence, thermopower in saturated molecules would be, in principle, sensitive to the molecule-electrode contact. [**328**,**348**]

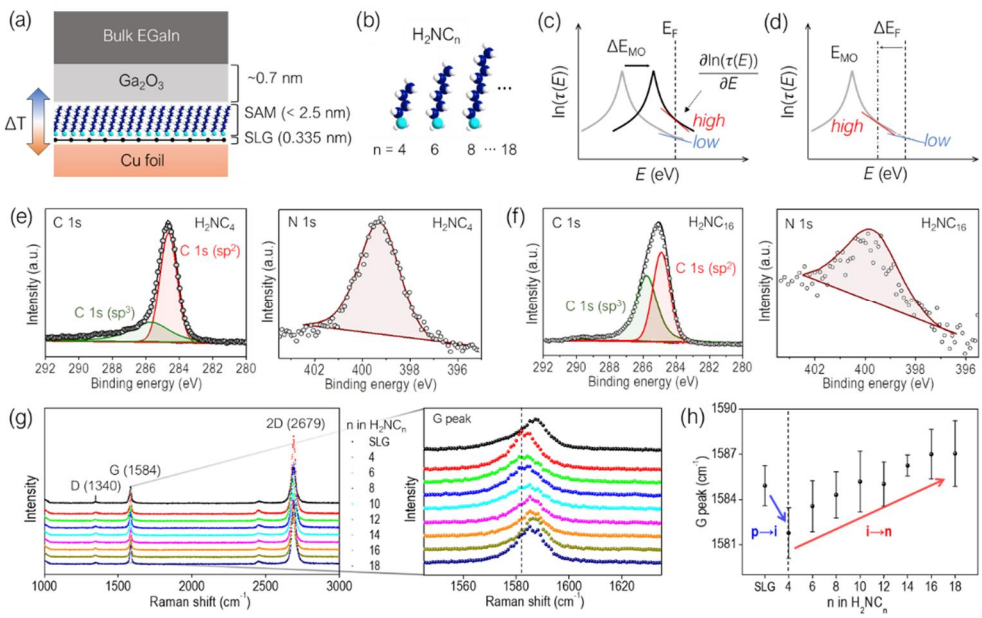

Figure 4-1. Schematics of experiments and Raman data. (a) Schematic describing the structure of large-area thermoelectric junction we used. (b) Molecules we used. (c, d) Correlation of energy barrier shape of molecular junction with S (the slope of transmission peak at E_F). (e, f) Exemplary high resolution XPS spectra of C 1s and N 1s regions for H_2NC_4 or H_2NC_{16} SAM on SLG. (Produced from S. P.) (g) Raman spectra for bare SLG and H_2NC_n (n = 4, 6, 8, ..., 18) SAM on SLG. (h) The G peak shift [cm^{-1}] in Raman spectra for H_2NC_n (n = 4, 6, 8, ..., 18) SAM on SLG. Each data point is averaged from measurements on separate junctions (the data summarized in Figure 4-6), of which the number is from 16 to 25. The 'p', 'I', and 'n' indicate p-type doped, intrinsic, and n-type doped SLGs, respectively. (Produced from J. K.)

4. 3. Experimental

4. 3. 1. Materials and Characterization

All reagents including n-alkylamines were purchased from Sigma-Aldrich, Alfa Aesar, and TCI and used as supplied unless otherwise specified. All organic solvents including methanol and tetrahydrofuran were purchased from Sigma-Aldrich and Daejung. High purity eutectic gallium-indium (EGaIn; 99.99%) was obtained from Sigma-Aldrich and used as supplied. PMMA; average Mw ~996,000 by GPC) and ammonium persulfate aqueous solution (≥ 98%) were obtained from Sigma-Aldrich. Copper foils (BHZ-Z-T) were purchased from JX Nippon Mining & Metals Corporation.

4. 3. 2. Synthesis of graphene

Graphene films were synthesized on copper foil, which has a thickness of 25 μm, by roll-to-roll (R2R) low pressure chemical vapor deposition (LPCVD) method.[**157**] The carbon precursor was methane gas (300 sccm) and the etchant was hydrogen gas (6 sccm). The vacuum level was kept at ~10^{-4} Torr (low vacuum condition) before injecting gases in a quartz tube. In a typical experiment, hydrogen gas was injected during the calcination process before crystal growth, in which the temperature roses from room temperature (RT) to 1000 ℃ within an hour. Next, methane gas with hydrogen gas was injected while maintaining the temperature for 30 minutes. Roll speed was 100 mm/min. After that, it was cooled down to RT for about 3 hours. At the same time, hydrogen gas was left as it was, while the injection of methane gas was stopped. Using this method, graphene was formed on both sides of the copper foil. To remove a relatively poor-quality graphene on one side, the RIE was applied on that side (power: 100 W, etching time: 20 seconds, plasma etchant: oxygen gas (20 sccm), and working pressure: 90 to 100 mTorr).

4. 3. 3. Transfer of graphene

We followed the graphene transfer process following previously reported procedures.[**157**] After complete synthesis of graphene on copper foil, the foil contained graphene layers at both sides. It was cut into 1×1 cm^2 and immediately used for thermoelectric analysis. For Raman spectroscopy analysis, the graphene layer was needed to be transferred on Si/SiO_2 substrate. One side of the graphene-synthesized copper foil was spin-coated with PMMA dissolved in chlorobenzene (Sigma-Aldrich) to protect the graphene from oxidation, and the other side was removed by RIE. For graphene transfer, copper was dissolved by 80 mM ammonium persulfate aqueous solution, and after rinsing with DI water, it was transferred on Si/SiO_2 wafer.

4. 3. 4. Fabrication of Graphene FET Devices

The source and drain electrodes of field effect transistor (FET) devices were fabricated by thermal deposition in order of chrome (3 nm) and gold (60 nm) metal layers on the Si/SiO_2 wafer with the patterned stencil masks. The graphene film on PMMA substrate was transferred onto the gold-patterned Si/SiO_2 wafer. Then, the substrate was dipped into acetone to remove PMMA for 1 hour. Each graphene device was isolated by EBL, with gate width and length of 100 and 40 μm, respectively. Finally, in order to remove impurities, charge puddles, and mechanical wrinkles, graphene device was thermally annealed at 200 ℃ for 5 hours under the atmosphere of argon as a carrier gas (100 sccm) in low vacuum condition. The structure of the FET formed with $SLG//H_2NC_n$ SAMs is shown in **Figure 4-2**.

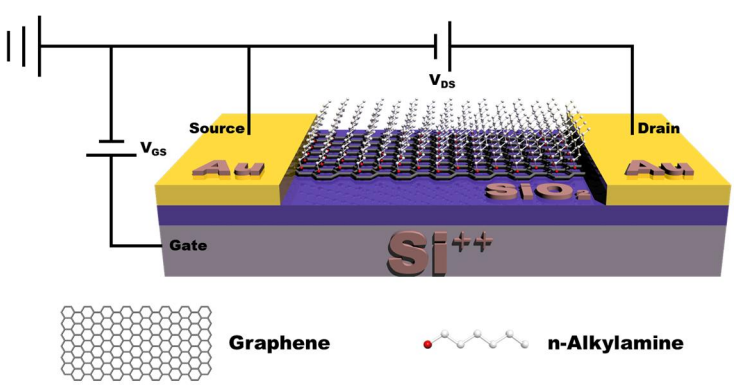

Figure 4-2. The structure of the FET formed with $SLG//H_2NC_n$ SAM.

4. 3. 5. Formation of SAM on Graphene Surface

SAM was prepared following previously reported procedures.[**349**] Graphene grown on copper was used as the substrate to form SAMs of *n*-alkylamine. Typically, as a solvent we used 10 mL of a mixture of methanol (HPLC grade) and tetrahydrofuran (THF, HPLC grade) with a volume ratio of 1:9 to dissolve *n*-alkylamine with a concentration of 18 mM. The solution was purged with N_2 for 15 minutes prior to the immersion of freshly SLG on Cu (for thermoelectric measurements and UPS characterizations) or SLG transferred on Si/SiO_2 wafer (for Raman spectra and FET analyses). The substrate was rinsed with the mixed solvent (three times, ~3 mL each time) and dried under steam of dry N_2.

4. 3. 6. Characterization of graphene films

For analysis of SLG using scanning tunneling microscopy (STM), high-resolution STM revealed that the adsorption of SLG onto Cu foil. STM measurements were performed using a Nanoscope V (Bruker, Santa Barbara, CA) with a commercial Pt/Ir (80/20) tip. All STM images were obtained using a constant height and current mode under ambient conditions at room temperature. Imaging conditions were in the range of +900 to −900 mV for the bias voltages and in the range of 0.30 to 0.50 nA for tunneling currents between tip and sample.

For Raman spectroscopy, the characteristic peaks of bare SLG and SLG/SAM on Si/SiO_2 wafer were analyzed by Raman Spectrometer (inVia-basis Raman Microscope, Renishaw, UK) using Ar laser with less than 1 mW of power. The wavelength of laser and grating are 514.5 nm, 2400 gr/mm.

For electrical transfer analysis of FET devices, the electrical property of graphene FET devices was measured by the 3-terminal (source, drain, and gate) probe station (MS Tech 5500, MS Tech, Korea) at ambient condition. We raised the gate voltage from −50 to +30 V, while keeping the source to drain voltage as 0.2 mV. (Agilent B2912A, Agilent Technologies, USA). We measured more than 30 FET devices. In FET measurements, we simultaneously measured channel current (I_{DS}) and resistance (R_{DS}) as function of gate voltage (V_{GS}) using a probe station. The measured R_{DS} values were calculated with the equation, $R_{DS} = V_{DS}/I_{DS}$ (Ohm's law), and thus the trend of R_{DS} was correlated with I_{DS}. The largest R_{DS} was recorded to be 2.2 kΩ, roughly consistent with the literature value,[**349**] validating our FET measurements.

For XPS analysis, the measurements were carried out on a Thermo Scientific K-Alpha photoelectron spectrometer with a monochromated Al $K\alpha$ (1486.6 eV) source. The peak shapes of the core level photoelectron spectra were analyzed with a XPS Peak Fit program. With a linear-type background correction, we analyzed the XPS Cu $2p$, C $1s$, and N $1s$ lines. The binding energies of Cu $2p$ were observed at 952.7 eV ($2p_{1/2}$) and 932.8 eV ($2p_{3/2}$). The C $1s$ signal was presented by combination of two peaks at 284.6 eV (sp^2 carbon) and 285.7 eV (sp^3 carbon). We calculated the peak intensity ratio of C $1s$ (sp^3) and C $1s$ (sp^2) and found that the ratio increased with increasing chain length, which confirms the formation of a *n*-alkylamine SAM on graphene and the ordered structure in monolayers.[**350**,**351**] The binding energies of N $1s$ was observed at 400 eV.

For UPS analysis, the measurements were carried out on Thetaprobe (Thermo) to determine the WF level of Cu//SLG//H_2NC_n SAM. $h\nu$ is incident photon energy (21.2 eV) of He I source, the WF level shown in **Figure 4-3**.

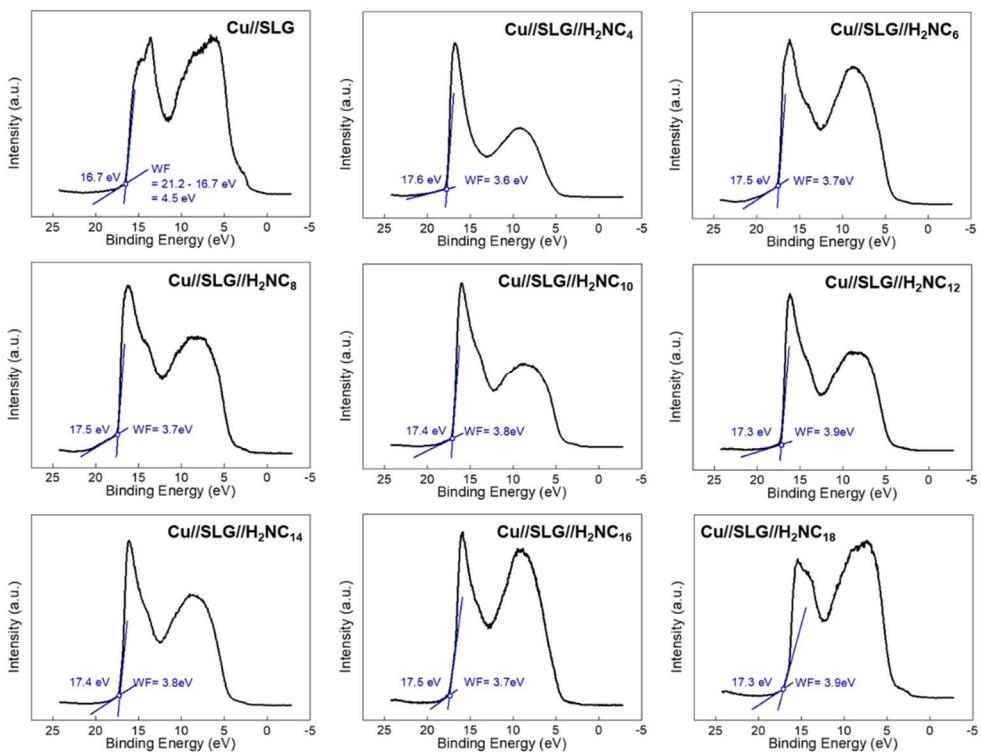

Figure 4-3. UPS spectra and WF for Cu//SLG and Cu//SLG//H_2NC_n SAM. (Produced from S. P.)

4. 3. 7. Preparation of the EGaIn Tip

An EGaIn conical tip of EGaIn was formed following a method reported in the literature.[**352**] Briefly, a 10 μL gas-tight syringe was filled with EGaIn (≥ 99.99%, Sigma Aldrich) and a drop of EGaIn was pushed to the tip of the syringe needle, where the hanging drop was brought into contact with a surface on which the EGaIn could stick (e.g., bare Au or Ag surfaces), and the needle was gently pulled away from the drop using a micromanipulator. Upon breaking from the bulk EGaIn on the surface, a conical tip was obtained. An EGaIn conical tip for tunneling junctions was newly formed for every junction in order to eliminate any complexities that may arise from contamination of the EGaIn surface by volatile organics in air. In the cases that visible whiskers formed during tip fabrication, the tip was discarded, and a new tip was formed.

4. 3. 8. Junction Formation and Thermoelectric Measurements

Our junction measurements relied on the EGaIn technique.[**326**] A SAM-bound SLG//Cu chip was placed on a hot chuck, and the rest of the area was covered with glass to block or minimize heat transfer to the EGaIn tip. The SAM was then gently brought into contact with a tungsten ground electrode. To measure the temperature of the bottom electrode, a thermocouple was placed and secured onto the electrode. Once the temperature of the substrate was monitored by the thermocouple, we found the heat transfer from the hot chuck to the SAM on gold was sufficient enough to carry out the desired experiments. To create a temperature difference, the temperature of the hot chuck was varied from 290 to 305 K. At each temperature, a few seconds were allowed to pass before the temperature measured at the bottom-electrode thermocouple was stabilized. Then using a micromanipulator, an EGaIn conical tip was gently brought into contact with the surface of the SAM, and the output voltage was measured. Thermoelectric voltages at 39 or 40 junctions at each ΔT were measured at least 2964 times and at most 3040 times. A freshly prepared EGaIn conical tip was used for measuring from 3 to 5 junctions. Usually, the measurement for a sample took a few hours: ~100 data points were collected in 0.5 minutes and thus, in principle, 6000 data points could be collected in ~5 hours. The yields of the working junctions were calculated using the ratio of non-shorting junctions to all measured junctions.

4. 3. 9. First-principle Calculation on SLG//H_2NC_n System

For examining the electronic structure of SLG//H_2NC_n SAM, we used quantum espresso (QE) for the calculation code.[**353**] This code meets a periodic boundary condition (PBC).[**353**,**354**] For DFT calculations, projector-augmented-wave (PAW) – Perdew-Burke-Ernzerhof (PBE) + vdW DFT-D3 was used. The PAW is a pseudopotential method that describes both organic/inorganic systems well,[**355**,**356**] and PBE is a method that describes the exchange-correlation function in the Consham equation for DFT.[**355**,**356**] In addition, one of the methods to describe vdW interactions in atom-molecular, molecular-molecular, and layered structures is Grime-D3.[**355**,**357**] The application of the "PAW–PBE + vdW DFT-D3" method is widely used for band structure of graphene.[**355**,**357**]

The force criterion (force convergence threshold) is the minimum force for ionic minimization. By setting this value, the electron-electron interaction can be well described; it was set to 0.002 Ry/Bohr.[**355**,**357**] The $\boldsymbol{K}$ point ($6 \times 6 \times 1,\ 4 \times 4 \times 1$) of cells were set for optimization of the structure. However, when calculating the electronic structure, the $\boldsymbol{K}$ point value was set larger ($36 \times 36 \times 1,\ 24 \times 24 \times 1$) for higher accuracy.[**358**]

4. 4. Results and Discussion

4. 4. 1. Preparation and Characterization of SLG and SAM formed by *n*-alkylamine

We prepared SLG on copper foil following the previously reported procedure based on CVD method[**4**] and confirmed the quality and single layer structure with Raman spectroscopy and STM. Noncovalent interaction of amine anchor with SLG allows reversible adsorption and desorption for self-repair, leading to well packed monolayers without alteration of the chemical structure of SLG.[**349**,**359**,**360**] To form SAMs, SLG on copper foil (Cu//SLG) was incubated in a 18 mM solution of H_2NC_n with methanol and THF mixed solvent.[**349**]

The formation of SAMs was confirmed by STM and XPS. In STM analysis, the hexagonal pattern of SLG disappeared upon adsorption of H_2NC_n (**Figure 4-4**). In high resolution XPS spectra, the C $1s$ signal was presented by a combination of two peaks at 284.7 and 285.8 eV, corresponding to sp^2 and sp^3 carbons, respectively. The peak integration ratio of sp^3 to sp^2 increased with increasing the alkane chain length (n in H_2NC_n; **Figure 4-1e and 4-1f**). The binding energies of N $1s$ were observed at 400 eV (**Figure 4-1e and 4-1f**). The integration ratio of N $1s$ to sp^3 C $1s$ peaks decreased as the alkane chain length increased (shown in **Table 4-1**). These observations confirmed the formation of desired SAM on SLG.[**350**,**351**]

The formation of SAM on SLG was further confirmed by Raman spectroscopy. The Raman spectra exhibited G and $2D$ bands at around 1580 cm^{-1} and 2680 cm^{-1}, respectively (**Figure 4-1g**). The G band is the main spectral feature of carbon-based materials including graphene, and $2D$ band means the perfect symmetry of graphene hexagonal lattice.[**42**,**225**,**229**] These bands represent the phonon interactions at the $\boldsymbol{\Gamma}$ and $\boldsymbol{K}$ points in the BZ, respectively, and the positions and intensities of the points verify doping level and the number of graphene layers. We also observed D band at 1340 cm^{-1}. The D band signifies disorder band due to lattice motion away from the middle of the BZ. The intensity of the D band of our SLG remained unchanged upon SAM formation regardless of the alkyl chain length (**Figure 4-1g**), confirming the no significant changes in the hexagonal symmetry structure by the noncovalent contact between SLG and H_2NC_n.[**188**,**323**,**361**] The crystallinity of SLG can be determined by the ratio I_{2D}/I_G where I_X is the intensity of X band in Raman spectra of SLG ($X = 2D$ or G): I_{2D} in single-crystalline SLG is large compared to that of G band.[**42**,**187**,**229**] The ratio I_{2D}/I_G of our SLG was above 2, indicating its good quality in terms of crystallinity.

For Raman spectroscopic analysis, we transferred SLG from Cu foil onto SiO_2/Si substrate. The transfer was especially intended to eliminate the dominant Raman signal of Cu. The transfer process inevitably involved water treatment and handling of sample in ambient conditions, which caused bare SLG to be p-type doped **(Figure 4-1h)**. In general, large-area graphene synthesized by the CVD method tends to be p-type doped compared to exfoliated graphene.[**362**] Upon SAM formation, the G band position was blue-shifted with respect to the position of intact SLG **(Figure 4-1g and 4-1h)**. This was attributed to n-type doping of SLG by the amine anchor.[**205**,**363**] Interestingly, as the alkyl chain length increased, the degree of blue shift of the G band gradually increased, which confirmed the formation of desired SAMs. The n-type doping of SLG upon SAM formation was further validated by the FET analysis.

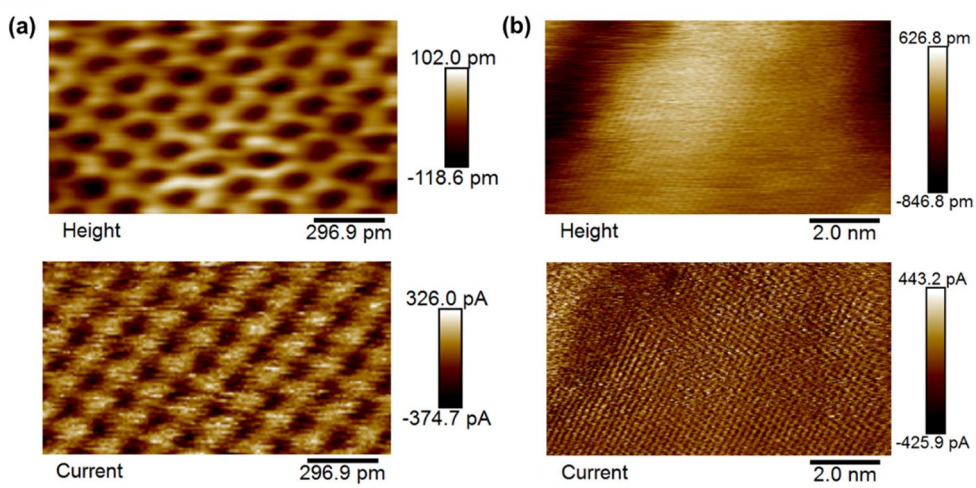

Figure 4-4. STM images of (a) bare SLG on SiO_2 and (b) H_2NC_n SAM//SLG on SiO_2 acquired at height and current modes in −800 mV. The hexagonal pattern of SLG disappeared upon adsorption of H_2NC_n. (Produced from S. P.)

n in H_2NC_n	C1s (sp^3)	N1s	N1s/C1s (sp^3)
4	3442792	182468	5.3×10^{-2}
6	4351073	178394	4.1×10^{-2}
8	5740200	172206	3.0×10^{-2}
10	7915000	166215	2.1×10^{-2}
12	7959550	159191	2.0×10^{-2}
14	8886706	151074	1.7×10^{-2}
16	21510882	146274	6.8×10^{-3}
18	61902173	142375	2.3×10^{-3}

Table 4-1. Integration of XPS peaks for C $1s$ (sp^3) and N $1s$ in Cu//SLG//H_2NC_n SAMs. (Produced from S. P.)

n in H_2NC_n	G peak (cm^{-1})	Number of measurements
0	1582.91 ± 1.32	25
4	1581.77 ± 1.68	18
6	1583.55 ± 1.69	22
8	1584.30 ± 1.53	21
10	1585.18 ± 2.02	21
12	1585.03 ± 1.46	21
14	1585.95 ± 0.70	22
16	1587.00 ± 1.65	19
18	1587.05 ± 2.17	16

Table 4-2. The position of averaged G peak (cm^{-1}) in Raman spectra for bare SLG and SLG//H_2NC_n SAMs. (Produced from S. P.)

4. 4. 2. Thermovoltage Measurements

We formed EGaIn conical tips, constructed junctions, and measured thermovoltage, ΔV [μV] following the methods reported in the literature.[**364**–**366**] **Figure 4-5a** shows exemplary histograms of ΔV obtained at different temperature differentials ($\Delta T = 4, 8, 12$ K). The yield of working thermoelectric junctions ranged from 64 to 93%. Through fitting of the histograms with single gaussian curves, we derived mean values of ΔV (ΔV_{mean}) and standard deviation ($\sigma_{\Delta V}$).

Figure 4-5b shows the ΔV trends as a function of ΔT for different H_2NC_n compounds. All the measured ΔV values were negative. All the SAMs exhibited increased ΔV as ΔT increased, which yielded positive S values. The value of $\sigma_{\Delta V}$ increased with increasing ΔT and with shortening the alkane chain length. The dependence of $\sigma_{\Delta V}$ on ΔT and the length could be explained by the difference in packing structure of monolayers. Strong lateral interaction between *n*-alkane backbone in long *n*-alkyl amines would yield solid-like monolayers whereas short *n*-alkylamine molecules generate relatively disordered monolayers, which is reminiscent of *n*-alkanethiolate SAMs.[**328**] Such a difference in the degree of structural disorder is likely responsible for the observed trend of $\sigma_{\Delta V}$. Through linear square fitting in the plot of ΔV_{mean} as a function of ΔT, we estimated *S* values of entire junctions, which were converted into S values of SAMs after considering thermopower of materials used to form circuits (shown in **Figure 4-6 and 4-7** for more details).

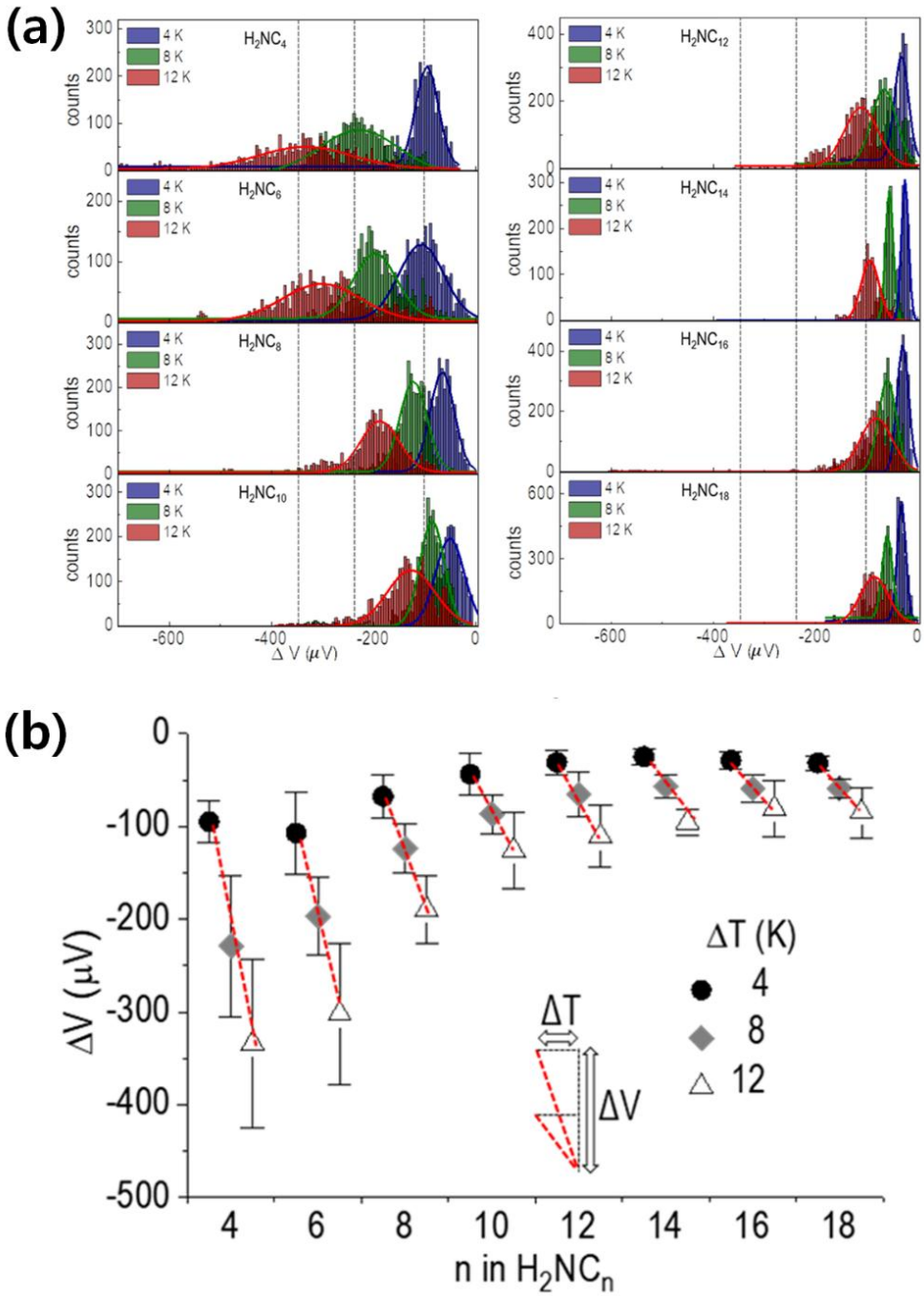

Figure 4-5. (a) Thermovoltage histograms for H_2NC_n (n = 4, 6, 8, ..., 18) SAMs. (b) Trends of ΔV as a function of various ΔT for the SAMs. (Produced from S. P.)

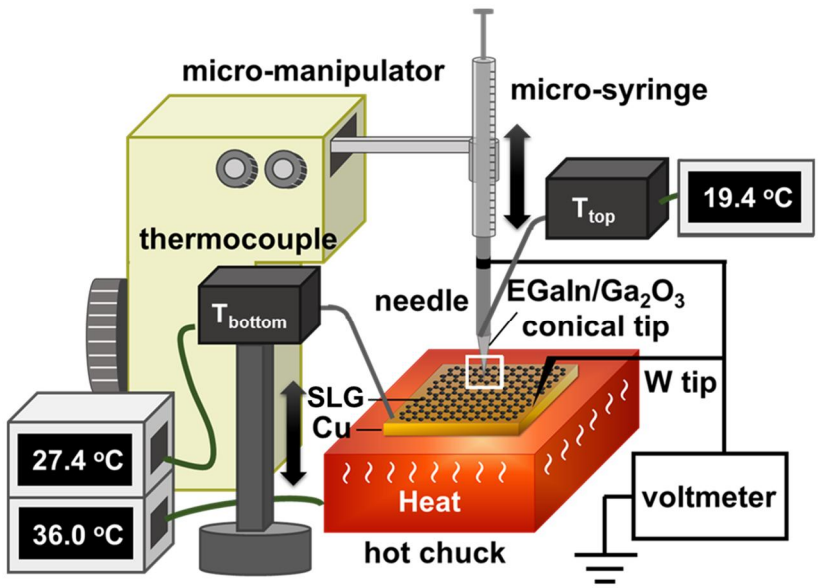

Figure 4-6. Schematic describing the structure of large-area thermoelectric junction we used in this work when the temperature difference (ΔT) between bare SLG (T_{bottom}) and EGaIn conical tip (T_{top}) is 8.0 °C. (Produced from S. P.)

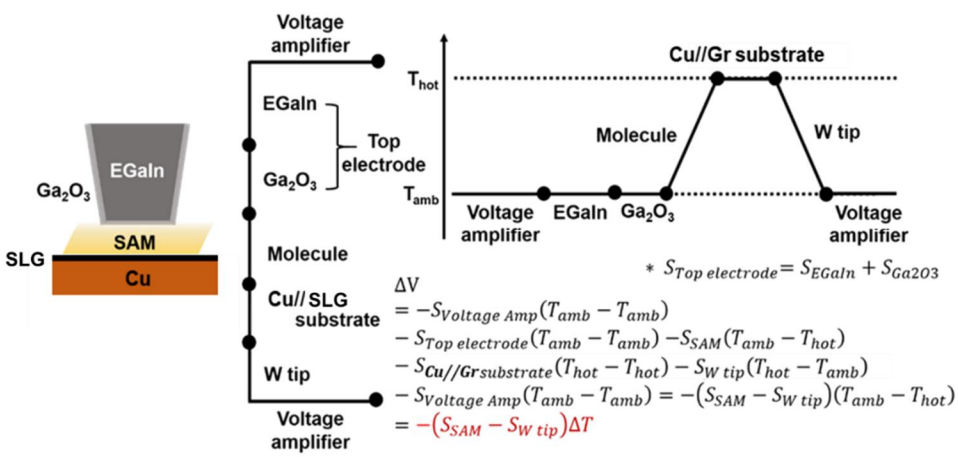

Figure 4-7. Thermopower analysis of the Cu//SLG//SAM//Ga_2O_3/EGaIn junction. (Produced from S. P.)

4. 4. 3. Enhanced S and Its Length Dependence

To examine the effect of noncovalent contact on thermopower, we compared S values for SLG//H_2NC_n//Ga2O_3/EGaIn and Au/SC_n//Ga_2O_3/EGaIn junctions. Note that these two junctions have identical EGaIn top-electrode and alkane backbone, which made it possible to single out reliably the effect of different contact nature. **Figure 4-8a** compares the length dependence of S values for Au/SC_n and SLG//H_2NC_n SAMs. Both systems exhibited the same crossover point, $n = 10$ (see below for detailed discussion on length dependence).

Notably, there were overall enhancements of S values in the noncovalent junction as compared to the analogous covalent junction **(Figure 4-8b)**. The value of S in SLG//H_2NC_4 (30.6 μV/K) was higher by a factor of five than that in Au/SC_4 (6.4 μV/K); there was a three-fold difference in the value of S between SLG//H_2NC_{18} (7.8 μV/K) and Au/SC_{18} (2.5 μV/K). These enhancements can be explained in two aspects: thermal boundary resistance and electronic structure at the interface. Loss of ΔT at the interface can be translated into reduced S. There is a noticeable difference in ΔT between covalent and noncovalent molecule-electrode contacts.[**367**–**374**] For example, the temperature drop at S/Au covalent contact is ~10 K, which is lower by two-fold than the temperature drops at $-CH_3$//Au vdW contact (~20 K). Q. Li *et al.* reported[**375**] that noncovalent $\pi - \pi$ stack between SLG and aromatic (benzene, anthracene) anchor can efficiently suppress phonon transport, leading to smaller phononic thermal conductance by an order of magnitude than that in the analogous junction with C–C covalent contact at 300 K. The amine-SLG interaction (0.22 eV) is five-fold weaker than the $\pi - \pi$ stack (1.01 eV), making our reasoning plausible.[**360**,**376**] Such a difference in the temperature drop between the covalent and noncovalent contacts is not trivial but cannot fully account for our observations. Our experiments (discussed below) indicate that the electronic structural effect contributes significantly to the observed difference in S values between SLG//H_2NC_n and Au/SC_n.

Length dependence of S can be explained by the following semiempirical parametric equation:[**324**,**377**]

$$S = S_C + \beta^S \times d \qquad \textbf{(4-3)}$$

where S_C is the Seebeck coefficient at the hypothetical non-shorting junction that does not possess an insulating organic component; β^S is the rate of Seebeck coefficient change as a function of molecular length (d in Å or the number of repeating units such as the number of carbon atoms). We observed a linear regression of S value against molecular length for the short molecules from H_2NC_4 to H_2NC_{10} (**Figure 4-8a**) The values of β^S and S_C for the regression was -3.1 ± 0.4 μV·(K·n_C)$^{-1}$ and 41.7 ± 3.5 μV/K.

Interestingly, there was a transition in β^S from −3.1 ± 0.4 to −0.47 ± 0.07 μV·(K·n_C)$^{-1}$ at H_2NC_{10}. Such a transition in the slope was consistent with the trend of Au/SC_n.[**328**]

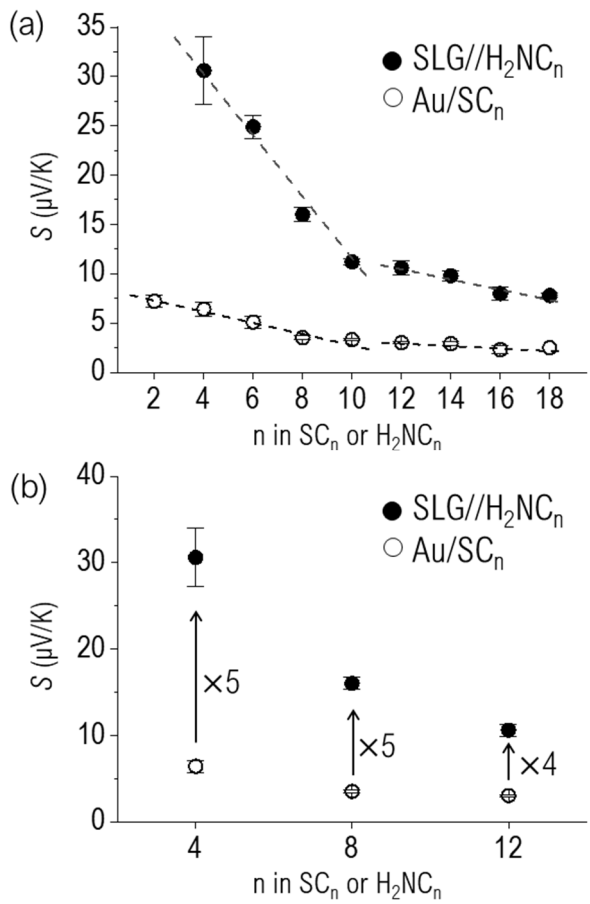

Figure 4-8. (a) Comparison of length dependence of Seebeck coefficient, S [μV/K] for noncovalent (SLG//H_2NC_n) and covalent (Au/SC_n) junctions. (b) Enhanced S values in the noncovalent interface as compared to the covalent one. (Produced from S. P.)

4. 4. 4. Electronic Structure-Thermopower Relationship

We conducted UPS measurements for Cu/SLG//H_2NC_n to determine WF (**Figure 4-3**). Our bare SLG on Cu foil exhibited WF of 4.5 eV, and, upon SAM formation, it decreased to 3.8 eV, which was consistent with previously reported WF of organic-doped graphene.[**378**,**379**] The reduction of WF in combination with the Raman spectroscopic analysis clearly indicates the n-type doping by the amine anchor.

We further characterized the electronic structure of SLG//H_2NC_n with the FET method. The FET method allows one to determine V_{CNP} (also called Dirac point voltage), which is intimately related to doping level, n (also called charge carrier concentration) and E_{F}, according to the **Equation (2-19) and (2-28)**, respectively, where ϵ_0 is the vacuum permittivity (= 8.854×10^{-12} F·m^{-1}); κ_{ox} is the relative permittivity of gate dielectric material, SiO_2 (= 3.9) with its thickness t_{ox} (= 300 nm); ΔV_{CNP} is the change of the applied gate voltage and e is the elementary charge (= 1.602×10^{-19} C); $\hbar$ is the reduced Planck constant as known as Dirac constant (= 1.055×10^{-34} J·s); v_{F} is the Fermi velocity (selected as the value of 2.5×10^{6} m·s^{-1}).[**241**] For n-type doping, V_{CNP} is expected to decrease.[**380**] We assumed that the intrinsic carrier concentration of SLG remained constant regardless of the presence of SAM with a different alkyl chain length as the noncovalent interaction between SLG and amine molecules of SAMs did not damage the hexagonal lattice structure of SLG. The Raman spectra showed no significant difference in I_{2D}/I_G ratio between SLG with and without SAM **(Figure 4-1g)**, proving our assumption.

We fabricated FET devices with our SAMs and measured V_{CNP} and derived E_{F}. The bare graphene exhibited $V_{\mathrm{CNP}} > 0$, which was indicative of p-type doping **(Figure 4-9a)**. This is due to the long exposure time in the air,[**134**,**140**,**143**,**205**] doping by water molecules during copper etch and wet transfer processes,[**146**,**147**,**381**,**382**] and back-gate in FET measurements.[**233**,**383**] The observed p-doping was consistent with the result of Raman spectroscopic analysis. The electrical transfer curve was measured on 30 different junctions with $V_{\mathrm{DS}} = 0.2$ mV. As shown in **Figure 4-9b**, upon the formation of SAM, V_{CNP} decreased relative to that of bare SLG, and the values of V_{CNP} gradually decreased as the alkyl chain length increased, indicating n-type doping **(Figure 4-9c)**, consistent with the result of Raman spectroscopic analysis **(Figure 4-1g)**. The results of the other SAMs are shown in **Figure 4-10**. The E_{F} value was correlated with the length of alkyl amine.

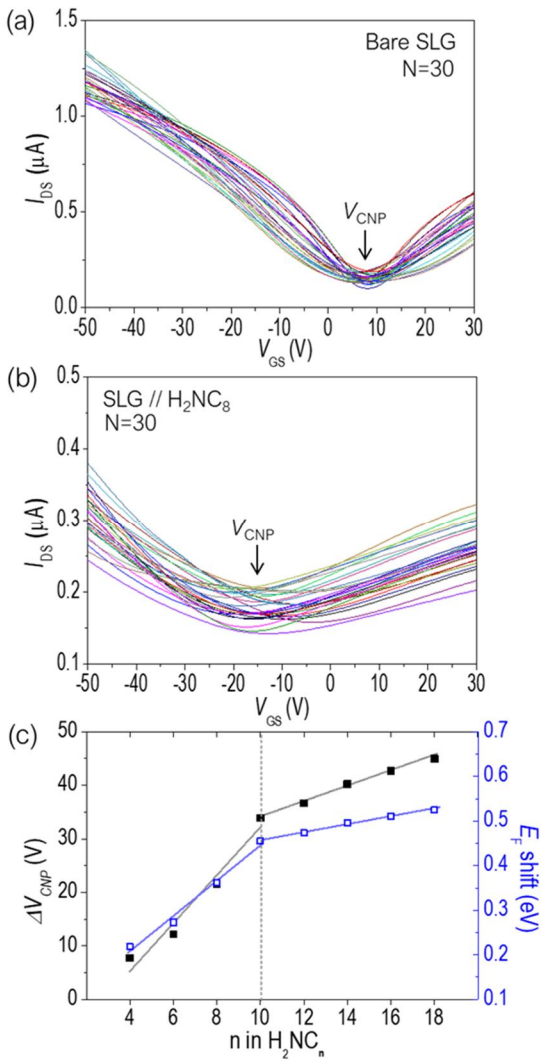

Figure 4-9. (a, b) Representative I_{DS}-V_{GS} curves obtained by FET analysis for bare SLG (Si/SiO_2//SLG) and SLG with H_2NC_8 SAM (Si/SiO_2//SLG//H_2NC_8). (c) Plots of V_{CNP} and degree of E_F shift as a function of alkyl chain length (n in H_2NC_n). Each data point is the average value of measurements on 30 separate devices.

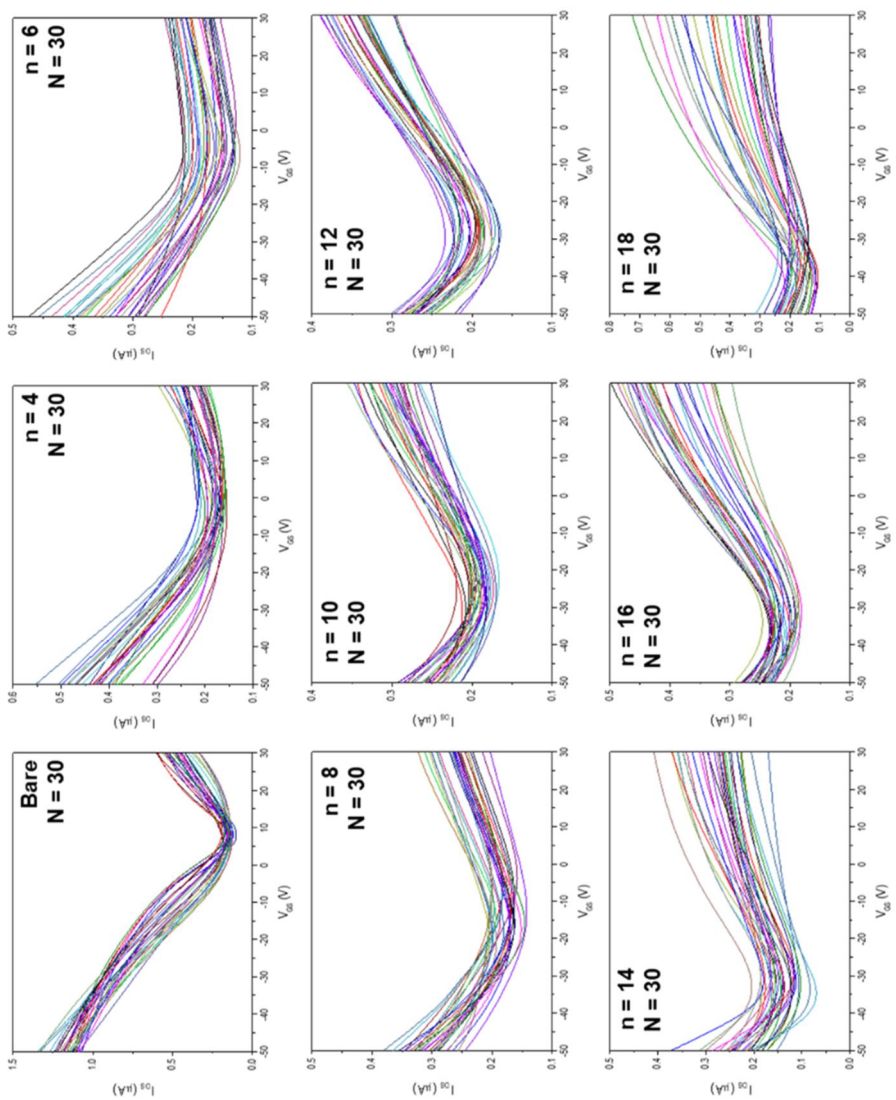

Figure 4-10. Electrical transfer curves of the FET devices with H_2NC_n SAMs.

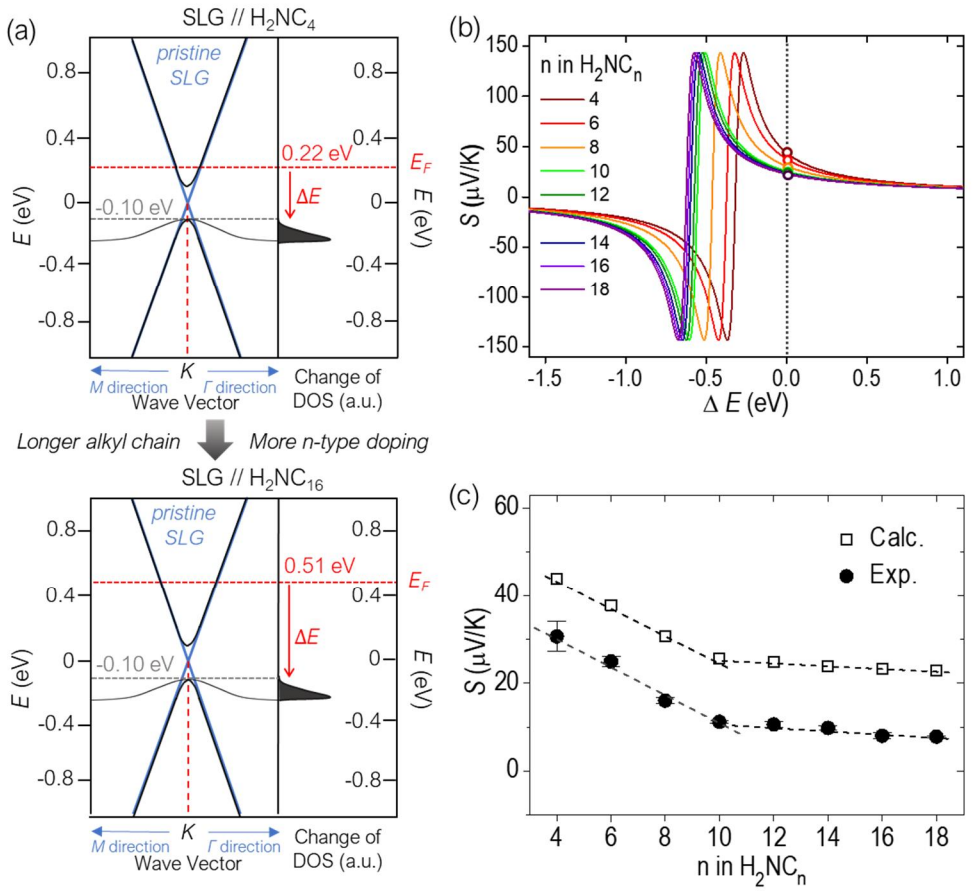

Figure 4-11. (a) Scheme of band structures with E_F shift and change of DOS for SLG//H_2NC_n SAM. (b) Plot of simulated Seebeck coefficient, S [μV/K]. (c) Comparison in length dependence between experimental and theoretical S values as a function of the molecular length.

4. 4. 5. Noncovalent Contact Induced Gap States

According to a TB approximation model, a perfect-crystalline, pure, and undoped SLG shows a band structure with zero gap, as known as Dirac cone (blue line in **Figure 4-12a**).[**384**,**385**] Mechanical behavior resulting in the change/fracture of hexagonal lattice system of graphene causes a small gap. Examples of such cases include the formation of crystal defects,[**21**,**25**,**26**] increase in strain,[**108**,**109**,**386**] doping induced by chemisorption or physisorption.[**384**,**387**–**390**]

In this physisorption, the nitrogen atom of the amine group ($-NH_2$) in H_2NC_n interacts with the carbon atoms that form the SLG to generate new in-gap states. We conducted ab initio calculations to examine the creation of such energy states upon physisorption of the amine molecules on SLG, and what factors do and do not influence the states. Upon the physisorption, new in-gap states near −0.1 eV appeared **(Figure 4-12)**. Interestingly, the newly generated in-gap states did not vary according to the length of alkyl chain, tilt angle of molecules with respect to the surface normal, and distance between SLG surface and nitrogen atom **(Figure 4-13, 4-14 and 4-15)**.

A noticeable feature in our calculations was that the binding energy of H_2NC_n molecules over SLG became more negative with increasing the alkyl chain length **(Figure 4-16)**. This indicates that, as the length of alkyl chain increases, the molecules are packed more densely. The higher packing density of molecules leads to more nitrogen atoms per unit area, better n-type doping, and more shift of E_F, which is consistent with the dependence of E_F shift on the alkyl chain length in **Figure 4-9c**. The literature explains that the surface coverage on graphene and the packing stabilization energy in H_2NC_n SAMs vary noticeably at $n = 10$,[**349**,**359**,**360**] which accounts for the transition in the slope of plots shown in **Figure 4-9c**. From the FET measurements, we also determined charge carrier concentration, n [10^{12} cm^{-2}]. It increased from 0.588 for H_2NC_4 to 3.231 for H_2NC_{18} **(Table 4-3)**. The increasing trend of n as the alkyl chain lengthens further confirms better packing density for longer molecules and the greater extent of n-type doping based on **Equation (2-19).**[**205**,**323**]

Figure 4-12a shows the band structures schematically drawn based on our calculations and FET analysis and summarizes the change of electronic structure before and after physisorption of the amine molecules. Physisorption of H_2NC_n SAM on SLG surface leads to creation of noncovalent contact induced gap states, and the increase of density of states (DOS) near the gap (black-filled peaks in **Figure 4-12a**).[**384**,**385**] As the alkyl chain increases, E_F is shifted to a more positive value, while the gap state is fixed at −0.1 eV **(Figure 4-12a)**. As a result, the energy offset increases. This is consistent with the FET analysis as shown in **Figure 4-9c**. Our experiments and calculation indicate that the noncovalent contact-induced gap-states and shift of E_F govern the thermopower of our junction.

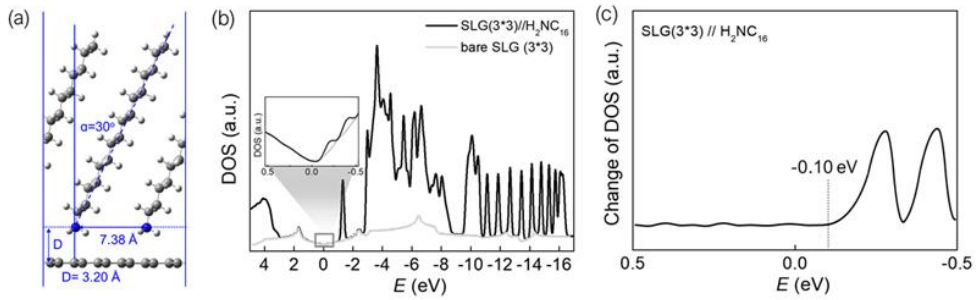

Figure 4-12. The system used for calculations. (a) The side view for the structure of H_2NC_{16} SAM on SLG with (3×3) unit cell. Here, α [°] is the tilt angle of molecule with respect to the surface normal, and D [Å] is the distance between SLG and nitrogen atom of amine group. The distance between molecules was set to be 7.38 Å (3×3). (b) The DOS spectra of bare SLG and SLG(3×3)//H_2NC_{16} SAM. (c) The plot for difference in DOS between SLG(3×3)//H_2NC_{16} and bare SLG. The new in-gap states appeared near −0.1 eV upon the physisorption.

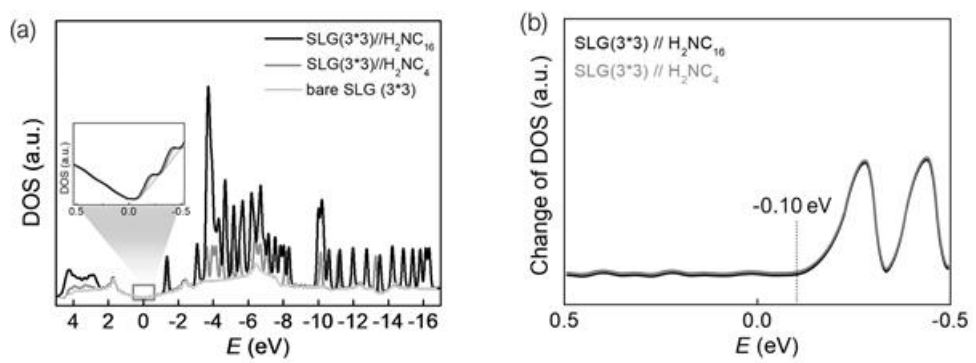

Figure 4-13. No response of energy level of in-gap state to the change in alkyl chain length (n in H_2NC_n). (a) The DOS spectra of bare SLG and SLG(3×3)//H_2NC_n SAM for different alkyl chain length (n = 4 or 16). (b) The corresponding plot of difference in DOS between SLG(3×3)//H_2NC_n and bare SLG. The in-gap states near −0.1 eV did not vary according to the change in the alkyl chain length. The α and D values were fixed to 30° and 3.2 Å, respectively.

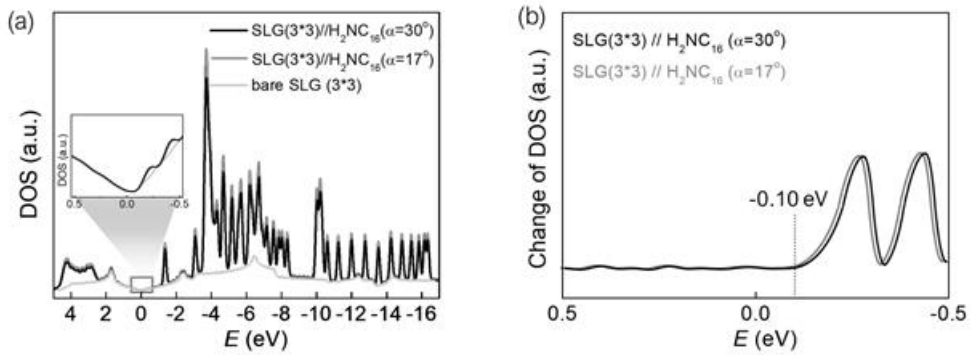

Figure 4-14. No response of energy level of in-gap state to the change in tilt angle of molecules. (a) The DOS spectra of bare SLG and SLG(3×3)//H_2NC_{16} for different tilt angles ($\alpha = 17$ or $30°$) of molecules with respect to the surface normal. (b) The corresponding plot of difference in DOS between SLG(3×3)//H_2NC_{16} ($\alpha = 17$ or $30°$) and bare SLG. The in-gap states near −0.1 eV did not vary according to the change in the tilt angle. The D value was fixed to 3.2 Å.

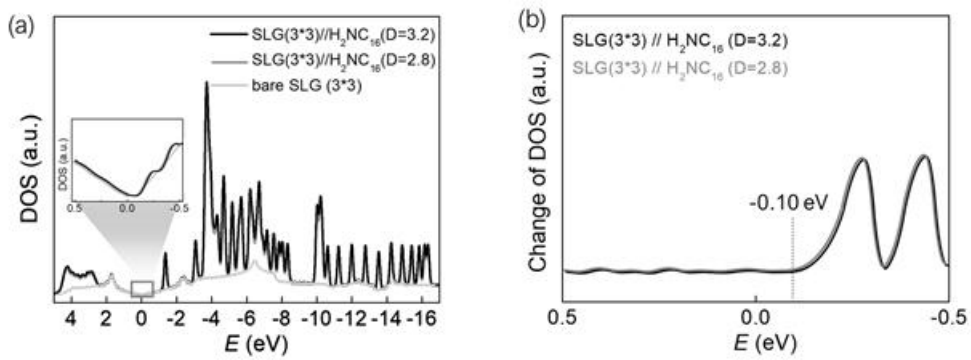

Figure 4-15. No response of energy level of in-gap state to the change in distance between SLG and nitrogen atom of amine group. (a) The DOS spectra of bare SLG and SLG(3×3)//H_2NC_{16} SAM for different distance between SLG surface and nitrogen atom ($D = 2.8$ or 3.2 Å). (b) The corresponding plot of difference in DOS between SLG(3×3)//H_2NC_{16} and bare SLG. The in-gap states near −0.1 eV did not vary according to the change in the distance between SLG and nitrogen atom. The α value was fixed to 30°.

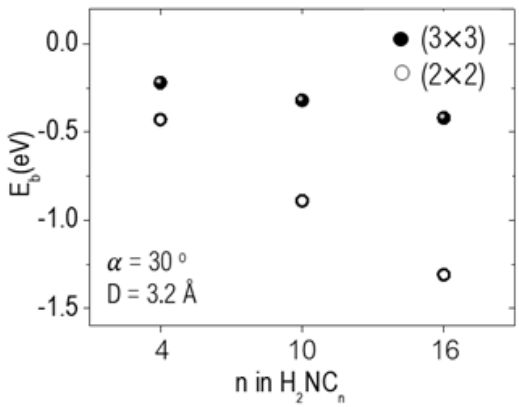

Figure 4-16. The binding energy, E_b [eV] with variations of the chain length (n in H_2NC_n).

n in H_2NC_n	n (10^{12} cm^{-2})	Number of measurements
4	0.588 ± 0.209	30
6	0.874 ± 0.136	30
8	1.544 ± 0.358	30
10	2.434 ± 0.161	30
12	2.633 ± 0.107	30
14	2.890 ± 0.140	30
16	3.065 ± 0.184	30
18	3.231 ± 0.352	30

Table 4-3. Carrier concentration, n of the FET devices with H_2NC_n SAMs. The data were averaged from 30 separate measurements.

4. 4. 6. Simulation of Seebeck Coefficient

Using **Equation (4-1) and (4-2)**, we simulated S values. For the sake of simplicity, we assumed that both top and bottom noncovalent contacts are identical. This allowed us to use $\Gamma = 0.050$ eV, which has been used for vdW contacts in EGaIn junctions.[**329**] **Figure 4-11b** shows the plot of transmission function simulated with ΔE values obtained from FET measurements. The calculated S values surprisingly well concurred with the experimental ones. The value of β^S varied from -3.1 ± 0.1 to -0.35 ± 0.03 μV/(K·n) at $n = 10$ in calculated data, which accounted for the experimentally observed transition of slope (-3.1 ± 0.4 to -0.43 ± 0.03 μV/(K·n) at $n = 10$). The change in β^S appearing around $n = 10$ would be due to the different packing structures of SAM of the chain length longer or shorter than H_2NC_{10}. It has been established that liquid-like SAMs transition into solid-like SAMs at SC_{10}. Similarly, in SLG//H_2NC_n SAMs, packing and surface coverage change gradually after H_2NC_{10}. One may argue that the change in β^S may be due to the transition in transport mechanism from direct tunneling to hopping. We eliminated this possibility given that no temperature dependence of current density has been reported in the analogous SAMs.[**349**]

While the overall trends of length dependence of simulated S values were consistent with those of experimentally determined ones, there were marginal deviations in absolute values of S between them **(Figure 4-11c)**. This could be explained by the following reasons. First, the deviations could be attributed to the complexity arising from the supramolecular packing structure in monolayers. In the model of **Equation (4-2)**, S is determined based on an ideal lorentzian-shaped transmission peak (as shown in **Figure 4-1c**), which can fit single-molecule systems well.[**325**,**331**,**333**,**341**] In a large-area junction, molecules within monolayers are disordered to some extent, and the defects can cause a change in the shape of transmission function from lorentzian to gaussian.[**364**] This may reduce the slope at E_F and be responsible for the decreased S values in experiments. Second, the effect of Γ on S would not be negligible. When $\Gamma = 0.050$ eV, values of S for $n \leq 10$ in H_2NC_n SAMs were 43.9, 37.7 and 30.6 μV/K, respectively. When Γ was increased by a factor of four (to 0.20 eV), the values of S were decreased to 39.0, 34.5 and 28.9 μV/K, respectively. In contrast, for the long molecular length regime ($n \geq 10$), the S value did not significantly depend on the variation of Γ. This result indicates that the S value becomes more sensitive to the change of Γ as ΔE is smaller and the alkane chain length of H_2NC_n is shorter. Therefore, the deviations between experimental and theoretical S values in the short molecules may reflect the uncertainty of Γ. Third, there may be a noticeable difference in ΔE between the SAMs with and without the EGaIn top-contact.[**391**] The top electrode-induced renormalization[**392**,**393**] may be nontrivial in our junctions and responsible for the observed deviations.

4. 4. 7. Comparison with Au/S Covalent Contact

Thermopower of both noncovalent (SLG//H_2NC_n) and covalent (Au/SC_n) junction relies on the orbital mixing between anchor and electrode at the contact, yet our work suggests that the underlying mechanism differs in detail. The thermopower of Au/SC_n system is governed by the chemisorption induced gap states (CIGS), which stems from orbital mixing of S-Au moiety with a small number of adjacent hydrocarbons of *n*-alkane chain.[**328**,**346**,**394**,**395**] In short n-alkyl chains ($n \leq 10$), the CIGS depends on the length of alkyl chain and dominates transmission coefficient, whereas it becomes insignificant in the regime of long alkanes ($n \geq 10$).[**346**,**394**] In contrast, our experiments revealed that the thermopower of SLG//H_2NC_n system is dominated by the new gap states and n-type doping caused by the amine-SLG noncovalent contact. One may argue that a higher Seebeck coefficient of bare SLG than gold could be the reason for our observations. However, the S value for SLG//Ga_2O_3/EGaIn (4.5 μV/K; see **Figure 4-17**) was similar to that for Au/Ga_2O_3/EGaIn (3.4 μV/K),[**326**] disproving the possibility.

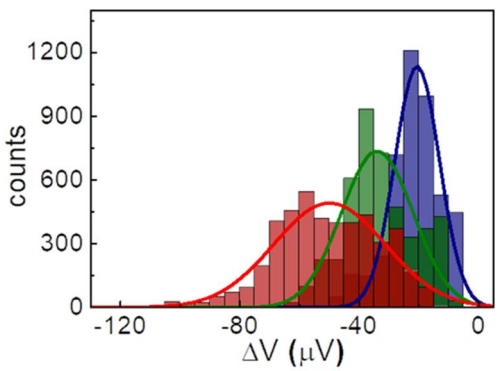

data	4484	4484	4484
junctions	59	59	59
mean	-21	-35	-49
sigma	8	12	17
yield (%)	90	83	78
slope	-3.5 ± 0.1		

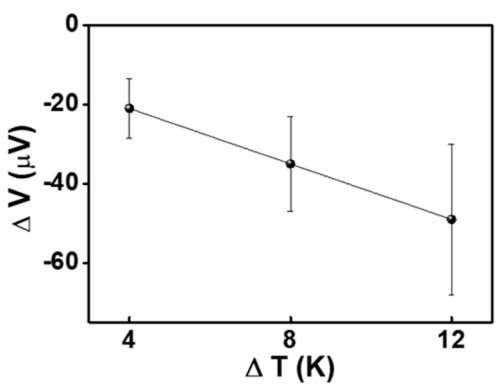

Figure 4-17. Histograms of thermoelectric voltage measured at the Cu//SLG//Ga_2O_3/EGaIn junctions. (i.e., SLG junctions without SAM), and estimated mean and standard deviation, σ values of thermoelectric voltage, ΔV from gaussian fitting curves. (Produced from S. P.)

4. 5. Conclusion

In summary, we have demonstrated that thermopower in saturated molecules can be enhanced by SLG electrode. Our experiments show S values in the noncovalent junction are larger (by up to five-fold) than those of the covalent junction. The underlying mechanism for the enhancement of S is revealed to be the generation of in-gap states and n-type doping induced by electronic interaction at the noncovalent contact between amine anchor and graphene. The chain length of the alkylamine molecules significantly affects the degree of doping (the position of E_{F}) but not the in-gap states, which account for the length dependence of thermopower. The simulation of S with the Mott formula proves our proposed mechanism. Our work demonstrates that control over molecule-electrode contact in molecular-scale devices can improve Seebeck coefficient of saturated molecules and may augur well for developing efficient organic thermoelectric generators.

Bibliography

[**1**] Wallace, P. R. The band theory of graphite. *Phys. Rev.* **71**, 622–634 (1947).

[**2**] Mermin, N. D. Crystalline order in two dimensions. *Phys. Rev.* **176**, 250–254 (1968).

[**3**] Novoselov, K. S. *et al.* Electric field in atomically thin carbon films. *Science* **306**, 666–669 (2004).

[**4**] Kim, K. S. K. S. *et al.* Large-scale pattern growth of graphene films for stretchable transparent electrodes. *Nature* **457**, 706–710 (2009).

[**5**] Li, X. *et al.* Large-area synthesis of high-quality and uniform graphene films on copper foils. *Science* **324**, 1312–1314 (2009).

[**6**] Geng, D., Wang, H. & Yu, G. Graphene single crystals: Size and morphology engineering. *Adv. Mater.* **27**, 2821–2837 (2015).

[**7**] Wang, M., Luo, D., Wang, B. & Ruoff, R. S. Synthesis of Large-Area Single-Crystal Graphene. *Trends Chem.* **3**, 15–33 (2021).

[**8**] Atif, R. & Inam, F. The Dissimilarities between Graphene and Frame-Like Structures. *Graphene* **05**, 55–72 (2016).

[**9**] Maffucci, A. & Miano, G. Electrical properties of graphene for interconnect applications. *Appl. Sci.* **4**, 305–317 (2014).

[**10**] Yang, G., Li, L., Lee, W. B. & Ng, M. C. Structure of graphene and its disorders: a review. *Sci. Technol. Adv. Mater.* **19**, 613–648 (2018).

[**11**] Armano, A. & Agnello, S. Two-Dimensional Carbon: A Review of Synthesis Methods, and Electronic, Optical, and Vibrational Properties of Single-Layer Graphene. *C — J. Carbon Res.* **5**, 67 (2019).

[**12**] Tuček, J. *et al.* Emerging chemical strategies for imprinting magnetism in graphene and related 2D materials for spintronic and biomedical applications. *Chem. Soc. Rev.* **47**, 3899–3990 (2018).

[**13**] Dash, G. N., Pattanaik, S. R. & Behera, S. Graphene for electron devices: The panorama of a decade. *IEEE J. Electron Devices Soc.* **2**, 77–104 (2014).

[**14**] Georgakilas, V., Perman, J. A., Tucek, J. & Zboril, R. Broad Family of Carbon Nanoallotropes: Classification, Chemistry, and Applications of Fullerenes, Carbon Dots, Nanotubes, Graphene, Nanodiamonds, and Combined Superstructures. *Chem. Rev.* **115**, 4744–4822 (2015).

[**15**] Ye, S. *et al.* Thickness-dependent strain effect on the deformation of the graphene-encapsulated Au nanoparticles. *J. Nanomater.* **2014**, (2014).

[**16**] Ago, H. CVD Growth of High-Quality Single-Layer Graphene. in *Frontiers of Graphene and Carbon Nanotubes* 3–20 (Springer Japan, 2015). doi:10.1007/978-4-431-55372-4_1.

[**17**] Banhart, F., Kotakoski, J. & Krasheninnikov, A. V. Structural defects in graphene. *ACS Nano* **5**, 26–41 (2011).

[**18**] Biró, L. P. & Lambin, P. Grain boundaries in graphene grown by chemical vapor deposition. *New J. Phys.* **15**, 035024 (2013).

[**19**] Huang, P. Y. *et al.* Grains and grain boundaries in single-layer graphene atomic patchwork quilts. *Nature* **469**, 389–392 (2011).

[**20**] Kim, K. *et al.* Grain boundary mapping in polycrystalline graphene. *ACS Nano* **5**, 2142–2146 (2011).

[**21**] Tsen, A. W. *et al.* Tailoring electrical transport across grain boundaries in polycrystalline graphene. *Science* **336**, 1143–1146 (2012).

[**22**] Wang, B., Puzyrev, Y. & Pantelides, S. T. Strain enhanced defect reactivity at grain boundaries in polycrystalline graphene. *Carbon* **49**, 3983–3988 (2011).

[**23**] Yang, B., Xu, H., Lu, J. & Loh, K. P. Periodic grain boundaries formed by thermal reconstruction of polycrystalline graphene film. *J. Am. Chem. Soc.* **136**, 12041–12046 (2014).

[**24**] Hashimoto, A., Suenaga, K., Gloter, A., Urita, K. & Iijima, S. Direct evidence for atomic defects in graphene layers. *Nature* **430**, 870–873 (2004).

[**25**] Kang, J., Bang, J., Ryu, B. & Chang, K. J. Effect of atomic-scale defects on the low-energy electronic structure of graphene: Perturbation theory and local-density-functional calculations. *Phys. Rev. B* **77**, 115453 (2008).

[**26**] Zhang, W., Lu, W. C., Zhang, H. X., Ho, K. M. & Wang, C. Z. Lattice distortion and electron charge redistribution induced by defects in graphene. *Carbon* **110**, 330–335 (2016).

[**27**] Ashcroft, N. W. & Mermin, N. D. *Solid state physics*. (Saunders College Publishing, 1976).

[**28**] Saito, R., Dresselhaus, G. & Dresselhaus, M. S. Tight Binding Calculation of Molecules and Solids. in *Physical Properties of Carbon Nanotubes* 17–33 (Imperial College Press, 1998). doi:10.1142/9781860943799_0002.

[**29**] Reich, S., Maultzsch, J., Thomsen, C. & Ordejón, P. Tight-binding description of graphene. *Phys. Rev. B* **66**, 354121–354125 (2002).

[**30**] Maffucci, A., Maksimenko, S. A. & Portnoi, M. E. Carbon Nanotubes and Graphene Nanoribbons for Terahertz Applications. in *NATO Science for Peace and Security Series B: Physics and Biophysics* 103–123 (Springer Netherlands, 2016). doi:10.1007/978-94-017-7478-9_6.

[**31**] Grundmann, M. *The physics of semiconductors: An introduction including devices and nanophysics*. (Springer-Verlag Berlin Heidelberg, 2006). doi:10.1007/3-540-34661-9.

[**32**] Castro Neto, A. H., Guinea, F., Peres, N. M. R., Novoselov, K. S. & Geim, A. K. The electronic properties of graphene. *Rev. Mod. Phys.* **81**, 109–162 (2009).

[**33**] Aharony, A. & Entin-Wohlman, O. *Introduction to Solid State Physics*. (Wiley, 2018). doi:10.1142/11041.

[**34**] Rogalski, M. S. & Palmer, S. B. *Solid state physics*. (Brooks/Cole, 2014). doi:10.1201/9781482283037.

[**35**] Cui, L., Wang, J. & Sun, M. Graphene plasmon for optoelectronics. *Rev. Phys.* **6**, 100054 (2021).

[**36**] Geim, A. K. & MacDonald, A. H. Graphene: Exploring carbon flatland. *Phys. Today* **60**, 35–41 (2007).

[**37**] van Haeringen, W. & Junginger, H. G. Pseudopotential approach to the energy band structure of graphite. *Solid State Commun.* **7**, 1723–1725 (1969).

[**38**] Kogan, E. & Nazarov, V. U. Symmetry classification of energy bands in graphene. *Phys. Rev. B* **85**, 115418 (2012).

[**39**] Jena, D. Graphene. in *Encyclopedia of Nanotechnology* 968–978 (Springer Dordrecht, 2012). doi:10.1007/978-90-481-9751-4_373.

[**40**] Jorio, A., Saito, R., Dresselhaus, G. & Dresselhaus, M. S. *Raman Spectroscopy in Graphene Related Systems*. (WILEY-VCH Verlag GmbH & Co. KGaA, Weinheim, 2011).

[**41**] Malard, L. M., Guimarães, M. H. D., Mafra, D. L., Mazzoni, M. S. C. & Jorio, A. Group-theory analysis of electrons and phonons in N -layer graphene systems. *Phys. Rev. B* **79**, 125426 (2009).

[**42**] Wu, J. Bin, Lin, M. L., Cong, X., Liu, H. N. & Tan, P. H. Raman spectroscopy of graphene-based materials and its applications in related devices. *Chem. Soc. Rev.* **47**, 1822–1873 (2018).

[**43**] Wang, H., Wang, Y., Cao, X., Feng, M. & Lan, G. Vibrational properties of graphene and graphene layers. *J. Raman Spectrosc.* **40**, 1791–1796 (2009).

[**44**] Reich, S. & Thomsen, C. Raman spectroscopy of graphite. *Phil. Trans. R. Soc. Lond. A* **362**, 2271–2288 (2004).

[**45**] Samsonidze, G. G. *et al.* Electron-phonon coupling mechanism in two-dimensional graphite and single-wall carbon nanotubes. *Phys. Rev. B* **75**, 155420 (2007).

[**46**] Yu, P. Y. & Cardona, M. *Fundamentals of Semiconductors: Physics and Materials Properties.* (Springer-Verlag Berlin Heidelberg, 2010).

[**47**] Rousseau, D. L., Bauman, R. P. & Porto, S. P. S. Normal mode determination in crystals. *J. Raman Spectrosc.* **10**, 253–290 (1981).

[**48**] Froehlicher, G. Optical spectroscopy of two-dimensional materials : graphene , transition metal dichalcogenides and van der Waals heterostructures. (Université de Strasbourg, 2017).

[**49**] Dresselhaus, M. S., Dresselhaus, G. & Jorio, A. *Group theory*. (Springer Berlin Heidelberg, 2008). doi:10.1007/978-3-540-32899-5.

[**50**] Ferrari, A. C. *et al.* Raman spectrum of graphene and graphene layers. *Phys. Rev. Lett.* **97**, 187401 (2006).

[**51**] Han, M. Y., Özyilmaz, B., Zhang, Y. & Kim, P. Energy band-gap engineering of graphene nanoribbons. *Phys. Rev. Lett.* **98**, 206805 (2007).

[**52**] Li, T. C. & Lu, S. P. Quantum conductance of graphene nanoribbons with edge defects. *Phys. Rev. B* **77**, 085408 (2008).

[**53**] Nakada, K., Fujita, M., Dresselhaus, G. & Dresselhaus, M. S. Edge state in graphene ribbons: Nanometer size effect and edge shape dependence. *Phys. Rev. B* **54**, 17954–17961 (1996).

[**54**] Qi, Z. J. *et al.* Correlating atomic structure and transport in suspended graphene nanoribbons. *Nano Lett.* **14**, 4238–4244 (2014).

[**55**] Rizzo, D. J. *et al.* Topological band engineering of graphene nanoribbons. *Nature* **560**, 204–208 (2018).

[**56**] Son, Y. W., Cohen, M. L. & Louie, S. G. Energy gaps in graphene nanoribbons. *Phys. Rev. Lett.* **97**, 216803 (2006).

[**57**] Srivastava, A., Jain, A., Kurchania, R. & Tyagi, N. Width dependent electronic properties of graphene nanoribbons: An ab-initio study. *J. Comput. Theor. Nanosci.* **9**, 1008–1013 (2012).

[**58**] Tapasztó, L., Dobrik, G., Lambin, P. & Biró, L. P. Tailoring the atomic structure of

graphene nanoribbons by scanning tunnelling microscope lithography. *Nat. Nanotechnol.* **3**, 397–401 (2008).

[**59**] Habiba, K. *et al.* Luminescent graphene quantum dots fabricated by pulsed laser synthesis. *Carbon* **64**, 341–350 (2013).

[**60**] Juang, R. S. *et al.* Highly fluorescent green and red emissions from boron-doped graphene quantum dots under blue light illumination. *Carbon* **176**, 61–70 (2021).

[**61**] Kang, S. H. *et al.* Ultrafast Method for Selective Design of Graphene Quantum Dots with Highly Efficient Blue Emission. *Sci. Rep.* **6**, 1–7 (2016).

[**62**] Kuamit, T., Ratanasak, M., Rungnim, C. & Parasuk, V. Effects of shape, size, and pyrene doping on electronic properties of graphene nanoflakes. *J. Mol. Model.* **23**, (2017).

[**63**] Moon, J. *et al.* One-step synthesis of N-doped graphene quantum sheets from monolayer graphene by nitrogen plasma. *Adv. Mater.* **26**, 3501–3505 (2014).

[**64**] Park, M. J., Kim, Y., Kim, Y. & Hong, B. H. Continuous Films of Self-Assembled Graphene Quantum Dots for n-Type Doping of Graphene by UV-Triggered Charge Transfer. *Small* **13**, 1603142 (2017).

[**65**] Ponomarenko, L. A. *et al.* Chaotic dirac billiard in graphene quantum dots. *Science* **320**, 356–358 (2008).

[**66**] Seyed-Talebi, S. M., Beheshtian, J. & Neek-Amal, M. Doping effect on the adsorption of NH3 molecule onto graphene quantum dot: From the physisorption to the chemisorption. *J. Appl. Phys.* **114**, (2013).

[**67**] Yang, H. Two-dimensional Materials: Graphene traps. *Nat. Phys.* **12**, 994–995 (2016).

[**68**] Park, J. & Yan, M. Covalent functionalization of graphene with reactive intermediates. *Acc. Chem. Res.* **46**, 181–189 (2013).

[**69**] Eda, G. *et al.* Blue photoluminescence from chemically derived graphene oxide. *Adv. Mater.* **22**, 505–509 (2010).

[**70**] Krishnamoorthy, K., Veerapandian, M., Yun, K. & Kim, S. J. The chemical and structural analysis of graphene oxide with different degrees of oxidation. *Carbon* **53**, 38–49 (2013).

[**71**] Kudin, K. N. *et al.* Raman spectra of graphite oxide and functionalized graphene sheets. *Nano Lett.* **8**, 36–41 (2008).

[**72**] Song, Y. *et al.* Intrinsically Honeycomb-Patterned Hydrogenated Graphene. *Small* **18**, 2102687 (2022).

[**73**] Fei, Y., Fang, S. & Hu, Y. H. Synthesis, properties and potential applications of hydrogenated graphene. *Chem. Eng. J.* **397**, 125408 (2020).

[**74**] Yagi, R. *et al.* Low-energy band structure and even-odd layer number effect in AB-stacked multilayer graphene. *Sci. Rep.* **8**, 1–7 (2018).

[**75**] Kim, Y. *et al.* Breakdown of the interlayer coherence in twisted bilayer graphene. *Phys. Rev. Lett.* **110**, 096602 (2013).

[**76**] Cao, Y. *et al.* Unconventional superconductivity in magic-angle graphene superlattices. *Nature* **556**, 43–50 (2018).

[**77**] Cao, Y. *et al.* Superlattice-Induced Insulating States and Valley-Protected Orbits in Twisted Bilayer Graphene. *Phys. Rev. Lett.* **117**, 116804 (2016).

[**78**] Lui, C. H., Li, Z., Mak, K. F., Cappelluti, E. & Heinz, T. F. Observation of an electrically tunable band gap in trilayer graphene. *Nat. Phys.* **7**, 944–947 (2011).

[**79**] Oostinga, J. B., Heersche, H. B., Liu, X., Morpurgo, A. F. & Vandersypen, L. M. K. Gate-induced insulating state in bilayer graphene devices. *Nat. Mater.* **7**, 151–157 (2008).

[**80**] Li, J. *et al.* Gate-controlled topological conducting channels in bilayer graphene. *Nat. Nanotechnol.* **11**, 1060–1065 (2016).

[**81**] Tabert, C. J. & Nicol, E. J. Dynamical conductivity of AA-stacked bilayer graphene. *Phys. Rev. B* **86**, 075439 (2012).

[**82**] Zhang, Y. *et al.* Direct observation of a widely tunable bandgap in bilayer graphene. *Nature* **459**, 820–823 (2009).

[**83**] Cao, Y. *et al.* Correlated insulator behaviour at half-filling in magic-angle graphene superlattices. *Nature* **556**, 80–84 (2018).

[**84**] Ohta, T., Bostwick, A., Seyller, T., Horn, K. & Rotenberg, E. Controlling the electronic structure of bilayer graphene. *Science* **313**, 951–954 (2006).

[**85**] Zhang, F., Sahu, B., Min, H. & MacDonald, A. H. Band structure of ABC-stacked graphene trilayers. *Phys. Rev. B* **82**, 035409 (2010).

[**86**] Yoo, H. *et al.* Atomic and electronic reconstruction at the van der Waals interface in twisted bilayer graphene. *Nat. Mater.* **18**, 448–453 (2019).

[**87**] Zhang, W. *et al.* Opening an electrical band gap of bilayer graphene with molecular doping. *ACS Nano* **5**, 7517–7524 (2011).

[**88**] Samuels, A. J. & Carey, J. D. Molecular doping and band-gap opening of bilayer graphene. *ACS Nano* **7**, 2790–2799 (2013).

[**89**] Denis, P. A., Pereyra Huelmo, C. & Martins, A. S. Band Gap Opening in Dual-Doped Monolayer Graphene. *J. Phys. Chem. C* **120**, 7103–7112 (2016).

[**90**] Gadelha, A. C. *et al.* Twisted Bilayer Graphene: A Versatile Fabrication Method and the Detection of Variable Nanometric Strain Caused by Twist-Angle Disorder. *ACS Appl. Nano Mater.* **4**, 1858–1866 (2021).

[**91**] Brar, V. W. *et al.* Scanning tunneling spectroscopy of inhomogeneous electronic structure in monolayer and bilayer graphene on SiC. *Appl. Phys. Lett.* **91**, 23–25 (2007).

[**92**] Yankowitz, M. *et al.* Electric field control of soliton motion and stacking in trilayer graphene. *Nat. Mater.* **13**, 786–789 (2014).

[**93**] Yoon, C., Jang, Y., Jung, J. & Min, H. Broken sublattice symmetry states in Bernal stacked multilayer graphene. *2D Mater.* **4**, 021025 (2017).

[**94**] Kumar, A., Banerjee, K. & Liljeroth, P. Molecular assembly on two-dimensional materials. *Nanotechnology* **28**, 082001 (2017).

[**95**] Xu, M., Liang, T., Shi, M. & Chen, H. Graphene-like two-dimensional materials. *Chem. Rev.* **113**, 3766–3798 (2013).

[**96**] Wang, Q. H. editorial Graphene is not alone. *Nat. Nanotechnol.* **7**, 683 (2012).

[**97**] Chaves, A. *et al.* Bandgap engineering of two-dimensional semiconductor materials. *npj 2D Mater. Appl.* **4**, 29 (2020).

[**98**] Kim, H. G. & Lee, H. B. R. Atomic Layer Deposition on 2D Materials. *Chem. Mater.* **29**, 3809–3826 (2017).

[**99**] Neto, A. H. C. & Novoselov, K. New directions in science and technology: two-dimensional crystals. *Reports Prog. Phys.* **74**, 082501 (2011).

[**100**] Yu, Y.-J. *et al.* Tuning the Graphene Work Function by Electric Field Effect. *Nano Lett.* **9**,

3430–3434 (2009).

[**101**] Meric, I. *et al.* Current saturation in zero-bandgap, top-gated graphene field-effect transistors. *Nat. Nanotechnol.* **3**, 654–659 (2008).

[**102**] Jung, J. & MacDonald, A. H. Theory of the magnetic-field-induced insulator in neutral graphene sheets. *Phys. Rev. B* **80**, 235417 (2009).

[**103**] Herbut, I. F. SO(3) symmetry between Néel and ferromagnetic order parameters for graphene in a magnetic field. *Phys. Rev. B* **76**, 085432 (2007).

[**104**] Wang, Y. *et al.* Room-Temperature Ferromagnetism of Graphene. *Nano Lett.* **9**, 220–224 (2009).

[**105**] Checkelsky, J. G., Li, L. & Ong, N. P. Divergent resistance at the Dirac point in graphene: Evidence for a transition in a high magnetic field. *Phys. Rev. B* **79**, 115434 (2009).

[**106**] Dedkov, Y. S. & Fonin, M. Electronic and magnetic properties of the graphene–ferromagnet interface. *New J. Phys.* **12**, 125004 (2010).

[**107**] Teague, M. L. *et al.* Evidence for Strain-Induced Local Conductance Modulations in Single-Layer Graphene on SiO 2. *Nano Lett.* **9**, 2542–2546 (2009).

[**108**] Forestier, A. *et al.* Strain and Piezo-Doping Mismatch between Graphene Layers. *J. Phys. Chem. C* **124**, 11193–11199 (2020).

[**109**] Ares, P. *et al.* Tunable Graphene Electronics with Local Ultrahigh Pressure. *Adv. Funct. Mater.* **29**, 1806715 (2019).

[**110**] Lee, H., Kim, I., Kim, M. & Lee, H. Moving beyond flexible to stretchable conductive electrodes using metal nanowires and graphenes. *Nanoscale* **8**, 1789–1822 (2016).

[**111**] Robinson, N. D., Edman, L. & Chhowalla, M. Graphene electrodes for organic metal-free light-emitting devices. *Phys. Scr.* **T146**, 014023 (2012).

[**112**] Han, T.-H. *et al.* Extremely efficient flexible organic light-emitting diodes with modified graphene anode. *Nat. Photonics* **6**, 105–110 (2012).

[**113**] Wu, W. *et al.* Control of thickness uniformity and grain size in graphene films for transparent conductive electrodes. *Nanotechnology* **23**, 035603 (2012).

[**114**] Han, T.-H. *et al.* Versatile p-Type Chemical Doping to Achieve Ideal Flexible Graphene Electrodes. *Angew. Chemie Int. Ed.* **55**, 6197–6201 (2016).

[**115**] Zhang, J. *et al.* Unravelling a Zigzag Pathway for Hot Carrier Collection with Graphene Electrode. *J. Phys. Chem. Lett.* **12**, 2886–2891 (2021).

[**116**] Kang, J. *et al.* High-Performance Graphene-Based Transparent Flexible Heaters. *Nano Lett.* **11**, 5154–5158 (2011).

[**117**] Kang, J. *et al.* An Ag-grid/graphene hybrid structure for large-scale, transparent, flexible heaters. *Nanoscale* **7**, 6567–6573 (2015).

[**118**] Agnoli, S. & Favaro, M. Doping graphene with boron: A review of synthesis methods, physicochemical characterization, and emerging applications. *J. Mater. Chem. A* **4**, 5002–5025 (2016).

[**119**] Usachov, D. Y. *et al.* Large-scale sublattice asymmetry in pure and boron-doped graphene. *Nano Lett.* **16**, 4535–4543 (2016).

[**120**] Cress, C. D. *et al.* Nitrogen-Doped Graphene and Twisted Bilayer Graphene via Hyperthermal Ion Implantation with Depth Control. *ACS Nano* **10**, 3714–3722 (2016).

[**121**] Deng, D. *et al.* Toward N-Doped Graphene via Solvothermal Synthesis. *Chem. Mater.* **23**,

1188–1193 (2011).

[**122**] Guo, B. *et al.* Controllable N-doping of graphene. *Nano Lett.* **10**, 4975–4980 (2010).

[**123**] Lin, L. *et al.* Nitrogen cluster doping for high-mobility/conductivity graphene films with millimeter-sized domains. *Sci. Adv.* **5**, eaaw8337 (2019).

[**124**] Son, M. *et al.* High-quality nitrogen-doped graphene films synthesized from pyridine via two-step chemical vapor deposition. *Carbon* **159**, 579–585 (2020).

[**125**] Usachov, D. *et al.* Nitrogen-doped graphene: Efficient growth, structure, and electronic properties. *Nano Lett.* **11**, 5401–5407 (2011).

[**126**] Wei, D. *et al.* Synthesis of n-doped graphene by chemical vapor deposition and its electrical properties. *Nano Lett.* **9**, 1752–1758 (2009).

[**127**] Xu, H., Ma, L. & Jin, Z. Nitrogen-doped graphene: Synthesis, characterizations and energy applications. *J. Energy Chem.* **27**, 146–160 (2018).

[**128**] Zhao, Y. *et al.* Direct synthesis of high-quality nitrogen-doped graphene via ion implantation. *Carbon* **139**, 732–739 (2018).

[**129**] Kang, B., Kang, S., Yan, S. & Lee, J. Y. Curvature Effect on the Barrier from the Physisorption to the Chemisorption of H_2 on Graphene. *Bull. Korean Chem. Soc.* **32**, 934–938 (2011).

[**130**] Omidvar, A. Reversible hydrogen adsorption on Co/N4 cluster embedded in graphene: The role of charge manipulation. *Chem. Phys.* **493**, 85–90 (2017).

[**131**] Mali, K. S., Greenwood, J., Adisoejoso, J., Phillipson, R. & De Feyter, S. Nanostructuring graphene for controlled and reproducible functionalization. *Nanoscale* **7**, 1566–1585 (2015).

[**132**] Kittel C. *Introduction to Solid State Physics*. (Wiley, 2005).

[**133**] Liu, H., Liu, Y. & Zhu, D. Chemical doping of graphene. *J. Mater. Chem.* **21**, 3335–3345 (2011).

[**134**] Sato, Y., Takai, K. & Enoki, T. Electrically controlled adsorption of oxygen in bilayer graphene devices. *Nano Lett.* **11**, 3468–3475 (2011).

[**135**] Ryu, S. *et al.* Atmospheric oxygen binding and hole doping in deformed graphene on a SiO2 substrate. *Nano Lett.* **10**, 4944–4951 (2010).

[**136**] Jeong, H. *et al.* Highly uniform monolayer graphene synthesis: Via a facile pretreatment of copper catalyst substrates using an ammonium persulfate solution. *RSC Adv.* **9**, 20871–20877 (2019).

[**137**] Singh, A. K. & Gupta, A. K. Reversible control of doping in graphene-on-SiO2 by cooling under gate-voltage. *J. Appl. Phys.* **122**, (2017).

[**138**] Miwa, R. H., Schmidt, T. M., Scopel, W. L. & Fazzio, A. Doping of graphene adsorbed on the a-SiO2 surface. *Appl. Phys. Lett.* **99**, (2011).

[**139**] Lei Wang, Zheyuan Chen, J. H. of Graphene in a Hexagonal Boron Structure. *ACS Nano* **6**, 9314–9319 (2012).

[**140**] Chang, J. K. *et al.* Spectroscopic studies of the physical origin of environmental aging effects on doped graphene. *J. Appl. Phys.* **119**, 235301 (2016).

[**141**] Melios, C., Giusca, C. E., Panchal, V. & Kazakova, O. Water on graphene: Review of recent progress. *2D Mater.* **5**, 022001 (2018).

[**142**] Moser, J., Verdaguer, A., Jiḿnez, D., Barreiro, A. & Bachtold, A. The environment of

graphene probed by electrostatic force microscopy. *Appl. Phys. Lett.* **92**, 123507 (2008).

[**143**] Levesque, P. L. *et al.* Probing charge transfer at surfaces using graphene transistors. *Nano Lett.* **11**, 132–137 (2011).

[**144**] Liu, L. *et al.* Graphene oxidation: Thickness-dependent etching and strong chemical doping. *Nano Lett.* **8**, 1965–1970 (2008).

[**145**] Wehling, T. O., Lichtenstein, A. I. & Katsnelson, M. I. First-principles studies of water adsorption on graphene: The role of the substrate. *Appl. Phys. Lett.* **93**, 202110 (2008).

[**146**] Alexandrou, K., Petrone, N., Hone, J. & Kymissis, I. Encapsulated graphene field-effect transistors for air stable operation. *Appl. Phys. Lett.* **106**, 113104 (2015).

[**147**] Alexandrou, K. *et al.* Effect of vacuum thermal annealing to encapsulated graphene field effect transistors. *J. Vac. Sci. Technol. B* **34**, 041805 (2016).

[**148**] Schedin, F. *et al.* Detection of individual gas molecules adsorbed on graphene. *Nat. Mater.* **6**, 652–655 (2007).

[**149**] Chen, J.-H. *et al.* Charged-impurity scattering in graphene. *Nat. Phys.* **4**, 377–381 (2008).

[**150**] Riedl, C., Starke, U., Bernhardt, J., Franke, M. & Heinz, K. Structural properties of the graphene-SiC(0001) interface as a key for the preparation of homogeneous large-terrace graphene surfaces. *Phys. Rev. B* **76**, 245406 (2007).

[**151**] Mallet, P. *et al.* Electron states of mono- and bilayer graphene on SiC probed by scanning-tunneling microscopy. *Phys. Rev. B* **76**, 041403 (2007).

[**152**] Huang, H., Chen, S., Wee, A. T. S. & Chen, W. Epitaxial growth of graphene on silicon carbide (SiC). in *Graphene* 3–26 (Elsevier, 2014). doi:10.1533/9780857099334.1.3.

[**153**] Tromp, R. M. & Hannon, J. B. Thermodynamics and kinetics of graphene growth on SiC(0001). *Phys. Rev. Lett.* **102**, 106104 (2009).

[**154**] Hass, J., De Heer, W. A. & Conrad, E. H. The growth and morphology of epitaxial multilayer graphene. *J. Phys. Condens. Matter* **20**, 323202 (2008).

[**155**] Emtsev, K. V. *et al.* Towards wafer-size graphene layers by atmospheric pressure graphitization of silicon carbide. *Nat. Mater.* **8**, 203–207 (2009).

[**156**] Virojanadara, C. *et al.* Homogeneous large-area graphene layer growth on 6H-SiC(0001). *Phys. Rev. B* **78**, 245403 (2008).

[**157**] Bae, S. *et al.* Roll-to-roll production of 30-inch graphene films for transparent electrodes. *Nat. Nanotechnol.* **5**, 574–578 (2010).

[**158**] Robertson, S. D. Graphite formation from low temperature pyrolysis of methane over some transition metal surfaces. *Nature* **221**, 1044–1046 (1969).

[**159**] Host, J. J., Dravid, V. P. & Teng, M. H. Systematic study of graphite encapsulated nickel nanocrystal synthesis with formation mechanism implications. *J. Mater. Res.* **13**, 2547–2555 (1998).

[**160**] Huang, W. *et al.* Synthesis and characterization of graphite nanofibers deposited on nickel foams. *Phys. Chem. Chem. Phys.* **4**, 5325–5329 (2002).

[**161**] Helveg, S. *et al.* Atomic-scale imaging of carbon nanofibre growth. *Nature* **427**, 426–429 (2004).

[**162**] Lee, S. T. *et al.* Heteroepitaxy of carbon on copper by high-temperature ion implantation. *Appl. Phys. Lett.* **59**, 785–787 (1991).

[**163**] Ong, T. P., Xiong, F., Chang, R. P. H. & White, C. W. Nucleation and growth of diamond

on carbon-implanted single crystal copper surfaces. *J. Mater. Res.* **7**, 2429–2439 (1992).

[**164**] Karu, A. E. & Beer, M. Pyrolytic formation of highly crystalline graphite films. *J. Appl. Phys.* **37**, 2179–2181 (1966).

[**165**] Fan, Q. H., Pereira, E. & Grácio, J. Diamond deposition on copper: studies on nucleation, growth, and adhesion behaviours. *J. Mater. Sci.* **34**, 1353–1365 (1999).

[**166**] Narayan, J., Godbole, V. P. & White, C. W. Laser Method for Synthesis and Processing of Continuous Diamond Films on Nondiamond Substrates. *Science* **252**, 416–418 (1991).

[**167**] Zhou, B. *et al.* Synthesis of Diamond-Like Carbon Film on Copper and Titanium Interlayer by Vacuum Cathode Arc Evaporation. *Appl. Mech. Mater.* **189**, 167–171 (2012).

[**168**] Galaburda, M. *et al.* Mechanochemical synthesis of carbon-stabilized Cu/C, Co/C and Ni/C nanocomposites with prolonged resistance to oxidation. *Sci. Rep.* **9**, 17435 (2019).

[**169**] Ding, L. *et al.* Selective Growth of Well-Aligned Semiconducting Single-Walled Carbon Nanotubes. *Nano Lett.* **9**, 800–805 (2009).

[**170**] Zhou, W. *et al.* Copper catalyzing growth of single-walled carbon nanotubes on substrates. *Nano Lett.* **6**, 2987–2990 (2006).

[**171**] Lee, G. W., Jurng, J. & Hwang, J. Synthesis of carbon nanotubes on a catalytic metal substrate by using an ethylene inverse diffusion flame. *Carbon* **42**, 682–685 (2004).

[**172**] Huh, Y., Green, M. L. H., Kim, Y. H., Lee, J. Y. & Lee, C. J. Control of carbon nanotube growth using cobalt nanoparticles as catalyst. *Appl. Surf. Sci.* **249**, 145–150 (2005).

[**173**] Zhang, Y. B., Lau, S. P. & Li, H. F. Field emission from nanoforest carbon nanotubes grown on cobalt-containing amorphous carbon composite films. *J. Appl. Phys.* **101**, 033524 (2007).

[**174**] Hamilton, J. C. & Blakely, J. M. Carbon segregation to single crystal surfaces of Pt, Pd and Co. *Surf. Sci.* **91**, 199–217 (1980).

[**175**] Zi-Pu, H., Ogletree, D. F., Van Hove, M. A. & Somorjai, G. A. Leed theory for incommensurate overlayers: Application to graphite on Pt(111). *Surf. Sci.* **180**, 433–459 (1987).

[**176**] Aizawa, T., Souda, R., Otani, S., Ishizawa, Y. & Oshima, C. Anomalous bond of monolayer graphite on transition-metal carbide surfaces. *Phys. Rev. Lett.* **64**, 768 (1990).

[**177**] Derbyshire, F. J., Presland, A. E. B. & Trimm, D. L. Graphite formation by the dissolution—precipitation of carbon in cobalt, nickel and iron. *Carbon* **13**, 111–113 (1975).

[**178**] Earnshaw, A. & Harrington, T. J. *The chemistry of the transition elements*. (Oxford Univeristy Press, 1973).

[**179**] Mattevi, C., Kim, H. & Chhowalla, M. A review of chemical vapour deposition of graphene on copper. *J. Mater. Chem.* **21**, 3324–3334 (2011).

[**180**] Sutter, P., Hybertsen, M. S., Sadowski, J. T. & Sutter, E. Electronic Structure of Few-Layer Epitaxial Graphene on Ru(0001). *Nano Lett.* **9**, 2654–2660 (2009).

[**181**] Mathieu, G., Guiot, S. & Cabané, J. Solubilite du carbone dans l'argent, le cuivre et l'or. *Scr. Metall.* **7**, 421–425 (1973).

[**182**] McLellan, R. B. The solubility of carbon in solid gold, copper, and silver. *Scr. Metall.* **3**, 389–391 (1969).

[**183**] López, G. A. & Mittemeijer, E. J. The solubility of C in solid Cu. *Scr. Mater.* **51**, 1–5 (2004).

[**184**] *ASM Handbook Volume 3: Alloy Phase Diagrams*. (ASM International, 2002).

[**185**] Eizenberg, M. & Blakely, J. M. Carbon monolayer phase condensation on Ni(111). *Surf. Sci.* **82**, 228–236 (1979).

[**186**] Eizenberg, M. & Blakely, J. M. Carbon interaction with nickel surfaces: Monolayer formation and structural stability. *J. Chem. Phys.* **71**, 3467–3477 (1979).

[**187**] Lee, Y. *et al.* Wafer-scale synthesis and transfer of graphene films. *Nano Lett.* **10**, 490–493 (2010).

[**188**] Shin, D., Kim, H. R. & Hong, B. H. Gold nanoparticle-mediated non-covalent functionalization of graphene for field-effect transistors. *Nanoscale Adv.* **3**, 1404–1412 (2021).

[**189**] Park, S., Kim, H. R., Kim, J., Hong, B. H. & Yoon, H. J. Enhanced Thermopower of Saturated Molecules by Noncovalent Anchor-Induced Electron Doping of Single-Layer Graphene Electrode. *Adv. Mater.* **33**, 1–9 (2021).

[**190**] Ogawa, Y. *et al.* Domain Structure and Boundary in Single-Layer Graphene Grown on Cu(111) and Cu(100) Films. *J. Phys. Chem. Lett.* **3**, 219–226 (2012).

[**191**] Sun, L. *et al.* Chemical vapour deposition. *Nat. Rev. Methods Primers* **1**, 5 (2021).

[**192**] Kobayashi, T. *et al.* Production of a 100-m-long high-quality graphene transparent conductive film by roll-to-roll chemical vapor deposition and transfer process. *Appl. Phys. Lett.* **102**, 023112 (2013).

[**193**] Polsen, E. S., McNerny, D. Q., Viswanath, B., Pattinson, S. W. & John Hart, A. High-speed roll-to-roll manufacturing of graphene using a concentric tube CVD reactor. *Sci. Rep.* **5**, 10257 (2015).

[**194**] Kim, D. J. *et al.* Confocal laser scanning microscopy as a real-time quality-assessment tool for industrial graphene synthesis. *2D Mater.* **7**, 045014 (2020).

[**195**] Kaymak, N., Bayram, O., Tataroğlu, A., Bilge Ocak, S. & Oz Orhan, E. Electrical properties of Graphene/Silicon structure with Al2O3 interlayer. *J. Mater. Sci. Mater. Electron.* **31**, 9719–9725 (2020).

[**196**] Jin, Y. *et al.* Roles of H2 in annealing and growth times of graphene CVD synthesis over copper foil. *J. Mater. Chem. A* **2**, 16208–16216 (2014).

[**197**] Vlassiouk, I. *et al.* Role of hydrogen in chemical vapor deposition growth of large single-crystal graphene. *ACS Nano* **5**, 6069–6076 (2011).

[**198**] Zhang, X., Wang, L., Xin, J., Yakobson, B. I. & Ding, F. Role of hydrogen in graphene chemical vapor deposition growth on a copper surface. *J. Am. Chem. Soc.* **136**, 3040–3047 (2014).

[**199**] Ramlan, A. H. *et al.* Effects of hydrogen during annealing process of graphene synthesis via chemical vapor deposition. *Mater. Today Proc.* **7**, 675–685 (2019).

[**200**] Kraus, J., Böbel, L., Zwaschka, G. & Günther, S. Understanding the Reaction Kinetics to Optimize Graphene Growth on Cu by Chemical Vapor Deposition. *Ann. Phys.* **529**, 1–16 (2017).

[**201**] Kim, Y. S. *et al.* Methane as an effective hydrogen source for single-layer graphene synthesis on Cu foil by plasma enhanced chemical vapor deposition. *Nanoscale* **5**, 1221–1226 (2013).

[**202**] Li, X. *et al.* Transfer of large-area graphene films for high-performance transparent conductive electrodes. *Nano Lett.* **9**, 4359–4363 (2009).

[**203**] Choi, K. *et al.* Reduced Water Vapor Transmission Rate of Graphene Gas Barrier Films for Flexible Organic Field-Effect Transistors. *ACS Nano* **9**, 5818–5824 (2015).

[**204**] Park, J.-U., Nam, S., Lee, M.-S. & Lieber, C. M. Synthesis of monolithic graphene–graphite integrated electronics. *Nat. Mater.* **11**, 120–125 (2012).

[**205**] Kim, Y. *et al.* Vapor-Phase Molecular Doping of Graphene for High-Performance Transparent Electrodes. *ACS Nano* **8**, 868–874 (2014).

[**206**] Cançado, L. G. *et al.* Quantifying Defects in Graphene via Raman Spectroscopy at Different Excitation Energies. *Nano Lett.* **11**, 3190–3196 (2011).

[**207**] Cançado, L. G. *et al.* General equation for the determination of the crystallite size La of nanographite by Raman spectroscopy. *Appl. Phys. Lett.* **88**, 163106 (2006).

[**208**] Beams, R., Gustavo Cançado, L. & Novotny, L. Raman characterization of defects and dopants in graphene. *J. Phys. Condens. Matter* **27**, 083002 (2015).

[**209**] Lee, J. E., Ahn, G., Shim, J., Lee, Y. S. & Ryu, S. Optical separation of mechanical strain from charge doping in graphene. *Nat. Commun.* **3**, 1024 (2012).

[**210**] Mohiuddin, T. M. G. *et al.* Uniaxial strain in graphene by Raman spectroscopy: G peak splitting, Grüneisen parameters, and sample orientation. *Phys. Rev. B* **79**, 205433 (2009).

[**211**] Neumann, C. *et al.* Raman spectroscopy as probe of nanometre-scale strain variations in graphene. *Nat. Commun.* **6**, 8429 (2015).

[**212**] Jie, W., Yu Hui, Y., Zhang, Y., Ping Lau, S. & Hao, J. Effects of controllable biaxial strain on the Raman spectra of monolayer graphene prepared by chemical vapor deposition. *Appl. Phys. Lett.* **102**, 223112 (2013).

[**213**] Basko, D. M., Piscanec, S. & Ferrari, A. C. Electron-electron interactions and doping dependence of the two-phonon Raman intensity in graphene. *Phys. Rev. B* **80**, 165413 (2009).

[**214**] Kovalchuk, N. G. *et al.* Possibility of Determining the Graphene Doping Level Using Raman Spectra. *J. Appl. Spectrosc.* **84**, 995–998 (2018).

[**215**] Mueller, N. S. *et al.* Evaluating arbitrary strain configurations and doping in graphene with Raman spectroscopy. *2D Mater.* **5**, 015016 (2017).

[**216**] Graf, D. *et al.* Spatially resolved raman spectroscopy of single- and few-layer graphene. *Nano Lett.* **7**, 238–242 (2007).

[**217**] Park, J. S. *et al.* G′ band Raman spectra of single, double and triple layer graphene. *Carbon* **47**, 1303–1310 (2009).

[**218**] Ma, B., Rodriguez, R. D., Ruban, A., Pavlov, S. & Sheremet, E. The correlation between electrical conductivity and second-order Raman modes of laser-reduced graphene oxide. *Phys. Chem. Chem. Phys.* **21**, 10125–10134 (2019).

[**219**] Testa-Anta, M., Ramos-Docampo, M. A., Comesaña-Hermo, M., Rivas-Murias, B. & Salgueiriño, V. Raman spectroscopy to unravel the magnetic properties of iron oxide nanocrystals for bio-related applications. *Nanoscale Adv.* **1**, 2086–2103 (2019).

[**220**] Lee, K. S. *et al.* Raman microspectroscopy for microbiology. *Nat. Rev. Methods Primers* **1**, 80 (2021).

[**221**] Issi, J.-P., Araujo, P. T. & Dresselhaus, M. S. Electron and Phonon Transport in Graphene in and out of the Bulk. in *Physics of Graphene* 65–112 (Springer International Publishing Switzerland, 2014).

[**222**] Zólyomi, V., Koltai, J. & Kürti, J. Resonance Raman spectroscopy of graphite and

graphene. *Phys. status solidi* **248**, 2435–2444 (2011).

[**223**] Luo, Z., Cong, C., Zhang, J., Xiong, Q. & Yu, T. The origin of sub-bands in the Raman D-band of graphene. *Carbon* **50**, 4252–4258 (2012).

[**224**] Ferrari, A. C. Raman spectroscopy of graphene and graphite: Disorder, electron-phonon coupling, doping and nonadiabatic effects. *Solid State Commun.* **143**, 47–57 (2007).

[**225**] Ferrari, A. C. & Basko, D. M. Raman spectroscopy as a versatile tool for studying the properties of graphene. *Nat. Nanotechnol.* **8**, 235–246 (2013).

[**226**] Yang, D. *et al.* Chemical analysis of graphene oxide films after heat and chemical treatments by X-ray photoelectron and Micro-Raman spectroscopy. *Carbon* **47**, 145–152 (2009).

[**227**] Martins Ferreira, E. H. *et al.* Evolution of the Raman spectra from single-, few-, and many-layer graphene with increasing disorder. *Phys. Rev. B* **82**, 125429 (2010).

[**228**] Zhang, L. *et al.* Catalyst-free growth of nanographene films on various substrates. *Nano Res.* **4**, 315–321 (2011).

[**229**] Malard, L. M., Pimenta, M. A., Dresselhaus, G. & Dresselhaus, M. S. Raman spectroscopy in graphene. *Phys. Rep.* **473**, 51–87 (2009).

[**230**] Dresselhaus, M. S., Jorio, A. & Saito, R. Characterizing Graphene, Graphite, and Carbon Nanotubes by Raman Spectroscopy. *Annu. Rev. Condens. Matter Phys* **1**, 89–108 (2010).

[**231**] Dresselhaus, M. S., Dresselhaus, G., Saito, R. & Jorio, A. Raman spectroscopy of carbon nanotubes. *Phys. Rep.* **409**, 47–99 (2005).

[**232**] Yoon, D. *et al.* Variations in the Raman Spectrum as a Function of the Number of Graphene Layers. *J. Korean Phys. Soc.* **55**, 1299–1303 (2009).

[**233**] Das, A. *et al.* Monitoring dopants by Raman scattering in an electrochemically top-gated graphene transistor. *Nat. Nanotechnol.* **3**, 210–215 (2008).

[**234**] Milani, A. *et al.* Raman spectroscopy as a tool to investigate the structure and electronic properties of carbon-atom wires. *Beilstein J. Nanotechnol. 649* **6**, 480–491 (2015).

[**235**] Pisana, S. *et al.* Breakdown of the adiabatic Born-Oppenheimer approximation in graphene. *Nat. Mater.* **6**, 198–201 (2007).

[**236**] Sze, S. M. & Ng, K. K. *Physics of Semiconductor Devices*. (John Wiley & Sons, Inc., Hoboken, New Jersey., 2007).

[**237**] Hummel, R. E. *Electronic Properties of Materials*. (Springer New York, 2011). doi:10.1007/978-1-4419-8164-6.

[**238**] Klekachev, A. V. *et al.* The Electrochemical Society Interface Graphene Transistors and Photodetectors. *Electrochem. Soc. Interface* **22**, 63 (2013).

[**239**] Lee, C., Wei, X., Kysar, J. W. & Hone, J. of Monolayer Graphene. *Science* **321**, 385–388 (2008).

[**240**] Bolotin, K. I. *et al.* Ultrahigh electron mobility in suspended graphene. *Solid State Commun.* **146**, 351–355 (2008).

[**241**] Novoselov, K. S. *et al.* Two-dimensional gas of massless Dirac fermions in graphene. *Nature* **438**, 197–200 (2005).

[**242**] Zhang, Y., Tan, Y. W., Stormer, H. L. & Kim, P. Experimental observation of the quantum Hall effect and Berry's phase in graphene. *Nature* **438**, 201–204 (2005).

[**243**] Wang, F. *et al.* Gate-variable optical transitions in graphene. *Science* **320**, 206–209 (2008).

[**244**] Bonaccorso, F., Sun, Z., Hasan, T. & Ferrari, A. C. Graphene photonics and optoelectronics. *Nat. Photonics* **4**, 611–622 (2010).

[**245**] Vakil, A. & Engheta, N. Transformation optics using graphene. *Science* **332**, 1291–1294 (2011).

[**246**] Lee, S. K. *et al.* All graphene-based thin film transistors on flexible plastic substrates. *Nano Lett.* **12**, 3472–3476 (2012).

[**247**] Kim, Y. D. *et al.* Bright visible light emission from graphene. *Nat. Nanotechnol.* **10**, 676–681 (2015).

[**248**] Liu, C. H., Chang, Y. C., Norris, T. B. & Zhong, Z. Graphene photodetectors with ultra-broadband and high responsivity at room temperature. *Nat. Nanotechnol.* **9**, 273–278 (2014).

[**249**] Koppens, F. H. L. *et al.* Photodetectors based on graphene, other two-dimensional materials and hybrid systems. *Nat. Nanotechnol.* **9**, 780–793 (2014).

[**250**] Liu, M., Yin, X. & Zhang, X. Double-layer graphene optical modulator. *Nano Lett.* **12**, 1482–1485 (2012).

[**251**] Son, S. K. *et al.* Graphene hot-electron light bulb: Incandescence from hBN-encapsulated graphene in air. *2D Mater.* **5**, 011006 (2018).

[**252**] Geim, A. K. & Novoselov, K. S. The rise of graphene. *Nat. Mater.* **6**, 183–191 (2007).

[**253**] Morozov, S. V. *et al.* Giant intrinsic carrier mobilities in graphene and its bilayer. *Phys. Rev. Lett.* **100**, 016602 (2008).

[**254**] Chen, F., Xia, J., Ferry, D. K. & Tao, N. Dielectric screening enhanced performance in graphene FET. *Nano Lett.* **9**, 2571–2574 (2009).

[**255**] Chen, J. H., Jang, C., Xiao, S., Ishigami, M. & Fuhrer, M. S. Intrinsic and extrinsic performance limits of graphene devices on SiO 2. *Nat. Nanotechnol.* **3**, 206–209 (2008).

[**256**] Yavari, F. & Koratkar, N. Graphene-Based Chemical Sensors. *J. Phys. Chem. Lett.* **3**, 1746–1753 (2012).

[**257**] Fu, W. *et al.* Graphene transistors are insensitive to pH changes in solution. *Nano Lett.* **11**, 3597–3600 (2011).

[**258**] Mišković, Z. L. & Upadhyaya, N. Modeling Electrolytically Top-Gated Graphene. *Nanoscale Res. Lett.* **5**, 505–511 (2010).

[**259**] Heller, I. *et al.* Influence of electrolyte composition on liquid-gated carbon nanotube and graphene transistors. *J. Am. Chem. Soc.* **132**, 17149–17156 (2010).

[**260**] Cheng, Z., Li, Q., Li, Z., Zhou, Q. & Fang, Y. Suspended graphene sensors with improved signal and reduced noise. *Nano Lett.* **10**, 1864–1868 (2010).

[**261**] Chen, F., Qing, Q., Xia, J., Li, J. & Tao, N. Electrochemical gate-controlled charge transport in graphene in ionic liquid and aqueous solution. *J. Am. Chem. Soc.* **131**, 9908–9909 (2009).

[**262**] Xia, J. L., Chen, F., Wiktor, P., Ferry, D. K. & Tao, N. J. Effect of Top Dielectric Medium on Gate Capacitance of Graphene Field Effect Transistors: Implications in Mobility Measurements and Sensor Applications. *Nano Lett.* **10**, 5060–5064 (2010).

[**263**] Ristein, J. *et al.* Characteristics of solution gated field effect transistors on the basis of epitaxial graphene on silicon carbide. *J. Phys. D. Appl. Phys.* **43**, 345303 (2010).

[**264**] Ang, P. K., Chen, W., Wee, A. T. S. & Kian, P. L. Solution-gated epitaxial graphene as pH sensor. *J. Am. Chem. Soc.* **130**, 14392–14393 (2008).

[**265**] Georgakilas, V. *et al.* Functionalization of graphene: Covalent and non-covalent approaches, derivatives and applications. *Chem. Rev.* **112**, 6156–6214 (2012).

[**266**] Bottari, G. *et al.* Chemical functionalization and characterization of graphene-based materials. *Chem. Soc. Rev.* **46**, 4464–4500 (2017).

[**267**] Dankerl, M. *et al.* Graphene solution-gated field-effect transistor array for sensing applications. *Adv. Funct. Mater.* **20**, 3117–3124 (2010).

[**268**] Zhang, W., Wu, L., Li, Z. & Liu, Y. Doped graphene: Synthesis, properties and bioanalysis. *RSC Adv.* **5**, 49521–49533 (2015).

[**269**] Lerner, M. B. *et al.* Scalable Production of Highly Sensitive Nanosensors Based on Graphene Functionalized with a Designed G Protein-Coupled Receptor. *Nano Lett.* **14**, 2709–2714 (2014).

[**270**] Lu, Y., Goldsmith, B. R., Kybert, N. J. & Johnson, A. T. C. DNA-decorated graphene chemical sensors. *Appl. Phys. Lett.* **97**, 083107 (2010).

[**271**] Wang, Y., Shao, Y., Matson, D. W., Li, J. & Lin, Y. Nitrogen-Doped Graphene and Its Application in Electrochemical Biosensing. *ACS Nano* **4**, 1790–1798 (2010).

[**272**] Park, S. J. *et al.* Ultrasensitive Flexible Graphene Based Field-Effect Transistor (FET)-Type Bioelectronic Nose. *Nano Lett.* **12**, 5082–5090 (2012).

[**273**] Danielson, E. *et al.* Graphene based field-effect transistor biosensors functionalized using gas-phase synthesized gold nanoparticles. *Sensors Actuators B Chem.* **320**, 128432 (2020).

[**274**] Zhou, L. *et al.* Novel Graphene Biosensor Based on the Functionalization of Multifunctional Nano-bovine Serum Albumin for the Highly Sensitive Detection of Cancer Biomarkers. *Nano-Micro Lett.* **11**, 20 (2019).

[**275**] Kwong Hong Tsang, D. *et al.* Chemically Functionalised Graphene FET Biosensor for the Label-free Sensing of Exosomes. *Sci. Rep.* **9**, 13946 (2019).

[**276**] Lu, Y. *et al.* Graphene-protein bioelectronic devices with wavelength-dependent photoresponse. *Appl. Phys. Lett.* **100**, 033110 (2012).

[**277**] Alava, T. *et al.* Control of the graphene-protein interface is required to preserve adsorbed protein function. *Anal. Chem.* **85**, 2754–2759 (2013).

[**278**] Niyogi, S. *et al.* Spectroscopy of covalently functionalized graphene. *Nano Lett.* **10**, 4061–4066 (2010).

[**279**] Englert, J. M. *et al.* Covalent bulk functionalization of graphene. *Nat. Chem.* **3**, 279–286 (2011).

[**280**] Xia, Z. *et al.* Graphene-Pyrene Nanocomposites Obtained Using Azide Chemistry. *J. Nanosci. Nanotechnol.* **18**, 1290–1295 (2017).

[**281**] Kong, B. S., Geng, J. & Jung, H. T. Layer-by-layer assembly of graphene and gold nanoparticles by vacuum filtration and spontaneous reduction of gold ions. *Chem. Commun.* 2174–2176 (2009).

[**282**] Zaniewski, A. M., Trimble, C. J. & Nemanich, R. J. Modifying the chemistry of graphene with substrate selection: A study of gold nanoparticle formation. *Appl. Phys. Lett.* **106**, 123104 (2015).

[**283**] Holmes, J. Photoelectron Spectroscopy. in *Encyclopedia of Spectroscopy and Spectrometry* 618 (Elsevier, 2017). doi:10.1016/B978-0-12-803224-4.00355-1.

[**284**] Kovtun, A. *et al.* Accurate chemical analysis of oxygenated graphene-based materials using X-ray photoelectron spectroscopy. *Carbon* **143**, 268–275 (2019).

[**285**] Estrade-Szwarckopf, H. XPS photoemission in carbonaceous materials: A 'defect' peak beside the graphitic asymmetric peak. *Carbon* **42**, 1713–1721 (2004).

[**286**] Prince, K. C. *et al.* Core-level photoemission from graphite. *Phys. Rev. B* **62**, 6866–6868 (2000).

[**287**] Klyushin, A. Y., Rocha, T. C. R., Hävecker, M., Knop-Gericke, A. & Schlögl, R. A near ambient pressure XPS study of Au oxidation. *Phys. Chem. Chem. Phys.* **16**, 7881–7886 (2014).

[**288**] Radnik, J., Mohr, C. & Claus, P. On the origin of binding energy shifts of core levels of supported gold nanoparticles and dependence of pretreatment and material synthesis. *Phys. Chem. Chem. Phys.* **5**, 172–177 (2003).

[**289**] Sankar, M. *et al.* Synthesis of stable ligand-free gold-palladium nanoparticles using a simple excess anion method. *ACS Nano* **6**, 6600–6613 (2012).

[**290**] Casaletto, M. P., Longo, A., Martorana, A., Prestianni, A. & Venezia, A. M. XPS study of supported gold catalysts: The role of Au0 and Au+δ species as active sites. *Surf. Interface Anal.* **38**, 215–218 (2006).

[**291**] Anderson, D. P. *et al.* Chemically-synthesised, atomically-precise gold clusters deposited and activated on titania. *Phys. Chem. Chem. Phys.* **15**, 3917–3929 (2013).

[**292**] Yang, Y. W. & Fan, L. J. High resolution XPS study of decanethiol on Au(111): Single sulfur-gold bonding interaction. *Langmuir* **18**, 1157–1164 (2002).

[**293**] Ohe, C. *et al.* Carboxylate-counterion interactions and changes in these interactions during photopolymerization of a long-chain diacetylene monocarboxylic acid at air-water interfaces: External infrared reflection absorption spectroscopic study. *J. Phys. Chem. B* **103**, 435–444 (1999).

[**294**] Ellis, H. A., White, N. A. S., Taylor, R. A. & Maragh, P. T. Infrared, X-ray and microscopic studies on the room temperature structure of anhydrous lead (II) n-alkanoates. *J. Mol. Struct.* **738**, 205–210 (2005).

[**295**] Uznanski, P., Zakrzewska, J., Favier, F., Kazmierski, S. & Bryszewska, E. Synthesis and characterization of silver nanoparticles from (bis)alkylamine silver carboxylate precursors. *J. Nanoparticle Res.* **19**, 121 (2017).

[**296**] Moulder, J. F., Stickle, W. F., Sobol, P. E. & Bomben, K. D. *Handbook of X-ray photoelectron spectroscopy: a reference book of standard spectra for identification and interpretation of XPS data. Surface and Interface Analysis* (Physical Electronics Division, Perkin-Elmer Corporation, 1992).

[**297**] González-Elipe, A. R., Espinós, J. P., Munuera, G., Sanz, J. & Serratosa, J. M. *Bonding-state characterization of constituent elements in phyllosilicate minerals by XPS and NMR. Journal of Physical Chemistry* vol. 92 (1988).

[**298**] Wagner, C. D. *et al.* Auger and photoelectron line energy relationships in aluminum–oxygen and silicon–oxygen compounds. *J. Vac. Sci. Technol.* **21**, 933–944 (1982).

[**299**] Chen, J. H. *et al.* Diffusive charge transport in graphene on SiO2. *Solid State Commun.* **149**, 1080–1086 (2009).

[**300**] Hwang, E. H., Adam, S. & Sarma, S. Das. Carrier transport in two-dimensional graphene layers. *Phys. Rev. Lett.* **98**, 186806 (2007).

[**301**] Love, J. C., Estroff, L. A., Kriebel, J. K., Nuzzo, R. G. & Whitesides, G. M. Self-Assembled Monolayers of Thiolates on Metals as a Form of Nanotechnology. *Chem. Rev.* **105**, 1103–1170 (2005).

[**302**] Pensa, E. *et al.* The chemistry of the sulfur-gold interface: In search of a unified model. *Acc. Chem. Res.* **45**, 1183–1192 (2012).

[**303**] Xue, Y., Li, X., Li, H. & Zhang, W. Quantifying thiol-gold interactions towards the efficient strength control. *Nat. Commun.* **5**, 1–9 (2014).

[**304**] Shin, D., Kim, K. & Shin, K. S. Adsorbate-Induced Changes in Surface Potential of Gold Nanoparticles Revealed by Raman Spectroscopy. *ChemPhysChem* **11**, 83–86 (2010).

[**305**] Liyanage, T., Nagaraju, M., Johnson, M., Muhoberac, B. B. & Sardar, R. Reversible Tuning of the Plasmoelectric Effect in Noble Metal Nanostructures Through Manipulation of Organic Ligand Energy Levels. *Nano Lett.* **20**, 192–200 (2020).

[**306**] Gao, W. & Huang, R. Thermomechanics of monolayer graphene: Rippling, thermal expansion and elasticity. *J. Mech. Phys. Solids* **66**, 42–58 (2014).

[**307**] Jiang, J. W., Wang, J. S. & Li, B. Thermal expansion in single-walled carbon nanotubes and graphene: Nonequilibrium Green's function approach. *Phys. Rev. B* **80**, 205429 (2009).

[**308**] Mounet, N. & Marzari, N. First-principles determination of the structural, vibrational and thermodynamic properties of diamond, graphite, and derivatives. *Phys. Rev. B* **71**, 205214 (2005).

[**309**] Yoon, D., Son, Y. W. & Cheong, H. Negative thermal expansion coefficient of graphene measured by raman spectroscopy. *Nano Lett.* **11**, 3227–3231 (2011).

[**310**] Langer, J. *et al.* Present and future of surface-enhanced Raman scattering. *ACS Nano* **14**, 28–117 (2020).

[**311**] Fang, W. *et al.* Quantizing single-molecule surface-enhanced Raman scattering with DNA origami metamolecules. *Sci. Adv.* **5**, eaau4506 (2019).

[**312**] Osváth, Z. *et al.* The structure and properties of graphene on gold nanoparticles. *Nanoscale* **7**, 5503–5509 (2015).

[**313**] Gao, J., Hu, Y., Li, S., Zhang, Y. & Chen, X. Adsorption of benzoic acid, phthalic acid on gold substrates studied by surface-enhanced Raman scattering spectroscopy and density functional theory calculations. *Spectrochim. Acta A* **104**, 41–47 (2013).

[**314**] Madzharova, F., Heiner, Z. & Kneipp, J. Surface-Enhanced Hyper Raman Spectra of Aromatic Thiols on Gold and Silver Nanoparticles. *J. Phys. Chem. C* **124**, 6233–6241 (2020).

[**315**] Guerrini, L. *et al.* Chemical speciation of heavy metals by surface-enhanced Raman scattering spectroscopy: Identification and quantification of inorganic- and methyl-mercury in water. *Nanoscale* **6**, 8368–8375 (2014).

[**316**] Han, D., Lim, S. Y., Kim, B. J., Piao, L. & Chung, T. D. Mercury(ii) detection by SERS based on a single gold microshell. *Chem. Commun.* **46**, 5587–5589 (2010).

[**317**] Guselnikova, O., Svorcik, V., Lyutakov, O., Chehimi, M. M. & Postnikov, P. S. Preparation of Selective and Reproducible SERS Sensors of Hg2+ Ions via a Sunlight-Induced Thiol–Yne Reaction on Gold Gratings. *Sensors* **19**, 2110 (2019).

[**318**] Guo, X. *et al.* Recyclable Raman chip for detection of trace Mercury ions. *Chem. Eng. J.* **390**, 124528 (2020).

[**319**] Sun, Z., Du, J. & Jing, C. Recent progress in detection of mercury using surface enhanced Raman spectroscopy — A review. *J. Environ. Sci.* **39**, 134–143 (2016).

[**320**] Iatsunskyi, I. *et al.* Raman spectroscopy of nanostructured silicon fabricated by metal-assisted chemical etching. *Opt. Micro- Nanometrology V* **9132**, 913217 (2014).

[**321**] Pisana, S. *et al.* Breakdown of the adiabatic Born-Oppenheimer approximation in graphene. *Nat. Mater.* **6**, 198–201 (2007).

[**322**] Kim, M., Safron, N. S., Huang, C., Arnold, M. S. & Gopalan, P. Light-driven reversible modulation of doping in graphene. *Nano Lett.* **12**, 182–187 (2012).

[**323**] Kim, Y. *et al.* A highly conducting graphene film with dual-side molecular n-doping. *Nanoscale* **6**, 9545–9549 (2014).

[**324**] Park, S., Kang, H. & Yoon, H. J. Structure–thermopower relationships in molecular thermoelectrics. *J. Mater. Chem. A* **7**, 14419–14446 (2019).

[**325**] Reddy, P., Jang, S. Y., Segalman, R. A. & Majumdar, A. Thermoelectricity in molecular junctions. *Science* **315**, 1568–1571 (2007).

[**326**] Park, S. & Yoon, H. J. New Approach for Large-Area Thermoelectric Junctions with a Liquid Eutectic Gallium-Indium Electrode. *Nano Lett.* **18**, 7715–7718 (2018).

[**327**] Cui, L., Miao, R., Jiang, C., Meyhofer, E. & Reddy, P. Perspective: Thermal and thermoelectric transport in molecular junctions. *J. Chem. Phys.* **146**, 092201 (2017).

[**328**] Park, S., Cho, N. & Yoon, H. J. Two Different Length-Dependent Regimes in Thermoelectric Large-Area Junctions of n-Alkanethiolates. *Chem. Mater.* **31**, 5973–5980 (2019).

[**329**] Kang, S. *et al.* Tunneling and thermoelectric characteristics of N-heterocyclic carbene-based large-area molecular junctions. *Chem. Commun.* **55**, 8780–8783 (2019).

[**330**] Paulsson, M. & Datta, S. Thermoelectric effect in molecular electronics. *Phys. Rev. B* **67**, 241403 (2003).

[**331**] Rincón-García, L., Evangeli, C., Rubio-Bollinger, G. & Agraït, N. Thermopower measurements in molecular junctions. *Chem. Soc. Rev.* **45**, 4285–4306 (2016).

[**332**] Wang, K., Meyhofer, E. & Reddy, P. Thermal and Thermoelectric Properties of Molecular Junctions. *Adv. Funct. Mater.* **30**, 1904534 (2020).

[**333**] Tan, A. *et al.* Effect of length and contact chemistry on the electronic structure and thermoelectric properties of molecular junctions. *J. Am. Chem. Soc.* **133**, 8838–8841 (2011).

[**334**] Li, Y., Xiang, L., Palma, J. L., Asai, Y. & Tao, N. Thermoelectric effect and its dependence on molecular length and sequence in single DNA molecules. *Nat. Commun.* **7**, 1–8 (2016).

[**335**] Hüser, F. & Solomon, G. C. From chemistry to functionality: Trends for the length dependence of the thermopower in molecular junctions. *J. Phys. Chem. C* **119**, 14056–14062 (2015).

[**336**] Widawsky, J. R. *et al.* Length-dependent thermopower of highly conducting Au-C bonded single molecule junctions. *Nano Lett.* **13**, 2889–2894 (2013).

[**337**] Chang, W. B. *et al.* Controlling the thermoelectric properties of thiophene-derived single-molecule junctions. *Chem. Mater.* **26**, 7229–7235 (2014).

[**338**] Malen, J. A. *et al.* The nature of transport variations in molecular heterojunction electronics. *Nano Lett.* **9**, 3406–3412 (2009).

[**339**] Chang, W. B., Russ, B., Ho, V., Urban, J. J. & Segalman, R. A. Gold nanocrystal arrays as a macroscopic platform for molecular junction thermoelectrics. *Phys. Chem. Chem. Phys.* **17**, 6207–6211 (2015).

[**340**] Sangtarash, S. & Sadeghi, H. Radical enhancement of molecular thermoelectric efficiency.

Nanoscale Adv. **2**, 1031–1035 (2020).

[**341**] Baheti, K. *et al.* Probing the chemistry of molecular heterojunctions using thermoelectricity. *Nano Lett.* **8**, 715–719 (2008).

[**342**] Cui, L. *et al.* Peltier cooling in molecular junctions. *Nat. Nanotechnol.* **13**, 122–127 (2018).

[**343**] Park, S., Kang, S. & Yoon, H. J. Power Factor of One Molecule Thick Films and Length Dependence. *ACS Cent. Sci.* **5**, 1975–1982 (2019).

[**344**] Gehring, P. *et al.* Complete mapping of the thermoelectric properties of a single molecule. *Nat. Nanotechnol.* **16**, 426–430 (2021).

[**345**] Butcher, P. N. Thermal and electrical transport formalism for electronic microstructures with many terminals. *J. Phys. Condens. Matter* **2**, 4869 (1990).

[**346**] Malen, J. A. *et al.* Identifying the length dependence of orbital alignment and contact coupling in molecular heterojunctions. *Nano Lett.* **9**, 1164–1169 (2009).

[**347**] Yee, S. K., Malen, J. A., Majumdar, A. & Segalman, R. A. Thermoelectricity in fullerene-metal heterojunctions. *Nano Lett.* **11**, 4089–4094 (2011).

[**348**] Cho, N. *et al.* Superexchange Coupling-Induced Enhancements of Thermoelectric Performance in Saturated Molecules. *Nano Lett.* **21**, 360–366 (2021).

[**349**] Song, P. *et al.* Noncovalent Self-Assembled Monolayers on Graphene as a Highly Stable Platform for Molecular Tunnel Junctions. *Adv. Mater.* **28**, 631–639 (2016).

[**350**] Kong, G. D. & Yoon, H. J. Influence of Air-Oxidation on Rectification in Thiol-Based Molecular Monolayers. *J. Electrochem. Soc.* **163**, G115–G121 (2016).

[**351**] Jiang, L., Yuan, L., Cao, L. & Nijhuis, C. A. Controlling leakage currents: The role of the binding group and purity of the precursors for self-assembled monolayers in the performance of molecular diodes. *J. Am. Chem. Soc.* **136**, 1982–1991 (2014).

[**352**] Chiechi, R. C. *et al.* Eutectic Gallium–Indium (EGaIn): A Moldable Liquid Metal for Electrical Characterization of Self-Assembled Monolayers. *Angew. Chemie Int. Ed.* **47**, 142–144 (2008).

[**353**] Giannozzi, P. *et al.* QUANTUM ESPRESSO: a modular and open-source software project for quantumsimulations of materials. *J. Phys. Condens. Matter* **21**, 395502 (2009).

[**354**] Pujari, B. S., Gusarov, S., Brett, M. & Kovalenko, A. Single-side-hydrogenated graphene: Density functional theory predictions. *Phys. Rev. B* **84**, 041402 (2011).

[**355**] Li, J. & Wang, F. Water graphene contact surface investigated by pairwise potentials from force-matching PAW-PBE with dispersion correction. *J. Chem. Phys.* **146**, 054702 (2017).

[**356**] Rusnak, A. J., Pinnick, E. R., Calderon, C. E. & Wang, F. Static dielectric constants and molecular dipole distributions of liquid water and ice-Ih investigated by the PAW-PBE exchange-correlation functional. *J. Chem. Phys.* **137**, 034510 (2012).

[**357**] Peng, Q. *et al.* Predicting Elastic Properties of β-HMX from First-Principles Calculations. *J. Phys. Chem. B* **119**, 5896–5903 (2015).

[**358**] Partoens, B. & Peeters, F. M. From graphene to graphite: Electronic structure around the K point. *Phys. Rev. B* **74**, 075404 (2006).

[**359**] O'Mahony, S. *et al.* Nanoscale dynamics and protein adhesivity of alkylamine self-assembled monolayers on graphene. *Langmuir* **29**, 7271–7282 (2013).

[**360**] Long, B. *et al.* Non-Covalent Functionalization of Graphene Using Self-Assembly of Alkane-Amines. *Adv. Funct. Mater.* **22**, 717–725 (2012).

[**361**] Chen, C. F. *et al.* Controlling inelastic light scattering quantum pathways in graphene. *Nature* **471**, 617–620 (2011).

[**362**] Woo Kim, N. *et al.* Infrared spectroscopy of large scale single layer graphene on self assembled organic monolayer. *Appl. Phys. Lett.* **104**, 041904 (2014).

[**363**] Pisana, S. *et al.* Breakdown of the adiabatic Born–Oppenheimer approximation in graphene. *Nat. Mater.* **6**, 198–201 (2007).

[**364**] Vilan, A., Aswal, D. & Cahen, D. Large-Area, Ensemble Molecular Electronics: Motivation and Challenges. *Chem. Rev.* **117**, 4248–4286 (2017).

[**365**] Xiang, D., Wang, X., Jia, C., Lee, T. & Guo, X. Molecular-Scale Electronics: From Concept to Function. *Chem. Rev.* **116**, 4318–4440 (2016).

[**366**] Sun, L. *et al.* Single-molecule electronics: from chemical design to functional devices. *Chem. Soc. Rev.* **43**, 7378–7411 (2014).

[**367**] Hung, S. W., Kikugawa, G. & Shiomi, J. Mechanism of Temperature Dependent Thermal Transport across the Interface between Self-Assembled Monolayer and Water. *J. Phys. Chem. C* **120**, 26678–26685 (2016).

[**368**] Kikugawa, G. *et al.* A molecular dynamics study on heat transfer characteristics at the interfaces of alkanethiolate self-assembled monolayer and organic solvent. *J. Chem. Phys.* **130**, 074706 (2009).

[**369**] Kuang, S. & Gezelter, J. D. Simulating interfacial thermal conductance at metal-solvent interfaces: The role of chemical capping agents. *J. Phys. Chem. C* **115**, 22475–22483 (2011).

[**370**] Luo, T. & Lloyd, J. R. Non-equilibrium molecular dynamics study of thermal energy transport in Au–SAM–Au junctions. *Int. J. Heat Mass Transf.* **53**, 1–11 (2010).

[**371**] Majumdar, S. *et al.* Vibrational mismatch of metal leads controls thermal conductance of self-assembled monolayer junctions. *Nano Lett.* **15**, 2985–2991 (2015).

[**372**] Sun, X. *et al.* Interfacial Heterogeneity of Surface Energy in Organic Field-Effect Transistors. *Adv. Mater.* **23**, 1009–1014 (2011).

[**373**] Patel, H. A., Garde, S. & Keblinski, P. Thermal Resistance of Nanoscopic Liquid−Liquid Interfaces: Dependence on Chemistry and Molecular Architecture. *Nano Lett.* **5**, 2225–2231 (2005).

[**374**] Goicochea, J. V., Hu, M., Michel, B. & Poulikakos, D. Surface functionalization mechanisms of enhancing heat transfer at solid-liquid interfaces. *J. Heat Transfer* **133**, (2011).

[**375**] Li, Q., Strange, M., Duchemin, I., Donadio, D. & Solomon, G. C. A Strategy to Suppress Phonon Transport in Molecular Junctions Using π-Stacked Systems. *J. Phys. Chem. C* **121**, 7175–7182 (2017).

[**376**] Zarudnev, E., Stepanian, S., Adamowicz, L. & Karachevtsev, V. Noncovalent Interaction of Graphene with Heterocyclic Compounds: Benzene, Imidazole, Tetracene, and Imidazophenazines. *ChemPhysChem* **17**, 1204–1212 (2016).

[**377**] Quek, S. Y., Choi, H. J., Louie, S. G. & Neaton, J. B. Thermopower of amine-gold-linked aromatic molecular junctions from first principles. *ACS Nano* **5**, 551–557 (2011).

[**378**] Yamada, T., Masuzawa, T., Ebisudani, T., Okano, K. & Taniguchi, T. Field emission characteristics from graphene on hexagonal boron nitride. *Appl. Phys. Lett.* **104**, 221603 (2014).

[**379**] Boutchich, M. *et al.* Atmospheric pressure route to epitaxial nitrogen-doped trilayer

graphene on 4H-SiC (0001) substrate. *Appl. Phys. Lett.* **105**, 233111 (2014).

[**380**] Fei, Z. *et al.* Gate-tuning of graphene plasmons revealed by infrared nano-imaging. *Nature* **487**, 82–85 (2012).

[**381**] Wang, L. *et al.* Negligible environmental sensitivity of graphene in a hexagonal boron nitride/graphene/h-BN sandwich structure. *ACS Nano* **6**, 9314–9319 (2012).

[**382**] Cao, G. *et al.* Chemical environment dominated Fermi level pinning of a graphene gas sensor. *Carbon* **124**, 57–63 (2017).

[**383**] Dawood, O. M. *et al.* Dynamic modulation of the Fermi energy in suspended graphene backgated devices. *Sci. Technol. Adv. Mater.* **20**, 568–579 (2019).

[**384**] Milowska, K. Z. & Majewski, J. A. Stability and electronic structure of covalently functionalized graphene layers. *Phys. status solidi* **250**, 1474–1477 (2013).

[**385**] Schiros, T. *et al.* Connecting dopant bond type with electronic structure in n-doped graphene. *Nano Lett.* **12**, 4025–4031 (2012).

[**386**] Lee, S. H. *et al.* Band gap opening by two-dimensional manifestation of peierls instability in graphene. *ACS Nano* **5**, 2964–2969 (2011).

[**387**] García-Lastra, J. M. Strong dependence of band-gap opening at the Dirac point of graphene upon hydrogen adsorption periodicity. *Phys. Rev. B* **82**, 235418 (2010).

[**388**] Boukhvalov, D. W. & Katsnelson, M. I. Tuning the gap in bilayer graphene using chemical functionalization: Density functional calculations. *Phys. Rev. B* **78**, 085413 (2008).

[**389**] Luo, B. *et al.* Synthesis of Diamond-like Carbon as a Dielectric Platform for Graphene Field Effect Transistors. *ACS Appl. Nano Mater.* **4**, 1385–1393 (2021).

[**390**] Walter, A. L. *et al.* Electronic structure of graphene on single-crystal copper substrates. *Phys. Rev. B* **84**, 195443 (2011).

[**391**] Cho, S. J. *et al.* Molecularly Controlled Stark Effect Induces Significant Rectification in Polycyclic-Aromatic-Hydrocarbon-Terminated n-Alkanethiolates. *Nano Lett.* **19**, 545–553 (2019).

[**392**] Neaton, J. B., Hybertsen, M. S. & Louie, S. G. Renormalization of molecular electronic levels at metal-molecule interfaces. *Phys. Rev. Lett.* **97**, 216405 (2006).

[**393**] Perrin, M. L. *et al.* Large tunable image-charge effects in single-molecule junctions. *Nat. Nanotechnol.* **8**, 282–287 (2013).

[**394**] Kaun, C. C. & Guo, H. Resistance of Alkanethiol Molecular Wires. *Nano Lett.* **3**, 1521–1525 (2003).

[**395**] Zhou, Y. X. *et al.* First-principles study of length dependence of conductance in alkanedithiols. *J. Chem. Phys.* **128**, 044704 (2008).

요 약 (국문초록)

비공유 화학적 도핑을 이용한 단일층 그래핀 소자의 전자특성 최적화

2004년 그래핀은 테이프를 이용한 (고배향 열분해성) 흑연(highly oriented pyrolytic graphite; HOPG)으로부터의 박리를 통해 최초 발견되었다. 이후 수많은 연구들에 의해 그래핀이 우수한 열적, 기계적, 전기적, 광학적 특성을 지녔음이 알려졌다. 2009년에 이르러 화학기상증착(chemical vapor deposition; CVD) 방식을 이용한 다결정 그래핀의 대면적 합성이 실험적으로 가능해졌고, 이로써 그래핀이 다양한 분야에 응용될 수 있는 발판이 마련되었다. 특히 그래핀의 응용분야 중 전기전자특성을 이용한 분야가 각광을 받고 있다. 그래핀은 높은 전자이동도, 전기전도도 및 열전도도를 지닌 재료이며, 밀접결합(tight-binding; TB) 근사 모형을 이용하여 계산한, 결함이 없는 단결정 단층 그래핀의 밴드갭(band gap)은 0임이 밝혀졌다.

재료의 전자특성 조절은 전자소자로의 응용에 필수적 공정이고, 도핑은 전자특성 조절에 주로 쓰이는 방법 중 하나이다. 그래핀에 도핑 처리를 함으로써 밴드갭, 전기전도도 및 일함수와 같은 전기전자특성을 조절할 수 있다. 그래핀에 대한 도핑 방법으로는 원자 치환, 전계 인가, 분자나 금속 나노입자 등의 물리적 흡착 등이 있다. 이 중 물리적 흡착 방식은 결함 없이 간단하고 우수한 도핑 효과를 얻을 수 있어 그래핀 도핑 방법으로 널리 사용되고 있다. 본 논문에서는 화학기상증착 방식으로 합성한 그래핀의 전자특성 최적화 방법 및 전자소자로의 응용에 관한 연구를 다루었다. 그래핀의 전자특성 최적화 방식으로 물리적 흡착을 통한 비공유 화학적 도핑을 택하였으며, 도핑된 그래핀의 전자소자로의 응용 가능성에 대하여 확인하였다.

제1장에서는 그래핀의 물리적 특성 중 전기전자특성에 초점을 맞춰 설명하였다. 또한, 연구에 사용한 도핑 방법과 도핑된 그래핀의 전하 이동현상에 관하여 소개하였다.

제2장에서는 그래핀의 합성, 전사 및 도핑 방법에 관하여 서술하였다. 연구에 사용된 그래핀은 화학기상증착 방식으로 합성되었으며, 합성된 그래핀은 구리 식각 및 전사 공정을 통해 소자 연구를 위한 시편으로 제작되었다. 그래핀은 자기조립단층(self-assembled monolayer; SAM)을 형성하는 분자 외 다양한 나노물질을 이용한 물리적 흡착 방식에 의해 화학적 도핑된다. 라만 분광분석을 통해 합성 및 도핑 직후의 그래핀 시편의 품질을 평가하였고, 3 전극 시스템을 이용한 전계효과 트랜지스터를 제작하여 그래핀의 전자특성을 분석하였다.

제3장에서는 화학기상증착 방식으로 합성한 그래핀에 다양한 나노물질을 차례로 제공함으로써 화학적 도핑 효과의 변화를 나타낸 전자소자 연구를 기술하였다. 그래핀 표면에 금 나노입자를 물리적 흡착 방식으로 도핑하여 비공유 기능화하고, 이를 이용한 그래핀을 전계효과 트랜지스터 소자로 제작하였다. 제작된 소자에 존재하는 금 나노입자에 4-머캅토벤조산(4-mercaptobenzoic acid; 4-MBA) 분자를 흡착시킴으로써 자기조립단층을 형성케 한다. 이때 수은 이온을 주입하면 자기조립단층을 형성한 4-MBA 분자의 카복시기(carboxyl group)가 리간드로 작용하여 수은 이온을 포획하면서 킬레이트(chelate) 복합체를 구성한다. 각 단계의 그래핀 전계효과 트랜지스터 소자의 전자특성 분석을 통해, 각 나노물질 요소에 의해 그래핀 표면의 도핑 효과가 미세 조정됨을 알 수 있다. 본 연구를 통해 그래핀 전계효과 트랜지스터의 화학적 기능화에 대한 가능성을 확인하였다.

제4장에서는 화학기상증착 방식으로 합성한 그래핀에 *n*-알킬아민(*n*-alkylamine; H_2NC_n) 분자를 도입함으로써, n형 도핑된 그래핀을 이용한 열전소자 성능의 향상에 관하여 기술하였다. *n*-알킬아민 분자는 그래핀 표면에서 자기조립단층을 형성하고 비공유 기능화를 통해 전자를 그래핀에 제공한다. 탄소사슬 길이가 각기 다른 *n*-알킬아민 분자를 이용하여 도핑한 그래핀을 3 전극 시스템을 통해 분석함으로써, 서로 다른 길이의 분자를 통해 그래핀 시편의 전하운반자 농도의 조절이 가능함을 확인하였다. *n*-알킬아민 분자의 자기조립단층이 형성된 각 그래핀 시편 위로 산화갈륨(Ga_2O_3) 박막층 및 갈륨-인듐 공융합금(eutectic Ga-In alloy; EGaIn) 벌크층을 차례로 적층하여 열전소자를 제작하였다. *n*-알킬아민 분자의 비공유 접합에 의해 유도 갭 상태(induced-gap state)가 그래핀 열전소자(SLG//H_2NC_n//Ga_2O_3/EGaIn)에 도입되었다. 금 박막층과 *n*-알케인싸이올레이트(*n*-alkanethiolates; SC_n) 분자의 접합으로 구성된 종래의 열전소자(Au/SC_n//Ga_2O_3/EGaIn)와의 비교를 통해, 상기한 방식으로 제작된 그래핀 열전소자가 우수한 열전특성을 지니고 있음을 증명하였다.

주요어: 그래핀, 화학적 도핑, 자기조립단층, 비공유 기능화, 전계효과 트랜지스터, 열전소자

학 번: 2016-20339